NUMERICAL SIMULATION OF NONLINEAR INTERACTION BETWEEN STRUCTURES AND STEEP WAVES

by

Qingwei Ma

B.Eng., MSc

A thesis submitted for the degree of

Doctor of Philosophy

Department of Mechanical Engineering

University College London

1998

ABSTRACT

Responding to great concerns about the interaction between steep waves and structures in naval architecture and offshore engineering, a methodology and corresponding numerical algorithm for computing three-dimensional inviscid flow with a free surface are developed based on a fully nonlinear theory in this thesis. The associated boundary value problem is solved using a finite element method. In order to chose an efficient solver for algebraic equations, a direct method and an iterative method with two different preconditioners are compared to each other, which leads to the suggestion that the conjugate gradient method with an SSOR preconditioner is the most suitable for the problem of concern. Furthermore, the radiation condition at a truncated boundary is imposed with an associated damping coefficient optimised to reduce the reflection of waves. In addition, an analytical solution for transient standing waves in a circular tank is derived using second order theory, which provides a tool to validate the numerical method.

The developed numerical method is first utilised in simulating the sloshing wave in a tank generated by initial disturbance on the free surface and by the translational motion of the tank. Numerical results are compared with analytical solutions in several cases, which show that the numerical method can be very accurate. The features of the steep sloshing waves are then examined.

In the second application, the interaction between vertical cylinders and waves generated by a wave maker is investigated. The motion of the wavemaker can be specified accordingly, in order to generate monochromatic, bichromatic or irregular progressive waves. The forces on one and two cylinders are obtained and compared with published data. The steep waves and their effects on hydrodynamic loads are analysed.

It is concluded that the developed methodology based on the finite element method is a good alternative to the existing techniques for the simulation of steep waves. Its accuracy, flexibility and efficiency demonstrated by various numerical examples appear to be quite favourable.

ACKNOWLEDGEMENTS

This study was carried out within the framework of two research contracts. One is entitled 'Interaction of steep waves with structures' included in the managed programme of research on the Uncertainties in Loads on offshore Structures (ULOS). The contract was funded by the Marine Technology Directorate Ltd and offshore industries. The other is 'Investigation of ringing by an intermediate method between fully nonlinear and slender body theories', which was funded by the UK Engineering and Physical Sciences Research Council. Both financial supports are gratefully acknowledged.

I would like to express my sincere gratitude to Dr. GX Wu for his guidance and constant encouragement and for his comments on the draft of the thesis. I would also like to thank Professor R. Eatock Taylor and Dr. A.G.L. Borthwick of University of Oxford for their invaluable suggestions and discussions in the collaboration of the above two projects.

In addition, I am indebted to Dr. D. Davis, Dr. D.M. Greaves and Dr. T.J. Sutton in this department, who read the manuscript in detail, and to Professor R. Eatock Taylor of University of Oxford who read Chapter 9. Their suggestions resulted in significant improvement.

I also thank my wife, my two daughters and my father for their unconditional support and endless patience, without which this work would not have been completed.

Finally I would like to take this opportunity to pay my sincere tribute to my mother, who passed away last year, during the course of my study, and to whom I dedicate this thesis.

CONTENTS

LIST OF FIGURES

LIST OF TABLES

LIST OF SYMBOLS

a	amplitude of wavemaker, standing wave and motion of a tank
c	phase velocity of wave
d	water depth
$\boldsymbol{e}_x, \boldsymbol{e}_y, \boldsymbol{e}_z$	unit vector in the x-, y- and z- direction respectively
e	represent an element
$e_1, e_2, e_3, \cdots$	represent elements in element patch
f	nondimensional force
f_p	velocity potential on the free surface at any time
f_n	normal velocity of bodies
g	acceleration due to gravity
k	wave number
$\boldsymbol{n}$	normal vector out of fluid domain
n_x, n_y, n_z	components of $\boldsymbol{n}$
p	water pressure; p in nondimensional form
t	time
Δt	time step
$\boldsymbol{u}$	velocity of fluid
u, v, w	velocity components of fluid
x, y, z	spatial coordinates in a fixed system unless mentioned otherwise
x_b, y_b, z_b	spatial coordinates in a moving system fixed on a body
x_d	coordinate of starting point of damping zone
$\{x\}$	unknown vector in algebraic equations
$[A]$	matrix of algebraic equations
A_{IJ}	influence coefficients in finite element analysis
a_{ij}	entries of $[A]$ in general case
B	width of a rectangular tank

$\{B\}$	right hand side of algebraic equations
B_I	known coefficients in finite element analysis
$[C]$	matrix used for preconditioner
$\boldsymbol{F}$	force on body with components being $\left(F_x, F_y, F_z\right)$
L	length of tank
$\boldsymbol{L}$	angular momentum
$[L]$	lower triangular matrix
M	mass of body
M_1	number of divisions in x-direction or radial direction
M_2	number of divisions in y-direction or circumferential direction
N	number of divisions in z-direction
N_I or N_J	shape function at nodes I or J (I and J are global numbers of nodes)
N_i^e	shape function defined on an element (i is local number of nodes)
N_c	moment about the mass centre
N_y	moment in y-direction about the bottom of a cylinder
R	radius of a circular tank
R_0	radius of a circular cylinder
S_b	body surface
S_c	vertical surface of fluid domain
S_d	bottom surface of fluid domain
S_f	free surface
S_n	surface on which the normal velocity is given
S_p	surface on which the velocity potential is given
ΔS^e	area of a surface of an element
T	wave period
$[T]$	transformation matrix from one coordinate system to another
$[\hat{T}]$	inverse matrix of $[T]$
T_{ij}	entries of $[T]$

$\boldsymbol{U}$	velocity vector of body or wave maker
U,V,W	components of $\boldsymbol{U}$
$\boldsymbol{U}_c$	velocity vector of the mass centre of body
U_c, V_c, W_c	components of $\boldsymbol{U}$
α,β,γ	Euler angles
μ	artificial coefficient in SSOR preconditioner
ν	artificial coefficient in damping zone
ν_0	magnitude of ν
θ	artificial coefficient in ILU preconditioner
ρ	water density
ϕ	velocity potential
ϕ_I	nodal value of velocity potential at node I
φ	initial velocity potential on the free surface
ϕ_n	velocity component of fluid in normal direction
τ	nondimensional time
$\Delta\tau$	nondimensional time step
ω	wave frequency
ζ	wave elevation
ψ	initial wave elevation
$\boldsymbol{\Omega}$	angular velocity of body
$\Omega_1,\Omega_2,\Omega_3$	components of $\boldsymbol{\Omega}$ in the x_b-, y_b- and z_b-directions
$\Re$	half bandwidth of matrix
$\forall$	volume of fluid domain
$\forall_e$	volume of an element
∇	gradient operator
∇^2	Laplace equation operator
$\frac{\partial}{\partial t}$	partial time derivative in fixed coordinate system, i.e. the rate of the change to time with all the space variables fixed

$\frac{d}{\delta t}$ defined as: $\frac{d}{\delta t} = \frac{\partial}{\partial t} + \frac{\partial \phi}{\partial z}\frac{\partial \zeta}{\partial t}$

$\frac{D}{Dt}$ defined as: $\frac{D}{Dt} = \frac{\partial}{\partial t} + \nabla\phi \cdot \nabla$

$\frac{\partial}{\delta t}$ partial time derivative in moving coordinate system

$\frac{\delta}{\delta t}$ defined as: $\frac{\delta}{\delta t} = \frac{\partial}{\delta t} + \frac{\partial}{\partial z_b}\frac{\partial \zeta_b}{\partial t}$

1. INTRODUCTION

1.1 Background

In order to explore and make use of the natural resources in the ocean, a wide variety of marine structures have been constructed. Well known examples include ships, Tension Leg platforms (TLPs), jacket-type platforms and moored floating storage tanks. They are all being used under severe environmental conditions which are a combination of tide, wind, current and waves. Although all of these effects should be considered in the design and construction of the structures, the effect of waves is of most concern. Waves may create very high loads on the structures and set them into motion, which will affect the safety, operation conditions and behaviour of the structures.

(a) Sloshing in a tank (b) Breaking wave on a ship

Figure 1.1.1 Some examples of large waves (from Faltinsen, 1990)

The waves may be quite small under mild weather conditions, but it is quite often necessary for the structures to withstand very large and steep waves. Two typical examples are demonstrated in Figure 1.1.1. Both breaking and sloshing waves can create large forces which may cause capsize of ships or can damage the structures. The other example is associated with the so-called 'ringing'. This is a kind of transient response of large offshore platforms such as TLPs at extremely high frequencies. Figure 1.1.2, plotted using results of Jefferys & Rainey (1994), illustrates a characteristic ringing event in a model test. The evidence of several experiments (for instance, Chaplin, Rainey, & Yemm, 1997 and Stansberg, C.T., Huse, E., Krokstad, J.R. & Lehn, E., 1995) suggested that the ringing is closely related to very steep waves such as shown in Figure 1.1.3.

The ringing motion can cause high level stress with high frequency in structures, which has alerted engineers to the possible failure due to fatigue.

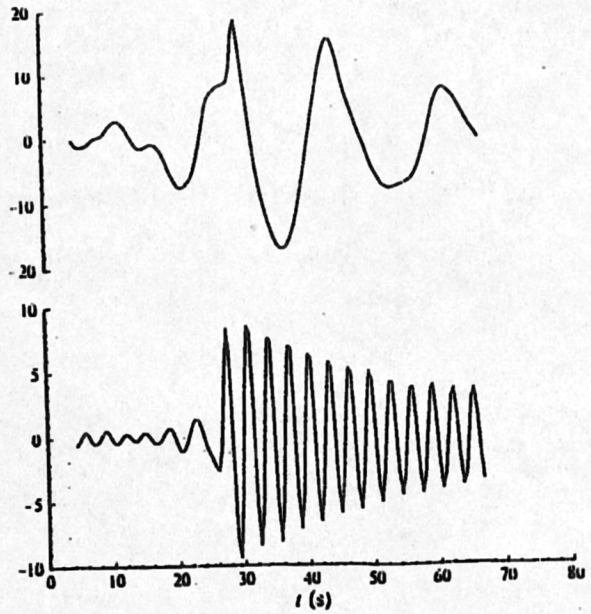

Figure 1.1.2 Experimental event of ringing on a TLP (upper curve is time history of wave and lower curve is a measured tension of structures)

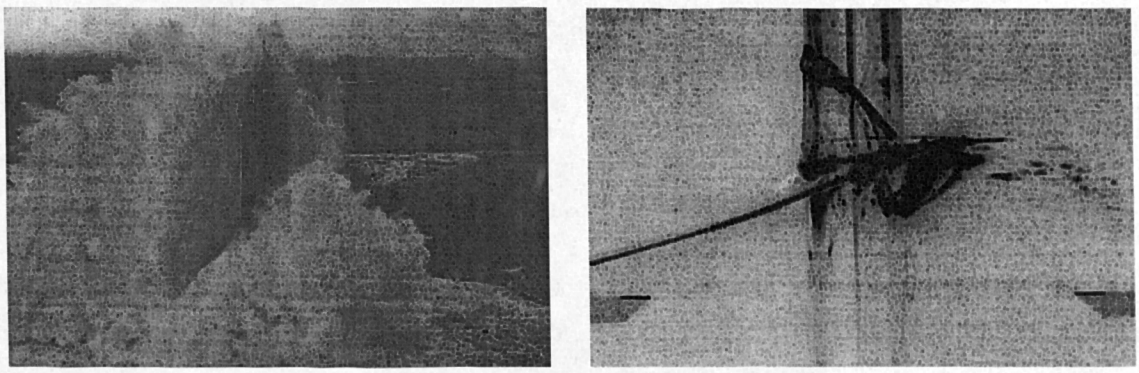

Figure 1.1.3 Large waves around cylindrical bodies

The above examples evidently show that the interaction between the structure and waves needs to be carefully investigated in order to improve and optimise the design. For the flows around large objects, the potential theory is commonly applied, which ignores the viscosity of fluid. The theory further neglects the surface tension and the

compressibility. Thus the velocity potential describing the flow satisfies the Laplace equation.

The Laplace equation is linear, but the problem is made nonlinear by the boundary conditions on the free surface, where a square term of fluid velocity is included and the elevation of the surface is unknown. Furthermore the position of a moving body cannot always be determined a priori. The nonlinearity renders the problem very difficult to analyse. Over the years, linearisation has been applied. The theory has greatly advanced our knowledge and has been found useful in capturing important phenomena such as resonance. However, this is valid only for waves of very small amplitude relative to the wave-length and the water depth. In order to investigate some problems in which the amplitude is moderate, a Stokes' perturbation expansion based on wave slope has been applied with the terms of the required order. In this approach, the second order expansion is often used, which has provided the good prediction of slowly-varying drift force and some high frequency forces. The third order analysis has also been found useful to investigate nonlinear loads on cylinders. It may seem that the analysis could be carried out by including higher order terms, but may be impossible in practice not only because the equation can become very complex but also because they contain high order derivatives which are not easy to compute numerically. On the other hand, to ensure the convergence of the perturbation expansion, it is necessary to restrict the wave amplitude. However, this restriction is not valid in many cases, such as the large sloshing waves and the steep waves associated with ringing. In these situations, the fully nonlinear formulation may be an appropriate choice.

The fully nonlinear formulation is usually solved by a time-step marching procedure (Longuet-Higgins & Cokelet,1976). This assumes that the wave profile and the position of the structure are known at a particular instant, and a mixed Dirichlet and Newmann boundary value problem is formed; this can then be solved by numerical techniques. The Bernoulli equation enables us to find the force on the structure; if the structure is not fixed, Newton's law will provide the new acceleration. The acceleration then gives a new velocity which further gives the new position of the structure. Similarly, the velocity obtained on the free surface will give a new free surface profile. All of these will enable the problem to be solved at the next time step. The procedure can be repeated for a desired number of time steps.

The physical problem may be studied experimentally. However it is expensive, and for each experiment that is set up, only one special model can be tested. Although the experiments can provide very useful and irreplaceable results, systematic investigation with different parameters and different configurations may be practically impossible. In contrast, numerical modelling may be relatively cheaper. Once the methodology and the computer code are established, many different runs can be easily performed.

1.2 Objectives of the study

This study will numerically simulate the fully nonlinear interaction problem between steep waves and three-dimensional bodies using the time-step marching procedure based on the potential flow theory. The main tasks are:

I. to develop a numerical methodology and algorithm based on a finite element method;

II. to apply the algorithm for two cases, namely, the simulation of sloshing waves in a tank and the investigation of forces acting on a cylinder by the propagating waves.

Quality meshes play a vital role for an effective numerical analysis. Nevertheless, our attention here is concentrated on the solution techniques, and a simple structured mesh is used. Although the fully nonlinear theory has no restriction to any wave situations, consideration is not given to the breaking and overturning waves.

1.3 Outline of the thesis

A review and a discussion of previous work are presented in Chapter 2. The mathematical formulation and the force calculation follows in Chapters 3 and 4 in turn. A numerical algorithm based on the finite element method is presented in Chapter 5. In Chapter 6, an investigation is carried out into the solution method of algebraic equations, to find a suitable solver for the problem of concern. Chapter 7 presents the application of the developed algorithm to sloshing waves. The simulation of the waves and their interaction with vertical cylinders in a wave-making tank is discussed in Chapter 8, followed by the conclusion and recommendations for the future work in Chapter 9.

2. REVIEW AND DISCUSSION OF PREVIOUS WORK

The interaction between waves and structures has received considerable attention from hydrodynamicists. This chapter will review and discuss previous studies and techniques, particularly those associated with steep waves.

2.1 Mathematical model

Even with the assumptions described in the last chapter, the wave problem still remains very complex. This is apparent from observing waves generated by a storm, by the motion of ships or simply by throwing a stone into water. Therefore people have established various mathematical models to formulate the problem, in order to obtain the desired results with as little effort as possible. The models may be grouped into:

1) linear model in the frequency domain;
2) linear model in the time domain;
3) high order model in the frequency domain;
4) high order model in the time domain;
5) fully nonlinear model;

In each model, the fluid flow can be considered as two- or three-dimensional.

2.1.1 Linear model in frequency domain

The problem described by this model has to possess the following properties:

a) Physical quantities of interest (such as velocity, pressure and so on) can be expressed as $\mathrm{Re}\left[f(\mathbf{x})e^{i\omega t}\right]$, where $f(\boldsymbol{x})$ represents any function dependent on spatial coordinate only; ω is frequency and $\mathrm{i}=\sqrt{-1}$. The physical meaning of this property is that the waves have been fully developed and become periodic. The wave form and amplitude do not change with time. Owing to this property, the time-independent analysis can be applied.

b) Wave amplitude is so small relative to other scales (such as wave length and water depth) that nonlinear terms in the free surface boundary conditions can be neglected and the resulting linearised conditions can be imposed on the mean free surface.

c) If a moving body is included, its oscillation excited by waves is also small, so that the body surface condition can be applied on its mean position.

This model is very simple, and has been widely used. The corresponding theory and techniques have been well established, and can be found in relevant literature, such as given by Newman (1977) and Mei (1989).

2.1.2 Linear model in the time domain

While the second and third requirements in the above model are also needed for this model, the first one is not necessary. Consequently, this model is capable of dealing with transient wave-structure interactions. It should be noted that the waves in the first model can be regarded as representing a periodic state of the transient flow. This implies that the second model is suitable for a wider range of problems than the first one. However, it is less popular than the first one in practice. The reason may be that the periodic state flow are frequently of interest, and furthermore, with the second model, one has to deal with the transient period in order to obtain periodic state results.

Nevertheless, this model is still used in numerous cases where transient behaviour may be of interest. For example, Marhell and Ursell (1970) considered the waves induced by a vibration of a floating body for which an initial displacement is specified. Lee and Leonard (1987) dealt with the waves generated by a wave maker and by a floating body that oscillates freely. More recently, Beck & Magee (1990), Bingham, Korsmeyer & Newman(1994) and Bratland, Korsmeyer & Newman (1997) employed the linear time domain model to investigate the interaction between the waves and bodies with or without forward speed, and even provide some examples to show how to obtain the added mass and damping coefficients at periodic state.

2.1.3 High order model in frequency domain

The problem described by this model should have the first property in Section 2.1.1. In addition, the ratio of the wave amplitude to other scales is assumed to be moderate. With these assumptions, a perturbation expansion is used and truncated at the required order, and boundary conditions are satisfied on their mean positions of the boundaries.

A large volume of work has been published based on perturbation theory. For the calculation of second order drift forces, Newman (1967) developed a far field method in terms of first order velocity potential. In the work of Eatock Taylor & Hung (1987), a semi-analytical solution was developed for a bottom-mounted vertical cylinder. More recently, Huang and Eatock Taylor (1996) suggested a semi-analytical method for

nonlinear interaction between waves and a truncated vertical cylinder. The wave drift damping, the forces acting on a floating structure with slowly drift motion, have also been modelled using the perturbation method (see, e.g. Zhao & Faltinsen (1989) and Grue & Palm (1993)). All of the above studies and many others are based on the second order analysis. Some effort has already been devoted to using third order analysis. Faltinsen, Newman & Vinje, (1995) gave a solution for nonlinear loads on a slender vertical cylinder using third order perturbation techniques. Malenica & Molin (1995) presented a third order harmonic analysis of wave diffraction about a vertical cylinder.

2.1.4 High order model in time domain

Similar to the third model above, the ratios of the wave amplitude to other scales are assumed be moderate within this model; however the transient behaviour of the waves is allowed. Perturbation expansion techniques are again used. Isaacson & Cheung (1990, 1991) used a second order approach to simulate wave diffraction about two- and three-dimensional structures. Isaacson & Ng (1993) and Ng & Isaacson (1993) applied the same approach to wave radiation and combined radiation and diffraction problems, respectively. More recently, Skourup, Buchmann & Bingham (1997) investigated the wave runup on a vertical cylinder and ship response to the incoming wave using the second-order time-domain analysis. Some efforts have also been made to use the third order analysis. For instance, Sclavounos & Kim (1995) have investigated a diffraction problem by means of a third-order time-domain analysis. Although this model may be quite efficient and remains valid for transient waves possessing moderate nonlinearity, its efficiency and capability have not yet been justified for very steep waves.

2.1.5 Fully nonlinear model

In this model, there is no extra limitation apart form the assumptions given in section 1.2. So free surface conditions include all terms, linear and nonlinear, and they are imposed on an instantaneous free surface, which is not known before the analysis. The body surface condition is linearly dependent on its velocity, but the position and the velocity of the body need to be determined during the analysis, which therefore renders the condition nonlinear as well. These nonlinearities imply that the model may be used in the time domain. Due to the use of fewer assumptions, the model is closer to the physical problem and is valid in a wider range of applications than those discussed above.

However it is much more difficult to use, and without the aid of a powerful computer, the results even for very simple cases are extremely difficult to obtain using this model. In spite of this, considerable attention has been given to this model since the 1970's and many interesting results have been published.

A very important contribution was made by Longuet-Higgins & Cokelet (1976), which subsequently made the use of this model more attractive. In their work, a time marching procedure is introduced, and the kinematic and dynamic free surface conditions are described by Lagrangian notation which allows the trajectories of the fluid particles in the free surface to be traced. Although they focused their attention on two-dimensional, spatially periodic waves, the results they obtained showed a high potential for their approach to be used for more complex problems. Soon afterwards Faltinsen (1977) applied this approach to studying a nonlinear free surface problem, including a harmonically oscillating body. Vinje and Brevig (1981) included multiple two-dimensional bodies submerged in fluid domain. In order to preserve spatial periodicity, they assumed that an array of identical bodies were present. Lin, Newman & Yue (1984) investigated the wave maker problem as well as that for the radiation waves caused by a oscillating cylinder. In their study, spatial periodicity was not assumed. The investigations into the two dimensional, fully nonlinear model following Longuet-Higgins & Cokelet (1976) have been continuing up until present. Many papers are worthy of mention, for instance, Haussling & Coleman(1977,1979), Greenhow & Lin(1985), Yim(1985), Greenhow(1987), Wang & Spaulding(1988), Yeung & Wu(1989), Sen(1993), Wu and Eatock Taylor(1994,1995) and others.

The three dimensional problems are naturally of greater interest to offshore and naval architecture engineers. However, compared to the two-dimensional analysis, only few papers are available. The reason for this is that, as might be expected, it is more difficult to address the three-dimensional, fully-nonlinear model. Two difficulties are apparent; firstly, a considerably large number of unknowns need to be solved in the numerical analysis, particularly when a realistic body is included. Secondly, tracing the waves and motion of the body is more complicated compared with two-dimensional cases, not only because the body and the free surface possess three-dimensional geometries but also because the moving waterline (3D curve-line) can often be troublesome to consider. Due to these difficulties, people have generally addressed bodies with simple geometries

and/or avoided free-surface piercing problems. For example, Dommermuth & Yue(1987b) and Kang & Troesch (1988) investigate vertical axisymmetric flow which is analogous to two-dimensional flow. Although Kang & Gong (1990) have extended the axisymmetric analysis to true three dimensional flows, the results they gave were only for a sphere moving in a horizontal direction, beneath the free surface. Problems associated with vertical and piercing cylinders have been treated by Isaacson(1982), Zhou & Gu(1990) and Chan & Calisal (1993), but the meshes they used were very coarse, which might not be sufficient to give convergent results. Ferrant (1994) used the three dimensional model to investigate the radiation and diffraction problem, and gave some results for a submerged sphere, which were obtained with quite a large number of elements on the free surface. Later, Ferrant (1995) calculated the runup on a vertical cylinder subject to a incoming wave, again using his algorithm. Although there are a number of other publications for this model (such as, Cao, Schultz & Beck (1991), Beck (1994), Xue and Yue (1995), Celebi & Kim (1997)), which have provided interesting and encouraging results, the development of robust and efficient methods are still in progress. This fully nonlinear three-dimensional model also forms the basis of this study.

2.2 Numerical methods for solving the boundary value problem

Regardless of which mathematical model is used, numerical techniques for solving the boundary value problem (BVP) play an important role, unless the analytical solution can be found, which is possible in only a few, very special cases. As mentioned above, the interaction between waves and structures can be described by the Laplace equation, the solution of which may be obtained using the well-known finite difference, finite volume, finite element or boundary element methods. However, the effectiveness of each method is problem dependent. The choice between the methods should be made carefully, especially when solving the fully-nonlinear, three-dimensional wave problem.

2.2.1 Finite difference and finite volume methods

These two methods have been widely used to solve the Navier-Stokes equations describing viscous flow. In addition, they have also been used to solve inviscid wave-flow problems in some cases. For example, a finite difference formulation was applied to the radiation problem due to a heaving cylinder by Telste (1985). Yeung and Wu (1989)

also proposed a finite difference procedure to simulate nonlinear fluid motion in a tank. In their work, boundary-fitted coordinates were employed, and the free surface particles, as well as their velocity potential, are advanced by a second-order predictor-corrector scheme. This procedure was later extended by Yeung & Vaidhanathan (1990) to nonlinear wave diffraction over submerged obstacles.

Besides the finite difference method, the finite volume method was also tested, e.g. by Mayer, Garapon & Sorensen (1997) in the simulation of wave flow. Using Euler equations as a basis, they investigated the case of a two-dimensional propagating wave in a narrow channel with a submerged bar. In their procedure, the kinematic boundary condition was expressed in terms of the local volume flux, which could be integrated to give the free surface elevation, and the velocities were evaluated using an irrotational correction. The correction function as well as pressure in the fluid satisfy Poisson's equation, which could be solved to update the velocity and the pressure. The authors compared their results with some experimental measurements, and fairly good agreement was achieved for the cases studied.

2.2.2 Boundary element method (BEM)

The boundary element method has provided a very powerful tool for solving linear or high-order interaction between waves and structures in a frequency domain, and has therefore become very popular. A distinct advantage of the method is that a Green function satisfying both Laplace equation and all the boundary conditions except that on the body surface can be found. As a result, it is necessary in numerical analysis to discretise only the body surface where unknown source-sinks are distributed, regardless of how big the fluid domain is. (In the case of the high order model, the discretisation on the free surface is also needed, but only for the integration of a known function over the surface). Owing to this advantage, other methods seem to be less efficient in these situations in terms of computational cost.

BEM can also be used in a similar way to solve linear problems in a time domain. However, in this case a Green function in the time domain satisfying Laplace equation and all the boundary conditions except that on the body surface is used. Such a Green function has long been available (Wehausen & Laitone, 1960), and it includes not only

the information of flow at present but also that in the past (called memory effect). The problem with using this Green function is that the CPU time and storage requirement, necessary for its evaluation, grow rapidly with time, due to the memory effect. This greatly restricts its application. Consequently, the methods are still sought to deal efficiently with it, see for example, Beck & Liapis (1987), Ferrant (1988), Clement (1997) and others.

With continued development of both the technology and the computer facilities, it is possible to extend the boundary element method to high-order models in the time domain as well as the fully nonlinear model. In these cases, a Green function similar to the above is not available. Instead, a source Green function (sometimes called a Rankine source) in an infinite fluid domain is used. This Green function is very simple to evaluate, but the distribution of sources on all of the boundaries of the fluid domain are necessary, instead of only on body surfaces. Many efforts, such as by Isaacson & Cheung (1990,1991), Isaacson & Ng (1993), Zhang & Willams (1996) and so on, have been made to simulate second order problems in a time domain associated with wave diffraction and radiation. Skourup, Buchmann & Bingham (1997) also applied this method to simulate wave runup on vertical cylinders. They took advantage of the perturbation expansion in their research, which allows the boundary conditions to be imposed on a fixed boundary, and therefore the calculation associated with the Green function is needed only once no matter how many time steps are simulated.

However, this advantage is lost when the boundary element method is applied to fully nonlinear wave problems, because at least one boundary of the fluid domain changes with time. Nevertheless, people have carried out many investigations on the use of the boundary element method for problems of this kind, and have provided many useful results . These not only include the early papers by Longuet-Higgins & Cokelet (1976), Faltinsen (1977), Vinje & Brevig (1981), Lin, Newman & Yue(1984), but also the recent publications by Kang & Gong (1990), Chan & Calisal (1993), Ferrant (1994), Xue and Yue (1995), Celebi & Kim (1997) and others.

As well known, singularities in BEM exist when sources are distributed on the real surface of the fluid boundary. The integration around the singularities usually requires special treatment, which can result in costly numerical calculation. To avoid this drawback, an alternative for BEM was proposed by Cao, Schultz & Beck(1991) and

Beck, Cao, Scorpio & Schultz (1994), in which the sources are distributed on an artificial surface outside the fluid domain, and the resulting formulation satisfies the conditions on the physical boundaries of the fluid domain. This method is referred as "desingularised" BEM. Unlike the conventional BEM, the Green function in the desingularised BEM does not have any singular points in the fluid domain and on its boundaries. Wang, Troesch & Maskew (1996) made a comparison between the two versions of the BEM. Their results seemed to show that both methods have comparable capability in dealing with the studied cases.

No matter which BEM, conventional or desingularised, is used to simulate the fully nonlinear waves, a common problem exists; that is, a fully populated coefficient matrix has usually to be tackled, which must be assembled and solved in each time step. Because of this feature, massive computing and storage requirements are needed to obtain results for even quite simple geometries.

2.2.3 Finite element method (FEM)

The finite element method has been well developed and widely used in the numerical analysis of structural mechanics, where the computational domain is usually finite, and also used in the simulation of some fluid problems with fixed boundaries, such as flow under dams or in shallow water. Zienkiewicz and Taylor(1994) have summarised the main accomplishments in this field.

Within the scope of the interaction between waves and structures, the FEM for the linear problem in a frequency domain was discussed by Mei (1989). Usually, the fluid domain is infinite and it is therefore not possible to discretise the whole domain. Bai & Yeung (1974) suggested a local finite element discretisation only around the body, matching with a series solution in the outer-domain which extends to infinity in the horizontal direction. Eatock Taylor & Zeitsman (1982) modified this method by replacing the series solution with a boundary integral discretisation at the fictitious matching surface. They modelled a problem of multiple bodies using this formulation. Later Wu & Eatock Taylor(1987) applied this method to linear diffraction by bodies with forward speed. Apart from the application of the FEM to the linear problem, the same formulation was also applied by Hung and Eatock Taylor (1987) and Clark, Bettess, Hearn & Downie (1991) to second order diffraction in frequency domains.

An example of time domain analysis of linear problems was given by Lee & Leonard (1987). They investigated the waves generated by a wave maker in a tank and a transient problem arising due to the free heave oscillation of a two-dimensional floating cylinder in calm water with an initial displacement. Comparison of their results for the heaving cylinder with an analytical solution of Ursell (1964) showed good agreement.

Recently, FEM has been applied by Wu and Eatock Taylor (1994, 1995) to cases of fully nonlinear interaction between waves and two-dimensional bodies. They investigated different formulations of the problem, by considering the velocity potential as unknown or the potential as well as two velocity components as unknown (hybrid FEM). It was suggested that the hybrid FEM seemed to be not as superior in terms of accuracy, despite considerably more memory and CPU time being required. The algebraic equations in their work were solved using the Choleski factorisation method. Remeshing was performed at each time step corresponding to the change in the fluid domain. They provided various results for two-dimensional waves, including waves generated by a piston wave maker, starting suddenly from rest or else undergoing harmonic oscillations, the standing waves in a container and forced oscillation of a cylinder. The reflected waves were avoided by truncating the fluid domain at relatively long distance from the bodies and stopping the calculation before the reflection become clearly visible. Later, Cai et al. (1998) developed a finite element formulation for fully-nonlinear water waves but based on a time-dependent mapping of the fluid domain to a fixed computational rectangle. This technique can avoid the need to remesh the fluid domain during the wave evolution. However, recently, Westhuis & Andonowati (1998) showed that this mapping technique may not give results as good as those obtained by the method in which the fluid domain is directly discretised, as used by Wu and Eatock Taylor (1994, 1995). In addition to the above papers, Nakayama & Washizu (1980) used FEM to investigate the sloshing wave in a two-dimensional tank.

To the author's knowledge, there have been no publications applying FEM to the simulation of fully-nonlinear three-dimensional interaction between waves and structures, as attempted in this thesis. Here, an iterative method with pre-conditioner will be used to solve the algebraic equations, and various techniques such as the recovery technique will be investigated in order to improve the accuracy without increasing the number of elements. The radiation condition is also suggested in the thesis, which helps to minimise

the reflection of waves when artificially truncated boundaries are inserted in the fluid domain. In addition, the methods for evaluating the fluid velocity and for calculating the forces on bodies are discussed.

Unlike the boundary element method, the finite element method requires the whole fluid domain to be discretised. Therefore, the number of nodes and unknowns in FEM is larger than in BEM. However, nonzero entries in the coefficient matrix for FEM may be much less than for BEM, implying that less computational cost and storage memory of the coefficient matrix might be required. To be specific, consider a rectangular-box fluid domain as an example. Dividing the domain by M_1+1, M_2+1 and $N+1$ planes along length, width and depth respectively leads to the number of nodes:

$$(M_1+1)(M_2+1)(N+1) = M_1M_2N + M_1M_2 + M_1N + M_2N + M_1 + M_2 + N + 1$$ in the whole domain

and

$$2(M_1M_2 + M_1N + M_2N + 1)$$ on all boundaries.

In the finite element formulation, any individual node is only affected by nodes connected to it through the mesh. In this discussed case, the maximum number of connecting nodes is 26, implying that no more than 27 coefficients are nonzero for each node. Consequently, the total number of nonzero coefficients for FEM is:

$$P_e \le 27(M_1M_2N + M_1M_2 + M_1N + M_2N + M_1 + M_2 + N + 1).$$

However, in the boundary element method, every node is affected by all others and therefor the total number of nonzero coefficients for BEM is:

$$P_b = 4(M_1M_2 + M_1N + M_2N + 1)^2.$$

It can be worked out that:

$$\frac{P_b}{P_e} \propto \frac{4}{9}\max(M_1, M_2, N)$$

This clearly shows that the number of nonzero values occurring in FEM is typically much less than in BEM in the fully nonlinear analysis, particularly when the number of divisions are very large. Wu and Eatock Taylor (1995) made a comparison between FEM and BEM for a two-dimensional wave radiation problem, and suggested that the finite element method was actually more efficient in terms of storage requirement and solution time than the equivalent boundary element method. It should be noticed that the BEM

version used for their comparison was based on a conventional BEM, and it could have been further optimised using the domain decomposition technique suggested by Wang, Yao & Tulin (1995). Even with the optimisation, however, the number of nonzero coefficients in FEM is still comparable to BEM (see the discussion in Ma, Wu & Eatock Taylor, 1997). The feasibility of the optimisation technique has yet to be justified for the three-dimensional simulations. A similar comparison was also made more recently by Westhuis & Andonowati (1998). Their results confirmed the conclusion of Wu and Eatock Taylor (1995).

2.3 Singularity on the waterline

In potential flow analysis, a well-known difficulty is the singularity at the waterline which is the intersection between the moving body surface and the free surface, see Lin, Newman & Yue (1984). This singularity was theoretically discussed by Peregrine (1972), who gave a solution for a steady flow towards a rigid wall and showed that the singularity in free surface elevation was logarithmical. Wang & Chwang (1989) and Rainey (1997) carried out a similar analysis on the flow near a vertical cylinder, and the singularity on the waterline was again found. Experimental confirmation was provided by Lin, Newman and Yue (1984) for an impulsive wave maker, and by Rainey (1997) for a wave motion around a cylinder.

It is anticipated therefore that numerical difficulties may be encountered at the waterline due to the singularity. There are two schemes which can successfully treat the singularity and lead to realistic solutions. The first was suggested by Lin, Newman and Yue (1984), who used the fact that the intersection points are common to both the moving rigid boundary and the free surface, and who thus imposed both the free surface condition and the body surface condition at one point. Their results confirmed that, with this treatment, the wave motion induced by the wave maker and an oscillating body can be successfully simulated. The second was discussed by Wang, Yao and Tulin (1995), who considered one intersection point as two points: one on the body surface and another on the free surface. At these points, the velocity potential was the same but its derivatives were not. The body condition was imposed at the body point. At the free surface point, an equation was derived to relate the normal and tangential derivatives, leaving one of them as an independent unknown variable, which could then be found

from the control equations. They mentioned that their scheme was reliable and concise for any wave-body intersection problem. The above two schemes were developed for a two-dimensional boundary element formulation.

2.4 Existing methods for the radiation condition

When the relevant physical domain is infinite, the computational domain must be truncated at a finite distance from the area of interest, because of the limitations on computer memory and CPU time. In order to ensure the wave field is not evidently disturbed by the artificial surface, an appropriate condition needs to be imposed. Various approximate schemes for this condition have been developed, and a review has been given by Romate(1989, 1992). Here we just briefly describe them and discuss some new developments since his work.

Using a large domain

The simplest method is to truncate the computational domain at very large distances from the body, where the velocity potential or the velocity of fluid are assumed to be undisturbed. Isaacson(1982) used this method to study the nonlinear wave effects on fixed and floating bodies. Generally, this method needs very large domain to allow long-time calculation , and thus the capability of computers can easily be exceeded.

Periodic boundary condition

This was employed by Longuet-Higgins & Cokelet(1976) for two-dimensional propagating waves. They assumed the waves to be periodic in space, and then transformed the fluid domain in one wave-length ("period") into a computational domain, closed by a simple contour corresponding to the free surface. In this method, no artificial boundary was inserted in the fluid domain and therefore no reflection was created. Vinje & Brevig (1981) used a similar condition for the interaction between waves and bodies, which were placed in such way that the periodicity in space could be created. Although this method is exact for periodic waves and easy to use, it cannot be adopted in many cases as the fully nonlinear waves are not always periodic in space. This is particularly true when a finite number of three dimensional bodies are included.

Damping zone method

This is also referred to as the "absorbing beach" method in some literature. In this approach, an artificial damping (or dissipative) term is introduced in a zone near the truncated boundary, in order to remove the transmitted energy of the waves and so to reduce the reflection. There are two ways to implement damping. The first is to add a damping term to the field equation, making the zone act like a sponge layer. The second is to add it to the free surface conditions, as a wave energy absorber mounted on the free surface. The latter is more suitable for the potential flow analysis.

Israeli & Orszag(1981) reviewed the application of the field-damped method to the one-dimensional wave equation, Schroedinger's equation and the Klein-Gordon equation. They showed that the effectiveness of the method could be satisfactory if the damping coefficient and the length of the damping zone were chosen carefully. Another example of this implementation can be found in Chan (1975), who added a linear damping to the momentum equation in his two-dimensional finite difference scheme.

In potential flow analysis, the second technique of the damping zone is more often found in the literature. Baker, Meiron & Orszag (1981) investigated a free surface problem using a vortex method and added a dissipative term to the equations for the wave elevation and for the vortex strength (in their case, these correspond to the kinematic and dynamic free surface conditions, respectively). Cointe, Geyer, King, Molin & Tanoni(1990) used a similar idea, but applied the dissipative term to the normal kinematic and dynamic conditions on the free surface, that is:

$$\frac{\mathrm{D}x}{\mathrm{D}t} = N.T - \nu(x_e)(x - x_e) \qquad (2.4.1)$$

$$\frac{D\phi}{\mathrm{D}t} = N.T - \nu(x_e)(\phi - \phi_e) \qquad (2.4.2)$$

where $N.T$ represents the normal terms; ϕ is the velocity potential; x is the coordinates of a pint on the free surface; subscript e corresponds to the reference configuration for the fluid and $\nu(x_e)$ is a damping coefficient (usually specified to be larger than zero). They suggested that the coefficient in the damping zone for the two dimensional problem can be assumed to be:

$$\nu(x_e) = \omega\left[\frac{k}{2\pi}(x - x_d)\right]^2, \qquad \text{where} \quad x_d \le x \le x_1 = x_d + \frac{2\pi}{k} \qquad (2.4.3)$$

where ω and k are wave frequency and wave number, respectively; the damping zone starts from x_d and ends at x_1. The scheme was also employed by Wang, Yao & Tulin (1995) in their simulation of a long 2D tank, with a modification to the above damping coefficient, being replaced by $\nu(x_e) = \vartheta_b \left(\frac{x - x_b}{L_b} \right)^2$, where L_b is the length of the zone and ϑ_b is the magnitude of the damping coefficient. The coefficient ϑ_b in their approach not only depends on the wave frequency but also on the wave elevation, the velocity potential and the velocities at the corresponding points. In his simulation of three dimensional diffraction waves, Ferrant (1994) applied this scheme to a perturbation part, which was the total wave potential subtracted by the incident wave potential. The damping zone in his case is an annulus surrounding the body, and the damping coefficient is taken as $\nu = 0.5\omega \left[\frac{k}{2\pi} \left(R(x) - R_b \right) \right]^2$, where R_b is the inner edge of the zone and $R(x)$ is the distance from the origin to the point x. He interpreted ϕ and x as the total potential and the position of the fluid particles convected by total flow velocity, respectively, while ϕ_e and x_e are determined by the incident wave. Apart from the above implementations with both two free surface conditions being modified, there is an alternative in which the damping term is added only to the dynamic condition, leaving the kinematic condition unchanged (see for instance, Bettess and Mohamad, 1982).

Although some satisfactory results with the above techniques have been presented by the researchers, a problem still exists, that is the added damping term in the dynamic condition may not always remove the energy from the fluid domain. When $\nu(x_e)(\phi - \phi_e) > 0$, the energy is taken out. However when $\nu(x_e)(\phi - \phi_e) < 0$, the energy is actually put into the fluid, implying that undesirable reflection will be generated. This has been discussed by Cao, Beck and Schultz (1994). They suggested the added term in the dynamic condition should take the form: $\nu \, \mathrm{sign}(\phi_n - \phi_{en}) |Q|$, where Q can be any function of ϕ and ϕ_n (the normal derivative of ϕ). With using this expression, the added term always absorbs energy from the fluid flow and therefore a well-behaved damping zone is expected.

In addition to the introduction of the damping term, a similar technique was developed for the two-dimensional wave tank problem by She, Greated & Easson(1992),

who assumed that the fluid velocities decreased exponentially in the zone near the truncated boundary. Good agreement has been achieved in their studied case compared with Stock's waves. However, as shown by Arai, Paul, Cheng & Inoue(1993), the reduction in horizontal velocity may invalidate the continuity of the flow. In order to overcome this problem, Arai, Paul, Cheng & Inoue(1993) combined the velocity reduction technique with the Sommerfeld condition, but applied the reduction of the velocity only to the vertical components. They also made some optimisation about the length of the damping zone to achieve as little reflection as possible.

Sommerfeld condition

The Sommerfeld condition can be written as $\frac{\partial \phi}{\partial t} + c\frac{\partial \phi}{\partial n} = 0$, where $\boldsymbol{n}$ is the normal vector out of fluid domain and c is the phase velocity of the wave. It was originally used as a radiation condition in linear wave problems, to ensure that the wave is outgoing. It was Orlanski (1976) who applied this condition to the truncated boundary for nonlinear hyperbolic flow. The phase velocity in his study was numerically calculated from the flow near the boundary. Chan(1977) used the same idea to study nonlinear wave-body interaction problems. The main advantage of the method for the evaluation of the phase velocity is that the wave frequency does not need to be known in advance. This is convenient for the nonlinear wave analysis, because the frequency in this case is not always specified. However, a difficulty can often exist with the way in which the phase velocity is calculated. That is, the scheme may fail to yield the proper value of the phase velocity at the crests and troughs of the velocity potential, even for a sinusoidal wave with a single celerity. To overcome this problem, the phase velocity has been replaced by one for shallow water waves in some studies, see for example, Lennon, et al (1982).

The Sommerfeld condition has also been used by many other authors, such as Yen & Hall(1981), Zhou & Gu(1990), Sen(1993), and so on.

Absorbing condition based on differential equations

This is given by $\prod_{i=1}\left(\frac{\partial}{\partial t} + c_i \frac{\partial}{\partial r_i}\right)\phi = 0$, where r_i is the direction of the i-th wave component. It is clear that the simplest example of this method is the Sommerfeld condition. Bayliss & Turkel (1982) have developed a higher order differential method

to absorb spherical waves. Romate(1989,1992), and Broeze & Romate (1992) used the same method to absorb free surface plane waves. In general, this kind of method requires knowledge of the wave directions or main directions (e.g., two main directions for a second-order differential equation). In the examples given by Broeze & Romate(1992) who assumed $c_i = c$, it was shown that the reflection can be successfully reduced for waves approaching the boundary in one or two directions. In the work of Zhang & Willams (1996), the second-order differential equation with $c_1 \neq c_2$ was employed to simulate the waves in flumes based on perturbation theory, and good results were obtained. It should be noted that this method is based on perturbation theory. Consequently, its effectiveness needs to be justified for the fully nonlinear wave-body interaction problem.

Matching with linear far field solutions

This method was proposed by Lin, Newman & Yue(1984) for the body-induced wave problem (radiation). In the method, the computational domain is divided into an inner domain and an outer domain. In the inner domain, all the conditions are satisfied exactly except for the radiation condition. In the outer domain, the problem is linearised, enabling an analytical expression to be determined. By matching the two different solutions on the interface, the equations for the numerical analysis in the inner domain can be formed. This method can avoid the numerical difficulty of the Sommerfeld condition. Furthermore, the linearized condition is adequate when the matching boundary is far away enough from the body, as the wave generated by a 3-D oscillating body in otherwise calm water will decay rapidly as the outer domain is approached. Nevertheless, for the wave-body interaction problem including diffraction, this method may not be consistently valid, because the incoming waves may not be necessarily linear in the far field.

Active wave absorber

The main idea of this method is that a wave maker is mounted at the truncated boundary, and absorbs the waves by controlling its motion, displacement and velocity which are determined by the wave information to be absorbed. The wave information may be the wave force obtained by integrating the pressure over the wavemaker surface, or the wave height. Maisondieu & Clement (1993) used the force signals to control the

motion of the wavemaker. In the work of Skourup & Schaffer (1997), the motion of the wavemaker was related to local wave height measured on its surface. They both applied the active wave absorber to simulate the waves in flumes, but Skourup & Schaffer claimed that the idea could be extended to three-dimensional situations by using an array of independently controlled 2D absorbers.

Combined techniques

Several schemes combining two of the techniques mentioned above have been suggested recently. Apart from the work of Arai, Paul, Cheng & Inoue(1993), who combined the velocity reduction method with the Sommerfeld condition, Contento & Casole (1995) coupled the normal damping zone method and the Sommerfeld condition. The phase velocity was numerically evaluated in their study, and a very rapid change in the time history of the phase velocity was shown. Clement & Domgin(1995) and Clement (1996) employed the active wave absorber and the damping zone method at the same time. The results demonstrated that the combined techniques worked well.

2.5 Existing methods for the calculation of forces

In the analysis of linear and nonlinear wave problems based on perturbation methods in the frequency domain, the forces and moments acting on bodies can be easily obtained by integration of the pressure over the body surfaces, once the velocity potential is found. However the story is different for nonlinear problems based on time domain analysis. The difficulty arises due to the term $\frac{\partial \phi}{\partial t}$ in the Bernoulli equation. The nodes or collocation points on the body surface move from one time step to another. As a result, a direct calculation of the term may be impossible unless using an approximate interpolation method; this however require a large storage of the information from previous time steps, and may produce unacceptable accumulated errors. Therefore, several methods have been proposed to overcome the difficulty associated with the force calculations.

Estimation of the material derivatives of the velocity potential

An estimation of the material derivatives of the velocity potential was proposed by Lin, Newman & Yue(1984). Under their scheme, the time derivative in the Bernoulli equation is expressed as:

$$\frac{\partial \phi}{\partial t} = \frac{D\phi}{Dt} - \nabla\phi \cdot \nabla\phi, \qquad (2.5.1)$$

where $\frac{D\phi}{Dt}$ is the time derivative obtained by following a fluid particle. Hence, the pressure is written alternatively as:

$$p = -\rho\left(\frac{D\phi}{Dt} - \frac{1}{2}\nabla\phi \cdot \nabla\phi + gz\right). \qquad (2.5.2)$$

They used the scheme to investigate body-induced wave problems. Sen (1993) used a similar scheme to calculate the pressure on a 2-D moving body, employing a slightly different expression for $\frac{\partial \phi}{\partial t}$, namely:

$$\frac{\partial \phi}{\partial t} = \frac{\partial \phi}{\delta t} - \mathbf{U} \cdot \nabla\phi, \qquad (2.5.3)$$

where U is the velocity of the body surface; and $\frac{\partial \phi}{\delta t}$ represents the rate of change of velocity potential obtained by following a point on the body surface. Now the pressure is expressed as:

$$p = -\rho\left(\frac{\partial \phi}{\delta t} - \mathbf{U} \cdot \nabla\phi + \frac{1}{2}\nabla\phi \cdot \nabla\phi + gz\right). \qquad (2.5.4)$$

Compared to the former, the later equation is more suitable for floating body problems.

As shown by Sen(1993), however, this kind of method may lead to "spikes" in the pressure history (and as a result, in the forces) due to the addition or deletion of elements on the body surface near the free surface. He suggested that the spikes could be removed if the total number of elements on the wetted body surface is kept constant during the change of the wetted surface. However this suggestion may not be valid for the case where the bodies have very large motions.

The spikes may not cause problems for fixed bodies or moving ones with prescribed motions. The story is different however for the case of bodies floating freely under the excitation of waves, because their motion is estimated by using the forces. Therefore, the spikes may produce unreasonable motion or even cause the procedure to break down.

Solving a boundary value problem

The term $\frac{\partial \phi}{\partial t}$ can also be found by solving a boundary value problem. The boundary value problem for $\frac{\partial \phi}{\partial t}$ is very similar to the one for the velocity potential itself. That is, $\frac{\partial \phi}{\partial t}$ satisfies the same equation in the fluid domain and the same boundary condition at infinity and on the sea bed as the potential. On a moving boundary surface, however, the normal derivative of $\frac{\partial \phi}{\partial t}$ is related to the acceleration of the body surface as well as the velocity. The acceleration is unknown before the force has been found, and in turn depends on the solution of $\frac{\partial \phi}{\partial t}$. In the literature, special attention has been paid to dealing with this boundary condition. Cointe, Geyer, King, Molin & Tanoni (1990) split the force into two parts. The first part is proportional to the acceleration and can be combined into the motion equation, while the second part is not directly dependent on the acceleration and can be solved without information of the acceleration. A similar technique has been adopted by Kang & Gong (1990), who used equation (2.5.3) and solved a boundary value problem for $\frac{\partial \phi}{\delta t}$ instead. In the approach of van Daalen (1993), the boundary value problem for $\frac{\partial \phi}{\partial t}$ was combined with the equation of the body motion, and the acceleration was eliminated.

More recently, Wu and Eatock Taylor (1996) introduced an artificial potential which satisfied a Neumann condition (only related to the configuration of the body) on the body surface and a Dirichlet condition on the free surface in order to avoid the difficulty. They obtained a relationship between the artificial potential and the force, which did not contain the term $\frac{\partial \phi}{\partial t}$. By solving the alternative potential, the force could be evaluated without involving $\frac{\partial \phi}{\partial t}$. This is very convenient from a numerical point of view, although the pressure may not be obtainable at the same time.

3. MATHEMATICAL FORMULATION

In this chapter, the general equations of fluid motion will be described based upon the assumptions given in Section 1.2. A right-hand Cartesian co-ordinate system *oxyz* is employed. The vertical *z*-axis points upwards and the *oxy* plane is located on the mean free surface. A sketch of the fluid domain and the co-ordinate system is shown in Figure 3.0.1. The figure also shows the coordinate system $o_b x_b y_b z_b$ (moving system) which is fixed on the body and coincides with *oxyz* initially.

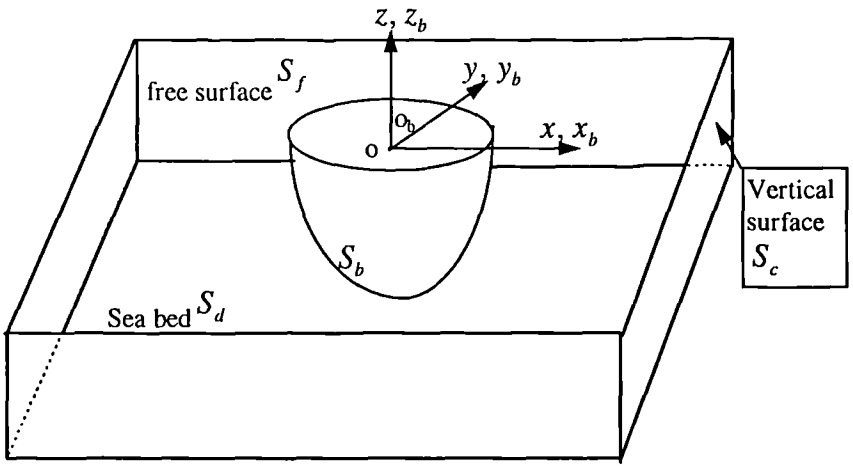

Figure 3.0.1 Coordinate system and fluid domain

3.1 Equations of fluid motion

Based on the assumptions of incompressibility, the velocity vector $\boldsymbol{u} = (u, v, w)$ of the fluid satisfies the continuity equation

$$\nabla \cdot \boldsymbol{u} = 0 \qquad (3.1.1)$$

and the momentum equation

$$\frac{\partial \boldsymbol{u}}{\partial t} + (\boldsymbol{u} \cdot \nabla)\boldsymbol{u} = -\frac{1}{\rho}\nabla p - g\boldsymbol{e}_z \qquad (3.1.2)$$

where $\nabla = \boldsymbol{e}_x \frac{\partial}{\partial x} + \boldsymbol{e}_y \frac{\partial}{\partial y} + \boldsymbol{e}_z \frac{\partial}{\partial z}$, ρ is the fluid density, g is the gravitational acceleration and p is the pressure of fluid; $\boldsymbol{e}_x$, $\boldsymbol{e}_y$ and $\boldsymbol{e}_z$ denote unit vectors in the x-, y- and z-directions, respectively.

Since the flow considered here is irrotational, the velocity $\boldsymbol{u}$ can be expressed as the gradient of a scalar function $\phi = \phi(x, y, z, t)$, called the velocity potential, i.e.

$$\boldsymbol{u} = \nabla\phi . \qquad (3.1.3)$$

Combining (3.1.3) with (3.1.1), it follows that the velocity potential will satisfy the Laplace equation:

$$\nabla^2\phi = 0 . \qquad (3.1.4)$$

This equation enables us to find one unknown scalar function rather than a vector function with three components. Once the scalar function is known, the velocity vector can be determined from equation (3.1.3). This clearly makes the problem easier.

After equation (3.1.3) is substituted into equation (3.1.2) and integration is performed, the well-known Bernoulli's equation is obtained:

$$-\frac{p}{\rho} = \frac{\partial\phi}{\partial t} + \frac{1}{2}|\nabla\phi|^2 + gz + c(t) \qquad (3.1.5)$$

where $c(t)$ is an arbitrary function of time independent of spatial variables. It can be usually omitted by redefining ϕ appropriately, ensuring that the velocity field remains unaffected. Hereafter, the constant will be taken as zero.

It can be seen therefore that when the velocity potential is solved from equation (3.1.4) with the appropriate boundary conditions, then the pressure of the fluid can be evaluated by equation (3.1.5).

3.2 Boundary and initial conditions for the velocity potential

The distinction between different fluid problems often comes from the conditions for the velocity potential on the boundaries of the fluid domain, and thus appropriate boundary conditions must be applied on the velocity potential according to the physical boundaries. Two types of boundaries are usually involved in the problem of interest here: the rigid boundary and the free surface boundary.

3.2.1 Condition on a rigid boundary

The sea bed, the sides of the fluid container and/or the body surface may all be the rigid boundaries. Some may be fixed and others may be moving. In either case, the physically relevant boundary condition for the fluid motion is that the normal component of the velocity of a fluid particle, $\boldsymbol{u}\cdot\boldsymbol{n}$, is equal to the normal velocity of the boundary surface at the corresponding point to the fluid particle. Expressed in terms of the velocity potential, this condition becomes

$$\frac{\partial\phi}{\partial n}=\boldsymbol{U}\cdot\boldsymbol{n}, \qquad (3.2.1)$$

where $\boldsymbol{n}$ is the normal vector pointing out of the fluid domain and $\boldsymbol{U}$ is the velocity at the corresponding point on the rigid surface. If a rigid boundary is fixed, the right-hand side of the above equation is simply equal to zero. For example, on the sea bed $z=-d(x,y)$ denoted by S_d in Figure 3.0.1, the above condition can be written as:

$$\frac{\partial\phi}{\partial x}\frac{\partial d}{\partial x}+\frac{\partial\phi}{\partial y}\frac{\partial d}{\partial y}+\frac{\partial\phi}{\partial z}=0. \qquad (3.2.2)$$

3.2.2 Condition on the free surface

The physical nature of the free surface requires two conditions: kinematic and dynamic conditions. The former states that a fluid particle on the free surface is assumed to stay on the free surface. The later requires that the pressure on the free surface must be atmospheric at all times. These conditions may be described using Eulerian notation, semi-Eulerian notation or Lagrangian notation. All of them are given below.

Free surface condition in Eulerian notation

Suppose the free surface is defined by

$$z=\zeta(x,y,t) \quad \text{or} \quad F(x,y,z,t)=\zeta(x,y,t)-z=0. \qquad (3.2.3)$$

The kinematic condition can be derived by requiring

$$\frac{\partial F}{\partial t}+\nabla\phi\cdot\nabla F=0 \qquad \text{on} \quad z=\zeta(x,y,t), \qquad (3.2.4)$$

that is

$$\frac{\partial \zeta}{\partial t}+\frac{\partial \phi}{\partial x}\frac{\partial \zeta}{\partial x}+\frac{\partial \phi}{\partial y}\frac{\partial \zeta}{\partial y}-\frac{\partial \phi}{\partial z}=0 \qquad \text{on} \quad z=\zeta(x,y,t). \tag{3.2.5}$$

The dynamic condition is obtained from equation (3.1.5). Taking the pressure as zero on the free surface and substituting ζ for z, equation (3.1.5) becomes:

$$\frac{\partial \phi}{\partial t}+\frac{1}{2}|\nabla \phi|^2+g\zeta=0 \qquad \text{on} \quad z=\zeta(x,y,t). \tag{3.2.6}$$

Free surface condition in Semi-Eulerian notation

Here the above kinematic condition, equation (3.2.5), is retained while the dynamic condition is rewritten as

$$\frac{d\phi}{\delta t}-\frac{\partial \phi}{\partial z}\frac{\partial \zeta}{\partial t}+\frac{1}{2}|\nabla \phi|^2+g\zeta=0, \tag{3.2.7}$$

where $\frac{d\phi}{\delta t}$ is related to $\frac{\partial \phi}{\partial t}$ by:

$$\frac{d}{\delta t}\left[\phi(x,y,\zeta,t)\right]=\frac{\partial \phi}{\partial t}+\frac{\partial \phi}{\partial z}\frac{\partial \zeta}{\partial t}. \tag{3.2.8}$$

The two time-derivatives have different meanings: $\frac{\partial}{\partial t}$ indicates the rate of the change with time when all the space variables are fixed while $\frac{d}{\delta t}$ means that the derivative with respect to time is taken with the space variables changing on a vertical line.

Free surface condition in Lagrangian notation

In this notation, the kinematic and the dynamic conditions on the free surface are specified by following the material points. They are written, respectively, as

$$\frac{Dx}{Dt}=\frac{\partial \phi}{\partial x}, \quad \frac{Dy}{Dt}=\frac{\partial \phi}{\partial y}, \quad \frac{Dz}{Dt}=\frac{\partial \phi}{\partial z}, \tag{3.2.9}$$

and

$$\frac{D\phi}{Dt}-\frac{1}{2}|\nabla \phi|^2+gz=0 \tag{3.2.10}$$

where $\frac{D}{Dt}$ is defined as

$$\frac{D}{Dt}=\frac{\partial}{\partial t}+\nabla\phi\cdot\nabla. \qquad (3.2.11)$$

The Eulerian notation is often employed for linear and high order perturbation theory. For the fully non-linear analysis in the time domain, Lagrangian or semi-Eulerian notation is usually used because of their suitability for time-step marching methods. These two notations have different features, however, since in contrast to the latter, the former does not need the slope of the free surface. This slope may be found by using a numerical differential method, which often introduces extra errors. Using the Lagrangian notation may result in sawtooth problems, as noticed by Longuet-Higgins and Cokelet (1976) and many others. The sawtooth problem may be avoided by remeshing or smoothing. However, both remeshing and smoothing techniques inevitably introduce errors, too. It would appear that there is no firm evidence suggesting that one of them is generally superior over the other, although there are some cases where the semi-Eulerian notation may not be suitable without domain transformation, for instance, in the wave maker problem discussed in Chapter 8 below.

3.2.3 Initial conditions

The fully non-linear wave problem will be solved in the time domain by using a time step procedure that starts from the initial state of the flow. This state is described by the initial values of the velocity potential on the free surface and the position of the surface itself. Mathematically, they can be written as:

$$\begin{aligned}&\zeta(x,y,0)=\psi(x,y)\\&\phi(x,y,\zeta(x,y,0),0)=\varphi(x,y).\end{aligned} \qquad (3.2.12)$$

If a body is included, its velocity and position at the starting instant must also be given.

3.3 Equations of a moving body

The motion equations corresponding to small motion have been widely used in naval architecture and ocean engineering, see for example Mei (1989) where the equations based on linearisation are derived. When a body is subjected to steep waves, its motion may be large and so the linearised equations may not give acceptable results in this instance. Here, the equations of motion in the general case are presented.

Suppose the velocity at the mass centre of a body is U_c and the angular velocity around the centre is Ω, then the total velocity U at any point on the body can be written as:

$$U = U_c + \Omega \times r_b, \tag{3.3.1}$$

where r_b is a vector from the mass centre to the point considered. Without loss of the generality, the mass centre will be assumed to coincide with the origin of the moving coordinate system. Newton's laws give the following two equations to the motion of the body:

$$M\frac{dU_c}{dt} = F \tag{3.3.2}$$

and

$$\frac{dL}{dt} = N_c, \tag{3.3.3}$$

where M is the mass of the body; F and N_c are the external force and the moment about the mass centre, respectively, which, if the gravity and the hydrodynamic force are present only , can be expressed as:

$$F = \iint_{S_b} pnds - Mge_z \tag{3.3.4}$$

$$N_c = \iint_{S_b} pr_b \times nds. \tag{3.3.5}$$

Finally, L, in equation (3.3.3), is the angular momentum and is defined as:

$$\begin{aligned} L &= \iiint_{\Xi} r_b \times (U_c + \Omega \times r_b) dm \\ &= \iiint_{\Xi} r_b \times U_c dm + \iiint_{\Xi} r_b \times \Omega \times r_b dm \\ &= \iiint_{\Xi} \left[|r_b|^2 \Omega - r_b (\Omega \cdot r_b) \right] dm \end{aligned} \tag{3.3.6}$$

where Ξ is the space occupied by the mass of the body.

For practical use, equations (3.3.2) and (3.3.3) need to be expressed in matrix form with elements composed of the projected components of the vectors. There are two

choices available for this: one is to express a vector in terms of its components in the *oxyz* system and the other is to do it in terms of its components in the $o_b x_b y_b z_b$ system. For convenience, the former is utilised for equation (3.3.2), i.e.:

$$[M]\begin{Bmatrix} \frac{dU_c}{dt} \\ \frac{dV_c}{dt} \\ \frac{dW_c}{dt} \end{Bmatrix} = \begin{Bmatrix} F_x \\ F_y \\ F_z \end{Bmatrix}, \qquad (3.3.7)$$

where U_c, V_c and W_c are the components of $\boldsymbol{U}_c$; and $[M]$ is a diagonal matrix, whose diagonal entries are all equal to the mass M. The derivatives of the velocities with respect to time can be related to the coordinates (x_c, y_c, z_c) of the centre of mass in the *oxyz* system by:

$$\left[\frac{dU_c}{dt}, \frac{dV_c}{dt}, \frac{dW_c}{dt}\right] = \left[\frac{d^2x_c}{dt^2}, \frac{d^2y_c}{dt^2}, \frac{d^2z_c}{dt^2}\right]. \qquad (3.3.8)$$

It can be seen that if equation (3.3.3) is also expressed in terms of the components in the system *oxyz*, then the components of $\boldsymbol{r}_b$ change with time. In order to avoid this, equation (3.3.3) needs to be expressed in the moving system $o_b x_b y_b z_b$. We first study $\boldsymbol{L}$ and its derivative. The components of $\boldsymbol{L}$ in the moving system can be derived from equation (3.3.6) as

$$L_i = \sum_{j=1}^{3} I_{ij}\Omega_j \qquad (i = 1,2,3), \qquad (3.3.9)$$

where 1,2 and 3 correspond to x_b, y_b and z_b, respectively; and I_{ij} are the moments of inertia defined as

$$I_{ij} = \iiint_{\Xi}\left[\delta_{ij}\sum_{k=1}^{3} x_{bk}{}^2 - x_{bi}x_{bj}\right]dm \qquad (i,j = 1,2,3), \qquad (3.3.10)$$

where $\delta_{ij} = \begin{cases} 1 & i = j \\ 0 & i \neq j \end{cases}$ and $r_b = x_b i_b + x_b j_b + x_b k_b$ has been used, with (i_b, j_b, k_b) representing the unit vectors in the x_b-, y_b- and z_b-directions, respectively. It is noted that I_{ij} is independent of time and therefore need only to be evaluated once. This is main advantage for expressing equation (3.3.3) in terms of moving-system variables.

However one should bear in mind that the time derivative in equation (3.3.3) has more complicated form in the $o_b x_b y_b z_b$ system. This time derivative is determined now using the following relationship (Marion 1965):

$$\frac{dL}{dt} = \frac{dL}{d_b t} + \Omega \times L, \qquad (3.3.11)$$

where $\frac{d}{d_b t}$ represents the time derivative in the moving system. This equation is valid for any vector; for example, for the angular velocity, we have:

$$\frac{d\Omega}{dt} = \frac{d\Omega}{d_b t} + \Omega \times \Omega = \frac{d\Omega}{d_b t}, \qquad (3.3.12)$$

which means that the time derivative of the angular velocity is the same in both two coordinate systems. Substituting equation (3.3.9) into equation (3.3.11) gives:

$$\frac{dL_i}{dt} = \sum_{j=1}^{3} I_{ij} \frac{d\Omega_j}{dt} + \sum_{j,k,l=1}^{3} \varepsilon_{ijk} \Omega_j I_{kl} \Omega_l \quad (i = 1, 2, 3), \qquad (3.3.13)$$

where

$$\varepsilon_{ijk} = \begin{cases} 0, & \text{for any index is equal to any other index;} \\ +1, & \text{if } i, j, k \text{ form an even permutation of 1,2,3;} \\ -1, & \text{if } i, j, k \text{ form an odd permutation of 1,2,3.} \end{cases} \qquad (3.3.14)$$

Equation (3.3.3) can now be rewritten in matrix form as

$$\begin{Bmatrix} \sum_{j=1}^{3} I_{1j}\dfrac{d\Omega_j}{dt} + \sum_{j,k,l=1}^{3} \varepsilon_{1jk}\Omega_j I_{kl}\Omega_l \\ \sum_{j=1}^{3} I_{2j}\dfrac{d\Omega_j}{dt} + \sum_{j,k,l=1}^{3} \varepsilon_{2jk}\Omega_j I_{kl}\Omega_l \\ \sum_{j=1}^{3} I_{3j}\dfrac{d\Omega_j}{dt} + \sum_{j,k,l=1}^{3} \varepsilon_{3jk}\Omega_j I_{kl}\Omega_l \end{Bmatrix} = \begin{Bmatrix} N_{c1} \\ N_{c2} \\ N_{c3} \end{Bmatrix} \qquad (3.3.15)$$

where the N_{ci} represent the moment components relative to the moving system.

The governing equations (3.3.7) and (3.3.15) have been written in two different coordinate systems, and therefore the transformation linking the two systems is required. This is given in Appendix A and has the form:

$$\begin{Bmatrix} x \\ y \\ z \end{Bmatrix} = \begin{Bmatrix} x_c \\ y_c \\ z_c \end{Bmatrix} + [T]\begin{Bmatrix} x_b \\ y_b \\ z_b \end{Bmatrix}. \qquad (3.3.16)$$

Here $[T]$ is the transform matrix defined as:

$$[T] = \begin{bmatrix} \cos\beta\cos\gamma & -\cos\beta\sin\gamma & \sin\beta \\ \sin\alpha\sin\beta\cos\gamma + \cos\alpha\sin\gamma & -\sin\alpha\sin\beta\sin\gamma + \cos\alpha\cos\gamma & -\sin\alpha\cos\beta \\ -\cos\alpha\sin\beta\cos\gamma + \sin\alpha\sin\gamma & \cos\alpha\sin\beta\sin\gamma + \sin\alpha\cos\gamma & \cos\alpha\cos\beta \end{bmatrix} \qquad (3.3.17)$$

where (α, β, γ) are Euler angles. The angular velocity can be expressed in terms of the Euler angles as (see A1.9 in Appendix A):

$$\Omega = \begin{Bmatrix} \Omega_1 \\ \Omega_2 \\ \Omega_3 \end{Bmatrix} = \begin{Bmatrix} \dot{\alpha}\cos\beta\cos\gamma + \dot{\beta}\sin\gamma \\ \dot{\beta}\cos\gamma - \dot{\alpha}\cos\beta\sin\gamma \\ \dot{\gamma} + \dot{\alpha}\sin\beta \end{Bmatrix} \qquad (3.3.18)$$

It is noted that the velocity U_c and the angular velocity Ω can be evaluated from equations (3.3.7) and (3.3.15) once the force and the moment are known. The co-ordinates (x_c, y_c, z_c) and the Euler angles can then be deduced from equations (3.3.8) and (3.3.18), respectively, thus enabling the position and orientation of the body be determined.

3.4 Equation and conditions in a moving coordinate system

It can sometimes be convenient to describe the fluid flow in a body-fixed co-ordinate system $o_b x_b y_b z_b$, as defined in Figure 3.0.1. In this system, the velocity potential ϕ is still governed by the Laplace equation, i.e.

$$\nabla^2\phi = 0, \tag{3.4.1}$$

but ∇^2 is now defined by $\nabla^2 = \frac{\partial^2}{\partial x_b^2} + \frac{\partial^2}{\partial y_b^2} + \frac{\partial^2}{\partial z_b^2}$. The condition on the rigid boundary surface also takes the same form as before, namely

$$\frac{\partial\phi}{\partial n} = \boldsymbol{U}\cdot\boldsymbol{n}. \tag{3.4.2}$$

The conditions on the free surface in contrast will have a different form because the partial time derivatives are different in the fixed and moving systems. The main task of this section is to derive the expression for the free surface condition in the moving system. Here, we describe the free surface only in semi-Eulerian notation, although a similar derivation may be applied in other notations.

From equation 3.3.16, the relationship between the two system is given by:

$$\boldsymbol{r} = \boldsymbol{r}_c + [T]\boldsymbol{r}_b, \tag{3.4.3}$$

where $\boldsymbol{r} = [x, y, z]'$, $\boldsymbol{r}_c = [x_c, y_c, z_c]'$ and $\boldsymbol{r}_b = [x_b, y_b, z_b]'$. Equation (3.4.3) can also be rewritten as

$$\boldsymbol{r}_b = [\hat{T}](\boldsymbol{r} - \boldsymbol{r}_c), \tag{3.4.4}$$

where $[\hat{T}] = [T]^{-1}$ which is the inverse matrix of $[T]$ and is defined as:

$$[\hat{T}] = \begin{bmatrix} \cos\beta\cos\gamma & \sin\alpha\sin\beta\cos\gamma + \cos\alpha\sin\gamma & -\cos\alpha\sin\beta\cos\gamma + \sin\alpha\sin\gamma \\ -\cos\beta\sin\gamma & -\sin\alpha\sin\beta\sin\gamma + \cos\alpha\cos\gamma & \cos\alpha\sin\beta\sin\gamma + \sin\alpha\cos\gamma \\ \sin\beta & -\sin\alpha\cos\beta & \cos\alpha\cos\beta \end{bmatrix} \tag{3.4.5}$$

The relationship between the partial time derivatives in the two coordinate systems is given by:

$$\left(\frac{\partial}{\partial t}\right)_{xyz} = \left(\frac{\partial}{\delta t}\right)_{x_b y_b z_b} + \left(\frac{\partial \mathbf{r}_b}{\partial t}\right)_{xyz} \cdot (\nabla)_{x_b y_b z_b}, \qquad (3.4.6)$$

where $\left(\frac{\partial}{\partial t}\right)_{xyz}$ denotes the partial time derivative with (x, y, z) fixed, and $\left(\frac{\partial}{\delta t}\right)_{x_b y_b z_b}$ represents the partial time derivative with (x_b, y_b, z_b) fixed. It follows from equation (3.4.4) that

$$\frac{\partial \boldsymbol{r}_b}{\partial t} = \frac{d[\hat{T}]}{dt}(\boldsymbol{r} - \boldsymbol{r}_c) - [\hat{T}]\frac{d\boldsymbol{r}_c}{dt} = \frac{d[\hat{T}]}{dt}[T]\boldsymbol{r}_b - [\hat{T}]\frac{d\boldsymbol{r}_c}{dt}, \qquad (3.4.7)$$

where $\frac{d[\hat{T}]}{dt}$ is derived in Appendix A. As shown by Korn & Korn (1968), the following relationship holds:

$$\frac{d[\hat{T}]}{dt}[T] = \begin{bmatrix} 0 & \Omega_3 & -\Omega_2 \\ -\Omega_3 & 0 & \Omega_1 \\ \Omega_2 & -\Omega_1 & 0 \end{bmatrix}, \qquad (3.4.8)$$

where Ω_i are the components of $\boldsymbol{\Omega}$ given in equation (3.3.18). As a result, equation (3.4.7) becomes:

$$\frac{\partial \boldsymbol{r}_b}{\partial t} = -(\boldsymbol{\Omega} \times \boldsymbol{r}_b + \boldsymbol{U}_c). \qquad (3.4.9)$$

The term in parenthesises is simply the velocity due to the body motion. Using equations (3.4.9) and (3.4.7), the dynamic condition in equation (3.2.6) is expressed in the moving system as

$$\frac{\partial \phi}{\delta t} - \nabla\phi \cdot (\boldsymbol{\Omega} \times \boldsymbol{r}_b + \boldsymbol{U}_c) + \frac{1}{2}\nabla\phi \cdot \nabla\phi + g z_c + g(T_{31}x_b + T_{32}y_b + T_{33}\zeta_b) = 0, \qquad (3.4.10)$$

where T_{ij} are entries in matrix $[T]$ and ζ_b is the free surface elevation measured in the $o_b x_b y_b z_b$ system. In the corresponding semi-Eulerian notation, we have:

$$\frac{\delta\phi}{\delta t}-\frac{\partial\phi}{\partial z_b}\frac{\partial\zeta_b}{\delta t}-\nabla\phi\cdot\left(\Omega\times r_b+U_c\right)+\frac{1}{2}\nabla\phi\cdot\nabla\phi+gz_c$$
$$+g\left(T_{31}x_b+T_{32}y_b+T_{33}\zeta_b\right)=0, \qquad (3.4.11)$$

where the relationship $\frac{\partial\phi\left[x_b,y_b,\zeta_b\left(x_b,y_b,t\right)\right]}{\delta t}=\frac{\delta\phi}{\delta t}-\frac{\partial\phi}{\partial z_b}\frac{\partial\zeta_b}{\delta t}$ has been used.

To derive the kinematic condition on the free surface, equation (3.2.3) is firstly transformed into the moving co-ordinate system, that is:

$$\begin{aligned}F=\zeta(x,y,t)-z&=(z_c+T_{31}x_b+T_{32}y_b+T_{33}\zeta_b)\\&\quad-\left(z_c+T_{31}x_b+T_{32}y_b+T_{33}z_b\right)\\&=T_{33}\left(\zeta_b-z_b\right)=\zeta_b-z_b=0.\end{aligned}$$

Using equations (3.2.4) and (3.4.6), the expression

$$\frac{\partial\zeta_b}{\delta t}+\left(\frac{\partial\phi}{\partial x_b}-U\right)\frac{\partial\zeta_b}{\partial x_b}+\left(\frac{\partial\phi}{\partial y_b}-V\right)\frac{\partial\zeta_b}{\partial y_b}-\left(\frac{\partial\phi}{\partial z_b}-W\right)=0 \qquad (3.4.12)$$

is obtained, where U, V and W are the components of $\left(\Omega\times r_b+U_c\right)$ in the x_b-, y_b-, and z_b-directions, respectively.

When a problem is solved in the moving system, the expression of fluid pressure may also be required in the same system. This can be obtained in the same way as for equation (3.4.10), i.e.

$$-\frac{p}{\rho}=\frac{\partial\phi}{\delta t}-\nabla\phi\cdot\left(\Omega\times r_b+U_c\right)+\frac{1}{2}\nabla\phi\cdot\nabla\phi+gz_c$$
$$+g\left(T_{31}x_b+T_{32}y_b+T_{33}\zeta_b\right). \qquad (3.4.13)$$

3.5 Equation and conditions for $\frac{\partial\phi}{\partial t}$

As mentioned in Chapter 2, a difficulty exists in the evaluation of $\frac{\partial\phi}{\partial t}$ in the time marching simulation. To overcome this, some researchers have attempted to solve a

boundary value problem for $\frac{\partial \phi}{\partial t}$. The equation and boundary conditions for $\frac{\partial \phi}{\partial t}$ in the oxyz system are described in this section.

It is evident that the term $\frac{\partial \phi}{\partial t}$ satisfies the Laplace equation, i.e.

$$\nabla^2 \frac{\partial \phi}{\partial t} = 0, \qquad (3.5.1)$$

On the free surface, the condition $p = 0$ leads to:

$$\frac{\partial \phi}{\partial t} = -g\zeta - \frac{1}{2}|\nabla \phi|^2, \qquad (3.5.2)$$

which gives the values of $\frac{\partial \phi}{\partial t}$ on the free surface once the problem for the potential is solved. Meanwhile on a fixed boundary, the condition

$$\frac{\partial}{\partial n}\frac{\partial \phi}{\partial t} = 0$$

holds. However, on a moving boundary, particularly on an accelerating boundary, the condition becomes complicated. Wu and Eatock Taylor (1996) have derived the equation

$$\frac{\partial}{\partial n}\frac{\partial \phi}{\partial t} = \left[\dot{U}_c + \dot{\Omega} \times r_b\right] \cdot n - U_c \cdot \frac{\partial \nabla \phi}{\partial n} + \Omega \cdot \frac{\partial}{\partial n}\left[r_b \times \left(U_c - \nabla \phi\right)\right] \quad \text{on} \quad S_b. \qquad (3.5.3)$$

Kang and Gong (1990) gave an expression different from equation (3.5.3); they defined:

$$\frac{\partial \phi}{\delta t} = \frac{\partial \phi}{\partial t} + U \cdot \nabla \phi, \qquad (3.5.4)$$

then proved that

$$\frac{\partial}{\partial n}\frac{\partial \phi}{\delta t} = \left(\dot{U}_c + \dot{\Omega} \times r_b - \Omega \times U\right) \cdot n \qquad \text{on} \quad S_b. \qquad (3.5.5)$$

The combination of equations (3.5.4) and (3.5.5) should be equivalent to equation (3.5.3) but it is not apparent. The extra derivation is given here to show they are indeed equivalent. To do so, let Γ be the last two terms in equation (3.5.3), i.e.

$$\Gamma = -\boldsymbol{U}_c \cdot \frac{\partial \nabla\phi}{\partial n} + \Omega \cdot \frac{\partial}{\partial n}\left[\boldsymbol{r}_b \times \left(\boldsymbol{U}_c - \nabla\phi\right)\right]$$
$$= \frac{\partial}{\partial n}\left\{-\boldsymbol{U}_c \cdot \nabla\phi + \Omega \cdot \left(\boldsymbol{r}_b \times \boldsymbol{U}_c\right) - \Omega \cdot \left(\boldsymbol{r}_b \times \nabla\phi\right)\right\}$$

which it is then rewritten as

$$\Gamma = \frac{\partial}{\partial n}\left\{-\boldsymbol{U} \cdot \nabla\phi + \left(\Omega \times \boldsymbol{r}_b\right) \cdot \nabla\phi + \Omega \cdot \left(\boldsymbol{r}_b \times \boldsymbol{U}_c\right) - \Omega \cdot \left(\boldsymbol{r}_b \times \nabla\phi\right)\right\}. \qquad (3.5.6)$$

Using $\boldsymbol{a} \cdot (\boldsymbol{b} \times \boldsymbol{c}) = \boldsymbol{b} \cdot (\boldsymbol{c} \times \boldsymbol{a})$ for arbitrary vectors $\boldsymbol{a}$, $\boldsymbol{b}$ and $\boldsymbol{c}$, equation (3.5.6) becomes

$$\Gamma = -\frac{\partial}{\partial n}\left(\boldsymbol{U} \cdot \nabla\phi\right) + \Omega \cdot \left(\boldsymbol{n} \times \boldsymbol{U}_c\right),$$

where $\dfrac{\partial \boldsymbol{r}_b}{\partial n} = \boldsymbol{n}$ has been used.

Using $\boldsymbol{a} \cdot (\boldsymbol{b} \times \boldsymbol{c}) = -\boldsymbol{b} \cdot (\boldsymbol{a} \times \boldsymbol{c})$ once more leads to

$$\Gamma = -\frac{\partial}{\partial n}\left(\boldsymbol{U} \cdot \nabla\phi\right) - \boldsymbol{n} \cdot \left(\Omega \times \boldsymbol{U}_c\right). \qquad (3.5.7)$$

Finally, substituting equation (3.5.7) into (3.5.3) gives

$$\frac{\partial}{\partial n}\frac{\partial \phi}{\partial t} = \left[\dot{\boldsymbol{U}}_c + \dot{\Omega} \times \boldsymbol{r}_b - \Omega \times \boldsymbol{U}_c\right] \cdot \boldsymbol{n} - \frac{\partial}{\partial n}\left(\boldsymbol{U} \cdot \nabla\phi\right) \qquad \text{on } S_b. \qquad (3.5.8)$$

which clearly shows that equation (3.5.3) is equivalent to the combination of equations (3.5.4) and (3.5.5).

If the moving boundary has no rotational motion, then equation (3.5.3) or (3.5.8) can be simplified to

$$\frac{\partial}{\partial n}\frac{\partial \phi}{\partial t} = \dot{\boldsymbol{U}}_c \cdot \boldsymbol{n} - \frac{\partial}{\partial n}\left(\boldsymbol{U}_c \cdot \nabla\phi\right). \qquad (3.5.9)$$

In particular, on the surface of the piston wave maker where the velocity $\boldsymbol{U}_c$ can be assumed as a function of the time variable only, equation (3.5.9) becomes:

$$\frac{\partial}{\partial n}\frac{\partial \phi}{\partial t} = \dot{\boldsymbol{U}}_c \cdot \boldsymbol{n} - \boldsymbol{U}_c \cdot \frac{\partial}{\partial n}\left(\nabla\phi\right) = -\dot{U}_c - U_c\left(\frac{\partial^2 \phi}{\partial z^2} + \frac{\partial^2 \phi}{\partial y^2}\right) \qquad (3.5.10)$$

where the fact that n opposite to the x-axis has been used, and $\frac{\partial^2 \phi}{\partial x^2}$ has been replaced by $-\left(\frac{\partial^2 \phi}{\partial z^2}+\frac{\partial^2 \phi}{\partial y^2}\right)$.

The problem for $\frac{\partial \phi}{\partial t}$ defined in equations (3.5.1) to (3.5.3) can be solved in a similar way as for the potential itself. However, it should be noted that the fluid velocity is included in the boundary condition for $\frac{\partial \phi}{\partial t}$. This means that solving for $\frac{\partial \phi}{\partial t}$ is possible only after the solution for ϕ has been found.

4. CALCULATION OF HYDRODYNAMIC FORCES

One of the primary reasons for studying the interaction between waves and structures is the desire to predict the forces and/or the moments acting on the body due to the dynamic pressure of the fluid. As mentioned in Chapter 2, their prediction is not trivial in the time marching procedure because of the difficulty associated with the evaluation of the $\frac{\partial \phi}{\partial t}$ term by a differential method. We attempt to avoid this difficulty here and employ the following two methods.

The forces and the moments are represented by integrals of the fluid pressure over the body surface, i.e.

$$\boldsymbol{F} = \iint_{S_b} p\,\boldsymbol{n}\,dS\,, \tag{4.1.1}$$

$$\boldsymbol{N}_c = \iint_{S_b} p\,\boldsymbol{r}_b \times \boldsymbol{n}\,dS\,, \tag{4.1.2}$$

where $\boldsymbol{n}$ is a normal vector pointing out of the fluid domain and hence into the body surface as before. Substituting for the fluid pressure in equation (3.1.5), it follows that

$$\boldsymbol{F} = -\rho \iint_{S_b} \left(\frac{\partial \phi}{\partial t} + \frac{1}{2}|\nabla \phi|^2 + gz \right) \boldsymbol{n}\,dS\,, \tag{4.1.3}$$

$$\boldsymbol{N}_c = -\rho \iint_{S_b} \left(\frac{\partial \phi}{\partial t} + \frac{1}{2}|\nabla \phi|^2 + gz \right) \boldsymbol{r}_b \times \boldsymbol{n}\,dS\,. \tag{4.1.4}$$

One possible method is to directly integrate equations (4.1.3) and (4.1.4) using the velocity values and $\frac{\partial \phi}{\partial t}$ obtained by solving the boundary value problem described in section 3.5. This method will be called the *direct force method* in this thesis. Clearly, extra effort is to solve for the term $\frac{\partial \phi}{\partial t}$. The corresponding computational cost depends on the methods used to solve the algebraic equations. If the direct solution method, such as Choleski factorisation method, is employed, the cost may be almost negligible if the inverse or factorisation of the matrix for solving the potential is usable. However if the

iteration solution method is used, the cost may be almost the same as that for solving the velocity potential itself and therefore may double the total cost.

Another method used for calculating the forces and moments has been proposed and published in the paper by Wu & Ma (1995). It is described here, as follows. Noting that p=0 on the free surface S_f, the equation (4.1.3) can be rewritten as

$$\boldsymbol{F} = -\rho \iint_{S_b+S_f} \left(\frac{\partial \phi}{\partial t} + \frac{1}{2}|\nabla\phi|^2 + gz \right) \boldsymbol{n}\, dS \,. \tag{4.1.5}$$

We then choose a fixed surface S_c which is closed laterally and is vertical near the free surface, as shown in Figure (3.0.1), to form a enclosed surface $\Sigma = S_b + S_f + S_c + S_d$. Following Newman (1977), we have

$$\begin{aligned} &\frac{d}{dt} \iint_{S_b+S_f+S_c+S_d} \phi\, \boldsymbol{n} dS = \frac{d}{dt} \iiint_{\forall} \nabla\phi\, d\forall = \iiint_{S} \nabla \frac{\partial \phi}{\partial t} d\forall + \iint_{S_b+S_f+S_c+S_d} \nabla\phi (V \cdot \boldsymbol{n}) dS \\ &= \iint_{S_b+S_f+S_c+S_d} \left[\frac{\partial \phi}{\partial t} \boldsymbol{n} + \nabla\phi (V \cdot \boldsymbol{n}) \right] dS, \end{aligned} \tag{4.1.6}$$

where $\boldsymbol{V}$ denotes the velocity of the surfaces.

It should be noted that integration on S_c may not be the same as that in the case of Newman because S_c here may intersect the free surface. As a result, the area of S_c changes with time. Hence, the time derivative and the integration over the surface can not be interchanged, that is, $\frac{\mathrm{d}}{\mathrm{d}t} \iint_{S_c} \phi\, \boldsymbol{n} \mathrm{d}S \neq \iint_{S_c} \frac{\partial \phi}{\partial t} \boldsymbol{n} \mathrm{d}S$. To obtain the relationship between them, let us consider

$$G(t) = \iint_{S_c} \phi\, \boldsymbol{n} dS \,.$$

As shown in Figure 4.1, the surface S_c may have a difference ΔS_c from t to $t + \Delta t$ and therefore

$$G(t+\Delta t) - G(t) = \iint_{S_c+\Delta S_c} \phi(\boldsymbol{r}, t+\Delta t)\, \boldsymbol{n} dS - \iint_{S_c} \phi(\boldsymbol{r}, t)\, \boldsymbol{n} dS \,,$$

where the vector $\boldsymbol{r}$ represents (x,y,z). Neglecting the higher order terms proportional to $(\Delta t)^m$ $(m=2,3,\cdots)$, we have

$$\phi(\boldsymbol{r},t+\Delta t)=\phi(\boldsymbol{r},t)+\Delta t\frac{\partial\phi}{\partial t},$$

and it follows that

$$G(t+\Delta t)-G(t)=\Delta t\iint_{S_c}\frac{\partial\phi(\boldsymbol{r},t)}{\partial t}\,\boldsymbol{n}dS+\iint_{\Delta S_c}\phi(\boldsymbol{r},t+\Delta t)\,\boldsymbol{n}dS\,.$$

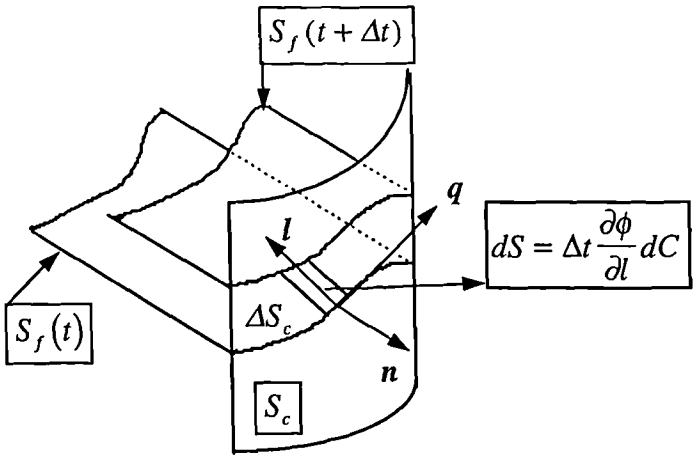

Figure 4.1 The change of surface with time (dC is a segment on the intersection C)

It is evident that the small surface ΔS_c created is due to the fluid motion on the free surface in the interval Δt, and consequently it is determined by $dS=\Delta t\frac{\partial\phi}{\partial l}dC$, as demonstrated in Figure 4.1. Letting $\Delta t\to 0$, it clearly follows that

$$\frac{dG}{dt}=\frac{\mathrm{d}}{\mathrm{d}t}\iint_{S_c}\phi\,\boldsymbol{n}\mathrm{d}S=\iint_{S_c}\frac{\partial\phi}{\partial t}\boldsymbol{n}\mathrm{d}S+\oint_c\phi\frac{\partial\phi}{\partial l}\boldsymbol{n}\mathrm{d}C,\tag{4.1.7}$$

where C is the instantaneous intersection of S_c and S_f, and $\boldsymbol{l} = \boldsymbol{n} \times \boldsymbol{q}$, with $\boldsymbol{q}$ being the tangential direction of C. Moreover, $\boldsymbol{q}$ points in a direction such that the fluid domain lies to the left of $\boldsymbol{q}$.

Substituting equations (4.1.7) into (4.1.6) and using $\frac{\mathrm{d}}{\mathrm{d}t}\iint_{S_d} \phi \boldsymbol{n}\mathrm{d}S = \iint_{S_d} \frac{\partial \phi}{\partial t}\boldsymbol{n}\mathrm{d}S$ yields

$$\iint_{S_b} \frac{\partial \phi}{\partial t}\boldsymbol{n}\mathrm{d}S = \frac{d}{dt}\iint_{S_b+S_f} \phi\, \boldsymbol{n} ds - \iint_{S_b} \nabla\phi(V\cdot\boldsymbol{n}) ds + \oint_c \phi \frac{\partial \phi}{\partial l}\boldsymbol{n} dC - \iint_{S_f}\left(\frac{\partial \phi}{\partial t}\boldsymbol{n} + \nabla\phi(V\cdot\boldsymbol{n})\right) ds$$

Thus the forces acting on the body can be written as

$$\begin{aligned} \boldsymbol{F} = & -\rho\frac{\mathrm{d}}{\mathrm{d}t}\iint_{S_b+S_f} \phi \boldsymbol{n}\mathrm{d}S - \rho\iint_{S_b+S_f} gz\,\boldsymbol{n}\mathrm{d}S \\ & -\rho\iint_{S_c+S_d}\left(\frac{\partial \phi}{\partial n}\nabla\phi - \frac{1}{2}\nabla\phi\nabla\phi\,\boldsymbol{n}\right)dS \\ & -\rho\oint_C \phi\frac{\partial \phi}{\partial l}\boldsymbol{n}\mathrm{d}C, \end{aligned} \tag{4.1.8}$$

where the following equation, which can be derived in a similar way to that for (4.89) of Newman (1977), has been used

$$\begin{aligned} \iint_{S_b}\left(\frac{\partial \phi}{\partial n}\nabla\phi - \frac{1}{2}\nabla\phi\cdot\nabla\phi\,\boldsymbol{n}\right)dS = & -\iint_{S_f}\left(\frac{\partial \phi}{\partial n}\nabla\phi - \frac{1}{2}\nabla\phi\cdot\nabla\phi\,\boldsymbol{n}\right)dS \\ & -\iint_{S_c+S_d}\left(\frac{\partial \phi}{\partial n}\nabla\phi - \frac{1}{2}\nabla\phi\cdot\nabla\phi\,\boldsymbol{n}\right)dS. \end{aligned}$$

It is evident that the distance between S_c and S_b is arbitrary. If S_c is chosen to be a vertical cylinder S_∞ at infinity, where the potential may be taken as the incident potential ϕ_i at any finite time step, then equation (4.1.8) changes to:

$$\begin{aligned} \boldsymbol{F} = & -\rho\frac{\mathrm{d}}{\mathrm{d}t}\iint_{S_b+S_f} \phi \boldsymbol{n}\mathrm{d}S - \rho\iint_{S_b+S_f} gz\,\mathrm{n}dS \\ & +\frac{\rho}{2}\iint_{S_b}\nabla\phi\nabla\phi\,\boldsymbol{n}\mathrm{d}S - \rho\oint_{C_\infty}\phi_i\frac{\partial \phi_i}{\partial l}\boldsymbol{n}\mathrm{d}C \\ & -\rho\iint_{S_\infty}\left(\frac{\partial \phi_i}{\partial n}\nabla\phi_i - \frac{1}{2}\nabla\phi_i\nabla\phi_i\boldsymbol{n}\right)dS \end{aligned} \tag{4.1.9}$$

Following the same procedure, the expression for the moments can also be obtained, which correspond to equations (4.1.8) and (4.1.9) in turn, i.e.

$$N_c = -\rho \frac{\mathrm{d}}{\mathrm{d}t} \iint_{S_b+S_f} \phi \boldsymbol{r}_b \times \boldsymbol{n} \mathrm{d}S - \rho g \iint_{S_b+S_f} z \boldsymbol{r}_b \times \boldsymbol{n} dS$$
$$- \rho \oint_C \phi \frac{\partial \phi}{\partial l} \boldsymbol{r}_b \times \boldsymbol{n} \mathrm{d}C - \rho \iint_{S_c+S_d} \boldsymbol{r}_b \times \left(\frac{\partial \phi}{\partial n} \nabla \phi - \frac{1}{2} \nabla \phi \nabla \phi \boldsymbol{n} \right) dS \quad (4.1.10)$$

$$N_c = -\rho \frac{\mathrm{d}}{\mathrm{d}t} \iint_{S_b+S_f} \phi \boldsymbol{r}_b \times \boldsymbol{n} \mathrm{d}S - \rho \iint_{S_b+S_f} g z \boldsymbol{r}_b \times \boldsymbol{n} dS$$
$$+ \frac{\rho}{2} \iint_{S_d} \nabla \phi \nabla \phi \boldsymbol{r}_b \times \boldsymbol{n} \mathrm{d}S - \rho \oint_{C_-} \phi_i \frac{\partial \phi_i}{\partial l} \boldsymbol{r}_b \times \boldsymbol{n} \mathrm{d}C \quad (4.1.11)$$
$$- \rho \iint_{S_-} \boldsymbol{r}_b \times \left(\frac{\partial \phi_i}{\partial n} \nabla \phi_i - \frac{1}{2} \nabla \phi_i \nabla \phi_i \boldsymbol{n} \right) dS,$$

The method for calculating the force and the moment using equations (4.1.8) to (4.1.11) is referred as the *integrated force method* in this thesis. It is obvious that any integration involving $\frac{\partial \phi}{\partial t}$ is absent from the formulae, and any partial time derivatives of velocity potential at individual points on bodies is not involved. Time derivatives are taken only on the integration of the velocity potential over the body and free surfaces, which is the first term included in the relevant equations. All these simplify the numerical evaluation of the forces and the moments. In addition, the terms in equations (4.1.9) and (4.1.11) associated with S_∞ can be ignored for the wave radiation problem. Compared with the direct force method mentioned above, the solution for $\frac{\partial \phi}{\partial t}$ is not required in this method.

However, integration applied to the first two terms has to be performed over the entire free surface. Thus the result is more likely to be affected by the error at the outer boundary of the computational domain (reflection for example). Another restriction on the use of the integrated force method is that the surface S_c has been fixed. On the other hand, the fluid domain may be discretised in numerical analysis by using some

planes (mesh surfaces). These mesh surfaces may move with time, and thus interpolation has to be employed to perform integration over the surface. Nevertheless, there are many cases where the fixed surface can be found, for example, when the fluid domain is truncated far away from the body, and the truncated surface may taken as fixed and can be considered as the surface S_c. Another example is when the semi-Eulerian notation is used and the mesh surface does not move in the horizontal direction, in which any mesh surface can be taken as the surface S_c. Furthermore, the integrated force method can provide only the total forces and moments acting on the body but not the pressure itself; if the pressure is required for a particular time step, it can be obtained by solving a boundary value problem for $\frac{\partial \phi}{\partial t}$.

5. A NUMERICAL ALGORITHM USING THE FINITE ELEMENT METHOD

5.1 Introduction

The fully nonlinear wave problem described in Chapters 3 and 4 will be solved by a numerical procedure. This procedure includes the following steps:

(1) start with initial values;

(2) solve the boundary value problem for the velocity potential;

(3) calculate the velocity of the fluid;

(4) calculate the forces on a body (and its acceleration if it is not fixed);

(6) update the positions of, velocity potential and
the velocities on the free surface (and the body surface if it is not fixed);

(7) go to (2) for the next time step.

The boundary value problem in step (2) requires solving the Laplace equation with relevant boundary conditions, which are summarised here for ease of reference:

$$\nabla^2\phi = 0 \qquad \text{in the fluid domain } \forall \qquad (5.1.1)$$

$$\frac{\partial\phi}{\partial n} = \boldsymbol{U}\cdot\boldsymbol{n} \qquad \text{on the rigid boundaries } S_n \qquad (5.1.2)$$

$$\phi = f_p \qquad \text{on } S_p \qquad (5.1.3)$$

where S_n represents all rigid boundaries, such as body surfaces, bottom surfaces and so on, where the velocity is known, whilst S_p denotes the boundaries where the velocity potential is known, which includes the free surface and may also include an artificial boundary surface (to be discussed in Chapter 8). On the free surface, $f_p = \phi[x, y, \zeta(x, y, t), t]$, where ζ and ϕ have been found from the solution at the previous time step by integrating the kinematic and dynamic free surface conditions of

Section 3.2.2. On the artificial boundary, f_p is also determined using the information of the previous time step.

This boundary value problem will be solved by a finite element method to obtain the velocity potential in the whole domain. Once the velocity potential is known, the velocity will be evaluated by a numerical differentiation method. All of these and other numerical techniques are discussed in the following sections.

5.2 Formulation of the finite element method

Usually, the above boundary value problem is transformed into an equivalent integral problem in order to employ the finite element method. There are several methods to do this (see Zienkiewicz & Taylor, 1994). Here the variational principle is adopted, and the following functional is used:

$$\Pi = \frac{1}{2}\iiint_{\forall} (\nabla\phi)^2 d\forall - \iint_{S_n} \phi f_n dS \qquad (5.2.1)$$

where $f_n = \boldsymbol{U}\cdot\boldsymbol{n}$. It is shown by Zienkiewicz & Taylor (1994) that if a potential function is taken as $\phi = f_p$ on S_p and satisfies $\delta\Pi = 0$ with respect to arbitrary changes $\delta\phi$ under the condition $\delta\phi = 0$ on S_p, then the function must be the solution of the problem defined in equations (5.1.1) and (5.1.3). In fact, letting $\delta\Pi = 0$ yields:

$$\begin{aligned} 0 = \delta\Pi &= \iiint_{\forall} \nabla\phi\cdot\nabla\delta\phi\, d\forall - \iint_{S_n} \delta\phi f_n dS \\ &= -\iiint_{\forall} \delta\phi\nabla^2\phi\cdot d\forall + \iint_{S_n} \delta\phi\left(\frac{\partial\phi}{\partial n} - f_n\right)dS + \iint_{S_p} \delta\phi\frac{\partial\phi}{\partial n}dS \\ &= -\iiint_{\forall} \delta\phi\nabla^2\phi\cdot d\forall + \iint_{S_n} \delta\phi\left(\frac{\partial\phi}{\partial n} - f_n\right)dS, \end{aligned}$$

where the Green theorem and $\delta\phi = 0$ on S_p have been used. This equation clearly shows that a potential ϕ satisfying $\delta\Pi = 0$ for any variation of $\delta\phi$ with $\delta\phi = 0$ on S_p is indeed the solution of the problem defined in equations (5.1.1) to (5.1.3). Therefore the above boundary value problem is equivalent to minimising the function Π.

An approximate solution minimising the function can be found by the following procedure. Firstly the fluid domain is discretised into small elements. The velocity

potential is then expressed by a shape function $N_J(x,y,z)$ and the unknown values ϕ_J on the nodes:

$$\phi = \sum_J \phi_J N_J(x,y,z), \tag{5.2.2}$$

where the sum is taken over all the nodes. Equation (5.2.1) is thus written as :

$$\Pi = \Pi(\phi_1,\phi_2,\cdots\cdots) = \frac{1}{2}\iiint_{\forall}\left|\sum_J \phi_J \nabla N_J\right|^2 d\forall - \iint_{S_n} f_n \sum_J \phi_J N_J dS_n, \tag{5.2.3}$$

and the arbitrary variation of $\delta\phi = \sum_J \delta\phi_J N_J(x,y,z)$ implies that

$$\delta\Pi = \frac{\partial\Pi}{\partial\phi_1}\delta\phi_1 + \frac{\partial\Pi}{\partial\phi_2}\delta\phi_2 + \frac{\partial\Pi}{\partial\phi_3}\delta\phi_3 + \cdots\cdots = \sum_J \frac{\partial\Pi}{\partial\phi_J}\delta\phi_J$$

Letting $\delta\Pi = 0$ and $\delta\phi = 0$ on S_p, and employing $\phi = f_p$ on S_p, it follows that

$$\iiint_{\forall} \nabla N_I \cdot \sum_{\substack{J \\ J\in S_p}} \phi_J \nabla N_J d\forall = \iint_{S_n} N_I f_n dS - \iiint_{\forall} \nabla N_I \cdot \sum_{\substack{J \\ J\in S_p}} (f_p)_J \nabla N_J d\forall \qquad (I \notin S_p) \tag{5.2.4}$$

which can be rewritten in matrix form:

$$[A]\{\phi\} = \{B\}, \tag{5.2.5}$$

where

$$\{\phi\} = [\phi_1,\phi_2,\phi_3\cdots\phi_I\cdots]' \qquad (I \notin S_p), \tag{5.2.6}$$

$$A_{IJ} = \iiint_{\forall} \nabla N_I \cdot \nabla N_J d\forall \qquad (I \notin S_p \text{ and } J \notin S_p), \tag{5.2.7}$$

$$B_I = \iint_{S_n} N_I f_n dS - \iiint_{\forall} \nabla N_I \sum_{\substack{J=1 \\ J\in S_p}} (f_p)_J \nabla N_J d\forall \qquad (I \notin S_p). \tag{5.2.8}$$

In equation (5.2.6), $[\ ]'$ denotes the transpose of a matrix. Equation (5.2.5) is an algebraic system with ϕ_j being the unknowns. The coefficient matrices $[A]$and $\{B\}$in equations (5.2.7) and (5.2.8) can be evaluated when the shape function is given.

It is should be noted that the term associated with the velocity potential on the free surface has appeared on the right hand side of equation (5.2.4). All the values of the potential, f_p, are known when solving the equation. Wu and Eatock Taylor (1994) have found that this can ease the well-known singularity problem at the waterline between the free surface and rigid boundaries.

5.3 Discretisation of the fluid domain

Before discussing the evaluation of matrices $[A]$ and $\{B\}$, the discretisation of the fluid domain is first presented. The discretisation of the fluid domain into a mesh of small elements is a fundamental part of a numerical procedure, and therefore a lot of effort has been devoted to corresponding techniques in the literature. A review about this may be found in Greaves (1995). The work here mainly concentrates on the development of the methodology. Therefore, a relatively simple technique for the mesh generation is used.

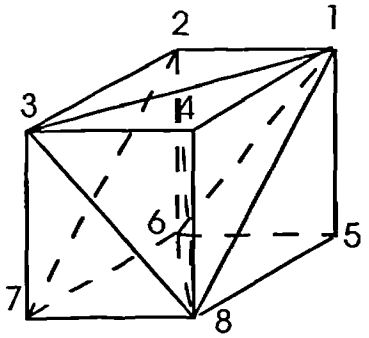

Figure 5.3.1 Division of a hexahedron

In the method used here, the fluid domain is first divided into a number of small hexahedra by three groups of different surfaces. One group consists of curved surfaces (referred to as horizontal surfaces) roughly lying in horizontal directions. The other two groups of the surfaces are each perpendicular to the bottom of the domain, as well as

being perpendicular to each other. The hexahedra generated in this way are then divided into six tetrahedra, as shown in Figure 5.3.1. The tetrahedra constitute the elements required. A typical mesh of a box-like domain generated in this way is illustrated in Figure 5.3.2 below.

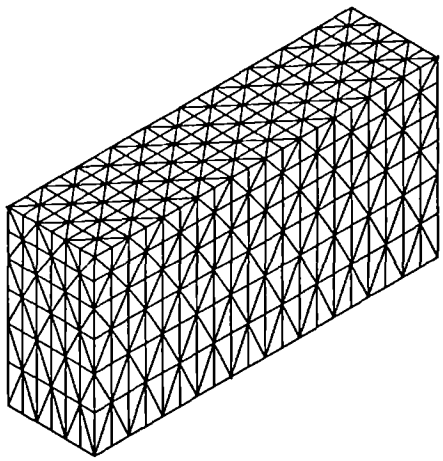

Figure 5.3.2 Sketch of the mesh of a rectangular domain

The distance between the surfaces may change in order to achieve a relatively finer discretisation in the area where the fluid velocity is expected to be larger, which may help to improve the accuracy without increasing the cost. Particularly, Wu and Eatock Taylor (1994, 1995) suggested that the distance between the horizontal surfaces near the free surface should be smaller and determined by:

$$z_j = \frac{e^{-\kappa(d+\zeta)} - e^{-\kappa(d+\zeta)\frac{j}{N}}}{1 - e^{-\kappa(d+\zeta)}}(d+\zeta) + \zeta, \qquad (5.3.1)$$

where z_j is the vertical coordinate of a node, d is the mean water depth, ζ is the wave elevation as defined before, N is the total number of divisions along the vertical direction, and $\kappa\ (\geq 0)$ is a coefficient which can be used to adjust the distribution of the nodes. A

larger value of κ means a finer mesh near the free surface. When $\kappa = 0$, the mesh is uniform in the vertical direction. Physically the amplitude of the fluid velocity in waves may decay with water depth from the free surface to the bottom, and the rate of the decay depends on the ratio of the wave length to the water depth: the smaller the ratio, the faster the decay. Thus a larger value of κ should be used, which leads to smaller elements near the free surface and larger ones near the bottom.

However, when the coefficient is chosen, care should be taken to avoid elements with very large (or small) aspect ratios (i.e. the ratio of one side of an element to the other). If the ratio is too large (or too small), the resulting coefficient matrix, $[A]$, may be ill-conditioned. The lower and upper limits on the ratio have been suggested to be 0.1 and 10.0, respectively (Reddy, 1984). In our case, if h_z represents the height of hexahedra in the z-direction and h_{xy} represents the length in the horizontal direction, then the aspect ratio can be measured by $\frac{h_z}{h_{xy}}$. It is clear that with increasing κ, the value of $\frac{h_z}{h_{xy}}$ becomes small near the free surface, and becomes large at the bottom. In order to restrict the ratio to the range of 0.1~10.0, the following limitation should be imposed:

$$\kappa < \min(\kappa_1, \kappa_2), \tag{5.3.2}$$

where κ_1 satisfies

$$\frac{e^{\kappa_1(d+\zeta)/N} - 1}{e^{\kappa_1(d+\zeta)} - 1} = \frac{h_{xy}}{10(d+\zeta)}, \tag{5.3.3}$$

while κ_2 is determined by

$$\frac{e^{-\kappa_2(d+\zeta)/N} - 1}{e^{-\kappa_2(d+\zeta)} - 1} = \frac{10h_{xy}}{(d+\zeta)}. \tag{5.3.4}$$

A general rule for determining the value of κ seems to be quite difficult to specify, but it has been found in our limited experience that the following empirical formula, subject to equation (5.3.2), may be used as a good guide within a practical range of frequencies:

$$\kappa = -0.31\frac{d}{g}\omega^2 + 2.29\sqrt{\frac{d}{g}}\omega - 1.47, \qquad 1.0 \le \sqrt{\frac{d}{g}}\omega \le 3.0, \tag{5.3.5}$$

where ω is the wave frequency.

5.4 Shape function

The fundamental idea of the finite element method is that the unknown function, such as the velocity potential of concern in this work, is expressed in terms of the nodal values of the function and an interpolation function (or shape function). The shape function needs to be properly chosen, and may be a linear, quadratic or higher-order polynomial function. In this work, the linear function is used. The basic reason for this choice is that the calculation of the coefficient matrix becomes relatively simple.

A shape function $N_j(x,y,z)$ has been introduced in equation (5.2.2) without any information on its evaluation. This function is defined on the whole fluid domain and will be called a global shape function. In order to express it explicitly, it should be related to local shape functions, each of which is defined on one element. Before the relationship between the global and local shape functions is given, the local shape function is first discussed in detail.

Attention is focused on one element e as shown in Figure 5.4.1, where the four nodes have been locally numbered as 1, 2, 3 and 4. The nodes are arranged in such way that 1-2-3 has an anticlockwise sense, when viewed from node 4. The local shape function defined on this element is denoted by $N_i^e(x,y,z)$ and is written as :

$$N_i^e = \frac{1}{6\forall_e}\left(a_i + b_i x + c_i y + d_i z\right) \qquad (i = 1,2,3,4) \quad \text{for } x,y,z \in e, \tag{5.4.1}$$

where $\forall_e$ is the volume of the element and can be expressed as:

$$\forall_e = \frac{1}{6}\det\begin{vmatrix} 1, & x_1, & y_1, & z_1 \\ 1, & x_2, & y_2, & z_2 \\ 1, & x_3, & y_3, & z_3 \\ 1, & x_4, & y_4, & z_4 \end{vmatrix}, \tag{5.4.2}$$

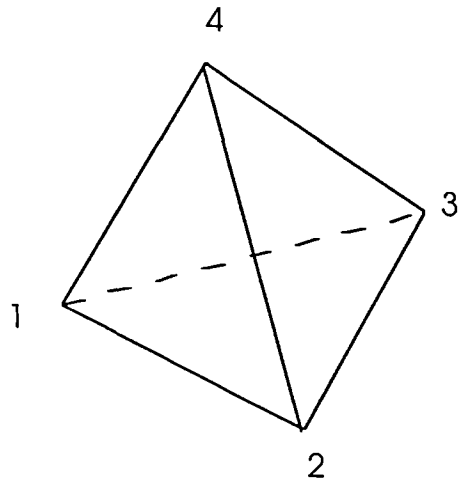

Figure 5.4.1 A tetrahedra element

and $x_i, y_i, z_i \ (i = 1, 2, 3, 4)$ are the coordinates of the nodes. The other constants in equation (5.4.1) are given as follows:

$$a_i = \det\begin{vmatrix} x_j, & y_j, & z_j \\ x_m, & y_m, & z_m \\ x_p, & y_p, & z_p \end{vmatrix} \qquad (i, j, m, p = 1,2,3,4), \tag{5.4.3}$$

$$b_i = -\det\begin{vmatrix} 1, & y_j, & z_j \\ 1, & y_m, & z_m \\ 1, & y_p, & z_p \end{vmatrix} \qquad (i, j, m, p = 1,2,3,4), \tag{5.4.4}$$

$$c_i = -\det\begin{vmatrix} x_j, & 1, & z_j \\ x_m, & 1, & z_m \\ x_p, & 1, & z_p \end{vmatrix} \qquad (i, j, m, p = 1,2,3,4), \tag{5.4.5}$$

and

$$d_i = -\det\begin{vmatrix} x_j, & y_j, & 1 \\ x_m, & y_j, & 1 \\ x_p, & y_j, & 1 \end{vmatrix} \qquad (i,j,m,p = 1,2,3,4), \tag{5.4.6}$$

where the cyclic interchange of subscripts is used, as illustrated by the figure below:

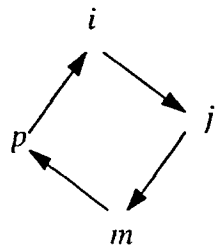

It can be verified that the shape function defined in equation 5.4.1 has the following property:

$$N_i^e(x_j, y_j, z_j) = \begin{cases} 1 & i = j \\ 0 & i \neq j \end{cases}. \tag{5.4.7}$$

With this shape function, the velocity potential within each element e can be written in the following form:

$$\phi = \sum_{j=1}^{4} \phi_j N_j^e(x,y,z) \qquad (x,y,z \in e). \tag{5.4.8}$$

This clearly shows that the velocity potential ϕ is linear in x, y and z, and $\phi = \phi_i$ when $x = x_i$, $y = y_i$, $z = z_i$ $(i = 1, 2, 3, 4)$ because of equation (5.4.7).

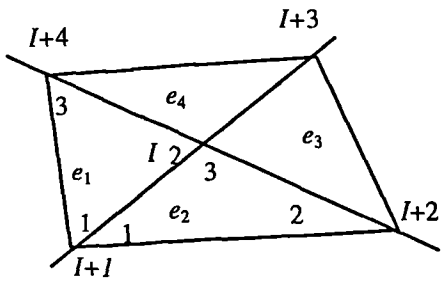

Figure 5.4.2 Elements connected with a particular node I

We next consider a patch of elements connected to one particular node, as shown in Figure 5.4.2, where each element has been represented by a triangle without loss of generality. It needs to distinguish I (J) from $i(j)$ $(i, j = 1, 2, 3, 4)$. I (J) and $i(j)$ may denote the same node; but I (J) is a global node number, while $i(j)$ is a local number. With this specification, it can be understood that for a global number I, the corresponding local number i may or may not be found in a particular element depending on whether the element includes I. If the corresponding number i for I does exist, it is often different in different elements. As shown in Figure 5.4.2, for instance, $i = 2$ in e_1 corresponds to the node I while in e_2 $i = 3$. Also for any J which is not equal to I, $I+1$ or $I+2$, the corresponding local number cannot be found in element e_2. An element patch attached to node I is denoted as E_I, for convenience of reference. In particular, the element patch in Figure 5.4.2 is composed of four elements and so $E_I = e_1 \cap e_2 \cap e_3 \cap e_4$.

Using equation (5.4.8), the velocity potential on E_I can be written as:

$$\phi = \begin{cases} \sum_{j=1}^{4} \phi_j N_j^{e_1}(x,y,z) & x,y,z \in e_1 \\ \sum_{j=1}^{4} \phi_j N_j^{e_2}(x,y,z) & x,y,z \in e_2 \\ \sum_{j=1}^{4} \phi_j N_j^{e_3}(x,y,z) & x,y,z \in e_3 \\ \sum_{j=1}^{4} \phi_j N_j^{e_4}(x,y,z) & x,y,z \in e_4 \end{cases} \qquad (5.4.9)$$

where each local shape function has been defined by equation (5.4.1). If the global shape function is defined as:

$$N_I(x,y,z) = \begin{cases} N_i^{e_I}(x,y,z) & (x,y,z) \in e_I \quad (e_I \subset E_I) \\ 0 & (x,y,z) \notin E_I \end{cases} \qquad (5.4.10)$$

and j in ϕ_j is changed to its corresponding global number, the expression in equation (5.4.9) can be extended to the entire fluid domain, i.e.

$$\phi = \sum_J \phi_J N_J(x,y,z), \qquad (5.4.11)$$

where the sum is taken over all the global nodes.

More discussion about (5.4.10) may be helpful for the following analysis. Supposing (x,y,z) to be a point in a particular element e_m, and letting J be any global node number, it follows from equation (5.4.10) that

$$N_J(x,y,z) = \begin{cases} N_j^{e_m}(x,y,z) & J \in e_m \\ 0 & J \notin e_m \end{cases} \qquad (5.4.12)$$

because in the latter case ($J \notin e_m$), (x,y,z) cannot be in patch E_J. In fact, equations (5.4.10) and (5.4.12) are equivalent; both of them relate the local and global shape functions together, but in a different manner. The former describes the relationship when considering one node with several associated elements, while the latter gives the relationship when considering one element with several associated nodes. From either equation, one can also obtain

$$N_I(x_J, y_J, z_J) = \begin{cases} 1 & I = J \\ 0 & I \neq J \end{cases}. \qquad (5.4.13)$$

5.5 Coefficient matrix

With the above definition of the shape function $N_I(x,y,z)$, we now consider the calculation of the coefficient matrices in equations (5.2.7) and (5.2.8). To this end, they are rewritten in terms of the integration over the elements:

$$A_{IJ} = \sum_k \iiint_{e_k} \nabla N_I \cdot \nabla N_J d\forall = \sum_k A_{IJ}^{e_k} \qquad \left(I \notin S_p \text{ and } J \notin S_p\right), \qquad (5.5.1)$$

$$B_I = \sum_k \iint_{\Delta S_n(e_k)} N_I f_n dS - \sum_k \iiint_{e_k} \nabla N_I \cdot \sum_{\substack{J \\ J \in S_p}} (f_p)_J \nabla N_J d\forall = \sum_k B_I^{e_k} \qquad \left(I \notin S_p\right), \qquad (5.5.2)$$

where $\sum_k$ is the sum taken over all the elements and $\Delta S_n(e_k)$ represents the triangular surface of element e_k, forming a part of the boundary S_n. If no surface in element e_k

lies on the boundary S_n, then $\Delta S_n(e_k)=0$. It is evident that $A_{IJ}^{e_k}$ and $B_I^{e_k}$ are the contributions from element e_k to A_{IJ} and B_I, respectively.

The contribution to A_{IJ} from the element e_k is firstly considered, that is

$$A_{IJ}^{e_k}=\iiint_{e_k}\nabla N_I\cdot\nabla N_J d\forall . \qquad (5.5.3)$$

According to equation (5.4.12), if at least one of I and J is not a node of e_k, then at least one of N_I and N_J is equal to zero, and as a result $A_{IJ}^{e_k}=0$. If ,on the other hand, both I and J are nodes of the element e_k, then $N_I=N_i^{e_k}$ and $N_J=N_j^{e_k}$. Consequently, the result

$$A_{IJ}^{e_k}=\frac{1}{36\forall_{e_k}}\left(b_ib_j+c_ic_j+d_id_j\right)_{e_k} \qquad (5.5.4)$$

is obtained, where the local numbers i and j of the nodes are used on the right hand side to retain the consistency with equation (5.4.1)

The contribution to B_I from the element may be split into two parts, i.e.

$$B_I^{e_k}=B_{I1}^{e_k}+B_{I2}^{e_k}, \qquad (5.5.5)$$

where

$$B_{I1}^{e_k}=-\iiint_{e_k}\nabla N_I\cdot\sum_{\substack{J\\ J\in S_p}}\left(f_p\right)_J\nabla N_J d\forall \qquad (5.5.6)$$

and

$$B_{I2}^{e_k}=\iint_{\Delta S_n(e_k)}N_I f_n dS . \qquad (5.5.7)$$

These two parts arise from different sources. The first part is the contribution from the node lying on S_p; this part is zero if there is no node on S_p or else if node I is not a number of this element. When the element contains I and J with J being on S_p, this part can be evaluated in the similar way as for $A_{IJ}^{e_k}$, i.e.

$$B_{I1}^{e_k}=\begin{cases}\dfrac{1}{36\forall_{e_k}}\sum_j\left(b_ib_j+c_ic_j+d_id_j\right)\left(f_p\right)_j & j(J)\in S_p \quad \text{and} \quad I,j(J)\in e_k \\ 0 & \text{otherwise.}\end{cases} \tag{5.5.8}$$

The term $B_{I2}^{e_k}$ results from the contribution of the surface of the element, which is part of the boundary S_n, and can be expressed precisely as:

$$B_{I2}^{e_k}=\begin{cases}\iint_{\Delta S_n(e_k)} N_I^{e_k} f_n dS & \Delta S_n(e_k)\neq 0 \text{ and } I\in\Delta S_n(e_k) \\ 0 & \text{otherwise } \left(I\notin e_k \text{ or } \Delta S_n(e_k)=0\right)\end{cases}. \tag{5.5.9}$$

To evaluate this integral analytically, f_n may be assumed to be a constant on $S_n(e_k)$ or else a linear function. With this assumption, it can be found:

$$\iint_{S_n(e_k)} N_I^{e_k} f_n dS=\begin{cases}\dfrac{\Delta S^{e_k}}{3} f_n & f_n \text{ is a constant on } e_k \\ \dfrac{\Delta S^{e_k}}{3}\left[\dfrac{(f_n)_i}{2}+\dfrac{(f_n)_j}{4}+\dfrac{(f_n)_m}{4}\right] & f_n \text{ is linear,}\end{cases} \tag{5.5.10}$$

where ΔS^{e_k} is the area of $\Delta S_n(e_k)$, and $(f_n)_i$ is the value of f_n at node i while $(f_n)_j$ and $(f_n)_m$ are the nodal values of f_n at other two nodes of $\Delta S_n(e_k)$. The derivation of the equation is presented in Appendix B. Usually, the constant f_n on $\Delta S_n(e_k)$ is assumed, but if f_n changes rapidly, the linear assumption may be used.

When the contributions from each element are known, the total values of A_{IJ} and B_I can be found by summing them properly . Here the relevant details are given to the assembly of A_{IJ}, and the similar manner can be used for B_I. For this purpose , Figure 5.4.2 is referred to again. Taking $A_{I\,I+1}$ as an example and noting that only elements e_1 and e_2 include both nodes I and I+1, the coefficient, therefore, is

$$A_{I\,I+1}=A_{I\,I+1}^{e_1}+A_{I\,I+1}^{e_2}.$$

By considering different J for the fixed I, all the A_{IJ} ($J=1,2,3,\cdots$) can be obtained. Other coefficients with different index I can be assembled in a similar way.

It should be noted that for all $J \notin E_I$, $A_{IJ} = 0$, and usually the number of $J \notin E_I$ is very large compared with the number of $J \in E_I$. As a result, only a few entries A_{IJ} for a fixed node I are nonzero. The number of $J \in E_I$ depends on the mesh and may be different for a different node I; this number does not exceed 27 for the mesh discussed in Section 5.3. Due to no limitation having been put on the node I, this property of A_{IJ} is also valid for any other nodes. This feature of the coefficients A_{IJ} makes the matrix $[A]$ sparse. That means that all the nonzero entries are bounded in a band, within which there may also be some zero entries. A sample pattern of the matrix is shown in Figure 5.5.1, where * denotes the nonzero coefficients. The number of entries from the first nonzero coefficient to the diagonal in each row is usually referred to the 'half bandwidth'. The half bandwidth is largely dependent on the geometry of the fluid domain, the mesh structure and the numbering system of the nodes. For a given domain and mesh, the optimisation of the numbering system of nodes may be utilised to achieve as small number of zero entries in the half bandwidth as possible. However, it should be noted that even with the use of the optimising technique, many zero entries may still be contained in the half bandwidth. In our calculation, the average half bandwidth often reaches to 300 ~500, which is far greater than the maximum number of the nonzero entries.

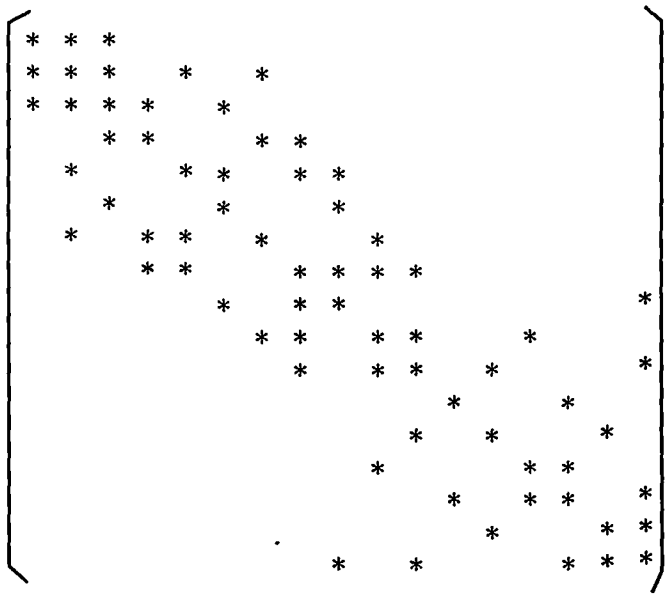

Figure 5.5.1 Matrix pattern

Apart from being sparse, the matrix $[A]$ is also symmetric. This can be seen from equation (5.5.1), where the value of the integration does not change with the interchange of I and J. Furthermore, the matrix is also positive definite (PD). This can be simply shown by considering:

$\iiint_{\forall} \nabla\phi \cdot \nabla\phi d\forall > 0$, for any non-constant velocity potential.

Inserting equation (5.4.11) into the above inequality gives:

$$\sum_I \sum_J \phi_I \phi_J \tilde{A}_{IJ} > 0, \qquad (5.5.11)$$

where $\tilde{A}_{IJ} = \iiint_{\forall} \nabla N_I \cdot \nabla N_J d\forall$ for any node number I and J. Equation (5.5.11) indicates that the matrix $[\tilde{A}]$ is positive definite. Of course, if the velocity potential is a constant, $\iiint_{\forall} \nabla\phi \cdot \nabla\phi d\forall = 0$, but this situation is of no interest because no flow would exist in this circumstance. It should be noted, however, that $[A]$ is different from $[\tilde{A}]$ because some entries have been moved to the right hand side in equation (5.2.4). Nevertheless $[A]$ can be shown to be a principal minor obtained by deleting some corresponding rows and columns of $[\tilde{A}]$. As is well known, if $[\tilde{A}]$ is symmetric positive definite, any principal minor is also symmetric positive definite (Pissanetzky, 1984). Hence, $[A]$ is positive definite.

Another aspect of concern is the storage of the matrix $[A]$. There are two basic ways of storing the matrix when coding the methodology. One way is to store only nonzero coefficients, while the other is to store all the coefficients in the half bandwidth including many zero entries. The choice from the two ways depends on methods used to solve the algebraic equations. An iterative method allows the former to be used, while a direct method requires the latter.

5.6 Velocity calculation

The fluid velocity on the free surface and on the body surface is required for the evolution of the waves and the evaluation of the forces acting on the body, as has already been seen in Chapter 3 and Chapter 4 above. The velocity elsewhere in the fluid domain may also be required, but it is not necessary for the simulation to proceed. Thus attention is paid here only to the velocity on the free surface and the body surface.

In order to calculate the velocity, one can solve a mixed boundary value problem with the velocity and potential being unknowns. The velocity can also be evaluated using a formulation based on the Galerkin method. Both techniques have been used by Wu & Eatock Taylor (1994), and were found to give satisfactory results. The authors, however, showed that both techniques may double the CPU time for the solution of potential itself. Therefore, they (Wu & Eatock Taylor, 1995) later suggested that the velocities could be calculated by a finite difference method once the potential was available, and achieved similarly satisfactory results with less calculation cost. The finite difference method will be used in this work. According to the mesh structure mentioned in Section 5.3, a slight modification will be made, as explained below.

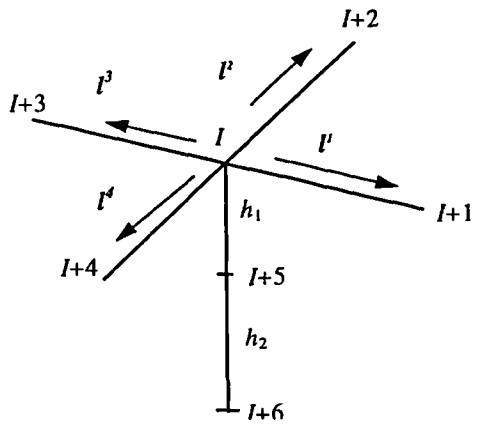

Figure 5.6.1 Node and its neighbours

The velocity on the free surface is addressed first. Suppose that the velocity at a node I on the free surface is sought, and that the node has several neighbours around it with two of them being below the free surface and being on a vertical line, as shown in Figure 5.6.1. The nodal values of the velocity potentials on the nodes are represented by

$\phi_I, \phi_{I+1}, \phi_{I+2}\cdots$, and corresponding vectors formed between the nodes $I+1, I+2,\cdots$ on the free surface and the node I are denoted by $l^1, l^2, \cdots$.

The vertical velocity is then evaluated using the nodal potential ϕ_I, ϕ_{I+5} and ϕ_{I+6} by the following equation:

$$w = \frac{2}{3h_1}\left(\frac{2h_1+h_2}{h_1+h_2}+\frac{1}{2}\right)\phi_I - \left(\frac{2}{3h_2}+\frac{1}{h_1}\right)\phi_{I+5} + \frac{2}{3h_1}\left(\frac{h_1}{h_1+h_2}\right)\phi_{I+6}. \qquad (5.6.1)$$

This equation is obtained by the combination of a two-point and a three-point differential formula.

The horizontal components are found by grouping the vectors on the free surface so that there are two vectors in each group, and at least one vector is different from those in other groups. For example, the four vectors in Figure 5.6.1 may be divided into four groups: (l^1, l^2), (l^2, l^3), (l^3, l^4) and (l^4, l^1). For each group, the following equations can be obtained:

$$u_i l_x^k + v_i l_y^k = \frac{\partial\phi}{\partial l^k} - w l_z^k \qquad (5.6.2)$$

$$u_i l_x^m + v_i l_y^m = \frac{\partial\phi}{\partial l^m} - w l_z^m \qquad (5.6.3)$$

where l_x^k, l_y^k and l_z^k are the components of the vector l^k $(k = 1, 2, \cdots)$, index i refers to the group, and $\frac{\partial\phi}{\partial l^k} = \frac{(\phi_{i+k} - \phi_i)}{l^k}$. Solutions of equations (5.6.2) and (5.6.3) yield the velocities related to the directions l^k and l^m. After the solutions in all the groups are found, the average is taken in order to give the horizontal velocities at the node I, that is

$$u = \frac{1}{q}\sum_{m=1}^{q} u_m, \qquad (5.6.4)$$

$$v = \frac{1}{q}\sum_{m=1}^{q} v_m, \qquad (5.6.5)$$

where q is the total number of groups..

On the rigid surface such as the body surface, the normal velocity is known. Only the tangential components need to be determined. In this case, all the neighbouring nodes,

corresponding to I, $I+1$, $I+2$, $I+3$ and $I+4$, are on the rigid surface, but the other nodes corresponding to $I+5$ and $I+6$ in the fluid domain are not needed. Equations (5.6.2) to (5.6.5) can be modified for the calculation of the tangential velocities. That is, the second term on the right hand side of both equations (5.6.2) and (5.6.3) is taken as zero, while equations (5.6.4) and (5.6.5) retain the same.

It should be noted that the above method may not be applicable to a general mesh because the vertical line containing three successive nodes may not exist. In this circumstance, the Galerkin formulation of the velocities or a least-square-based method may be used.

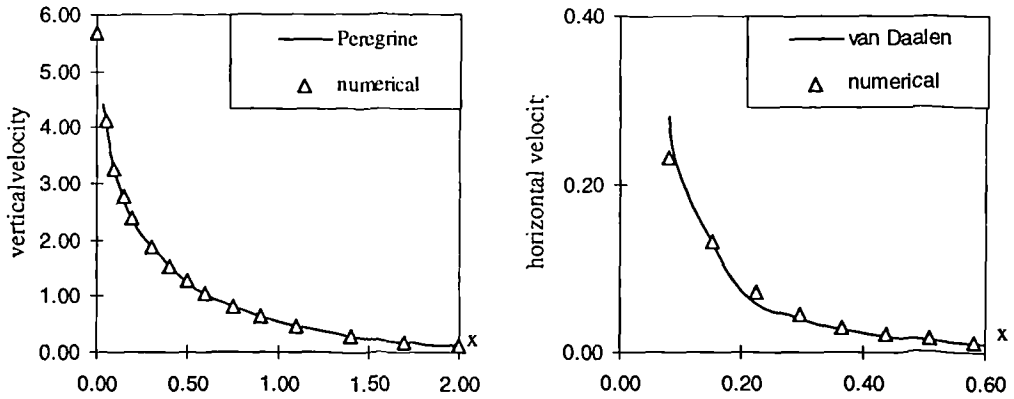

(a) Vertical velocity (t=0) (b) Horizontal velocity $t = \Delta t$

Figure 5.6.2 Comparison of the vertical and horizontal components of the velocity on the free surface generated by a wave maker with impulsive motion (the values of velocity shown have been divided by $\sqrt{gd}$ and $\Delta t = 0.005\sqrt{d/g}$)

To verify the above method, the problem of a wave maker suddenly starting to move at time $t = 0$ with velocity $U = \sqrt{gd}$ in a rectangular tank of length $L = 5d$ and width $B = 0.5d$ is solved. The right hand coordinate system is specified such that the wave maker is mounted at $x = 0$ and the free surface is at $z = 0$ before the start of motion. The mesh used is similar to that in Figure 5.3.2, and is generated by $M_1 + 1$ transverse planes, $M_2 + 1$ longitudinal planes and $N + 1$ horizontal surfaces. The values of M_1, M_2 and N are taken as 100, 6 and 16, respectively. The smooth scheme given in section 5.9 is applied. For a similar problem with infinite tank length, Peregrine (1972) has given a first order solution using a perturbation method with the time being the small parameter, and van Daalen (1993) extended it to second order. Their solution

is used to check the results obtained here. Figure 5.6.2 shows the comparison between the numerical results and their analytical solutions. It can be seen that excellent agreement has been achieved in this case. Further validation will be given in Chapter 7 and Chapter 8, where the numerical waves are compared with some known analytical solution, and this will indirectly check the velocity calculation method.

5.7 Integration to update the information on the free surface

The solution of the velocities at nodes enables us to calculate the new nodal values of the free surface elevation and the potential on the free surface, by using equations (3.5.2) and (3.2.7) for Semi-Eulerian notation, or (3.2.9) and (3.2.10) for Lagrangian notation. These new values provide conditions on the new boundaries for the analysis at the next time step.

It has been seen in Chapter 3 that the free surface conditions give the time derivatives of the potential and the position of the free surface. Numerical integration must be performed to obtain the new values. There are many schemes for this. The method used here is based on the open trapezoidal rule (Korn & Korn,1968) which is described as follows.

Suppose that the time derivative of a function y is known, i.e. $\left.\frac{dy}{dt}\right|_t = f$ at time t, the value of the function y at the next time step is determined from

$$y_{t+\Delta t} = y_t + \frac{\Delta t}{2}(3f_t - f_{t-\Delta t}) \qquad (5.7.1)$$

where Δt is the time step and assumed to be constant. The accuracy of the equation is in order of $(\Delta t)^2$

When the semi-Eulerian notation is used, there is no difficulty in the implementation of equation (5.7.1). However, when the Lagrangian notation is used, remeshing is often required to avoid over-distortion of the elements. If remeshing is performed, the time derivative $f_{t-\Delta t}$ at the previous step becomes problematical. The reason is that the same fluid particle must be followed in equation (5.7.1). When remeshing is used, however, node J at time t and node J at time $t-\Delta t$ may not represent the same particle. For example, node J at time t may be situated at the position Q at the time $t-\Delta t$, as shown

in Figure 5.8.1. The derivative at node J at time $t-\Delta t$ is then not available. Moreover, the position of the point Q is also unknown, and it must be derived from the position of node J. It is clear that in order to find $f_{t-\Delta t}$ in this case, the position of Q should first be found and then $f_{t-\Delta t}$ may be obtained by interpolation of the values at nodes a, b, and c at time $t-\Delta t$.

In order to find the position Q, it is assumed that the coordinates of node J are obtained by the following equation (actually, they are obtained by the interpolation from a', b' and c', see the next section):

$$x_J = x_Q + \bar{u_Q}\Delta t \qquad (5.7.2)$$

$$y_J = y_Q + \bar{v_Q}\Delta t, \qquad (5.7.3)$$

where (x_J, y_J) and (x_Q, y_Q) are the coordinates of node J and Q, respectively, and $\bar{u_Q}$ and $\bar{v_Q}$ are the velocity components at the point Q at time $t-\Delta t$. These two velocity components are unknown but may be interpolated from the velocities at a, b and c, in the following manner:

$$\bar{u_Q} = a_1 + b_1 x_Q + c_1 y_Q, \qquad (5.7.4)$$

$$\bar{v_Q} = a_2 + b_2 x_Q + c_3 y_Q, \qquad (5.7.5)$$

where the constants a_i, b_i and c_i (i=1,2) depend on the velocities and position of the points a, b and c, and they can be obtained by replacing (q_1, q_2, q_3) with $\left[(\bar{u_Q})_a, (\bar{u_Q})_b, (\bar{u_Q})_b\right]$ (for i=1) and $\left[(\bar{v_Q})_a, (\bar{v_Q})_b, (\bar{v_Q})_b\right]$ (for i=2) in equation (C.5) in Appendix C, respectively. Substituting equations (5.7.4) and (5.7.5) into equations (5.7.2) and (5.7.3) yields:

$$(1+\Delta t\, b_1)x_Q + \Delta t\, c_1\, y_Q = x_I - \Delta t\, a_1, \qquad (5.7.6)$$

$$(1+\Delta t\, b_2)x_Q + \Delta t\, c_2\, y_Q = y_I - \Delta t\, a_2. \qquad (5.7.7)$$

The solutions of equation (5.7.6) and (5.7.7) give the coordinates of the point Q which are used to interpolate the time derivatives, that is

$$\left(f_{t-\Delta t}\right)_Q = a_f + b_f x_Q + c_f y_Q, \qquad (5.7.8)$$

where $\left(a_f, b_f, c_f\right)$ is also obtained by equation (C.5) with $\left(q_1, q_2, q_3\right)$ being replaced by $\left[\left(f_{t-\Delta t}\right)_a, \left(f_{t-\Delta t}\right)_b, \left(f_{t-\Delta t}\right)_c\right]$. It should be noted that equations (5.7.2) and (5.7.3) are different from equation (5.7.1). However, if equation (5.7.1) is used for the purpose of finding the coordinates of the point Q at time $t-\Delta t$, its position and velocity at time $t-2\Delta t$ must be involved, and making the calculation even more complicated.

5.8 Remeshing and interpolation

If the nodes are simply followed, the configuration of elements may change during the time-marching process. It is possible that the elements may become so distorted that the calculation breaks down. To overcome this problem, the fluid domain may need to be remeshed at each time step or after every several time steps. It has been seen that at each new time step the free surface position and the velocity potential on the surface are obtained by integration, using the corresponding nodal values at the previous time step. When remeshing is performed, the new nodal values may become unavailable and hence interpolation may be required in this case.

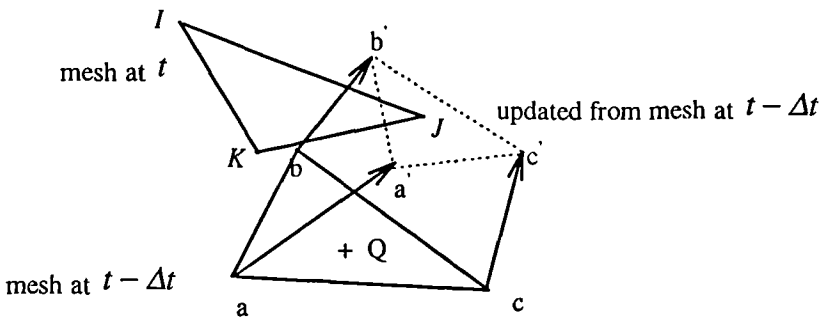

Figure 5.8.1 Illustration of remeshing

Whether or not interpolation is necessary depends on the notation used and the method of remeshing. If the semi-Eulerian notation is used and the vertical planes for the mesh generation are not changed, then the nodes on the free surface only move up and down. Consequently, the remeshing performed does not result in new nodes on the free surface, and thus interpolation is not necessary. If the Lagrangian notation is used, however, the nodes move in all directions. If the fluid domain is remeshed in this case, the new nodes on the free surface may not coincide with the old nodes and thus the free

surface elevation and the potential values on the new nodes must be found. Figure 5.8.1 can be used to illustrate this situation. Triangle abc is a part of the free surface at time $t-\Delta t$. After the solution is found, the nodes a, b, and c are updated to a', b' and c', respectively. Consequently, the triangle changes to $a'b'c'$. If remeshing is performed at this time level, new triangles on the free surface are formed (triangle IJK in the figure denoting one of them). The new nodes (I, J, K,$\cdots$) may not necessarily coincide with the old nodes $(a', b', c', \cdots)$. All the information is held at the nodes a', b' and c', but the values at the nodes I, J, K are needed for calculation at time t. In the following, the triangle $a'b'c'$ is referred to as the 'old triangle', while IJK is referred to as the 'new triangle'.

In order to find the new nodal values, interpolation is employed. It is quite straightforward because the interpolation method for the triangle on the free surface has been developed in Appendix C. We must, however, find which old triangle each new node such as J belongs to, before using that formula. This is because when the domain is remeshed , the new nodes cannot automatically be attached to a particular old triangle. To find the corresponding old triangle, the following method will be used.

Consider node J specifically. For convenience, the triangle $a'b'c'$ is projected on to the oxy plane to form $a''b''c''$, as shown below in Figure 5.8.2.

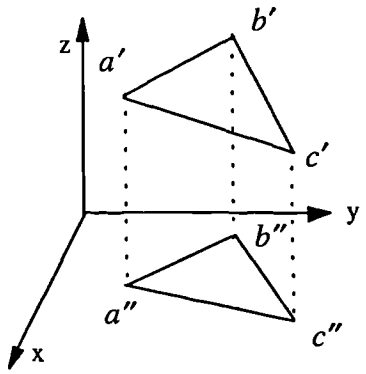

Figure 5.8.2 Projection of triangle $a'b'c'$ onto the x-y plane

Then, the following six vectors can be defined:

$$VJ_1 = \{x_J - x_{a''},\quad y_J - y_{a''}\},$$

$$VJ_2 = \{x_J - x_{b''}, \quad y_J - y_{b''}\},$$

$$VJ_3 = \{x_J - x_{c''}, \quad y_J - y_{c''}\},$$

$$V_{ba} = \{x_{b''} - x_{a''}, \quad y_{b''} - y_{a''}\},$$

$$V_{cb} = \{x_{c''} - x_{b''}, \quad y_{c''} - y_{b''}\},$$

$$V_{ac} = \{x_{a''} - x_{c''}, \quad y_{a''} - y_{c''}\},$$

where x, y, and z are the coordinates of corresponding points denoted by the indices. If the node J is inside the triangle $a'b'c'$, it must follow that:

$$\begin{cases} VJ_1 \times V_{ba} \geq 0 \\ VJ_2 \times V_{cb} \geq 0 \\ VJ_3 \times V_{ac} \geq 0. \end{cases} \qquad (5.8.1)$$

If one of inequalities in (5.8.1) is not satisfied , node J must be outside the triangle. The required triangle containing the node J can then be found by searching the old triangles using the condition given in (5.8.1).

After finding the triangle containing node J, for example, $a'b'c'$, formula (C.5) can be used to obtain all the information at node J, including the free surface elevation, the nodal potential and so on, which enables the problem to be solved on the new mesh at time t.

Numerical evidence has suggested that if the remeshing is carried out too frequently, for example, remeshing after every time step, the interpolation used above may cause a loss of energy. The interpolation based on a quadratic function has also been tested but the problem of energy loss still exists, although it may be slightly reduced. To overcome this problem, remeshing may be performed after a sufficient number of time steps. On the other hand, as mentioned at the beginning of the section, over-distortion may occur if remeshing is applied less frequently than necessary. In this work, remeshing is carried out after very 20 to 100 steps depending on the wave length. However the further investigation on remeshing and interpolation is required for future work on other practical problems not included here.

5.9 Smoothing and recovery techniques

Like other numerical methods, the finite element method can only offer an approximation to the exact solution of the physical problem. The difference between the exact solution and the finite element solution may be a result of modelling a continuum with a computational model that has a finite number of degrees of freedom and representing a continuous function with a piecewise interpolation function. Although the difference, or error, may decrease with increasing the number of the elements, or using a higher order interpolation function, a very large number of elements and/or a very complicated interpolation function are not always economical or practical. In solid mechanics where the finite element method has been widely used, a lot of effort has been devoted to the development of a good postprocessing method and adaptive mesh procedure, see for example Zienkiewicz & Taylor (1994), Zienkiewicz & Zhu (1992) and Wiberg, Abdulwahab & Ziukas (1994). These two distinct research areas have the same aim, that is to achieve higher accuracy without the obvious increase in the computational costs. Postprocessing techniques aim to provide more accurate results by properly treating the finite element solution. In contrast, the adaptive mesh is employed to try to achieve more accurate results by optimising the distribution of elements so that finer meshes are used in regions of large variable gradient, and coarser meshes used elsewhere. This optimisation procedure is performed by adjusting the mesh according to the errors obtained through successively solving the same problem. The core of the adaptive technique is error estimation which is based on some postprocessing results. Therefore it can be seen that postprocessing is fundamental to improving the quality of the finite element solution. In solid mechanics, postprocessing is mainly performed on stresses (derivatives) if the finite element method is based on displacements. Several techniques have been used to postprocess the stresses, such as nodal averaging, global projection and so on, see Zienkiewicz & Taylor (1994). Among them is superconvergent patch recovery, recently developed by Zienkiewicz & Zhu (1992), which is believed to be the most practical and effective.

In this work, we do not attempt to use the adaptive meshes, but instead attempt to improve the finite element results by means of some postprocessing techniques. Two techniques will be discussed. One is smoothing and the other is the patch recovery technique.

Smoothing technique

A 5-point smoothing scheme is used to smooth the velocity at nodes situated in a plane. Longuet-Higgins & Cokelet (1976) have used this scheme in their boundary element analysis , which successfully removed the saw-tooth problem. For five equally-spaced points, the relevant formula is written as:

$$\overline{w}_J = \frac{1}{16}\left(-w_{J-2} + 4w_{J-1} + 10w_J + 4w_{J+1} - w_{J+2}\right),$$

where w is the function to be smoothed and $\overline{w}_J$ is the smoothed value at node J; nodes $J-2$, $J-1$, $J+1$, $J+2$ are situated on both sides of the node J, as shown in Figure 5.9.1.

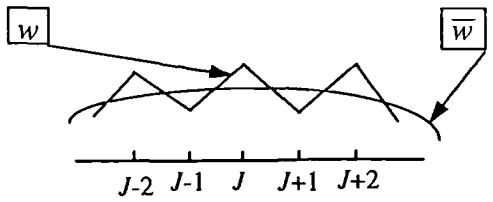

Figure 5.9.1 Sketch of smoothing procedure

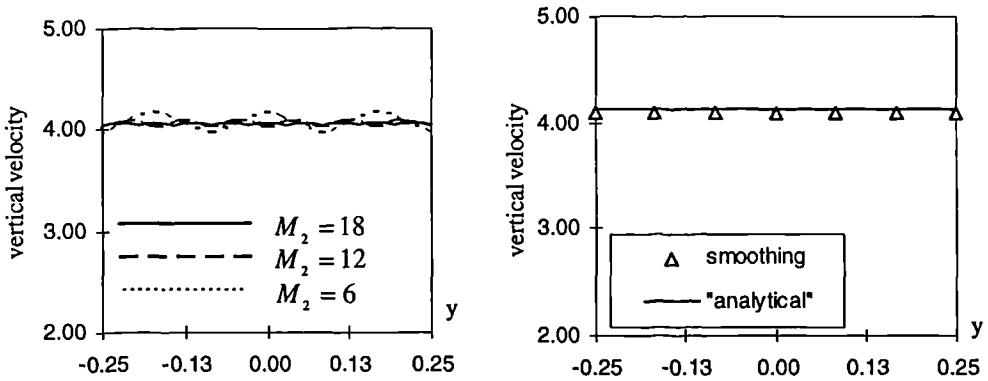

(a) different meshes without smoothing (b) with smoothing ($M_2 = 6$)

Figure 5.9.2 Vertical velocity at x=0.05 for impulsive motion of the wave maker (the values of velocity shown have been divided by $\sqrt{gd}$)

As an example, this scheme is now used for the problem of impulsive motion of the wave maker, as described in Section 5.6. Similar meshes to Figure 5.6.2 are used but M_2 is taken as a different number in order to obtain a different mesh size in the y-direction. Figure 5.9.2a gives the numerical solution of the vertical velocity on the free surface at $x = 0.05$, which is not smoothed . It can be seen that variation along the y-direction is evident, although physically this problem is two dimensional, and hence the solution should not be a function of y. The comparison of the velocity obtained by different numbers of divisions in the y-direction shows that the variation decreases, and that the results converge to the analytical solution with increasing the division level, although the rate of convergence is quite slow. Figure 5.9.2b shows the comparison of between the analytical solution and the smoothed numerical results corresponding to $M_2 = 6$. It can be found that the calculated velocity has no visible variation and is in good agreement with the analytical solution. This example shows that this smoothing technique may improve the results dramatically.

However, the smoothing technique mentioned above has limited practical use because it requires the mesh to be regular and five nodes to be on the same plane. These requirements may not be easily met in many cases. For example, when a cylinder is mounted in the wave tank, a different mesh structure in the area around the cylinder from that in the area near the wave maker has to be used, and thus the smoothing technique is not applicable. In such a case, an alternative, patch recovery technique, may be employed.

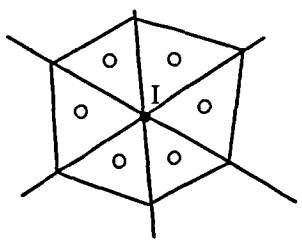

Figure 5.9.3 Triangular patch
(∘: sampling point)

Patch recovery technique

The fundamental idea behind the patch recovery technique is that the velocity is assumed to be fitted by a polynomial over a patch on the free surface. Such a patch consists of a union of triangles containing this node, as shown in Figure 5.9.3 where there are six triangles in the patch associated with node *I*. This polynomial can be simply written as:

$$w_I^* = a + bx + cy\,, \qquad (5.9.1)$$

where w_I^* denotes a fitted-velocity component on the free surface, and the subscript refers to the patch around the node *I*. The coefficients *a*, *b* and *c*, included in equation (5.9.1), are to be determined by a least-square method fitting to a set of sampling points. That means that the following function is minimised:

$$\Lambda = \sum_{i=1}^{n} (a + bx_i + cy_i - w_i^h)^2\,, \qquad (5.9.2)$$

where x_i and y_i are the horizontal coordinates of the sampling points (as shown in Figure 5.9.4); w_i^h is the velocity at the sampling points, and *n* is the number of triangles in this patch. The minimisation of equation (5.9.2) leads to:

$$\begin{bmatrix} 1 & \sum_{i=1}^{n} x_i & \sum_{i=1}^{n} y_i \\ \sum_{i=1}^{n} x_i & \sum_{i=1}^{n} x_i^2 & \sum_{i=1}^{n} x_i y_i \\ \sum_{i=1}^{n} y_i & \sum_{i=1}^{n} x_i y_i & \sum_{i=1}^{n} y_i^2 \end{bmatrix} \begin{Bmatrix} a \\ b \\ c \end{Bmatrix} = \begin{Bmatrix} \sum_{i=1}^{n} w_i^h \\ \sum_{i=1}^{n} x_i w_i^h \\ \sum_{i=1}^{n} y_i w_i^h \end{Bmatrix}.$$

Once this equation is solved, substitution of *a*, *b* and *c* into equation (5.9.1) enables the new velocity $\overline{w}_I$ to be evaluated at node *I*. We refer to $\overline{w}_I$ as the recovered velocity, and it is used in place of the corresponding velocity calculated in Section 5.6. Clearly, the new velocity found in this way is determined by the velocities at the sampling points, w_i^h. If the w_i^h have higher accuracy (i.e. better approximation to the exact velocity),

$\overline{w}_I$ may be more accurate than those calculated in Section 5.6. The sampling point is then called a *superconvergent* point.

The question now is whether or not the *superconvergent* points exist. Zienkiewicz & Zhu (1992) stated that when using triangular elements with a linear interpolation function in the finite element analysis, the centroid of a element is a superconvergent point where the solution obtained by the finite element method is more accurate than that in other places. Therefore, the sampling point is simply the central point of the triangles.

The w_i^h at the sampling points can be easily estimated by the interpolation given in C.5 of Appendix C, that is

$$w_i^h = a^h + b^h x_i + c^h y_i,$$

where a^h, b^h and c^h are calculated using C.5 with (q_1, q_2, q_3) replaced by (w_I, w_J, w_K) which are the nodal velocities of the triangle containing the sampling point *i*.

However, a difficulty with using the recovery technique may occur at the domain boundaries, where a patch may include fewer triangles, as shown in Figure 5.9.4. Although various techniques have been suggested to deal with the problem, none is perfect. One of them is given by Zienkiewicz & Zhu (1992), in which the boundary values of stresses is obtained using the patches of internal nodes, somewhat like extrapolation.

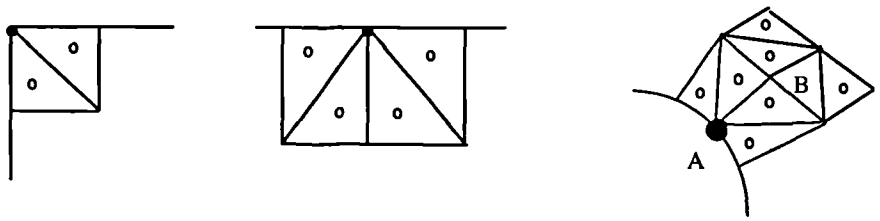

a). on a corner b). On a plane surface c) on a curve

Figure 5.9.4 Patch around the boundary nodes

In our work, different treatments are used for different boundaries. If the boundaries are composed of the planes, such as a) and b) in Figure 5.9.4, the smoothing technique

mentioned above is used. If the boundary is a curved surface like case c) in Figure 5.9.4, we simply follow the idea of Zienkiewicz & Zhu (1992), based on the extrapolation technique. That is the value at point A in Figure 5.9.4c is found by the patch associated with internal point B.

To demonstrate the accuracy of the recovery technique, the same problem of impulsive motion of the wave maker mentioned above is solved again. Similar results to Figure 5.9.2b are plotted in Figure 5.9.5, together with the analytical solution. It can be seen that the good agreement is also achieved here.

All the results given in Chapter 7 and Chapter 8 have been postprocessed using the above techniques, unless mentioned otherwise.

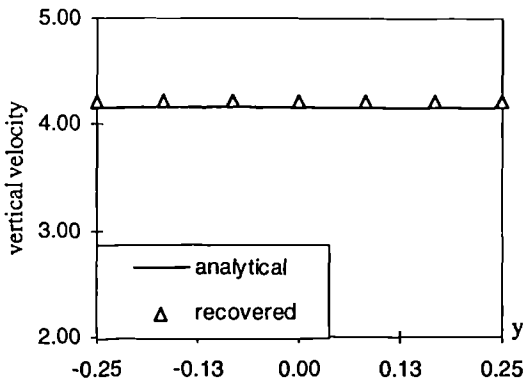

Figure 5.9.5 Comparison of the vertical velocity obtained by using the recovery technique with the analytical solution, at $x/d = 0.05$, for the impulsive wave maker (the values of velocity shown have been divided by $\sqrt{gd}$)

6. SOLUTION METHODS FOR THE ALGEBRAIC SYSTEM

6.1 Introduction

After the fluid domain is discretised, the differential equation and boundary conditions are transformed into a set of linear algebraic equations in this thesis, as discussed in Chapter 5, i.e.

$$[A]\{x\}=\{B\} \qquad (6.1.1)$$

where $[A]=\left(a_{ij}\right)_{n\times n}$ is the coefficient matrix and $\{B\}=\left(b_i\right)_n$ is a vector containing the known components. To be consistent with mathematical books, entries of $[A]$ and $\{B\}$ are represented by a_{ij} and b_i, respectively, instead of A_{IJ} and B_I as in Chapter 5, and the vector of unknowns is denoted by $\{x\}$.

In Chapter 5, it has been shown that the matrix $[A]$ is sparse and symmetric positive definite (SPD) in this study. The sparsity is determined by the half bandwidth (hereafter denoted by $\Re$) and the number of non-zero entries in $\Re$, which is dependent on the geometry of the problem, the mesh structure and the numbering system of the nodes.

The solution of this algebraic system is a key part of the analysis of the interaction between structures and non-linear waves discussed in this theses. The efficiency of the corresponding code largely depends on the efficiency of the solution techniques. There are a number of possible methods for solving the system, but the efficiency of each method is largely problem-dependent. The application of FEM to steep wave problems is currently being investigated. It is not as mature as its application in other fields, such as solid mechanics. Therefore the choice of the methods for solving the corresponding algebraic system is not straightforward.

There are essentially two different types of methods available for solving the linear equation (6.1.1): the *direct* method and the *iterative* method. Both of them have a wide variety of forms, depending on the type of problems to be solved. There is no intention here to discuss all the detail. The discussion will be made especially with regard to the property of matrix $[A]$ associated with the steep wave problem.

A well-known approach in direct strategies is the *Choleski factorisation method*, used to solve algebraic systems with SPD matrices. In this method, the matrix is factorised into triangular factors, and the corresponding unknowns are then found by the forward and backward substitution of the triangular system. The alternative to the direct method is the iterative procedure, in which the unknowns are found by computing a sequence of their approximations. Not all iterative procedures can be applied to the problem in this thesis, but it is hoped that the preconditioned conjugate gradient (PCG) solver is suitable because it has been successfully used in many problems with SPD matrices.

The two methods have different advantages and disadvantages. In the direct method, the solution can be found directly, and would be exact if there would be no round-off errors. The cost of calculation can be predicted *a priori*, and does not need a control error. In addition, once the factors of $[A]$ are obtained, they can be used to find the solutions corresponding to every columns in $\{B\}$ if it contains two columns. In the case where the factorisation calculation dominate the requirement for CPU time, the cost of the solving for the two columns may not be significantly larger than for one column. This may be advantageous when both the velocity potential and the term $\frac{\partial \phi}{\partial t}$ need to be solved. The main problem with this method may be the memory requirement for storing $[A]$. Although it is only necessary to store the entries in half bandwidth of the matrix, a large number of zero coefficients will still normally be included, because the half bandwidth usually comprises a much larger number of zero coefficients than non-zero coefficients in each row. The zero entries in the half bandwidth will be filled in during the process of factorisation, that is, the zero entries may become nonzero. This feature of the Choleski method leads to dramatic storage requirement for solving large problems. In contrast, the iterative procedure only handles the matrix-vector products and does not change the entries in $[A]$ during the process. Thus, there is no need for storing the zero entries of the matrix, and consequently, the iterative method requires considerable less storage than the direct one. In some cases, the iterative method, such as PCG, may be much faster than the direct one if an efficient preconditioner is employed. Nevertheless, the determination of the preconditioner is not trivial and is very much problem-dependent. Also the iterative method needs a control error which largely affects the

computational costs. Moreover, if the two columns are included in $\{B\}$, the cost for solving the algebraic system may be almost doubled.

The purpose of this chapter is to try to answer the questions: Which solver, Choleski or PCG, is more suitable for solving our problem? When the PCG method is adopted, what kind of preconditioner should be used?

6.2 Choleski method

The Choleski method has been widely used and thoroughly investigated both in theory and in practice. Thus only a brief description will be given here.

If $[A]$ is an SPD matrix, a triangular decomposition of $[A]$ yields

$$[A]=[L][\Lambda][L]' \qquad (6.2.1)$$

where $[L]$ is an unit lower-triangular matrix with $L_{ii}=1\,(i=1,2,3\cdots n)$, $[L]'$ is its transpose, and $[\Lambda]$ is a diagonal matrix which is often written as

$$[\Lambda]=\mathrm{diag}(\rho_1,\rho_2,\cdots\rho_n)\,. \qquad (6.2.2)$$

The entries in $[L]$ and $[\Lambda]$ can be determined recursively by

$$\rho_1=a_{11}, \qquad (6.2.3)$$

and

$$t_{ij}=a_{ij}-\sum_{k=1}^{j-1}t_{ik}l_{kj} \qquad l_{ij}=t_{ij}/\rho_j \qquad (j=I_j,\cdots i-1), \qquad (6.2.4)$$

$$\rho_i=a_{ii}-\sum_{k=1}^{i-1}t_{ik}l_{ik}\,, \qquad (6.2.5)$$

for $i=2,3,\cdots n$. In equation (6.2.4), I_j represents the first non-zero entry in the i-th row. It can be seen that even if a coefficient a_{ij} lying in the half bandwidth is zero, the corresponding l_{ij} may become nonzero. In addition, ρ_i are always positive because $[A]$ is an SPD matrix.

When $[A]$ is expressed as in equation (6.2.1), the following transformation can be made:

$$[L]\{y\} = \{B\}, \tag{6.2.6}$$

so that

$$[L]^{'}\{x\} = [\Lambda]^{-1}\{y\}. \tag{6.2.7}$$

The unknowns $\{x\}$ are then found by using the forward substitution

$$\begin{cases} y_1 = b_1 \\ y_i = b_i - \sum_{k=1}^{i-1} l_{ik} y_k \qquad (i = 2,3,\cdots n), \end{cases} \tag{6.2.8}$$

and the backward substitution

$$\begin{cases} x_n = \dfrac{y_n}{\rho_n} \\ x_i = \dfrac{y_i}{\rho_i} - \sum_{k=i+1}^{n} l_{ki} x_k \qquad (i = n-1,\cdots 2,1). \end{cases} \tag{6.2.9}$$

In practice, a large portion of the computational cost for the above procedure occurs during the factorisation in equations (6.2.3) to (6.2.5). Specifically, the computational cost of the factorisation is roughly proportional to $n\Re^2$, while the cost of the forward and backward substitution is roughly proportional to $n\Re$ (Pissanetzky, 1984). Hence, once decomposing the matrix $[A]$, problems with two right-hand side vectors can be solved using equations (6.2.8) and (6.2.9) twice. The CPU time required may increase by only a small fraction of solving one-vector problems.

6.3 PCG iterative method

The iterative method comprises a wide range of forms. An extensive survey has been given recently by Bruaset (1995) who grouped the widely used iterative methods into two classes. The first class is based on matrix splitting, such as Jacobi, Gauss-Seidel, successive overrelaxation and symmetric successive overrelaxation (SSOR) methods. The second class is based on the Krylov subspace. The conjugate gradient method is a popular method in the second class for symmetric positive definite problems. As shown

by Bruaset (1995), the full effectiveness of the conjugate gradient method cannot be achieved unless a suitable preconditioner is employed, which multiplies the original matrix $[A]$ in a suitable way. The evidence given by Bruaset (1995) showed that a good preconditioner may considerably speed up the convergence of the iterative method. The algorithm for the preconditioned conjugate gradient (PCG) method is discussed next. Only a brief description will be given, and all the details can be seen in the work of Bruaset (1995) and the books of Axelsson (1976, 1994).

6.3.1 Conjugate gradient method for a minimisation problem

The conjugate gradient method comes from considering the minimisation of the quadratic problem

$$H(x)=\frac{1}{2}(x,Ax)-(B,x), \tag{6.3.1}$$

where (x,Ax) and (B,x) represent inner products defined by

$$(x,Ax)=\{x\}'[A]\{x\} \quad \text{and} \quad (B,x)=\{B\}'\{x\}. \tag{6.3.2}$$

It can be shown that if $[A]$ is an SPD matrix, i.e. $(x,Ax)>0$ for all $\{x\}\neq\{0\}$, the minimisation of (6.3.1) is equivalent to solving $[A]\{x\}=\{B\}$ in equation (6.1.1). In fact, letting $\bar{x}$ satisfy $[A]\{\bar{x}\}=\{B\}$, equation (6.3.1) can be rewritten as:

$$\begin{aligned} H(x) &= \frac{1}{2}(x-\bar{x}+\bar{x},A(x-\bar{x}+\bar{x}))-(B,x-\bar{x}+\bar{x}) \\ &= H(\bar{x})+\frac{1}{2}(x-\bar{x},A(x-\bar{x})), \end{aligned} \tag{6.3.3}$$

where $(A\bar{x},x-\bar{x})=(\bar{x},A(x-\bar{x}))=(B,x-\bar{x})$, since $[A]$ is symmetric, has been used. Equation (6.3.3) shows that $H(x)$ reaches its minimum, $H(\bar{x})$, if and only if $\{x\}=\{\bar{x}\}$, since $(x-\bar{x},A(x-\bar{x}))>0$ when $\{x\}\neq\{\bar{x}\}$. This means that we can obtain the solution of equation (6.1.1) by minimising $H(x)$ in equation (6.3.1).

This minimisation problem can be solved by the conjugate gradient method. In this method, the minimiser of $H(x)$ is found step by step, by searching a sequence of

approximate vectors in a particular way described now. Letting $\{x\}^{(k)}$ denotes the approximation obtained at stage k, the approximation at stage $k+1$ is constructed by:

$$\{x\}^{(k+1)} = \{x\}^{(k)} + \lambda_k \{p\}^{(k)}, \tag{6.3.4}$$

in such a way that $H\left(x^{(k)} + \lambda_k p^{(k)}\right)$ is minimised. To achieve this, the constant λ_k and $\{p\}^{(k)}$ (called as a searching direction) have to be determined properly. In order to find λ_k, inserting equation (6.3.4) into (6.3.1) and using $\dfrac{\partial H\left(x^{(k)} + \lambda_k p^{(k)}\right)}{\partial \lambda_k} = 0$ yields:

$$\left(r^{(k)}, p^{(k)}\right) - \lambda_k \left(p^{(k)}, Ap^{(k)}\right) = 0, \tag{6.3.5}$$

that is, $\lambda_k = \dfrac{\left(r^{(k)}, p^{(k)}\right)}{\left(p^{(k)}, Ap^{(k)}\right)}$ (6.3.6)

where $\{r\}^{(k)} = \{B\} - \{A\}\{x\}^{(k)}$ defines a residual of $\{x\}^{(k)}$.

The vector $\{p\}^{(k)}$ in equation (6.3.4) can be constructed as

$$\{p\}^{(k)} = \{r\}^{(k)} + \alpha_k \{p\}^{(k-1)}, \tag{6.3.7}$$

where α_k is another constant which is determined by imposing

$$\left(p^{(k)}, Ap^{(k-1)}\right) = 0. \tag{6.3.8}$$

Substituting equation (6.3.7) into (6.3.8), it follows that

$$\alpha_k = -\frac{\left(r^{(k)}, Ap^{(k-1)}\right)}{\left(p^{(k-1)}, Ap^{(k-1)}\right)}. \tag{6.3.9}$$

Once the values of α_k and λ_k are obtained, equation (6.3.4) gives a new approximation to $\{x\}$.

Equations (6.3.6) and (6.3.9) are not the best in terms of calculation time. They may however be transformed into other forms. In fact, as shown by Axelsson (1994), the above procedure for constructing $\{x\}^{(k+1)}$ and $\{p\}^{(k)}$ ensures that

$$\left(r^{(k+1)}, r^{(j)}\right) = 0 \qquad \left(j = 0,1,2\cdots k\right), \tag{6.3.10}$$

$$\left(r^{(k+1)}, p^{(j)}\right) = 0 \qquad \left(j = 0,1,2\cdots k\right), \tag{6.3.11}$$

$$\left(p^{(k+1)}, Ap^{(j)}\right) = 0 \qquad \left(j = 0,1,2,\cdots k\right). \tag{6.3.12}$$

Using these equations, the alternative formulae

$$\lambda_k = \frac{\left(r^{(k)}, r^{(k)}\right)}{\left(p^{(k)}, Ap^{(k)}\right)} \tag{6.3.13}$$

and

$$\alpha_k = \frac{\left(r^{(k)}, r^{(k)}\right)}{\left(r^{(k-1)}, r^{(k-1)}\right)}. \tag{6.3.14}$$

may be derived. Equations (6.3.13) and (6.3.14) are more effective than equations (6.3.6) and (6.3.9) because in the former case, the evaluation of the inner products $\left(r^{(k)}, Ap^{(k-1)}\right)$ is avoided, and also the numerators are equal.

Another issue to be addressed concerns the situation where $\{p\}^{(k)}$ may be zero, and hence λ_k could not be determined by (6.3.13). However, it can be shown that this case will never happen in practice. Actually, using equations (6.3.7) and (6.3.11), one can obtain:

$$\left(r^{(k)}, p^{(k)}\right) = \left(r^{(k)}, r^{(k)}\right) + \alpha_n \left(r^{(k)}, p^{(k-1)}\right) = \left(r^{(k)}, r^{(k)}\right). \qquad (6.3.15)$$

From this equation, it is clear that $\{p\}^{(k)} = 0$ implies that $\left(r^{(k)}, r^{(k)}\right) = 0$, which in turn implies that $\{r\}^{(k)} = \{B\} - [A]\{x\}^{(k)} = 0$. Thus, a zero searching direction occurs only when the exact solution is obtained, but by then the iteration procedure would have been stopped.

6.3.2 Iterative algorithm based on the conjugate gradient method

In a computer code, the above minimisation procedure can be realised by the following algorithm. Supposing that an arbitrary initial approximation $\{x\}^{(0)}$ and tolerance error ε are given, the algorithm can be written as:

Algorithm I:

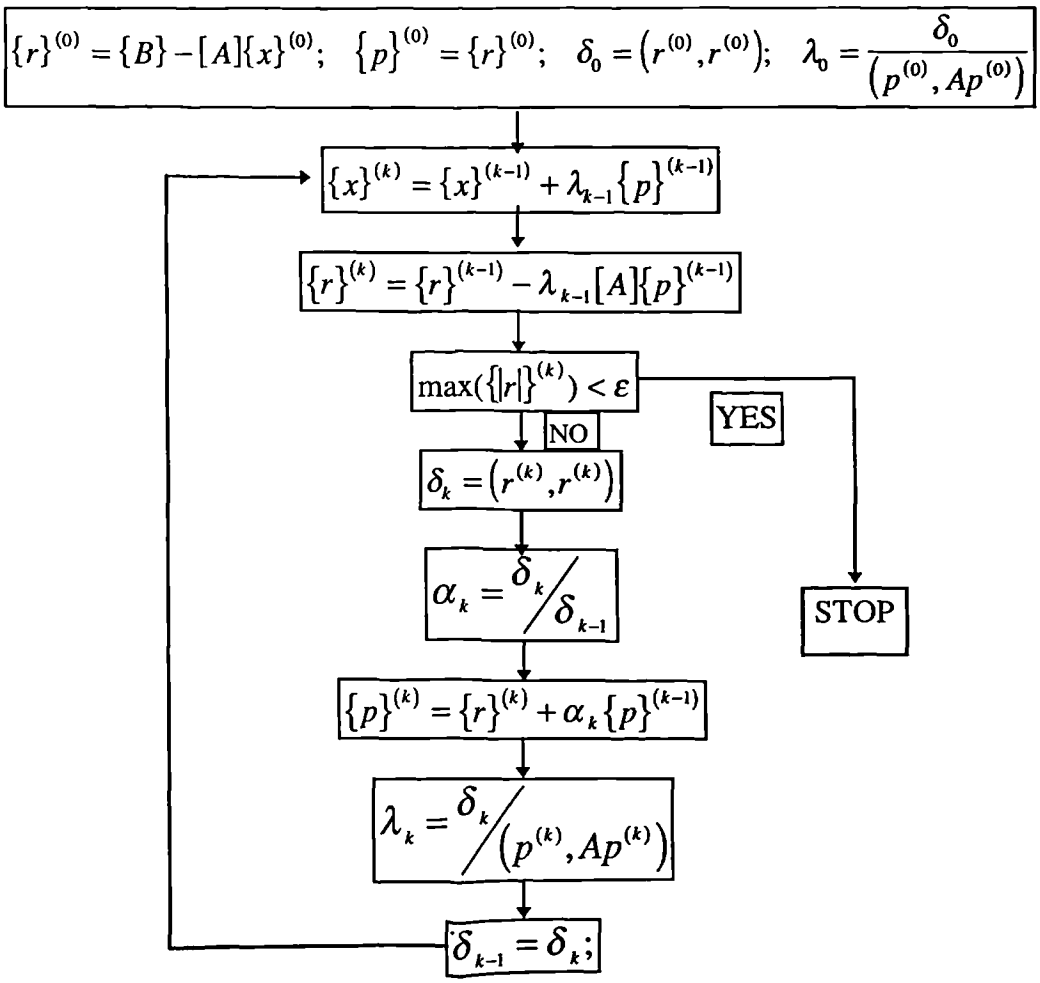

where $\{|r|^{(k)}\} = \left[|r_1|^{\{k\}}, |r_2|^{\{k\}}, \cdots |r_n|^{\{k\}}\right]'$. In this algorithm, none of the entries of $[A]$ changes during the procedure, and therefore it is only necessary to store the non-zero entries, which saves on storage requirement significantly. It can be seen that almost every matrix-vector multiplication is associated with the residual $\{r\}$, which is related to the right hand side vector $\{B\}$. This means that if $\{B\}$ includes two columns, the cost for finding each corresponding solution may be almost equal. Compared with the direct method of Section 6.3, the iterative procedure may be inferior in this case, if both methods have roughly similar cost for the one-column problem.

The convergence properties of this algorithm depend upon the eigenvalue distribution of the matrix $[A]$ (see Bruaset, 1995). Specifically, the number of iterations needed for a given ε is determined by the 'condition' of this matrix, which is defined as the ratio of the maximum eigenvalue to the minimum eigenvalue for SPD matrix. Consequently, the convergence properties may be improved by changing the eigenvalue distribution of $[A]$. This may be achieved by 'preconditioning' the matrix $[A]$.

6.3.3 Iterative algorithm based on the preconditioned conjugate gradient method

Preconditioning the matrix $[A]$ means transforming the matrix into another, which may possess a more favourable eigenvalue distribution. Let us introduce an arbitrary non-singular matrix $[C]$ and multiply the both sides of equation (6.1.1) by $[C]^{-1}$. This gives

$$[C]^{-1}[A]\{x\} = [C]^{-1}\{B\}. \qquad (6.3.16)$$

If $[C]^{-1}$ is chosen approporately, the resulting preconditioned matrix $[C]^{-1}[A]$ may have a good eigenvalue distribution. The method for choosing $[C]$ will be discussed in Section 6.4. Our attention here is focused on the application of *Algorithm I* to the new system in equation (6.3.16). It has been shown that the above algorithm is established on the basis of the SPD matrix . To ensure that $[C]^{-1}[A]$ is an SPD matrix, the matrix

$[C]$ is also required to be an SPD matrix (Axelsson, 1994). Applying *Algorithm I* to $[C]^{-1}[A]$ and performing some necessary changes, the following algorithm is formed:

Algorithm II:

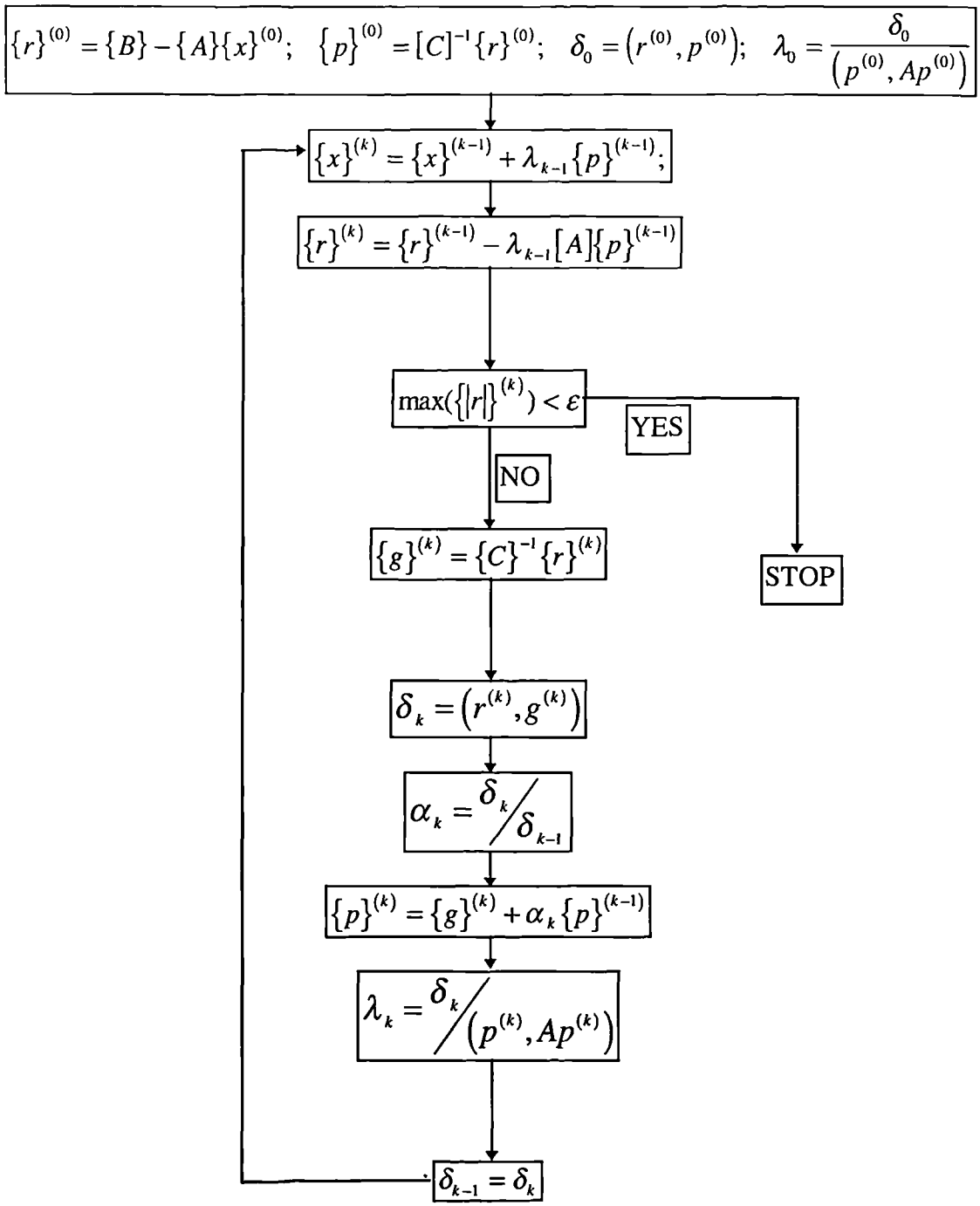

Compared with *Algorithm I*, almost all of the calculations in this algorithm are identical except for the inclusion of an additional computation in each iteration, namely $\{g\}^{(k)} = [C]^{-1}\{r\}^{(k)}$. It would appear that solving for $\{g\}^{(k)}$ is similar to solving an problem, such as equation (6.1.1). However, if $[C]$, to be able to chosen arbitrarily, has the form $[C] = [L][L]^{'}$, the solution for $\{g\}^{(k)}$ can be easily and effectively found by the forward and backward substitution techniques described in equations (6.2.7) and (6.2.8). It is evident that the effectiveness of the procedure largely depends on the form of $[C]$.

6.4 Preconditioner

When choosing $[C]$, several issues must be considered in order to ensure that $[C]$ will accelerate the convergence without giving rise to a noticeable increase in CPU and storage requirement. These include: (1) the resemblance between $[C]^{-1}$ and $[A]$; (2) the cost of its construction; (3) the cost of computing $(g)^{(k)} = [C]^{-1}\{r\}^{(k)}$ and (4) the cost of its storage. The first requirement is to ensure that the condition of $[C]^{-1}[A]$ is better than that of $[A]$; the second and the third ones are concerned with the cost of applying the preconditioner, which should require a little computational effort; finally with the fourth issue, it is expected that the storage requirement of the preconditioner is less than, or at least comparable to, that of $[A]$. Although the above four requirements may be in conflict with each other, there are a large number of preconditioners which can reasonably satisfy the requirements or at least some of them. Bruaset (1995) grouped them into three families:

1) Preconditioner based on matrix splitting associated with basic iterative methods like the Jacobi and SSOR (symmetric successive overrelaxation) methods.
2) Preconditioners based on incomplete factorisation (ILU)
3) Preconditioners based on approximation inversion

In the following, the two preconditioners, based on SSOR and the incomplete factorisation, will be discussed.

6.4.1 SSOR preconditioner

This preconditioner comes from the SSOR iterative method which can be described in matrix form as

$$[C]\{x\}^{(k+1)} = [R]\{x\}^{(k)} + \{B\}, \qquad (6.4.1)$$

where $[R] = [C] - [A]$ and the matrix $[C]$ on the left hand side is defined by:

$$[C] = \left([D] + \mu[L]\right)[D]^{-1}\left([D] + \mu[L]^T\right)\frac{1}{2-\mu} \qquad (6.4.2)$$

where μ is a constant called the relaxation coefficient; $[D]$ is a diagonal matrix formed by the diagonal entries of $[A]$; and $[L]$, with its diagonal entries equal to zero, is the lower-triangular part of $[A]$.

What we are interested in here is not the procedure of equation (6.4.1) but the matrix $[C]$ defined in equation (6.4.2). This matrix is considered as a preconditioner and possesses the following properties:

1) Its factors are triangular and therefore a system like $[C]\{g\}^{(k)} = \{r\}^{(k)}$ can be efficiently solved by backward and forward substitutions.
2) All of the elements in the factors are directly determined by those in $[A]$, and therefore it is not necessary to calculate and to store them. When solving the system $[C]\{g\}^{(k)} = \{r\}^{(k)}$, the required entries are just taken from the corresponding elements of $[A]$.
3) The $[C]$ is always an SPD matrix whenever $[A]$ is an SPD matrix, as proved by Axelsson (1976).

Adjusting the constant μ included in equation (6.4.2) may lead $[C]^{-1}[A]$ to have a good condition. Generally, it should be in the range $0 < \mu < 2$. Axelsson (1976) showed an optimal value based on the condition of $[A]$, but it is not available in the iteration process. The proper value of μ may be found by numerical tests.

6.4.2 Preconditioner based on incomplete factorisation with modification

The preconditioner $[C]$ constructed in this way was originally suggested by Meijerink & van der Vorst (1977). Their method is based on a scheme similar to but different from the Choleski factorisation method described in Section 6.2 above. As mentioned there, the sparsity within the band of a matrix will be lost during the factorisation. The fundamental idea of the incomplete factorisation method is to reject all, or part, of those fill-in entries according to a chosen sparsity pattern. Thus the factorisation becomes approximate, or incomplete. The resulting matrix in this way is used as a preconditioner.

If the sparsity pattern is represented by a set of matrix indices (i,j), $i \neq j$, which refer to non-zero entries, then the sparsity pattern of a symmetric matrix $[A]$ is written as:

$$P_A = \{(i,j), a_{ij} \neq 0, j \leq i\} \tag{6.4.3}$$

When using incomplete factorisation, the sparsity pattern for $[C]$ can be specified accordingly. Once the sparsity pattern is given, the incomplete factorisation is performed as follows:

$$\hat{\rho}_1 = a_{11}, \tag{6.4.4}$$

and

$$\hat{t}_{ij} = \begin{cases} a_{ij} - \sum_{k=1}^{j-1} \hat{t}_{ik}\hat{l}_{kj} & (i,j) \in P_c \\ 0 & (i,j) \notin P_c \end{cases}; \tag{6.4.5}$$

$$\hat{l}_{ij} = \hat{t}_{ij}/\hat{\rho}_j \qquad (j = 1,2\cdots i-1); \tag{6.4.6}$$

$$\hat{\rho}_i = \hat{a}_{ii} - \sum_{k=1}^{i-1} \hat{t}_{ik}\hat{l}_{ik}\,. \tag{6.4.7}$$

for $i = 2,3,\cdots n$. The matrix $[C]$ is then expressed in the form:

$$[C] = [\hat{L}][\hat{\Lambda}][\hat{L}]', \tag{6.4.8}$$

with $[\hat{L}] = (\hat{l}_{ij})$ and $[\hat{\Lambda}] = \text{diag}(\hat{\rho}_1, \hat{\rho}_2, \cdots \hat{\rho}_n)$.

It can be seen that the procedure described by equations (6.4.4) to (6.4.7) is similar to that described by equations (6.2.3) to (6.2.5). The only difference is that all the entries with $(i,j) \notin P_c$ have been set to be zero here. Bearing in mind that there is a large number of zero entries in the half bandwidth of the matrix $[A]$, one can understand that this restriction leads the cost of the incomplete factorisation method to be dramatically smaller than that of the full factorisation method in Section 6.2, if $P_C = P_A$. The preconditioner matrix $[C]$ in equation (6.4.8) has the following properties:

1) It enables equations like $[C]\{r\}^{(k)} = \{g\}^{(k)}$ to be solved efficiently by backward and forward substitution.
2) Its elements on the non-zero set P_c are equal to those of $[A]$, i.e. $c_{ij} = a_{ij}$ for $(i,j) \in P_c$. This can be seen from equation (6.4.6) above.
3) If P_c includes all the indices in the band of $[A]$, then $[C] = [A]$; if P_c just includes the diagonal entries of $[A]$, then $[C] = \text{diag}(a_{11}, a_{22}, a_{33}, \cdots a_{nn})$. Any other choice of P_c in between leads to different approximations of $[C]$ to $[A]$. It is obvious that the more the elements included in P_c, the faster the associated PCG iterative method will converge but also the more it costs to construct and store $[C]$. A common choice is $P_C = P_A$. This is a reasonable compromise between the cost and convergence rate. This choice will be used in the work here.

In the complete factorisation of Section 6.2, the diagonal element ρ_i is always positive at all stages, if the matrix $[A]$ is SPD. However, in the case of the incomplete factorisation, the positive diagonal entries $\hat{\rho}_i$ are not guaranteed even when $[A]$ is an SPD matrix. If $\hat{\rho}_i \leq 0$, the PCG method would fail because $[C]^{-1}[A]$ may not be an SPD matrix. On the other hand, even when $\hat{\rho}_i > 0$ is achieved in some cases, $[C]^{-1}[A]$ may not necessarily have the best condition for the given sparsity pattern.

To avoid the difficulty of $\hat{\rho}_i \leq 0$ and also to adjust $[C]$ for a given sparsity pattern, Manteuffel (1980) suggested a *shifted incomplete factorisation.* In his method, the

matrix $[A]$ is replaced by a new matrix $[A]+\theta[D]$, where θ is a constant and $[D]=\text{diag}(a_{11},a_{22},a_{33},\cdots a_{nn})$. Then the above incomplete factorisation procedure is applied to $[A]+\theta[D]$ to give the corresponding matrix $[C]$. It is apparent that the condition of the resulting matrix $[C]^{-1}[A]$ depends on the coefficient θ. For a particular value of θ , $[C]^{-1}[A]$ may have a better condition than for any other values. This particular value is called the 'best value'. Manteuffel (1980) also investigated the influence of the coefficient θ and showed that the best value of θ is in the range of (θ_l,θ_u), where θ_l is the minimum value of θ necessary to guarantee that all of the diagonal entries are positive, and $\theta_u\ (>0)$ is the value of θ, above which the condition of $[C]^{-1}[A]$ is worse than$[A]$. The value θ_l may be either positive or negative. Unfortunately, neither θ_l nor θ_u, let alone the best value of θ, can be easily obtained without numerical tests.

6.5 Investigation on the influence of μ and θ

In the above sections, two preconditioners were described. In each one of them, a constant is included. The constants affect the condition of $[C]^{-1}[A]$ and therefore the convergence rate of the PCG method. In this section, the influence of the constants will be investigated by numerical tests.

During the tests, the condition of $[C]^{-1}[A]$ is not of direct concern, although the changes in the values of μ and θ directly affect the condition. Instead, attention is focused on the convergence rate of the PCG. The reasons for this are two-fold: firstly the eigenvalues of $[C]^{-1}[A]$ cannot be easily obtained and secondly the ultimate purpose of the investigation is to try to find good values for μ or θ which can give good convergent properties for the PCG method.

The numerical tests are based on the impulsive wavemaker problem already used in Chapter 5. The mesh will be generated in the same way as there, but the dimensions of the tank and the velocity of the wave maker may vary accordingly here. The test cases are listed in Table 6.5.1 which includes cases with different mesh sizes (Cases A, B and C), with different number of nodes but the same mesh size (Cases B and D) and with different velocity (Cases D to G).

Table 6.5.1 Test cases

Case	$U/\sqrt{gd}$	B/d	L/d	Number of nodes
A	1.0	0.5	4	22275
B	1.0	0.5	4	5187
C	1.0	0.5	4	3731
D	1.0	0.5	10	13031
E	0.5	0.5	10	13031
F	1.5	0.5	10	13031
G	2.0	0.5	10	13031

All of the cases are first solved using an incomplete factorisation matrix as a preconditioner. The value of θ is taken in the range $(-0.18, 0)$. For each value, the error defined by $\text{error}(k) = \max(\{|r|\}^{(k)})$ via the number of iteration can be obtained. The convergent surfaces are then plotted as shown in the left columns of Figure 6.5.1 to Figure 6.5.7, in which $\alpha = -\theta$ is used to avoid the negative symbol. From these results, one can also plot the corresponding curves of the number of iteration against α for a fixed error, e.g. $error < 10^{-8}$, as shown in the right columns of Figure 6.5.1 to Figure 6.5.7. It can be seen from these figures that although the convergent property may be different for different cases, the best values of α or θ, at which the number of iterations is a minimum, are almost the same, i.e. $\alpha = -\theta \approx 0.12$, for the given desired accuracy. It can also be seen that the convergent rate is not very sensitive to these values, that is in a quite wide range of $\alpha \in (0, 0.16)$, the iteration number required for obtaining the desired accuracy does not change significantly. However, when $\alpha > 0.16$, the convergent rate may be dramatically slow, as also shown in these figures. According to these tests, it is recommended that θ should be taken in the range $(-0.12, 0)$ for the problem described in this work.

All of the cases are now solved again using the SSOR preconditioner. Although similar convergent surfaces to those in Figure 6.5.1 and Figure 6.5.7 can also be plotted, the results presented in Figure 6.5.8 are only for the iteration numbers against μ with error$< 10^{-8}$. These figures show that the iteration number required for a given error may be quite sensitive to the choice for value μ in some cases, such as in Case D or Case G. However, the best value of μ is almost the same for all cases, as with θ in the incomplete factorisation preconditioner. This value seems to be estimated as $\mu \approx 1.618$.

Comparing Figure 6.5.8 with those of the corresponding cases in the right columns of Figure 6.5.1 to 6.5.7, it is found that the iteration numbers corresponding to the best value of μ or θ in turn are roughly same, although the number for SSOR preconditioner appears to be somewhat larger in all of the cases.

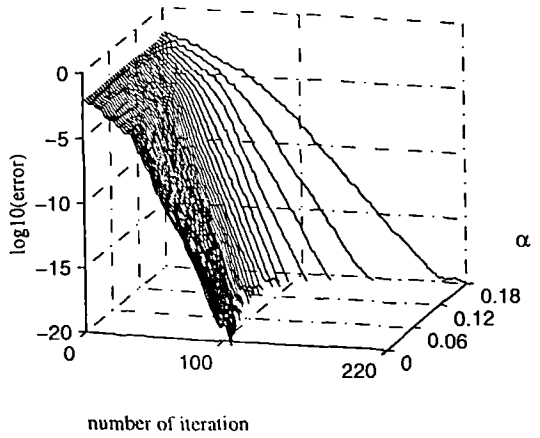

(a) Convergence surfaces

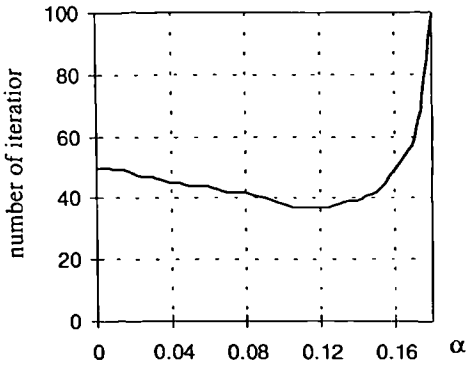

(b) iteration number for error < 10^{-8}

Figure 6.5.1 The convergent studies on the incomplete factorisation preconditioner (Case A)

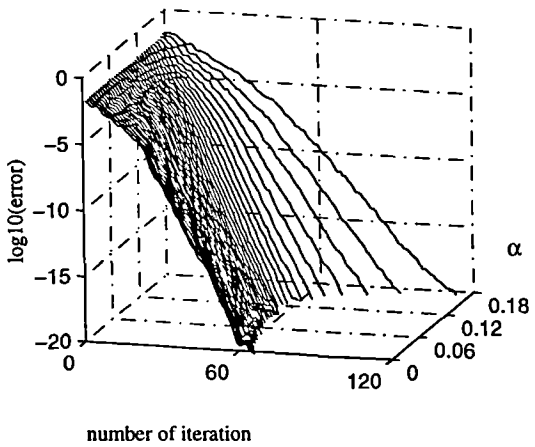

(a) Convergence surfaces

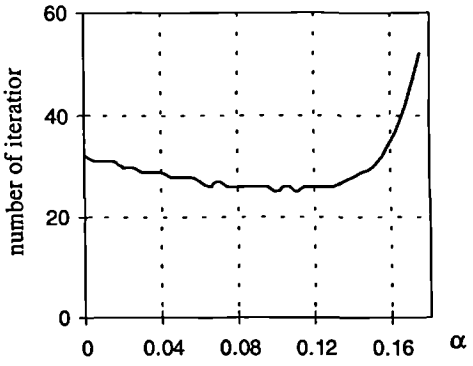

(b) iteration number for error < 10^{-8}

Figure 6.5.2 The convergent studies on the incomplete factorisation preconditioner (Case B)

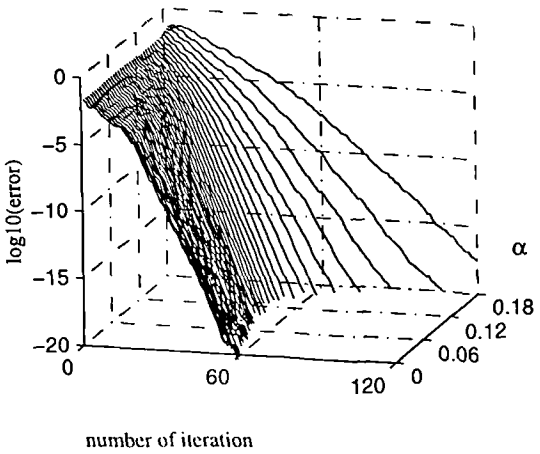

(a) Convergence surfaces

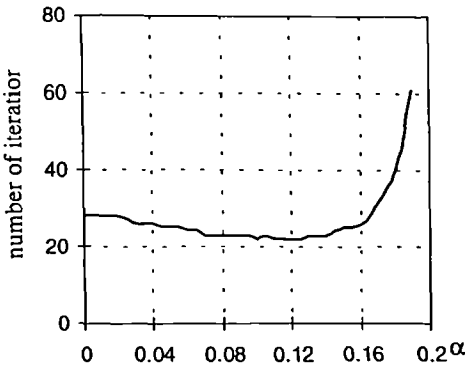

(b) iteration number for error < 10^{-8}

Figure 6.5.3 The convergent studies on the incomplete factorisation preconditioner (Case C)

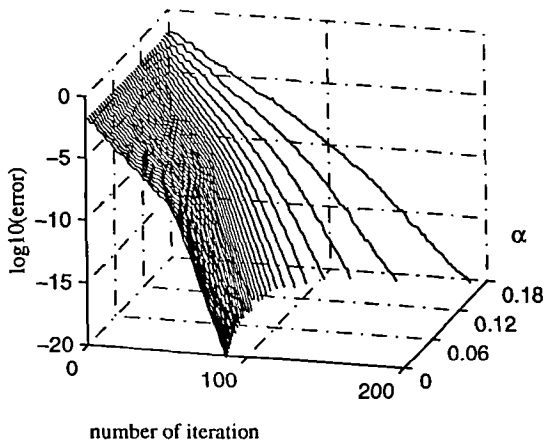

(a) Convergence surfaces

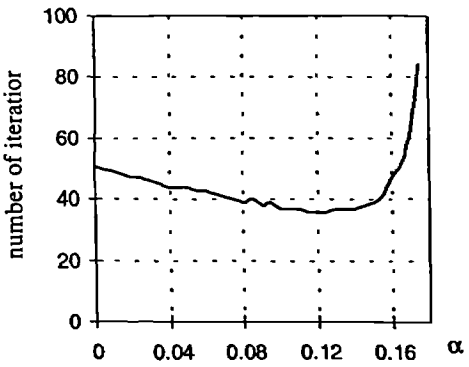

(b) iteration number for error < 10^{-8}

Figure 6.5.4 The convergent studies on the incomplete factorisation preconditioner (Case D)

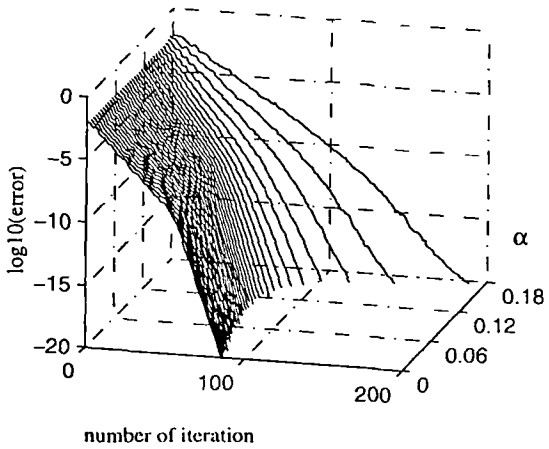

(a) Convergence surfaces

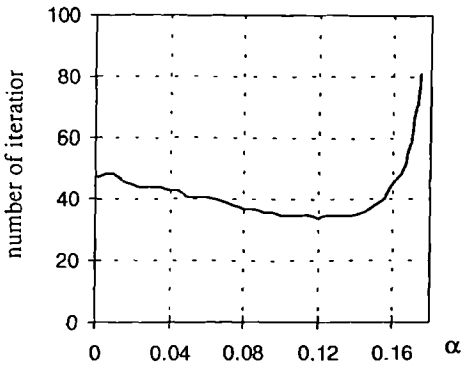

(b) iteration number for error < 10^{-8}

Figure 6.5.5 The convergent studies on the incomplete factorisation preconditioner (Case E)

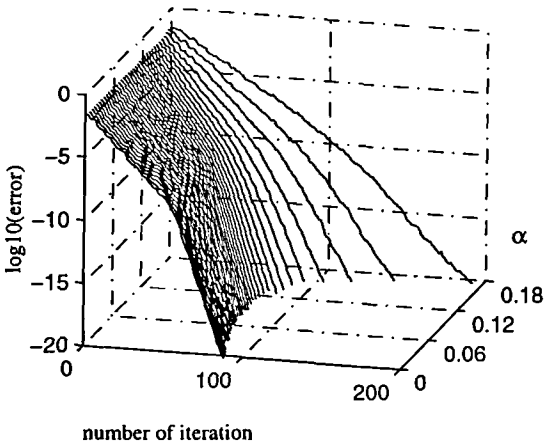

(a) Convergence surfaces

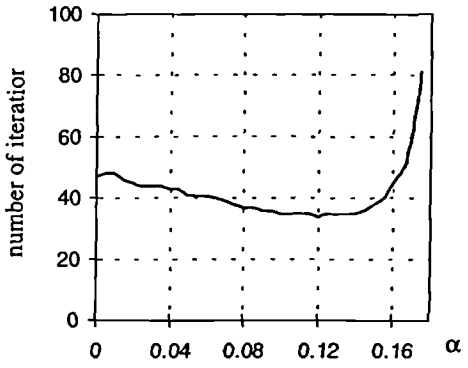

(b) iteration number for error < 10^{-8}

Figure 6.5.6 The convergent studies on the incomplete factorisation preconditioner (Case F)

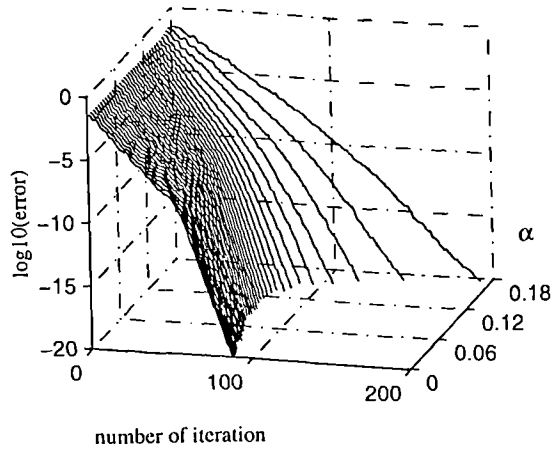

(a) Convergence surfaces

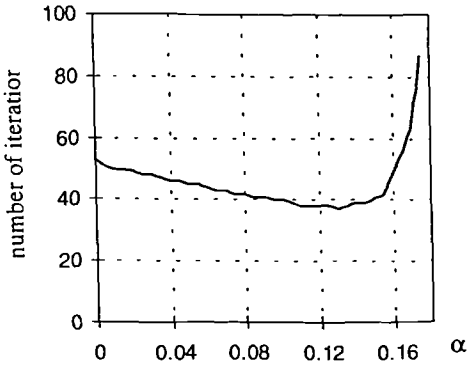

(b) iteration number for error < 10^{-8}

Figure 6.5.7 The convergent studies on the incomplete factorisation preconditioner (Case G)

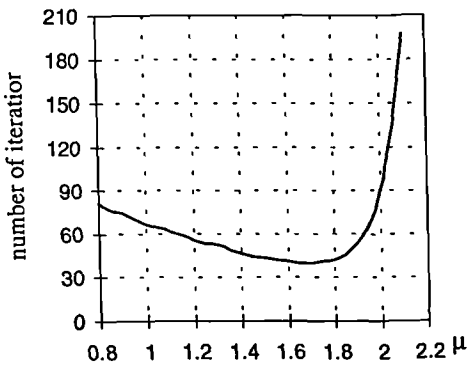

Figure 6.5.8 (a) Case A

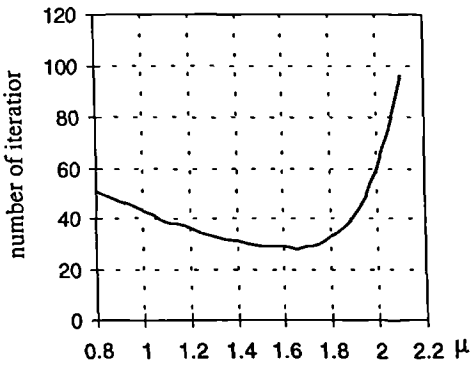

Figure 6.5.8 (b) Case B

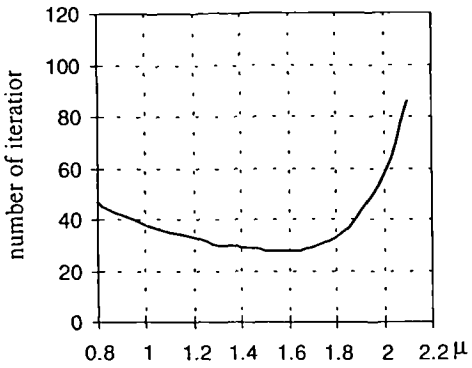

Figure 6.5.8 (c) Case C

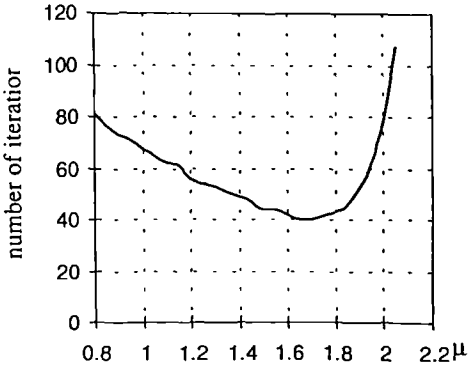

Figure 6.5.8 (d) Case D

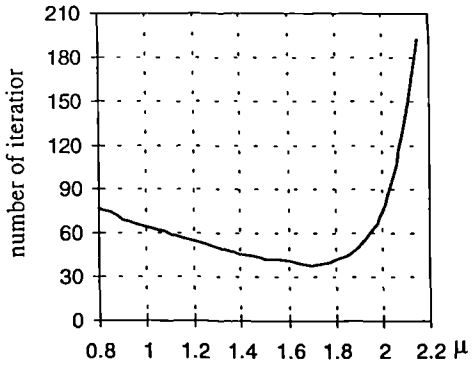

Figure 6.5.8 (e) Case E

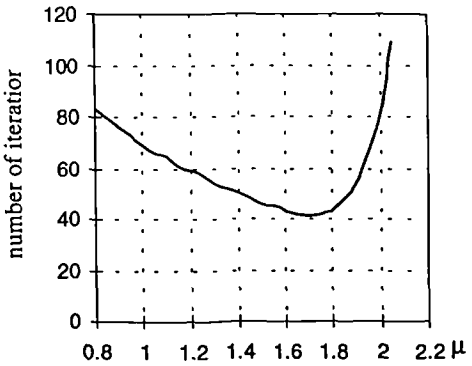

Figure 6.5.8 (f) Case F

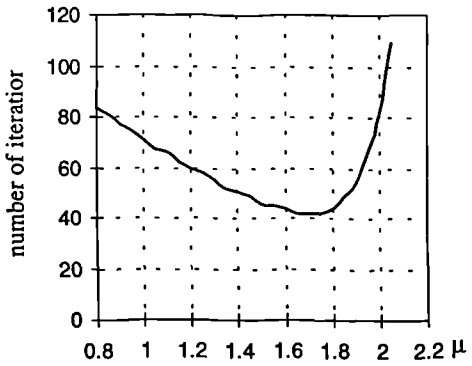

Figure 6.5.8 (g) Case G

Figure 6.5.8 The convergent studies on SSOR preconditioner
(control error is given as error<10^{-8})

6.6 Comparison between direct and iterative methods

The comparison is carried out using numeral tests. The test model is once more the impulsive wave maker in a rectangular tank. The tank may have different dimensions, that is, $L/d = 5, 10$ and $B/d = 0.5,\ 1.0,\ 1.5,\ 3.0$. The variation of width is used in order to give different half bandwidths of the matrix $[A]$. The mesh is generated in a similar way to that mentioned in the previous section. The velocity of the wave maker is specified as $U/\sqrt{gd} = 1.0$. When the direct method is used, the numbering system of the nodes is optimised to achieve minimum total half bandwidth, which is the sum of the half band width over all rows. When iterative methods are used, the starting approximation of the solution is taken as zero, and the control error tolerance is taken as being less than 10^{-8}. The constants, μ or θ, are chosen according to the analysis of the previous section. Attention is paid to the CPU time spent to solve the various cases, using the three different methods. The CPU time is collected based on the total calculation including the mesh generation, the formulation of the matrix $[A]$, the velocity evaluation, the solution of the algebraic equations and so on. However in the direct method, the CPU time spent on the optimisation of the numbering system is not included because it usually needs to be performed once only for practical simulations if the same mesh structure is used at every time step. The results obtained are summarised in Table 6.6.1. In each case, the CUP time has been divided by the CPU time required by the iterative method with the SSOR preconditioner. The half bandwidth $\Re$, relevant to the direct method, in the table is the average value, which is obtained by dividing the total half bandwidth by the number of the nodes.

The results in this table show that the CPU time for the direct method is roughly proportional to $\Re^2$, comparing the c3 with c12, in which the number of the nodes is roughly the same. Furthermore, when the average half bandwidth is quite small, say less than 120, the CPU time spent by the direct method is comparable to that spent by the two iterative methods. However, when the half bandwidth is large, for instance 340, the CPU time of the direct method is considerably (even ten times) more than that of the iterative methods. The comparison of the direct method and the iterative methods is also made for a problem with a circular cylinder subject to the harmonic wave generated by the wave maker. The CPU time of the direct method is also found to be over ten times

more than that of the iterative methods, when the average half bandwidth is quite large (Ma, Wu & Eatock Taylor, 1997). All of these investigations indicate that the direct method should not be the first choice except for cases where the half bandwidth is quite small, even when two columns are included in right hand side of equation 6.1.1.

Table 6.6.1 Comparison of CPU time required by direct and iterative methods

Case definition		Number	Half	Direct	ILU	SSOR
Case	Dimension($L \times B$)	of Nodes	Bandwidth	Method	--CG	--CG
c1	1×0.5	1547	99	1.63	1.03	1.0 (0.32sec)
c2	3×0.5	4879	124	2.43	1.15	1.0 (0.79sec)
c3	5×0.5	7973	123	2.24	1.17	1.0 (1.39sec)
c4	10×0.5	15827	123	1.97	1.04	1.0 (3.39sec)
c5	15×0.5	23919	124	1.97	0.98	1.0 (5.50sec)
c6	20×0.5	31773	124	1.94	0.91	1.0 (7.69sec)
c7	30×0.5	47719	123	1.96	0.90	1.0 (12.52sec)
c8	1×1.5	4199	242	8.04	1.01	1.0 (0.69sec)
c9	3×1.5	13243	358	16.51	1.22	1.0 (2.26sec)
c10	5×1.5	21641	347	12.59	1.24	1.0 (4.45sec)
c11	10×1.5	42959	--------	--------	1.09	1.0 (11.04sec)
c12	1×3	7735	235	7.63	1.10	1.0 (1.31sec)
c13	2×3	16065	534	36.49	1.15	1.0 (2.99sec)
c14	3×3	24395	--------	--------	1.20	1.0 (5.00sec)
c15	5×3	39865	--------	--------	1.13	1.0 (9.27sec)
c16	8×3	63665	--------	--------	1.14	1.0 (17.65sec)

The results in Table 6.6.1 above seem to suggest that the CPU required by the two iterative methods is similar in all cases, although a slight difference exits. Therefore, as

regards the CPU time, either of them can be chosen to solve the problems. However, when the incomplete factorisation conditioner is used, the storage of matrix $[C]$ is required whereas this requirement is not necessary when using the SSOR preconditioner. Therefore preference may be given to the iterative method with the SSOR preconditioner when storage requirement is taken into account.

When the comparison between the direct method and the iterative method was made, the control error tolerance of less than 10^{-8} for the iterative method was imposed. If a smaller error were specified, the CPU time required by the iterative methods would be larger. However, it should be noticed that a smaller error does not seem to be necessary according to the comparison of numerical results with analytical solution, as shown in Chapter 5 where the numerical results were obtained using the iterative method.

It should also be noticed that in the time marching process, the starting approximation solution at each step is actually estimated from the solution of the previous steps. This may enable the iterative method to be more efficient. It is clear, however, that the number of the iteration required at each step depends on the length of the time step. The smaller the time step, the smaller the iterative number. Therefore, this factor needs to be taken into account when choosing the length of the time step.

Unless mentioned otherwise, the results presented in this thesis are all obtained by the iteration method with an SSOR preconditioner.

7. TRANSIENT SLOSHING WAVES IN A TANK

7.1 Introduction

We will now move on to the validation and application of our methodology described in previous chapters. Two different types of wave problem are considered: transient sloshing waves in a tank and transient waves generated by a wave maker in a channel, with or without a body. The first type of the problem is considered in this chapter.

Sloshing waves may be caused by tank motion, by a disturbance (initial wave elevation, velocity potential and so on) on the free surface, or by both. Sloshing waves are associated with various engineering problems, such as liquid oscillations of large storage tanks caused by earthquakes, fuel motions in aircrafts and spacecrafts, liquid motions in containers and water flow on ship decks. The loads produced by the wave motion can cause structural damage and loss of the motion stability of solid objects, such as ships.

There has been a considerable amount of work on wave sloshing. For the case of small motion, Abramson (1966) used linear theory, and Solaas & Faltinsen (1997) adopted perturbation theory. For large motion, Jones & Hulme (1987), Faltinsen(1978), Okamoto & Kawahara (1990), Chen, Haroun & Liu (1996) and Armenio & La Rocca (1996) used various numerical methods for two dimensional problems. For three dimensional problems, Huang and Hsiung (1996) used the shallow water equations for the flow on a ship deck.

This body of work has significantly advanced our knowledge of sloshing waves in a tank. It is now well understood that in addition to normal standing waves, other wave forms, such as travelling waves and bores, can occur. Under certain conditions, high pressure and impact forces will be created on the side walls of the tank. This can have several serious implications, for example: (1) high pressures may create excessive stress and deformation within the walls, so that structural failure may become more likely; and (2) for a structure such as a ship, the high pressure may create an overturning moment in roll, which could be large enough to cause capsize. The publications mentioned above are either based on a two dimensional method or a shallow water formulation. The

answers they offer to these concerns are applicable only when their adopted assumptions are valid.

The methodology developed in this work provides another alternative to explore this kind of problem. Fully nonlinear theory is used. No restriction is imposed on water depth, and the tank can be three dimensional. It tends to provide some new understanding of the phenomenon associated with sloshing waves.

Although our method can be applied to a tank of an arbitrary shape and undergoing any excitation , the results presented in this chapter are for a circular tank with an initial free surface disturbance (wave elevation and/or velocity potential) and for a rectangular tank undergoing translational motion. The method and code will be first validated. It is then used to show how the waves behave in a practical three dimensional tank. Numerical results have been compared with some analytical solutions, and extensive investigations have been made, particularly for the case of sloshing waves generated by the motion of a rectangular three dimensional tank. The cases with different geometry and excitation are arranged as follows:

1) Standing waves in a circular tank with or without an inner cylinder, subjected to the initial free surface disturbance are given in Section 7.2.
2) The force calculation on the inner cylinder for a particular initial free surface disturbance is discussed in Section 7.3.
3) Waves in a rectangular tank subject to translational motions are presented in Section 7.4

7.2 Standing waves in a circular tank

The geometry of the tank is circular in this case, and there may also be a circular vertical cylinder mounted in the centre. The water is initially still, and the wave elevation and the potential value on the surface are specified. An important reason for considering this problem is that we can find an analytical solution in the time domain, which can be used to verify the numerical method directly.

7.2.1 Analytical solution of standing wave in a circular tank.

Various analytical solutions are available for first and second order problems in the frequency domain, see for example, Hunt & Baddour(1980,1981). Far fewer are available in the time domain. Among them are the cases of a two dimensional wavemaker problem (Eatock Taylor, Wang & Wu 1994) and the case of a vertical circular cylinder in the open sea (McIver 1994). However, both of these solutions are fully linearised, i.e. they are valid only for small amplitude waves. Here the fully nonlinear numerical method in the time domain needs to be validated and therefore nonlinear effects are important. In this sub-section, the work of Wu and Eatock Taylor (1994) is extended to three dimensions with a fluid domain bounded by cylinders. First order and second order solutions will be derived by expanding the potentials into a series of eigenfunctions.

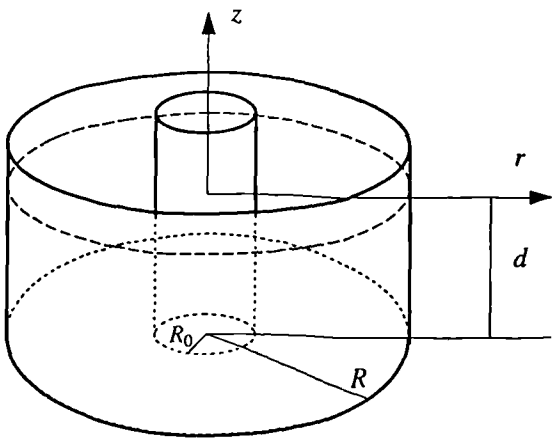

Figure 7.2.1 Sketch of a circular tank

Consider the configuration in Figure 7.2.1, where the radii of the inner and the outer cylinders are R_0 and R , respectively. Our analysis is restricted to the axisymmetric problem, although the developed method can be extended to more general cases. The velocity potential, therefore, can be written as:

$$\phi = \phi(r,z,t),$$

where (r, z) represents a cylindrical coordinate system with the origin being at the centre of the tank, z pointing upwards and $z = 0$ corresponding to the mean free surface, as shown in Figure 7.2.1.

In the system, the equations and boundary conditions for a Cartesian coordinate system mentioned in Chapter 3 can be rewritten as follows:

$$\frac{1}{r}\frac{\partial}{\partial r}r\left(\frac{\partial\phi}{\partial r}\right)+\frac{\partial^2\phi}{\partial z^2}=0 \qquad \text{in the fluid domain,} \tag{7.2.1}$$

$$\frac{\partial\phi}{\partial r}=0 \qquad r=R_0 \text{ and } r=R\ , \tag{7.2.2}$$

$$\frac{\partial\phi}{\partial z}=0 \qquad z=-d\ , \tag{7.2.3}$$

$$\frac{\partial^2\phi}{\partial t^2}+g\frac{\partial\phi}{\partial z}+\frac{\partial|\nabla\phi|^2}{\partial t}+\frac{1}{2}\nabla\phi\cdot\nabla|\nabla\phi|^2=0 \qquad z=\zeta\ , \tag{7.2.4}$$

$$\zeta=-\frac{1}{g}\left(\frac{\partial\phi}{\partial t}+\frac{1}{2}|\nabla\phi|^2\right). \tag{7.2.5}$$

If there is no inner cylinder, equation (7.2.2) is applied only on r=R. Equations (3.2.5) and (3.2.6) have been combined to give the free surface boundary condition in equation (7.2.4), which is more convenient for the perturbation analysis. The initial condition is specified as:

$$\begin{cases}\phi(r,\psi,0)=\varphi(r)\\ \zeta(r,0)=\psi(r).\end{cases} \tag{7.2.6}$$

The above equations correspond to the fully nonlinear problem. A solution can be found based on the perturbation theory. Although more general cases may be considered, here $\varphi(r)$ and $\psi(r)$ in equation (7.2.6) are assumed to be determined by the parameter of first order, denoted by φ_1 and ψ_1. The perturbation theory, up to the second order of wave slope, gives

$$\phi=\phi_1+\phi_2+\cdots, \tag{7.2.7}$$

$$\zeta=\zeta_1+\zeta_2+\cdots, \tag{7.2.8}$$

where ϕ_1 and ζ_1 are the potential and wave elevation of the first order, respectively, being proportional to the wave slope, while ϕ_2 and ζ_2 are the counterparts of the second

order, being proportional to the square of the wave slope. Substituting the two expressions into equations (7.2.4) and (7.2.6), and rearranging the results in terms of the order of the wave slope, the equations for ϕ_1, ϕ_2, ζ_1 and ζ_2 can be obtained:

$$\frac{\partial^2 \phi_1}{\partial t^2} + g\frac{\partial \phi_1}{\partial z} = 0 \qquad \text{on} \qquad z = 0, \tag{7.2.9}$$

$$\zeta_1 = -\frac{1}{g}\frac{\partial \phi_1}{\partial t} \qquad \text{on} \qquad z = 0, \tag{7.2.10}$$

$$\begin{cases} \phi_1(r,0,0) = \varphi_1(r) \\ \zeta_1(r,0) = \psi_1(r), \end{cases} \tag{7.2.11}$$

and

$$\frac{\partial^2 \phi_2}{\partial t^2} + g\frac{\partial \phi_2}{\partial z} = q(r,t) \qquad \text{on} \qquad z = 0, \tag{7.2.12}$$

$$\zeta_2 = -\frac{1}{g}\frac{\partial \phi_2}{\partial t}\bigg|_{z=0} - \frac{1}{g}\left[\zeta_1 \frac{\partial^2 \phi_1}{\partial z \partial t} + \frac{1}{2}\left|\nabla \phi\right|_1^2\right]_{z=0}, \tag{7.2.13}$$

$$\begin{cases} \phi_2(r,0,0) = -\psi_1 \dfrac{\partial \phi_1}{\partial z}\bigg|_{z=0,t=0} \\ \zeta_2(r,0) = 0 \end{cases}, \tag{7.2.14}$$

where

$$q(r,t) = -\left[\zeta_1 \frac{\partial}{\partial z}\left(\frac{\partial^2 \phi_1}{\partial t^2} + g\frac{\partial \phi_1}{\partial z}\right) + \frac{\partial}{\partial t}\left(\nabla \phi_1\right)^2\right]_{z=0}. \tag{7.2.15}$$

Both ϕ_1 and ϕ_2 also satisfy equations (7.2.1) to (7.2.3).

The solution for the first order potential $\phi_1(r,t)$ can be found by the variable separation method which leads to:

$$\phi_1 = G_0^{(1)}(t) + \sum_{m=1}^{\infty} G_m^{(1)}(t) Z_m(r) f_m(z), \tag{7.2.16}$$

where $Z_m(r)$ and $f_m(z)$ are defined by:

$$Z_m(r) = J_0(\alpha_m r) + B_m Y_0(\alpha_m r) \tag{7.2.17}$$

$$f_m(z) = \frac{\cosh(\alpha_m(z+d))}{\cosh(\alpha_m d)} \tag{7.2.18}$$

and J_n and Y_n (n=0,1,...) are Bessel functions of the first and the second kind of order n, respectively. The coefficients α_m and B_m in equation (7.2.17) are obtained from the boundary conditions on the surfaces of the cylinders. This leads to:

$$B_m = -\frac{J_1(\alpha_m R_0)}{Y_1(\alpha_m R_0)}, \tag{7.2.19}$$

and α_m are the solutions of

$$\left[J_1(\alpha_m r) + B_m Y_1(\alpha_m r)\right]_{r=R} = 0. \tag{7.2.20}$$

B_m in equation (7.2.19) should be taken as zero when there is no inner cylinder. Substituting equation (7.2.16) into (7.2.9), it follows that:

$$\phi_1 = a_0 t + b_0 + \sum_{m=1}^{\infty}(a_m \sin\omega_m t + b_m \cos\omega_m t)Z_m(r) f_m(z), \tag{7.2.21}$$

where

$$\omega_m^2 = g\alpha_m \tanh\alpha_m d. \tag{7.2.22}$$

The set of functions $\{1, Z_m | m = 1,2,3,\cdots\}$ are orthogonal and complete (with weighting function r) within $R_0 \le r \le R$ (see MacCluer, 1994), and therefore any continuous functions $\varphi_1(r)$ and $\psi_1(r)$ can be expanded in terms of these functions. Upon doing this and substituting (7.2.21) into the initial condition in equation (7.2.11), the coefficients, a_m and b_m, are obtained

$$a_0 = -\frac{2g}{R^2 - R_0^2}\int_{R_0}^{R} r\psi_1(r)dr, \tag{7.2.23}$$

$$a_m = -\frac{g}{\omega_m}\int_{R_0}^{R} r\psi_1(r)Z_m(r)dr \Big/ \int_{R_0}^{R} rZ_m^2 dr\,, \tag{7.2.24}$$

$$b_0 = \frac{2}{R^2 - R_0^{\,2}}\int_{R_0}^{R} r\varphi_1(r)dr\,, \tag{7.2.25}$$

$$b_m = \int_{R_0}^{R} r\varphi_1(r)Z_m(r)dr \Big/ \int_{R_0}^{R} rZ_m^2 dr\,. \tag{7.2.26}$$

The coefficient a_0 is related to the mean position of the initial free surface and so it is made zero due to the choice of the coordinate system. Without loosing generality, $\varphi_1(r)$ can be chosen in such a way that b_0 is also zero. Under these conditions the wave elevation can be written as:

$$\zeta_1 = -\frac{1}{g}\sum_{m=1}^{\infty}\omega_m\left(a_m\cos\omega_m t - b_m\sin\omega_m t\right)Z_m(r)\,. \tag{7.2.27}$$

Substituting the first order solutions in equations (7.2.21) and (7.2.27) into (7.2.15), the term on the right-hand side of equation (7.2.12) can be written as:

$$\begin{aligned} q(r,t) = \frac{1}{2}\sum_{m=1}^{\infty}\sum_{n=1}^{\infty}\Big[&\beta_{mn}\left(a_m a_n + b_m b_n\right)\sin(\omega_m - \omega_n)t \\ &+\gamma_{mn}\left(a_m a_n - b_m b_n\right)\sin(\omega_m + \omega_n)t \\ &+\beta_{mn}\left(b_m a_n - a_m b_n\right)\cos(\omega_m - \omega_n)t \\ &+\gamma_{mn}\left(b_m a_n + a_m b_n\right)\cos(\omega_m + \omega_n)t\ \Big]\ , \end{aligned} \tag{7.2.28}$$

where

$$\beta_{mn} = \omega_n\left(\alpha_m^2 - K_m^2\right)W_{mn} + \left(\omega_m - \omega_n\right)\left(\alpha_m\alpha_n U_{mn} + K_m K_n W_{mn}\right), \tag{7.2.29}$$

$$\gamma_{mn} = \omega_n\left(\alpha_m^2 - K_m^2\right)W_{mn} - \left(\omega_m + \omega_n\right)\left(\alpha_m\alpha_n U_{mn} + K_m K_n W_{mn}\right), \tag{7.2.30}$$

$$W_{mn} = W_{mn}(r) = Z_m(r)Z_n(r)\,, \tag{7.2.31}$$

$$U_{mn} = U_{mn}(r) = \left[J_1(\alpha_m r) + B_m Y_1(\alpha_m r)\right]\left[J_1(\alpha_n r) + B_n Y_1(\alpha_n r)\right], \tag{7.2.32}$$

and

$$K_m = \frac{\omega_m^2}{g}. \tag{7.2.33}$$

The expression for the second order wave elevation in equation (7.2.13) can be divided into two parts, i.e.

$$\zeta_2 = \zeta_{21} + \zeta_{22}, \tag{7.2.34}$$

where

$$\zeta_{21} = -\frac{1}{g}\left[\zeta_1 \frac{\partial^2 \phi_1}{\partial z \partial t} + \frac{1}{2}\left|\nabla \phi_1\right|^2\right]_{z=0}, \tag{7.2.35}$$

and

$$\zeta_{22} = -\frac{1}{g}\frac{\partial \phi_2}{\partial t}\bigg|_{z=0}. \tag{7.2.36}$$

The first part can be calculated directly using the first order solution given above. Substituting equations (7.2.21) and (7.2.27) into (7.2.35), one can obtain:

$$\begin{aligned}\zeta_{21} = -\frac{1}{2g}\sum_{m=1}^{\infty}\sum_{n=1}^{\infty}\Big[&\mu_{mn}\left(a_m b_n - b_m a_n\right)\sin(\omega_m - \omega_n)t \\ &+\lambda_{mn}\left(a_m b_n + b_m a_n\right)\sin(\omega_m + \omega_n)t \\ &+\mu_{mn}\left(b_m b_n + a_m a_n\right)\cos(\omega_m - \omega_n)t \\ &+\lambda_{mn}\left(b_m b_n - a_m a_n\right)\cos(\omega_m + \omega_n)t\ \Big],\end{aligned} \tag{7.2.37}$$

where

$$\lambda_{mn} = \frac{1}{2}\left(\alpha_m \alpha_n U_{mn} + K_m K_n W_{mn}\right) + \frac{\omega_m \omega_n}{g} K_n W_{mn}, \tag{7.2.38}$$

$$\mu_{mn} = \frac{1}{2}\left(\alpha_m \alpha_n U_{mn} + K_m K_n W_{mn}\right) - \frac{\omega_m \omega_n}{g} K_n W_{mn}. \tag{7.2.39}$$

To determine the second part of the second order wave elevation, one has to find the second order potential which satisfies equation (7.2.1) to (7.2.3) plus (7.2.12) and

(7.2.14). An expression for the second order potential can be constructed in a similar way to the first order case as follows:

$$\phi_2 = G_0^{(2)}(t) + \sum_{m=1}^{\infty} G_m^{(2)}(t) Z_m(r) f_m(z), \tag{7.2.40}$$

where $Z_m(r)$ and $f_m(z)$ have been defined in equations (7.2.17) and (7.2.18) respectively. The initial conditions for ϕ_2 are then written as:

$$\phi_2(r,0,0) = \sum_{i=1}^{\infty}\sum_{j=1}^{\infty} \frac{K_i \omega_j}{g} a_i b_j W_{ij}(r), \tag{7.2.41}$$

$$\frac{\partial \phi_2(r,0,0)}{\partial t} = g\zeta_{21}(r,0). \tag{7.2.42}$$

Inserting equation (7.2.40) into (7.2.12) leads to the following equation governing $G_m^{(2)}$:

$$G_0^{(2)''}(t) + \sum_{m=1}^{\infty}\left[G_m^{(2)''}(t) + \omega_m^2 G_m^{(2)}(t)\right] Z_m(r) = q(r,t), \tag{7.2.43}$$

where ω_m has been defined in equation (7.2.22). Using the expansion of $q(r,t)$ in equation (7.2.28), a special solution $g_m(t)$ of equation (7.2.43) can be found:

$$\begin{aligned} g_0(t) = &-\frac{1}{2}\sum_{i=1}^{\infty}\sum_{j=1}^{\infty}\left[\frac{E_0(i,j)\left(a_i a_j - b_i b_j\right)}{\left(\omega_i + \omega_j\right)^2}\sin(\omega_i + \omega_j)t\right. \\ &\left. + \frac{E_0(i,j)\left(b_i a_j + a_i b_j\right)}{\left(\omega_i + \omega_j\right)^2}\cos(\omega_i + \omega_j)t\right] \\ &-\frac{1}{2}\sum_{i=1}^{\infty}\sum_{\substack{j=1 \\ j\neq i}}^{\infty}\left[\frac{D_0(i,j)\left(a_i a_j + b_i b_j\right)}{\left(\omega_i - \omega_j\right)^2}\sin(\omega_i - \omega_j)t\right. \\ &\left. + \frac{D_0(i,j)\left(b_i a_j - a_i b_j\right)}{\left(\omega_i - \omega_j\right)^2}\cos(\omega_i - \omega_j)t\right], \end{aligned} \tag{7.2.44}$$

$$g_m(t)=\frac{1}{2}\sum_{i=1}^{\infty}\sum_{j=1}^{\infty}\left[\frac{D_m(i,j)\left(a_ia_j+b_ib_j\right)}{\omega_m^2-\left(\omega_i-\omega_j\right)^2}\sin(\omega_i-\omega_j)t\right.$$
$$\left.+\frac{E_m(i,j)\left(a_ia_j-b_ib_j\right)}{\omega_m^2-\left(\omega_i+\omega_j\right)^2}\sin(\omega_i+\omega_j)t\right]$$
$$+\frac{1}{2}\sum_{i=1}^{\infty}\sum_{j=1}^{\infty}\left[\frac{D_m(i,j)\left(b_ia_j-a_ib_j\right)}{\omega_m^2-\left(\omega_i-\omega_j\right)^2}\cos(\omega_i-\omega_j)t\right. \qquad (7.2.45)$$
$$\left.+\frac{E_m(i,j)\left(b_ia_j+a_ib_j\right)}{\omega_m^2-\left(\omega_i+\omega_j\right)^2}\cos(\omega_i+\omega_j)t\right] \qquad (m>0)$$

where

$$D_0(i,j)=\frac{2}{R^2-R_0{}^2}\int_{R_0}^{R}r\beta_{ij}(r)dr, \qquad (7.2.46)$$

$$E_0(i,j)=\frac{2}{R^2-R_0{}^2}\int_{R_0}^{R}r\gamma_{ij}(r)dr, \qquad (7.2.47)$$

$$D_m(i,j)=\int_{R_0}^{R}r\beta_{ij}(r)Z_m(r)dr\Big/\int_{R_0}^{R}rZ_m^2dr \quad (m>0), \qquad (7.2.48)$$

$$E_m(i,j)=\int_{R_0}^{R}r\gamma_{ij}(r)Z_m(r)dr\Big/\int_{R_0}^{R}rZ_m^2dr \quad (m>0). \qquad (7.2.49)$$

The general solution of $G_m^{(2)}$ can therefore be written as:

$$G_0^{(2)}=g_0(t)+a_0^{(2)}t+b_0^{(2)}, \qquad (7.2.50)$$

$$G_m^{(2)}=g_m(t)+a_m^{(2)}\sin\omega_m t+b_m^{(2)}\cos\omega_m t \quad (m>0). \qquad (7.2.51)$$

Using the initial conditions in equations (7.2.41) and (7.2.42) yields:

$$b_m^{(2)}=\sum_{i=1}^{\infty}\sum_{j=1}^{\infty}\left[P_0(i,j)a_ib_j\right]-g_m(0) \qquad (m\geq 0), \qquad (7.2.52)$$

$$a_0^{(2)}=-g_0'(0)-\frac{1}{2}\sum_{i=1}^{\infty}\sum_{j=1}^{\infty}\left[\ X_0(i,j)\left(b_ib_j+a_ia_j\right)+Y_0(i,j)\left(b_ib_j-a_ia_j\right)\ \right], \qquad (7.2.53)$$

$$a_m^{(2)} = -\frac{g_m'(0)}{\omega_m} - \frac{1}{2\omega_m}\sum_{i=1}^{\infty}\sum_{j=1}^{\infty}\Big[\, X_m(i,j)\big(b_i b_j + a_i a_j\big) + Y_m(i,j)\big(b_i b_j - a_i a_j\big)\,\Big] \quad (m>0), \tag{7.2.54}$$

where

$$X_0(i,j) = \frac{2}{R^2 - R_0^{\,2}}\int_{R_0}^{R} r\mu_{ij}(r)dr, \tag{7.2.55}$$

$$Y_0(i,j) = \frac{2}{R^2 - R_0^{\,2}}\int_{R_0}^{R} r\lambda_{ij}(r)dr, \tag{7.2.56}$$

$$X_m(i,j) = \int_{R_0}^{R} r\mu_{ij}(r)Z_m(r)dr \Big/ \int_{R_0}^{R} rZ_m^2(r)dr \qquad (m>0), \tag{7.2.57}$$

$$Y_m(i,j) = \int_{a}^{R} r\lambda_{ij}(r)Z_m(r)dr \Big/ \int_{a}^{R} rZ_m^2(r)dr \qquad (m>0), \tag{7.2.58}$$

$$P_0(i,j) = \frac{2}{R^2 - R_0^{\,2}}\int_{R_0}^{R} r\frac{K_i\omega_j}{g}dr$$

$$P_m(i,j) = \int_{R_0}^{R} r\frac{K_i\omega_j}{g}Z_m(r)dr \Big/ \int_{R_0}^{R} rZ_m^2(r)dr \qquad (m>0).$$

The second part of second order wave elevation in equation (7.2.34) can then be obtained by substituting (7.2.40) into (7.2.36)

$$\zeta_{22} = -\frac{1}{g}\sum_{m=1}^{\infty}\Big[g_m'(t) + \omega_m a_m^{(2)}\cos\omega_m t - \omega_m b_m^{(2)}\sin\omega_m t\Big]Z_m(r) - \frac{1}{g}\big(a_0^{(2)} + g_0'(t)\big). \tag{7.2.59}$$

7.2.2 Comparison between numerical results and analytical solution

The above analytical solution will be used as a benchmark to validate the numerical results. For this purpose, only a simple case with an initial disturbance $\varphi_1 = 0$ and $\psi_1 = aZ_k(r)$ (k=1 is used in the following) is considered, where a is the amplitude. The analytical expression for the corresponding wave elevation is:

$$\zeta_1 = aZ_k(r)\cos\omega_k t \tag{7.2.60}$$

$$\zeta_{21} = -\frac{ga^2}{2\omega_k^2}\left(\mu_{kk} - \lambda_{kk}\cos 2\omega_k t\right) \tag{7.2.61}$$

$$\begin{aligned}\zeta_{22} = \frac{ga^2}{\omega_k^2}\Bigg\{ & \frac{E_0(k,k)}{4\omega_k}\left(\cos 2\omega_k t - 1\right) + \frac{1}{2}X_0(k,k) - \frac{1}{2}Y_0(k,k) \\ & - \sum_{m=1}^{\infty}\frac{\omega_k E_m(k,k)}{\omega_m^2 - 4\omega_k^2}Z_m(r)\cos 2\omega_k t \\ & + \sum_{m=1}^{\infty}\left[\frac{\omega_k E_m(k,k)}{\omega_m^2 - 4\omega_k^2} + \frac{1}{2}X_m(k,k) - \frac{1}{2}Y_m(k,k)\right]Z_m(r)\cos\omega_m t\Bigg\}.\end{aligned} \tag{7.2.62}$$

The sum of ζ_1, $\zeta_2^{(1)}$ and $\zeta_2^{(2)}$ gives the total wave elevation up to the second order at any time:

$$\zeta = \zeta_1 + \zeta_{21} + \zeta_{22}. \tag{7.2.63}$$

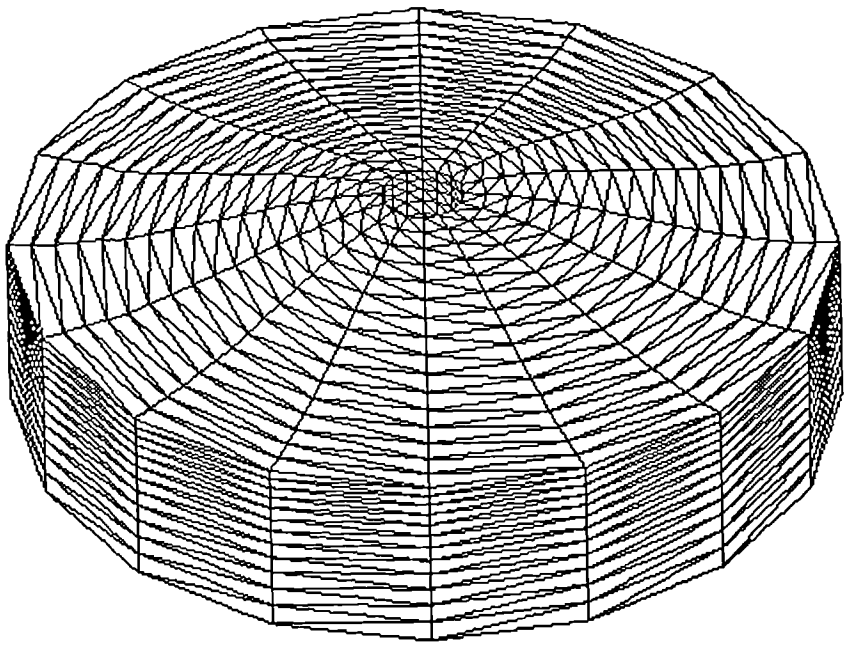

Figure 7.2.2 Mesh for the circular tank domain

In the numerical simulation for this case, the fluid domain is discretised as shown in Figure 7.2.2. The mesh here is generated in a similar way to that in Chapter 5. However, the two sets of planes perpendicular to the bottom are now radial vertical

planes (M_1), and concentric circular cylinder surfaces (M_2)whose common centre coincides with that of the tank. Here N is again used to denote the number of mesh surfaces in the horizontal direction.

It should be noted that in this and Section 7.3 the algebraic system is solved by the direct method, and the recovery and smooth techniques in Chapter 5 are not applied. The reasons are that: (1) these results are obtained in the early stage of this study, when the iterative method in Chapter 6 and the recovery (smooth) techniques in Chapter 5 had not yet been investigated and adopted; (2) the main aim here is to validate the numerical method, instead of seeking a way to save computer resources.

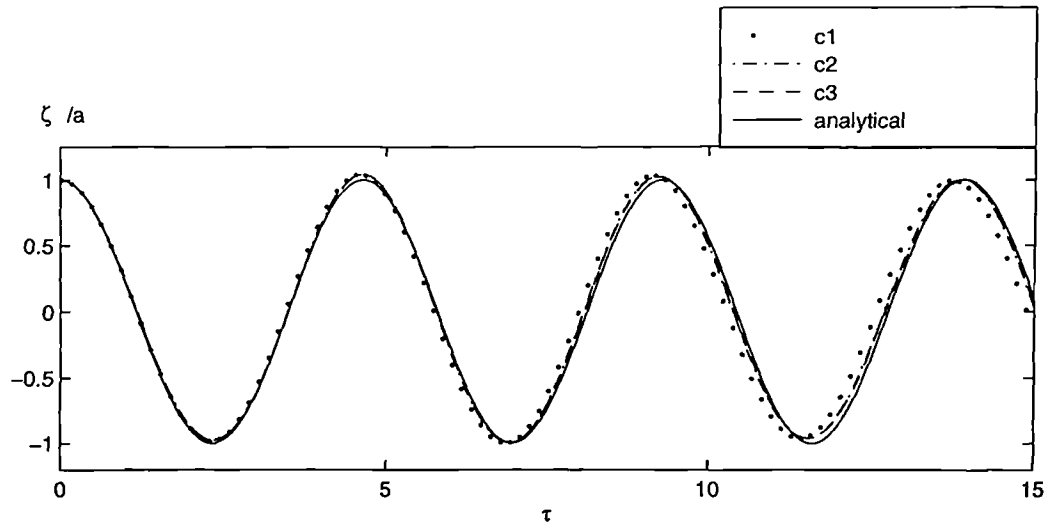

Figure 7.2.3 Wave elevation history at the centre of tank without the inner cylinder ($R/d = 2.0$, $a/d = 0.03$)

Firstly the influence of the mesh size and time step is investigated. The tank has a scaled radius, $R/d = 2.0$, without the inner cylinder. The amplitude of the initial free surface elevation is taken as $a = 0.03d$. Figure 7.2.3 presents the comparison of wave history at the centre of the tank between the numerical results and the analytical solution given in equation (7.2.63). Here τ, as in following figures, is nondimensional time and defined by $\tau = t\sqrt{\frac{g}{d}}$. The numerical results corresponding to different parameters used to discretise the space and the time are denoted by c1, c2 and c3:

c1: $(\Delta\tau = 0.03,\quad N = 10,\quad M_1 = 12,\quad M_2 = 10)$

c2: $(\Delta\tau = 0.05,\quad N = 15,\quad M_1 = 24,\quad M_2 = 16)$

c3: $(\Delta\tau = 0.03,\quad N = 15,\quad M_1 = 24,\quad M_2 = 16).$

It can be seen from Figure 7.2.3 that the difference between the analytical and the numerical results is invisible in case c3. Figure 7.2.4, for the case with an inner cylinder of radius $R_0 = 0.4d$ in the same tank with a scaled amplitude (a/d) equal to 0.05, plots similar results on the surface of the inner cylinder. In this figure, c4, c5 and c6 are defined by:

c4: $(\Delta\tau = 0.02,\quad N = 10,\quad M_1 = 16,\quad M_2 = 10)$

c5: $(\Delta\tau = 0.03,\quad N = 15,\quad M_1 = 32,\quad M_2 = 16)$

c6: $(\Delta\tau = 0.02,\quad N = 15,\quad M_1 = 32,\quad M_2 = 16).$

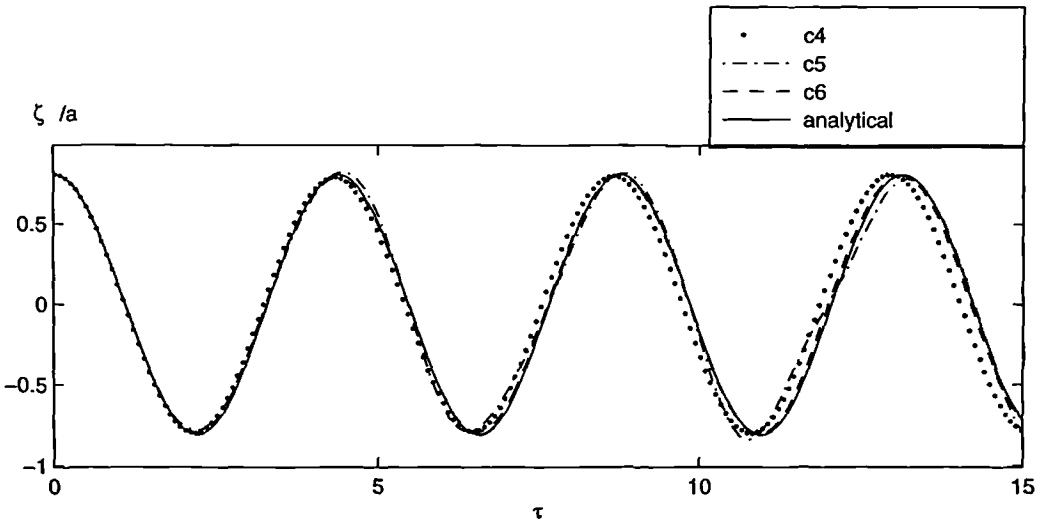

Figure 7.2.4 Wave elevation history on the surface of the inner cylinder
$(R/d = 2.0, R_0/d = 0.4, a/d = 0.05)$

It is shown that a smaller mesh size and a smaller time step ($\Delta\tau = 0.02, N = 15, M_1 = 32$ and $M_2 = 16$) than the case in Figure (7.2.3) are needed

to obtain similar agreement with analytical results. The difference between the two cases is that they have different values of $\alpha_m R$ solved from equation (7.2.20), specifically, $\alpha_1 R \approx 3.832$ for the first case while $\alpha_1 R \approx 4.236$ for the second case. The higher the value, the higher the frequency of oscillation. The different convergent properties of the two cases illustrate that the higher values of the frequency and the wave slope may require a finer mesh and a smaller time step when the numerical simulation is employed.

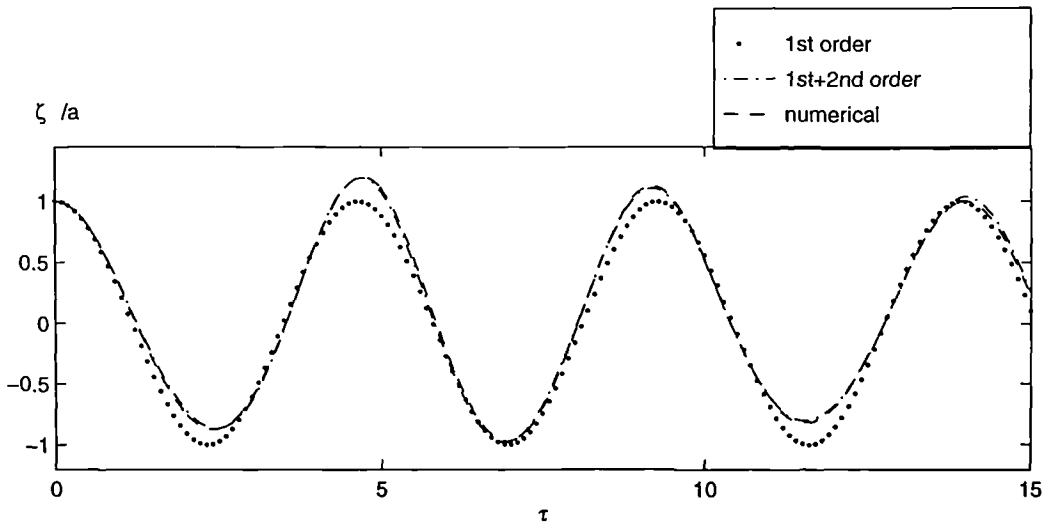

Figure 7.2.5 Comparison of wave elevation history at the centre of the tank with the analytical solution ($R/d = 2.0$, $a/d = 0.15$)

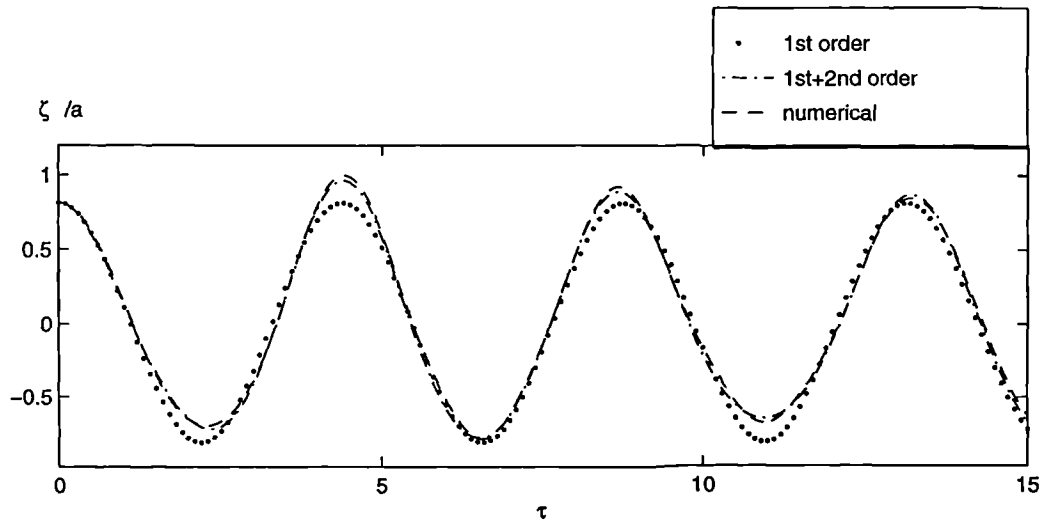

Figure 7.2.6 Comparison of wave elevation history on the surface of the inner cylinder with the analytical solution ($R/d = 2.0$, $R_0/d = 0.4$, $a/d = 0.2$)

To check effects of nonlinearity, the above configurations are further considered with larger initial amplitudes in Figures 7.2.5 and 7.2.6, respectively. In order to illustrate how important the nonlinear effects are in these cases, the corresponding linear (first order) and nonlinear (up to second order) analytical results are plotted separately. Figure 7.2.5 is for the case without the inner cylinder, and Figure 7.2.6 with the cylinder. These two figures show that the fully nonlinear numerical solutions have some discrepancies with the linear solution but the difference is evidently reduced when the second order correction is included.

7.3 Force calculation on a inner cylinder

It should be noted that the force has not been considered in the above cases because the total force on the cylinder is equal to zero. In order to consider a case where the force is not zero, the initial free surface disturbance in this section is specified as:

$$\zeta(x,y,0) = a\,\mathrm{e}^{-k(|x|+|y|)}\sin kx\,. \qquad (7.3.1)$$

Two methods, *direct and integrated force methods*, mentioned in Chapter 4 will be employed to evaluate the force. Although an analytical solution is not sought for this case, the numerical results of the force obtained by the two different methods can be compared.

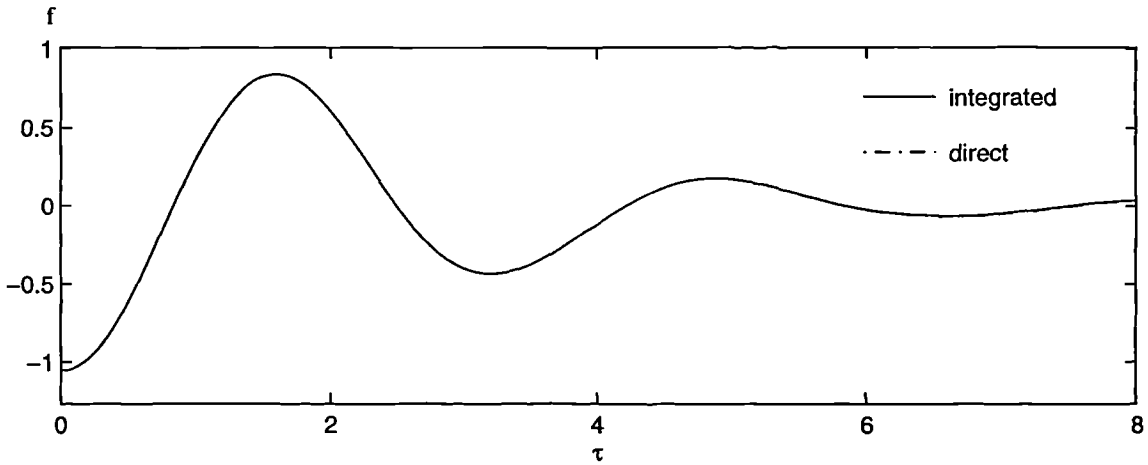

Figure 7.3.1 Force on the inner cylinder ($R_0/d = 0.2, R/R_0 = 20, kd = 2.5,\ a/d = 0.1$)

A similar configuration is considered to that of the previous section with the dimensions of the cylinder and the tank here being taken as $R_0/d = 0.2$ and $R/R_0 = 20$, respectively. The amplitude a in equation (7.3.1) is chosen as $a/d = 0.1$ and the parameter k taken as $kd = 2.5$. The mesh for the numerical analysis is similar to that in Figure 7.2.2 with $N = 15$, $M_1 = 320$, $M_2 = 16$.

Figure 7.3.1 gives the force in the x-direction on the inner cylinder mounted on the tank bottom obtained with the two methods. Here f is defined by $f = F_x/\rho g a R_0^2$. The evaluation associated with the integrated method is obtained by equation (4.1.8). Excellent agreement between results obtained by the two methods can be found.

A truncated inner circular cylinder with different draft is further considered. The radii of the cylinder and the tank are the same as those in Figure 7.3.1 while the draft of the inner cylinder is taken as $0.7d$ and $0.4d$, respectively. Once again, the results for the force calculated by two methods are graphically indistinguishable. Owing to this reason, only the force by the direct method is presented in Figure 7.3.2.

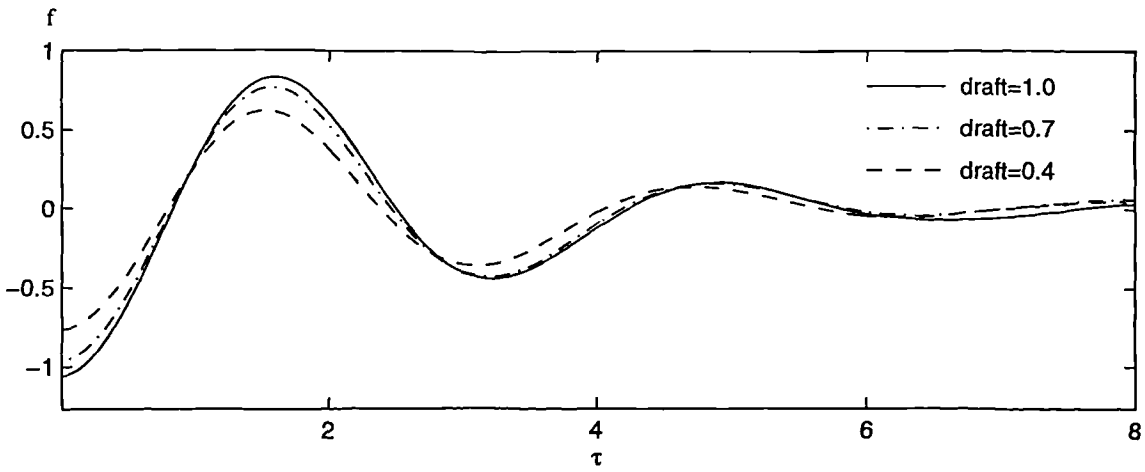

Figure 7.3.2 Force history on the inner cylinder with different drafts
($R_0/d = 0.2, R/R_0 = 20, kd = 2.5, a/d = 0.1$)

7.4 Sloshing wave generated by the translational motion of a tank

The geometry in this section is changed to a rectangular tank. The fluid flow is induced by the translational motion of the tank. Compared with the problem in the previous two sections, the fluid velocity on the rigid boundary is not zero, which makes the problem somewhat different. As discussed in section 3.2.2, Semi-Eulerian or Lagrangian notation of the free surface conditions may be used in the numerical method. In this section, the former will be employed to avoid the interpolation on the free surface. From now on, the algebraic system will be solved by the iterative method discussed in Chapter 6, and the recovery techniques in Chapter 5 are used for all the following results.

7.4.1 Governing equations

A Cartesian coordinate system fixed on the tank is established as shown in Figure 7.4.1. The origin of the system has been chosen at the centre of the undisturbed free surface. Here xyz is used to denote the moving coordinate system for simplicity without confusion with Chapter 3 where $x_b y_b z_b$ denotes the moving system. The displacements of the tank due to its translational motion in the directions of the Cartesian axes are defined as:

$$\boldsymbol{r}_c = \left[x_c(t),\quad y_c(t),\quad z_c(t)\right]. \tag{7.4.1}$$

The corresponding governing equations in the moving system have been given in section 3.4 for the case with the general motion of a body. They can be used to give the governing equations of the fluid flow induced by the translational motion considered in this section after the angular velocity is taken as zero in equations (3.4.11) and (3.4.12). That is:

$$\nabla^2\phi = 0 \qquad \text{in the domain fluid} \tag{7.4.2}$$

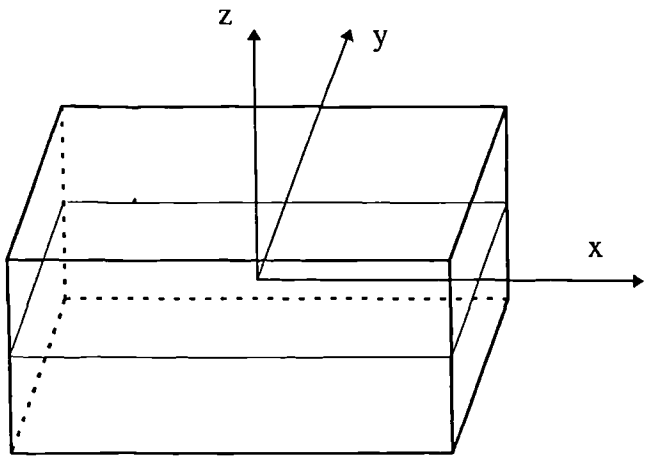

Figure 7.4.1 The coordinate system

$$\frac{\partial \phi}{\partial n} = \boldsymbol{U} \cdot \boldsymbol{n} \qquad \text{on the walls of the tank} \qquad (7.4.3)$$

$$\frac{\partial \zeta}{\partial t} + \left(\frac{\partial \phi}{\partial x} - \frac{dx_c}{dt}\right)\frac{\partial \zeta}{\partial x} + \left(\frac{\partial \phi}{\partial y} - \frac{dy_c}{dt}\right)\frac{\partial \zeta}{\partial y} - \left(\frac{\partial \phi}{\partial z} - \frac{dz_c}{dt}\right) = 0 \qquad \text{on the free surface} \qquad (7.4.4)$$

$$\frac{\delta \phi}{\delta t} - \frac{\partial \phi}{\partial z}\frac{\partial \zeta}{\partial t} - \nabla\phi \bullet \frac{d\boldsymbol{r}_c}{dt} + \frac{1}{2}\nabla\phi \bullet \nabla\phi + g(\zeta + z_c) = 0 \qquad \text{on the free surface} \qquad (7.4.5)$$

where $\boldsymbol{U} = \dfrac{d\boldsymbol{r}_c}{dt}$ is the velocity of the tank and $\boldsymbol{n}$ is a normal vector out of fluid, and the free surface elevation $\zeta(x, y, t)$ is measured in the moving system. Other parameters in the above equations have already been given in Chapter 3. They are not repeated here.

The velocity potential, ϕ, is now split as follows:

$$\phi = \varphi + xU + yV + zW \qquad (7.4.6)$$

where U, V and W are the components of $\boldsymbol{U}$ in x, y and z directions, respectively. Substituting this equation into equations (7.4.3) to (7.4.5), it follows that:

$$\nabla^2 \varphi = 0 \qquad \text{in the fluid domain} \qquad (7.4.7)$$

$$\frac{\partial \varphi}{\partial n} = 0 \qquad \text{on the side walls} \qquad (7.4.8)$$

$$\frac{\partial \zeta}{\partial t} = -\frac{\partial \varphi}{\partial x}\frac{\partial \zeta}{\partial x} - \frac{\partial \varphi}{\partial y}\frac{\partial \zeta}{\partial y} + \frac{\partial \varphi}{\partial z} \qquad \text{on the free surface} \qquad (7.4.9)$$

$$\frac{\delta \varphi}{\delta t} = \frac{\partial \varphi}{\partial z}\frac{\partial \zeta}{\partial t} - \frac{1}{2}\nabla\varphi \bullet \nabla\varphi - g\zeta - x\frac{dU}{dt} - y\frac{dV}{dt} - \zeta\frac{dW}{dt} \qquad \text{on the free surface} \qquad (7.4.10)$$

where the term $c(t) = \frac{1}{2}|U|^2 - gz_c$ has been deleted from equation (7.4.10) because it is independent of the spatial coordinates. The condition on the walls in equation (7.4.8) becomes homogeneous. The kinematic condition becomes simpler but more terms are introduced to the dynamic condition as shown in equations (7.4.9) and (7.4.10).

The tank is assumed to start from rest with $\phi = 0$ on free surface, implying the initial conditions for φ are given as:

$$\varphi(x, y, 0, 0) = -xu(0) - yv(0) \qquad (7.4.11)$$

$$\zeta(x, y, 0) = 0. \qquad (7.4.12)$$

The pressure in the fluid can be obtained by using equations (7.4.6) and (3.4.13):

$$-\frac{p}{\rho} = \frac{\partial \varphi}{\partial t} + \frac{1}{2}\nabla\varphi \bullet \nabla\varphi + gz + x\frac{dU}{dt} + y\frac{dV}{dt} + z\frac{dW}{dt}. \qquad (7.4.13)$$

7.4.2 *Numerical results for surging motion*

We consider a case in which the displacement of the tank is governed by $x_c(t) = a\sin(\omega t)$, $y_c = 0$ and $z_c = 0$, where a is the amplitude and ω is the frequency. The corresponding velocity is $U = a\omega\cos(\omega t)$, and $V = W = 0$. This two-dimensional case has been investigated by many people, e.g. Faltinsen (1978), Okamoto & Kawahara (1990), Chen, Haroun & Liu (1996). Their results may be used here for comparison. The dimensions of the tank are chosen as $L/d = 2.0$ and $B/d = 0.2$, (the same as those used in the experiment by Okamoto and Kawahara , 1990), where L, B are the length and the width of the tank, respectively. A linearised solution for φ can easily be found from the results of Faltinsen (1978):

$$\varphi = a\sum_{n=0}^{\infty}\left(C_n \cos\omega t - \left(C_n + \frac{H_n}{\omega^2}\right)\cos\omega_n t\right)\frac{\cosh k_n(z+d)}{\cosh k_n d}\sin k_n x \qquad (7.4.14)$$

where $k_n = \frac{2n+1}{L}\pi$, , $H_n = \omega^3 \frac{4}{L}\frac{(-1)^n}{k_n^2}$, $C_n = \frac{H_n}{\omega_n^2 - \omega^2}$ and $\omega_n^2 = gk_n \tanh k_n d$

(which is the natural frequency). The dynamic pressure and the wave elevation can then be obtained from:

$$p = -\rho g\left(\frac{\partial\varphi}{\partial t} + x\frac{dU}{dt}\right) \qquad (7.4.15)$$

$$\zeta = \eta_1 + \eta_2 \qquad (7.4.16)$$

where

$$\eta_1 = \frac{a}{g}\left(x\omega^2 + \sum_{n=0}^{\infty} C_n \omega \sin k_n x\right)\sin\omega t$$

$$\eta_2 = -\frac{a}{g}\sum_{n=0}^{\infty}\omega_n\left(C_n + \frac{H_n}{\omega^2}\right)\sin k_n x \sin\omega_n t\,.$$

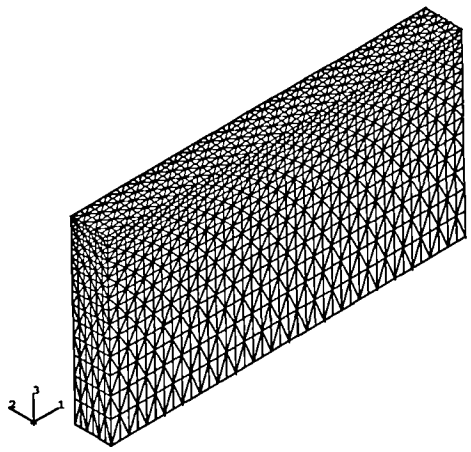

Figure 7.4.2 Initial mesh for sloshing wave

In the numerical analysis, the fluid domain is discretised in a similar way to that for Figure 5.6.2. A typical initial mesh is illustrated in Figure 7.4.2. In the following, M_1,

M_2 and N are still used to represent the number of surfaces used for dividing the fluid domain as in Chapter 5.

Some parameters in the following discussion are nondimensionalized as follows:

$$(x, y, z, L, B, a) \rightarrow (x, y, z, L, B, a)d\,,\ t \rightarrow \tau\sqrt{\frac{d}{g}}\,,\ \omega \rightarrow \omega\sqrt{\frac{g}{d}}\,,\ k \rightarrow k/d \qquad (7.4.17)$$

and then

$$\omega_n^2 = gk_n \tanh k_n d \ \rightarrow \omega_n^2 = k_n \tanh k_n\,.$$

To compare with the linear analytical results, the numerical simulation is carried out with a small amplitude $a = 0.00186$. The excitation frequency is either higher or lower than the first natural frequency $\omega_0 = \sqrt{k_0 \tanh k_0}$. In the calculation, we have chosen $M_1 = 40,\ \ M_2 = 6\ \ N = 16$ and $\Delta\tau = 0.0111$. The time history of the free surface elevation at $x = -L/2$ is presented in Figure 7.4.3. Comparison between the analytical solution and the numerical results shows that they are in an excellent agreement.

It is interesting to see from Figures 7.4.3a and 7.4.3c that the wave history is very similar to that due to two harmonic wave trains of slightly different frequencies. This amplitude modulated wave can be understood from equation (7.4.16). The expression is composed of two parts: one, η_1, corresponds to the excitation frequency ω and the other , η_2, corresponds to the natural frequencies $\omega_0, \omega_1, \omega_2, \omega_3, \cdots$. Of the latter, the wave of the first frequency ω_0 is dominant and others have far less contribution due to $\omega \approx \omega_0$. As a result, the entire wave is actually dominated by two waves of frequencies ω and ω_0, respectively. As well known, the frequency of the envelope of the amplitude-modulated wave is $\Delta\omega = |\omega - \omega_0|$ and its time period is $2\pi/\Delta\omega$, which can clearly be seen in Figures 7.4.3a and 7.4.3c ($2\pi/\Delta\omega \approx 52.25$ from the linear theory).

One can see from Figure 7.4.3b that the wave amplitude increases with time. Indeed, the magnitude of ζ/a has reached around 30 at $\tau \approx 50$. However, it does not of course suggest that the amplitude will tend to infinity with time, even based on the linear theory. The result is due to $\Delta\omega$ being very small , which leads to a very long period ($2\pi/\Delta\omega \approx 6283$) and a very large amplitude of the wave envelope.

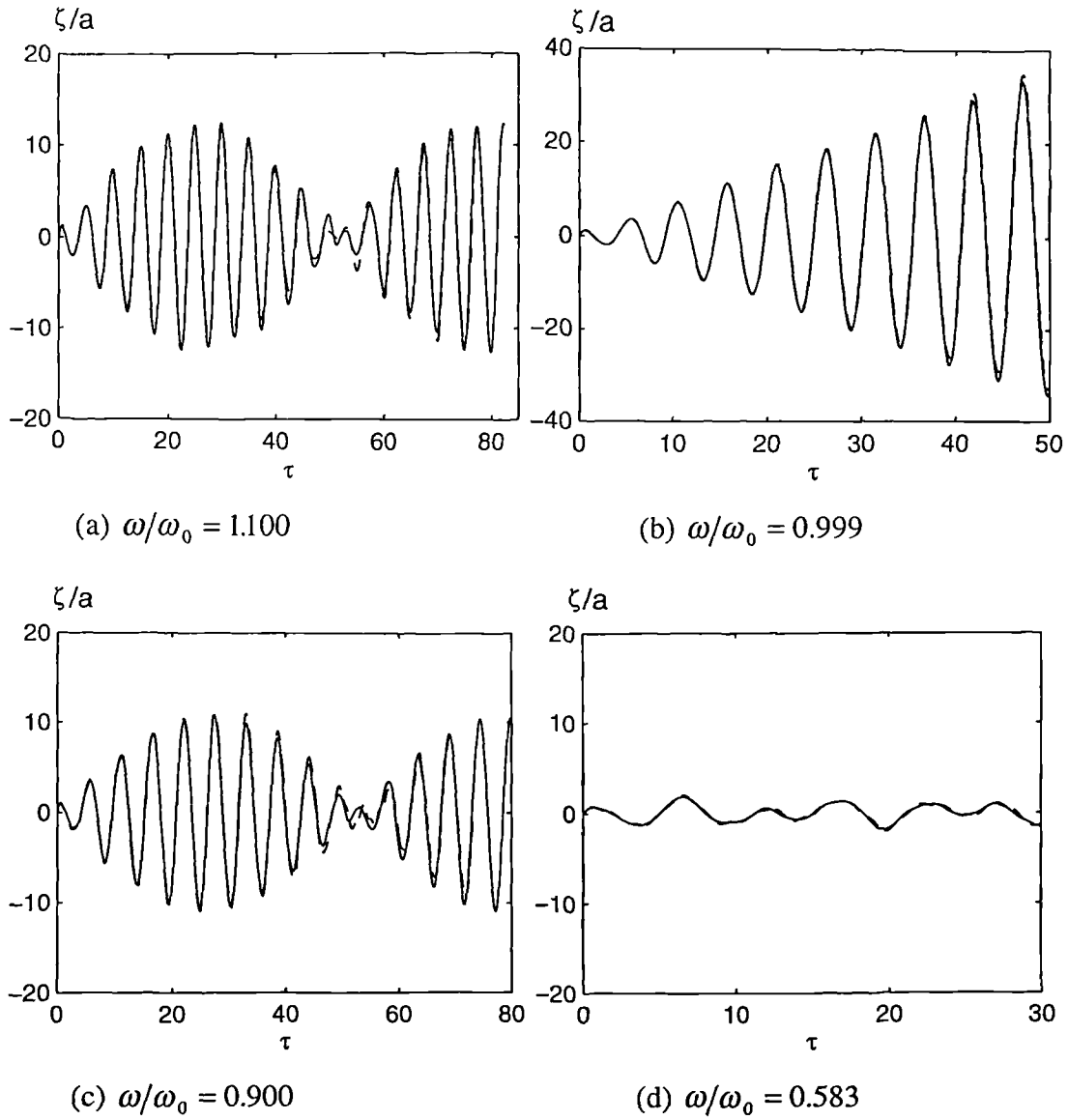

Figure 7.4.3 Time history of free surface elevation at $x = -L/2$ for different frequencies (solid line: analytical; dashed line: numerical)

Figure 7.4.4 shows "snapshots" of the free surface profiles between $\tau = 5.3153$ and $\tau = 15.5031$, at intervals equal to 0.443, for the case of $\omega / \omega_0 \approx 0.999$. Figure 7.4.5 gives corresponding comparisons of the numerical pressure with the analytical solution through the water depth. Again a good agreement between the analytical and numerical results is found.

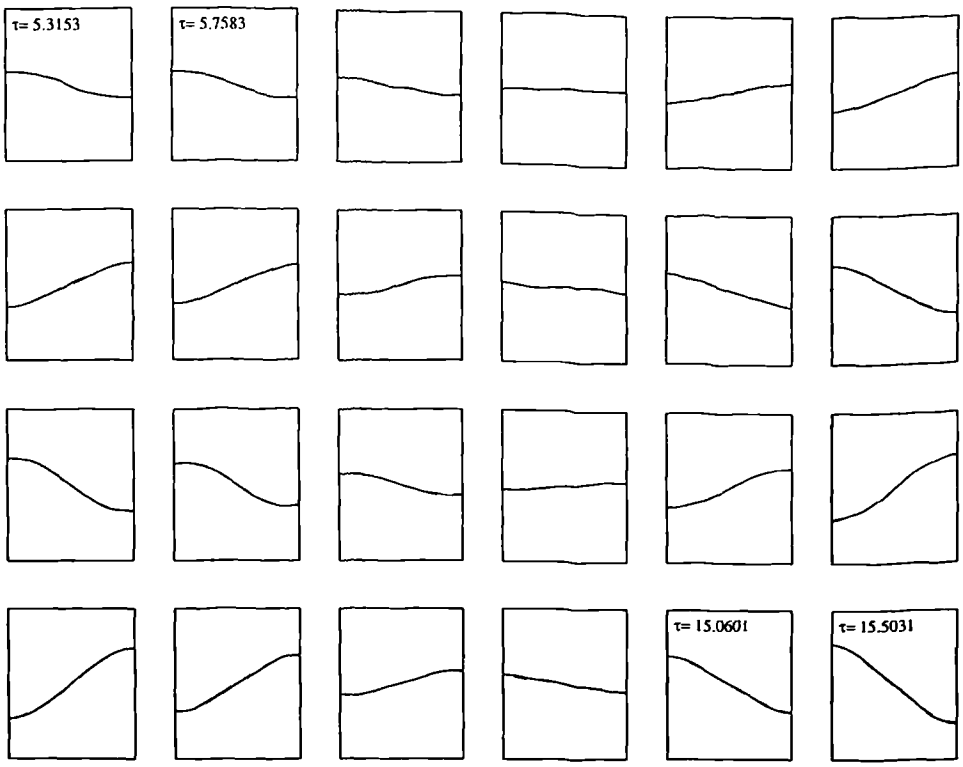

Figure 7.4.4 Free surface profiles for $\omega / \omega_0 \approx 0.999$
(solid line: analytical; dashed line: numerical)

The present numerical method is now used to analyse cases with larger amplitude, still with $\omega / \omega_0 \approx 0.999$. We consider the surging motion with $a = 0.0186$, which is ten times larger than that in the previous case. Figure 7.4.6 plots the free surface elevation measured from the bottom of the tank at two time steps, as obtained from the experimental data (Okamoto and Kawahara,1990), the linear analytical solution and the non-linear numerical simulation. It can be seen that the numerical simulation gives better agreement with the experimental data, although the linear solution still gives good results in this case.

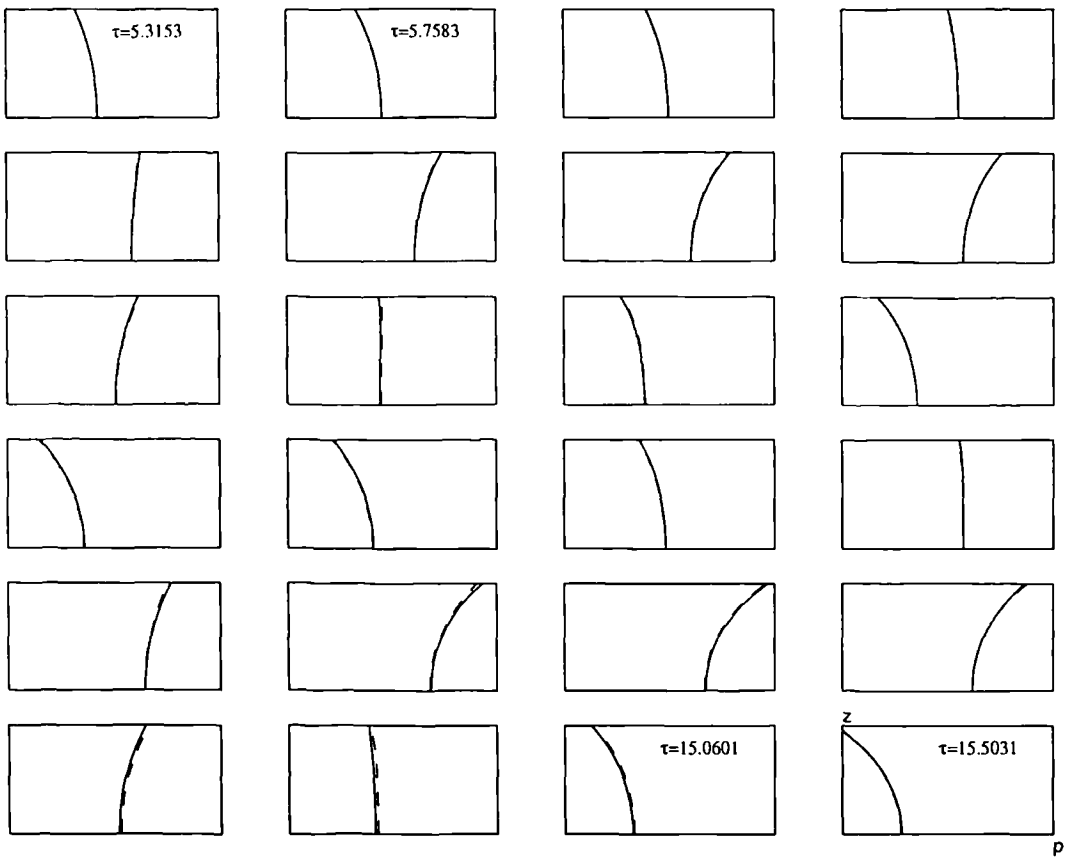

Figure 7.4.5 Comparison of numerical pressure along the water depth $(x = L/2,\ y = 0)$ for $\omega / \omega_0 \approx 0.999$ with analytical solution
(Solid line: analytical solution; dashed line: numerical simulation)

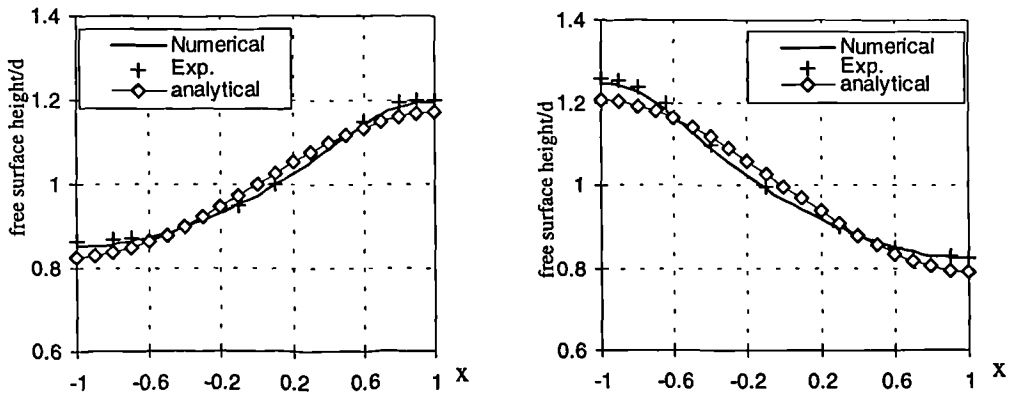

(a) $\tau = 13.0667$ (b) $\tau = 15.725$

Figure 7.4.6 Comparison of free surface elevation with experimental data

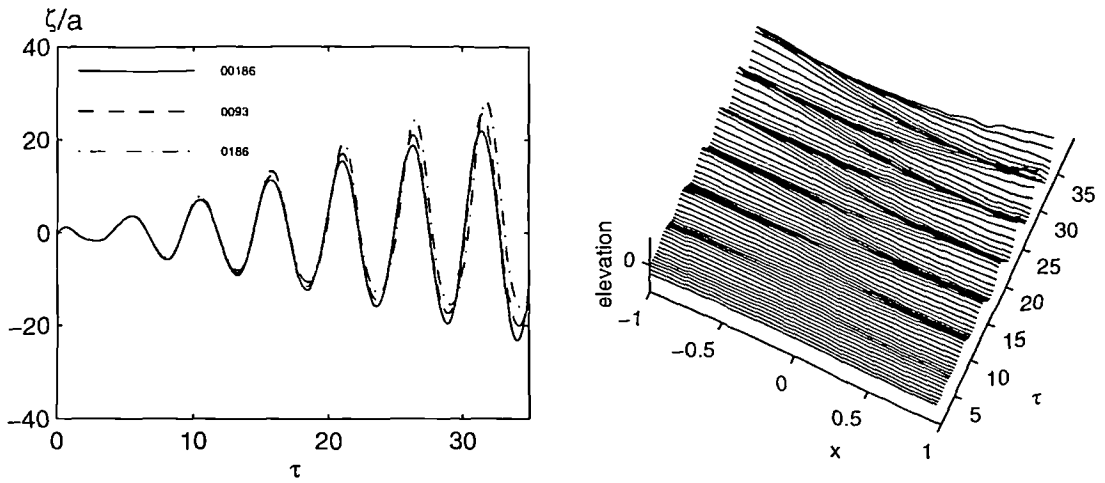

(a) Wave history ($x = -L/2$) ($a = 0.00186, 0.0093, 0.0186$)

(b) Wave profile, $a = 0.0186$

Figure 7.4.7 Wave history and profile for $\chi = 0.5$

To further demonstrate the effects of non-linearity, the results for different excitation amplitudes are plotted in Figure 7.4.7, where $\chi = d / L$ and $\omega / \omega_0 \approx 0.999$. It can be observed that with increase of amplitude, the crests become sharper, the troughs become flatter and the period tends to be longer. All these effects have also been noted by Armenio and La Rocca (1996) for the two-dimensional roll motion. The gradual increase of the period is also discussed by Greaves (1995) and Tsai & Jeng (1994) for the case of free oscillation in a tank.

The motion near the first natural frequency ω_0 has some interesting features. Apart from the normal standing wave, a travelling wave and a bore may exist. Based on their investigation into the two dimensional roll motion, Armenio and La Rocca (1996) have mentioned that these three waves may all appear, depending on χ. Huang and Hsiung (1996) have also noticed the bore, when using a shallow water formulation.

Our analysis shows the occurrence of a normal standing wave in Figure 7.4.7(b). We now consider two cases, with $\chi = 0.125, 0.04$, to demonstrate a travelling wave and a bore. In the first case, the tank length is taken as $L = 8$. Two different amplitudes

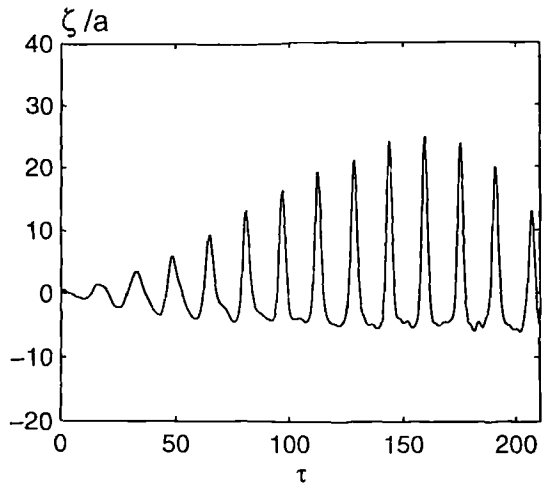

(a) Wave history at $x = -L/2$

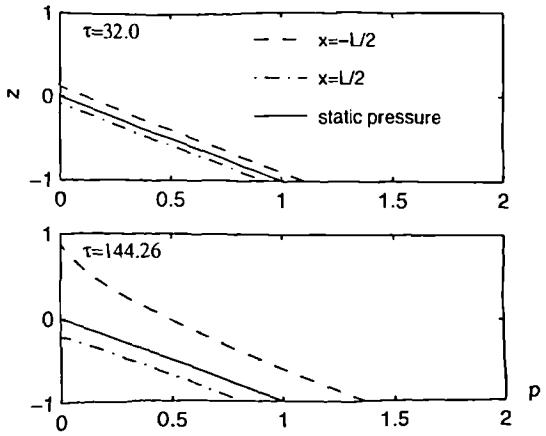

(b) Pressure $p = p/\rho gd$

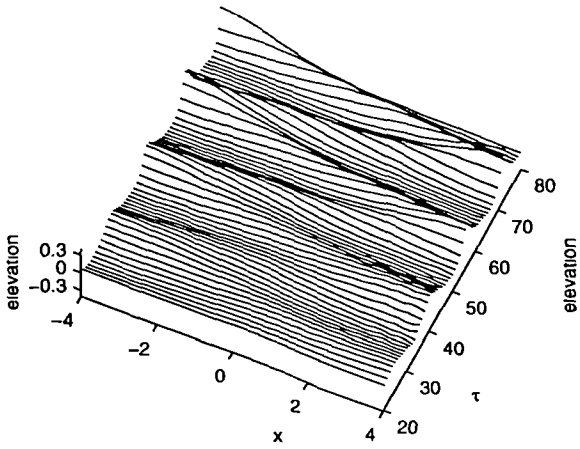

(c) Wave profile ($\tau = 20 \sim 80$)

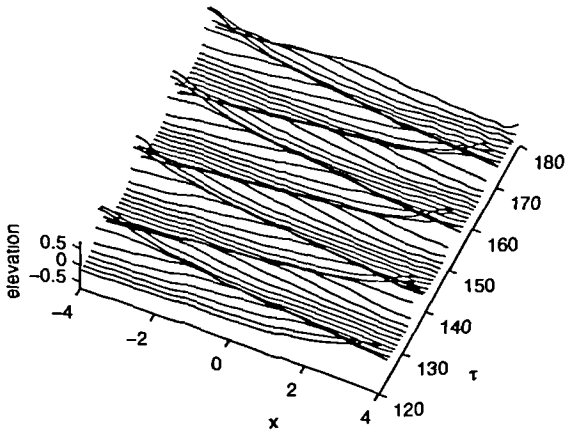

(d) Wave profile ($\tau = 120 \sim 180$)

Figure 7.4.8 Wave history, profile and pressure($\omega = 0.9998\omega_0, a = 0.0372$)

of the motion are considered with the same frequency, $\omega = 0.9998\omega_0$. The mesh is generated using $M_1 = 40$, $M_2 = 6$, $N = 16$ and the time step is chosen as $\Delta\tau = 0.0273$. Figure 7.4.8 presents the wave profile, wave history and pressure on the side walls for the amplitude $a = 0.0372$. Figure 7.4.8d clearly exhibits a wave with one peak travelling in the tank. When the peak reaches the wall, the pressure is apparently larger than the static pressure, as shown in Figure 7.4.8b. The travelling wave does not appear immediately after the tank starts to move. Instead, there is a transient period during which the wave changes gradually from standing wave to travelling wave, as illustrated in Figure 7.4.8c. Figure 7.4.8 also shows that the wave history is very different from that in Figure 7.4.7. The non-linear effects are even more significant and

the peaks are even sharper here. The peaks are modulated but the modulation frequency is no longer equal to the difference between the excitation frequency and the first natural frequency ($2\pi / \Delta\omega \approx 8.2 \times 10^5$ from the linear theory).

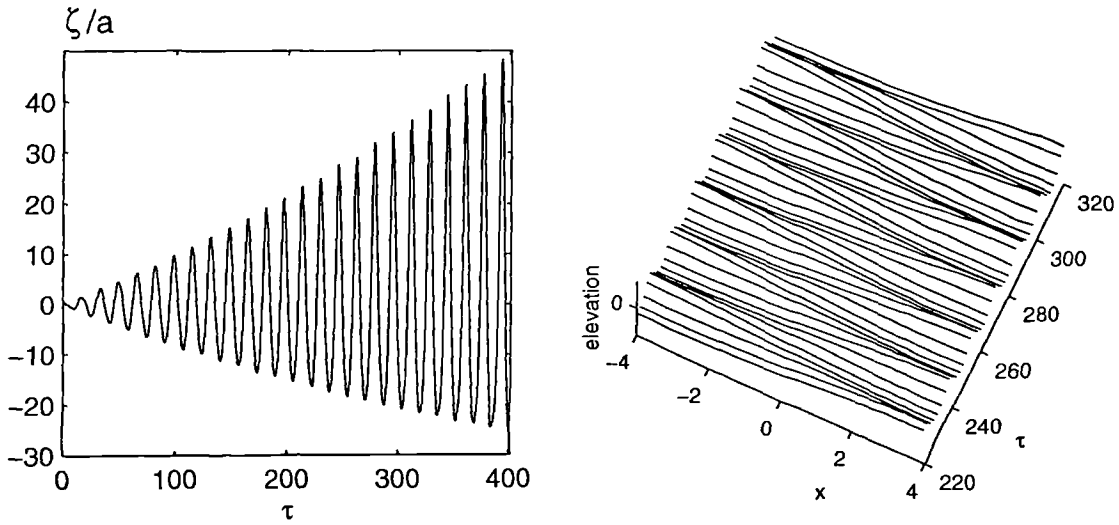

(a) Wave history ($x = -L/2$) (b) Wave profile

Figure 7.4.9 Wave history and profile ($\omega = 0.9998\omega_0$, $a = 0.00372$)

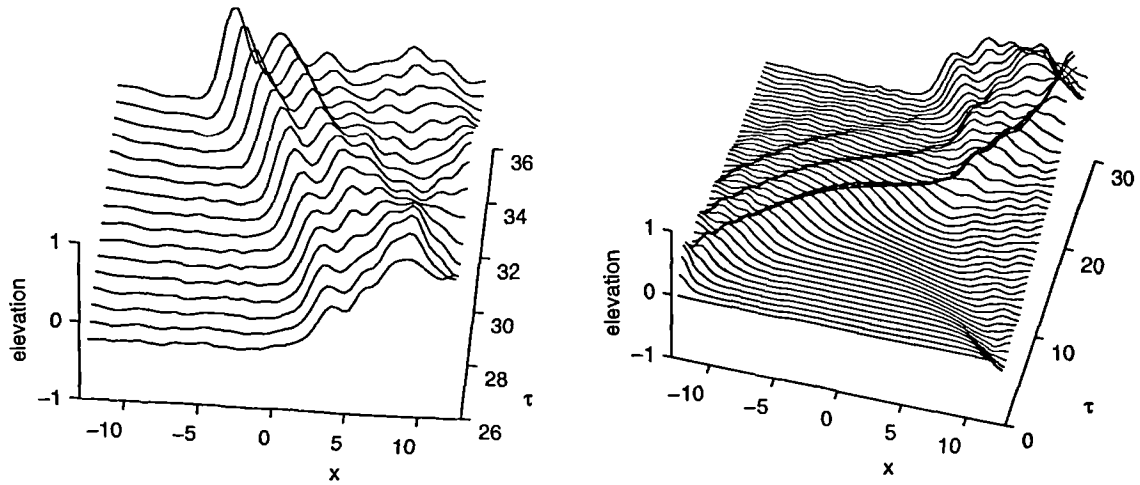

(a) wave profile $\tau = 26 \sim 36$ (b) Wave profiles $\tau = 0 \sim 30$

Figure 7.4.10 Wave profile for $a = 2.5$ and $\omega = 0.9973\omega_0$

Figure 7.4.9 shows results for the same case as Figure 7.4.8, except that the amplitude $a = 0.00372$ is now ten times as small. The results in Figures 7.4.8 and 7.4.9 are clearly very different. Figure 7.4.9b does not show any visible travelling waves even when

$\tau \approx 320$. Instead the results are similar to those in Figure 7.4.7. This suggests that the wave form in a sloshing tank depends not only on the depth/length ratio of the tank but also on the motion amplitude.

In the second case, the length is taken as $L = 25$, which corresponds to very shallow water. The excitation frequency is taken as $\omega = 0.9973\omega_0$ and the amplitude $a = 2.5$. The wave profiles are shown in Figure 7.4.10. It can be seen that a bore appears after about $\tau \approx 26$. To the left of the bore, the water surface is almost flat and the free surface elevation is small. To the right of the bore, the wave elevation is much higher. In addition, there is some higher frequency undulation superimposed on the right. This is different from the bore observed by Huang and Hsiung (1996) using the shallow water approximation. Their equation is essentially based on the Airy theory, in which there are no dispersive terms to permit modelling of undulations, see Peregrine (1966). In the case here, it is more appropriate to base the shallow water approximation on the Boussinesq equations, which allow waves of relatively short length. Further, in Figure 7.4.10, there is also a period of transition before the bore is formed as in Figure 7.4.8c. It should be mentioned that the bore has never been observed in our calculation if the motion is very small.

Chester (1968) and Chester & Bones (1968) have also studied the behaviour of sloshing waves around resonance by an approximate method and by experiments. The results from the two methods were given in separate figures and the comparison seems to be favourable qualitatively. Their data have shown that the history of the wave elevation may have one, two or more peaks within each period, depending on the frequency and amplitude of the excitation, and the depth. In particular, at $\omega = \omega_0$, one peak can be observed when $\chi = 1/12$ and two peaks when $\chi = 1/24$. Figures 7.4.8 and 7.4.10 seem to display some similarity to this kind of behaviour, but our results are not entirely identical to theirs. The difference seems to be mainly due to the fact that the profiles they gave are those in the steady periodic stage, but the modulation still exists in our calculation, even after a long simulation. A longer simulation was not attempted here, because to reduce the accumulated error, a very fine mesh and small time steps would have to be used, which requires prohibitive computer resources.

7.4.3 Three Dimensional Cases

The tank in these cases is subjected to motions defined by $x_c(\tau) = a_x \sin(\omega_x \tau)$, $y_c(\tau) = a_y \sin(\omega_y \tau)$ and $z_c(\tau) = a_z \sin(\omega_z \tau)$, where a_{x_i} and ω_{x_i} $(x_1 = x, x_2 = y, x_3 = z)$ are the amplitudes and frequencies in surge, sway and heave modes, respectively. The corresponding velocities are then $U(\tau) = \omega_x a_x \cos(\omega_x \tau)$, $V(\tau) = \omega_y a_y \cos(\omega_y \tau)$ and $W(\tau) = \omega_z a_z \cos(\omega_z \tau)$.

Table 7.4.1 The cases for three dimensional sloshing

	dimension		frequency			amplitude		
case	L	B	ω_x	ω_y	ω_z	a_x	a_y	a_z
A	4	4	$.9999\,\omega_{0x}$	$.9999\,\omega_{0y}$	0.0	0.372×10^{-3}	0.372×10^{-3}	0.0
B	4	4	$.9999\,\omega_{0x}$	$.9999\,\omega_{0y}$	0.0	0.0372	0.0372	0.0
C	4	4	$.9995\,\omega_{1x}$	$.9995\,\omega_{1y}$	0.0	0.0186	0.0186	0.0
D	4	2	$.9999\,\omega_{0x}$	$.9999\,\omega_{0y}$	0.0	0.0372	0.0186	0.0
E+	4	4			$2.04\,\omega_{0x}$			0.2
F	4	4	$.9995\,\omega_{1x}$	$.9995\,\omega_{1y}$	$2.04\,\omega_{0x}$	0.0186	0.0186	0.2
G	8	8	$.9999\,\omega_{0x}$	$.9999\,\omega_{0y}$	0.0	0.0372	0.0372	0.0
H	8	4	$.9999\,\omega_{0x}$	$.9999\,\omega_{0y}$	0.0	0.0372	0.0186	0.0
S	25	25	$.998\,\omega_{0x}$	$.998\,\omega_{0y}$	0.0	1.2	1.2	0.0

+: horizontal velocity disturbance is applied only at $\tau = 0$ (see equation 7.4.25)

The wave motion in the three dimensional tank is much more complicated than that in the two dimensional case. Several cases with different parameters, as listed in Table 7.4.1, are considered below to demonstrate how they influence the waves induced in the tank. ω_{ix} and ω_{iy} $(i = 0,1)$ in the table are the natural frequencies based on the linear analysis corresponding to the x and y directions. It should be noted that the natural frequencies in the three dimensional cases are $\sqrt{(m\pi/L)^2 + (n\pi/B)^2}\tanh\sqrt{(m\pi/L)^2 + (n\pi/B)^2}$ $(m,n = 0,1,2\cdots)$. Among them, the terms

with $m = 1,3,5\cdots, n = 0$ and $n = 1,3,5\cdots, m = 0$ correspond to the anti-symmetric motions in the x and y directions, respectively. Thus the first and second natural frequencies in the x direction, ω_{0x} and ω_{1x} in the table, are obtained by taking $m = 1,\ n = 0$ and $m = 3,\ n = 0$, respectively. Similarly ω_{0y} and ω_{1y} are obtained by taking $m = 0,\ n = 1$ and $m = 0,\ n = 3$, respectively.

Table 7.4.2 Parameters for convergence study

case	M_1	M_2	N	$\Delta\tau$
c1	60	60	12	0.0111
c2	40	40	12	0.0111
c3	40	40	16	0.0111
c4	80	80	18	0.0111
c5	40	40	12	0.0146
c6	40	40	12	0.0219

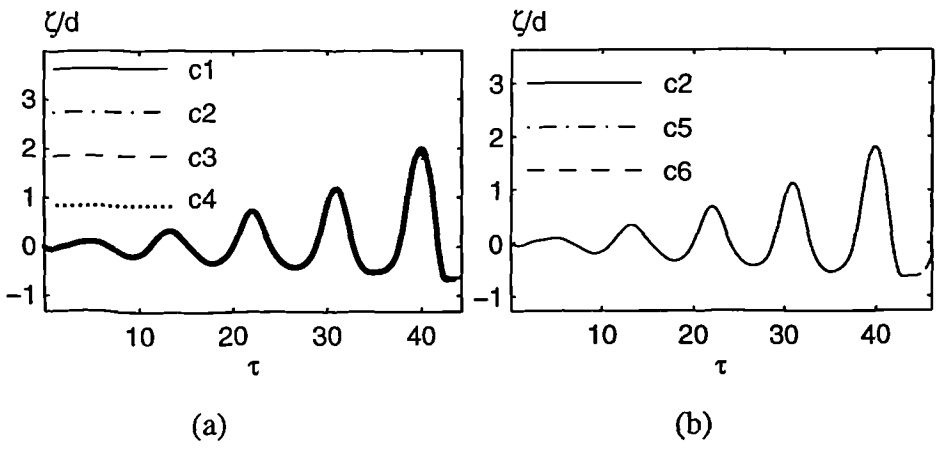

Figure 7.4.11 Comparison of wave elevation history at $(L/2,\ B/2)$ for different meshes and time steps

Convergence study

Case B is taken as an example for the convergence study. The mesh is generated in a similar way to that shown in Figure 7.4.2. Table 7.4.2 lists the parameters used for this examination of convergence.

Figure 7.4.11 presents the time history of the free surface elevation for all cases in Table 7.4.2, taken at the corner $(L/2, B/2)$ where the wave is found to be very steep (see Figure 7.4.13 below). Figure 7.4.11a is for cases c1-c4 where the time steps are the same but the meshes are different; while Figure 7.4.11b is for c2, c5 and c6 where the meshes are the same but the time steps are different. The figures show that the results from these meshes and time steps are in good agreement. This suggests that between 40 to 80 divisions in each wave length and 400 time steps in each wave period are needed to obtain the converged results. But these parameters clearly very much depend on the time period over which the calculation is made and other factors such as the wave amplitude. In the following analysis, these parameters are chosen in such a way that the same degree of accuracy is maintained

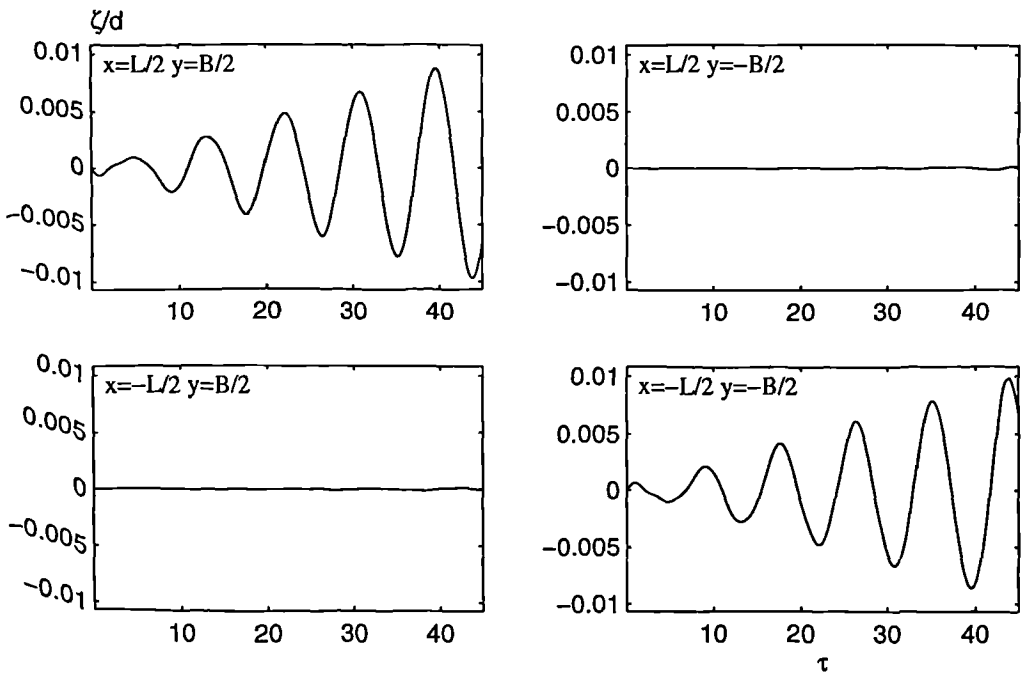

Figure 7.4.12 Wave elevation history at four corners (Case A)

Sloshing waves in Cases A to F

In all these cases the tank has the same length. The varying parameters are the width, the frequency and the excitation amplitude. In Case A, the motion is very small. The fluid domain is discretised using $M_1 = 40$, $M_2 = 40$ and $N = 12$, and the time step is taken as $\Delta\tau = 0.0146$. The wave elevation histories at the four corners of the tank are given in Figure 7.4.12. It can be seen that the wave amplitude at two corners $(L/2, B/2)$ and $(-L/2, -B/2)$ increases with time while the wave elevations at the other two corners are almost zero.

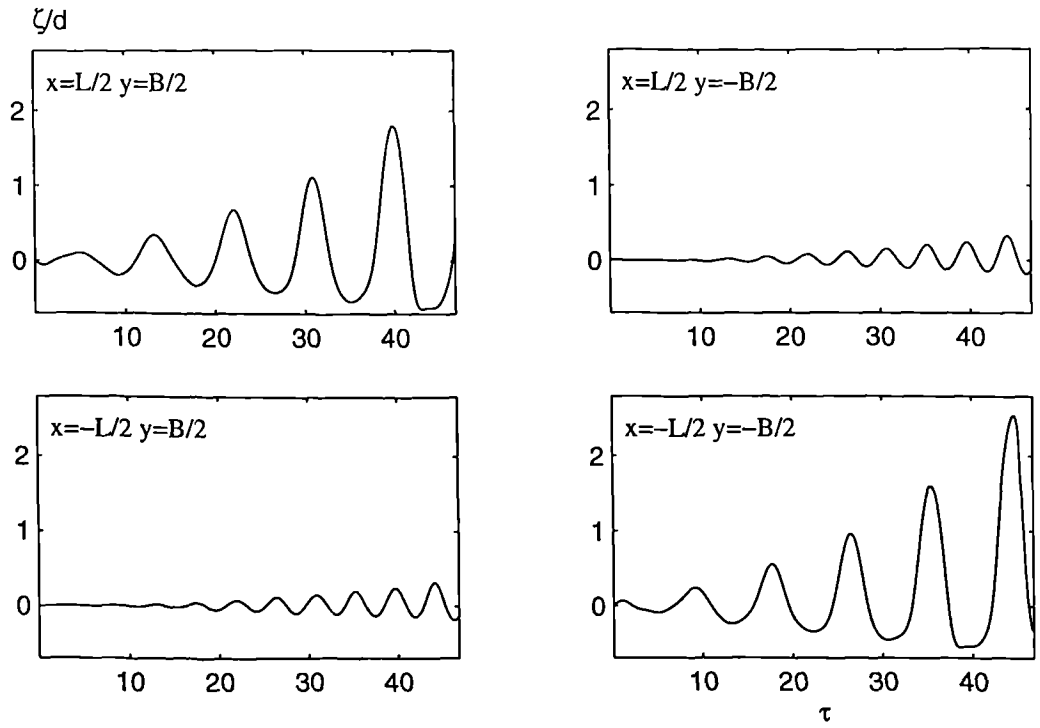

Figure 7.4.13 Wave elevation history at four corners (Case B)

In Case B, the excitation amplitude is one hundred times bigger than that in Case A. Figure 7.4.13 presents the wave elevation history at the four corners. Unlike in Case A, the free surface elevation at corners $(L/2, -B/2)$ and $(-L/2, B/2)$ is no longer invisible and, especially after $\tau \approx 20$, the increase of the amplitude with time becomes evident. The peak at the other two corners $(L/2, B/2)$ and $(-L/2, -B/2)$ can become quite large, indeed it is about three times bigger than the initial water depth after $\tau \approx 40$.

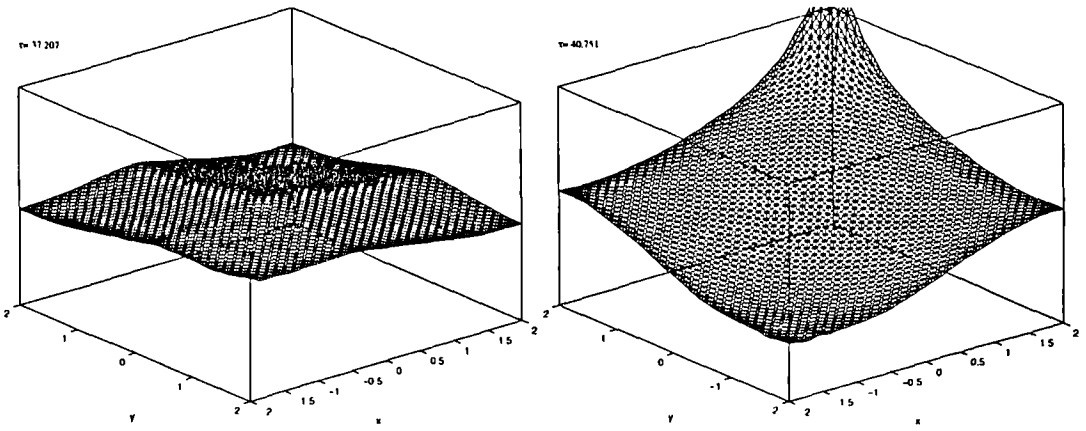

Figure 7.4.14 Snapshots of the free surface for Case B (height of the box=2*d*)

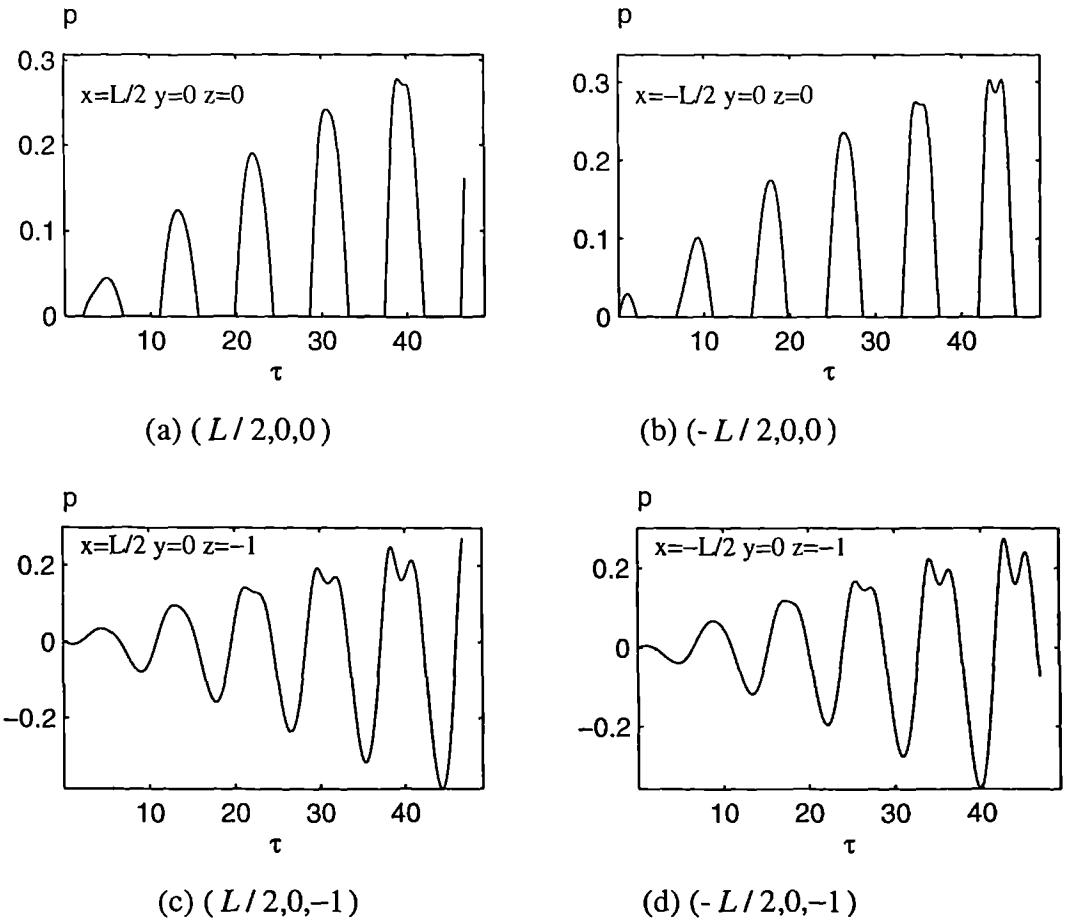

Figure 7.4.15 Pressure history at a point on the tank wall (Case B)

Two typical snapshots of the free surface are illustrated in Figure 7.4.14, where the height of the plotted box is $2d$. Figure 7.4.15 provides the pressure history (excluding

the contribution from the static pressure) recorded at four points: two at the mean free surface and two on the bottom. It shows that as the time progress, double peaks appear in the time history of the pressure, which is particularly evident on the bottom. This is very similar to that observed by Nagai (1969) in the pressure in steady-state standing waves, and that observed by Cooker, Weidman & Bale (1997) in the force on a vertical wall subject to a solitary wave.

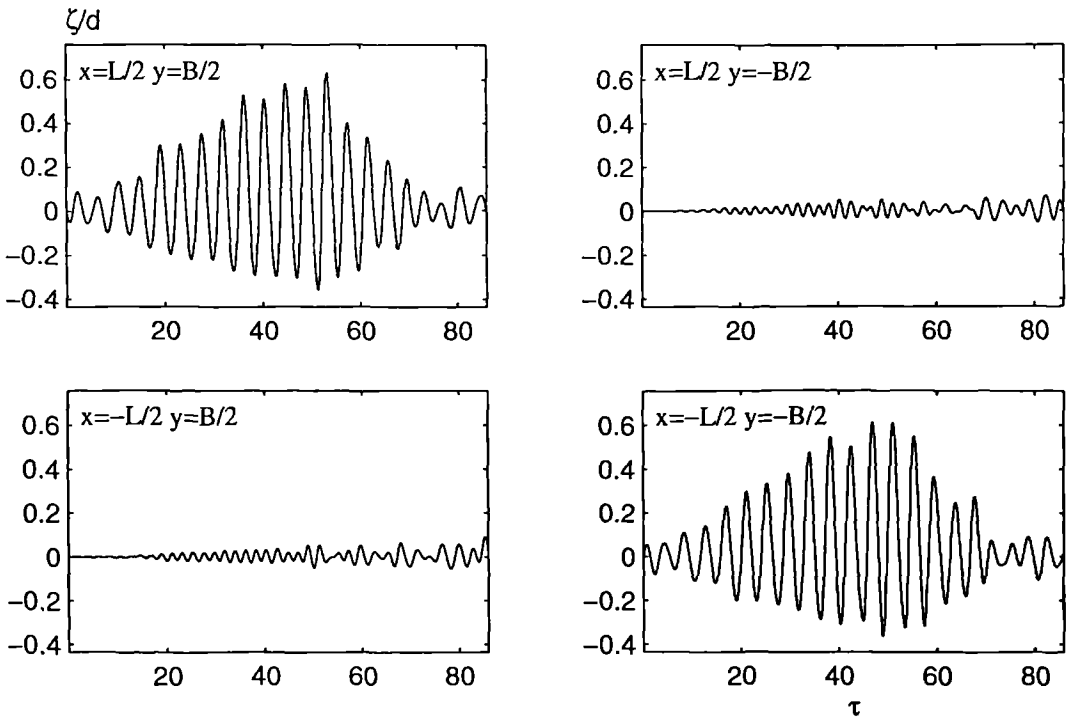

Figure 7.4.16 Wave elevation history at four corners (Case C)

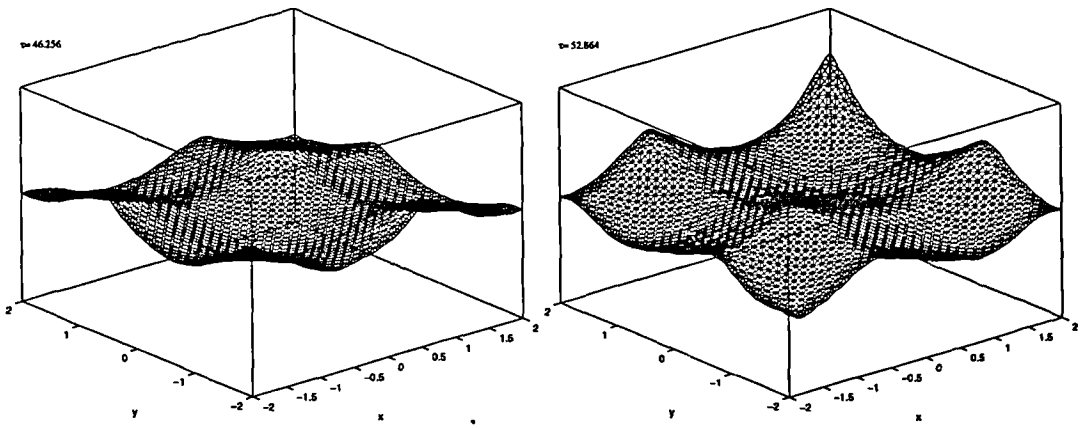

Figure 7.4.17 Snapshots of the free surface for Case C (height of the box=2*d*)

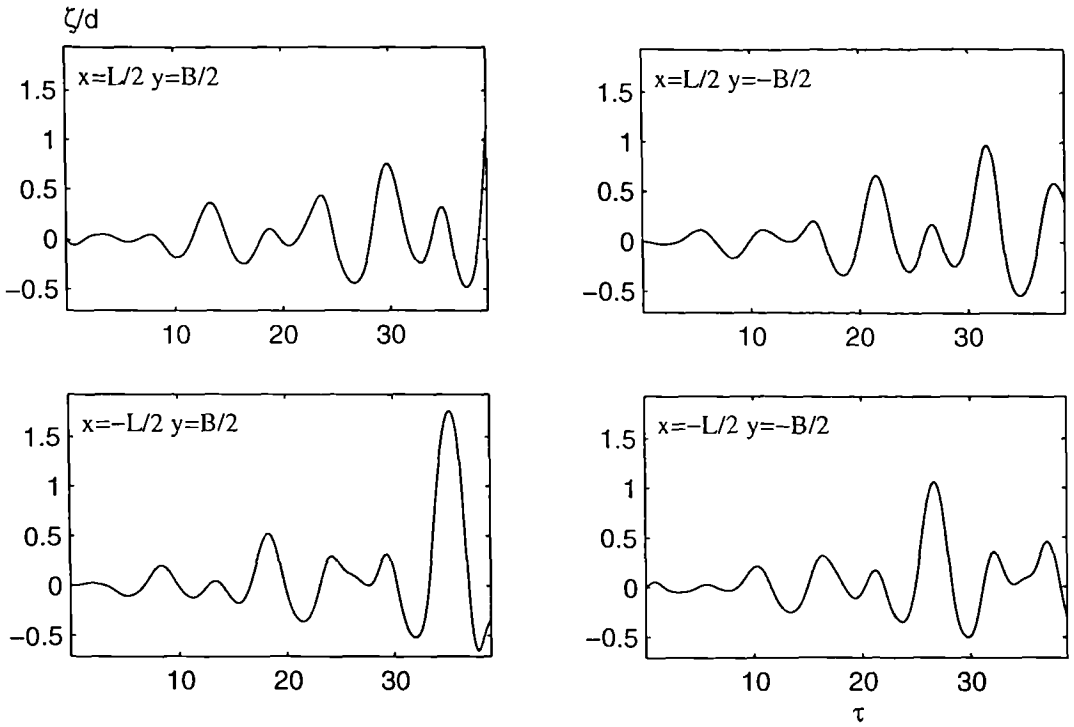

Figure 7.4.18 Wave elevation history at four corners (Case D)

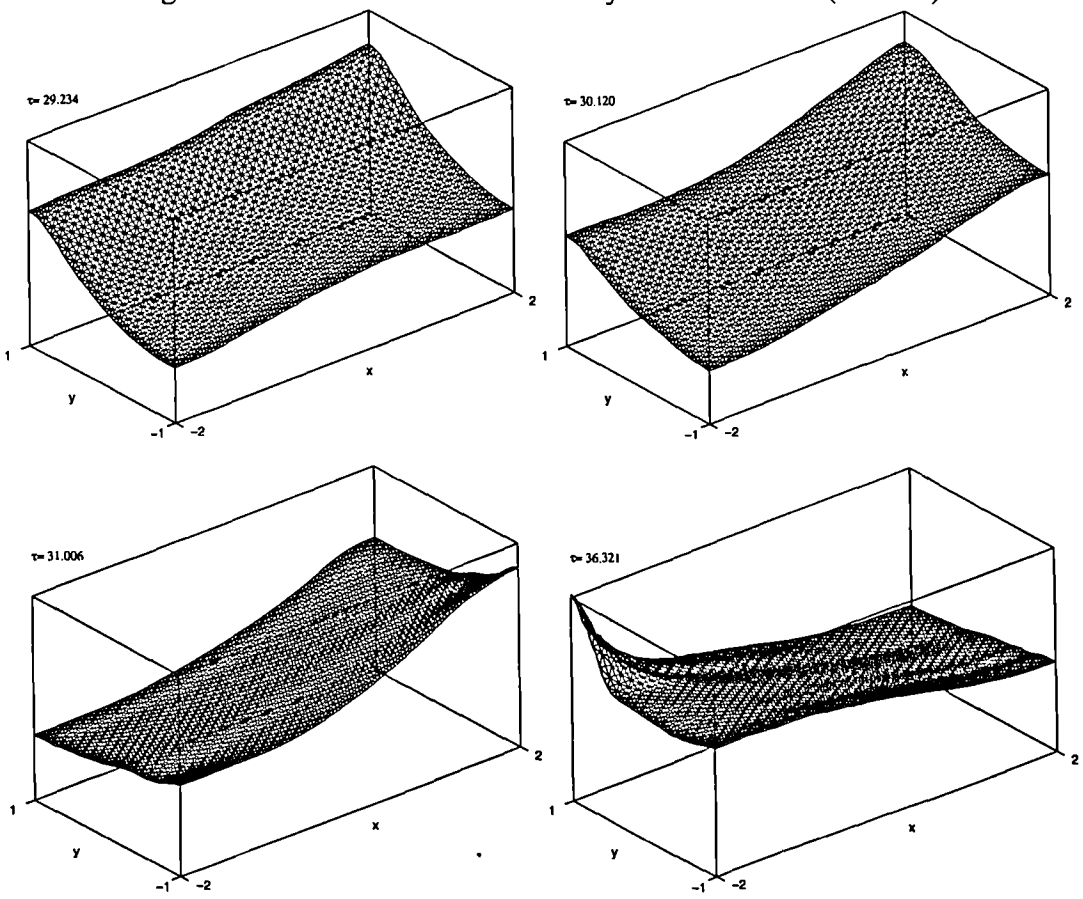

Figure 7.4.19 Snapshots of sloshing wave for Case D (height of the box=2*d*)

In the above two cases the excitation frequency is approximately equal to the first natural frequency of the tank. In Case C, this frequency is increased to near the second natural frequency of the tank. Figure 7.4.16 shows the wave elevations at the four corners. It should be noticed that both the velocity amplitude ($\omega_x a_x$) and the acceleration amplitude ($\omega_x^2 a_x$) of the excitation in this case are larger than those in Case B, but the wave amplitude here is much smaller. The snapshots of the wave elevation are shown in Figure 7.4.17, which shows that the wave is shorter than that in Figure 7.4.14, as expected.

In the three cases considered above, both the tank and the external disturbance are symmetrical about the vertical plane joining the two corners ($L/2, B/2$) and ($-L/2, -B/2$). The wave motion is therefore also symmetrical. In Case D the property of symmetry no longer exists. The mesh in this case is generated using $M_1 = 60$, $M_2 = 40$ and $N = 12$, and the time increment is $\Delta\tau = 0.0111$. Figure 7.4.18 show the time histories of the wave elevations at the four corners. As can be seen, the water surface can become very high at all corners, instead of just at two corners as in the previous cases. This can be more clearly seen in Figure 7.4.19, which shows that the big wave can occur at other places along the walls.

We now consider the cases including the vertical motion. In Case E, the tank oscillates only vertically but with a small initial perturbation of the horizontal velocities. The excitation is defined by:

$$\begin{cases} u(\tau) = v(\tau) = \begin{cases} 0.0283 & \tau = 0 \\ 0 & \tau > 0 \end{cases} \\ w(\tau) = \omega_z a_z \cos(\omega_z \tau) \end{cases} \qquad (7.4.25)$$

The frequency of the vertical motion is taken to be about twice the first natural frequency in the horizontal direction. The waves generated by the vertical oscillation are called Faraday waves. Benjamin & Ursell (1954) explained the mechanism of Faraday waves by analysing Mathieu's equations derived from the linear theory. Since then, a considerable number of papers have been published on this topic, which have been reviewed by Miles & Henderson (1990) and Jiang, Ting, Perlin & Schultz (1996). Here we try to demonstrate the transient behaviour of the Faraday waves.

The mesh for this case is the same as that used in Case B and the time increment is taken as 0.0107. The wave elevations at the four corners are plotted in Figure 7.4.20. The results without a horizontal perturbation (dashed line) is also included in this figure for comparison. It can be seen that the motion of the free surface is not at the excitation frequency but at the first natural frequency of the tank. A similar case was reported by Su and Wang (1986), based on their solution of the Navier-Stokes equations. We have investigated other cases with excitation frequencies $\omega_z = 0.5\omega_{0x}, 1.0\omega_{0x}, 1.5\omega_{0x}$ and $2.5\omega_{0x}$ but fixed acceleration amplitude ($a_z\omega_z^2 = 0.428$ as in Figure 7.4.20) were considered. The results, indicated in Figure 7.4.21, show that the history of the wave elevation in all the cases is almost the same. This suggests that the wave evolution during the transient period generated by the vertical excitation with a given horizontal perturbation may be determined only by the acceleration amplitude of the excitation. To further confirm this, Figure 7.4.22 presents the wave history generated by the excitation with the same frequency $\omega_z = 0.5\omega_{0x}$, but different amplitudes, corresponding to $a_z\omega_z^2 = 0.428$ and $a_z\omega_z^2 = 0.129$ respectively. It shows that the results in these cases are very different.

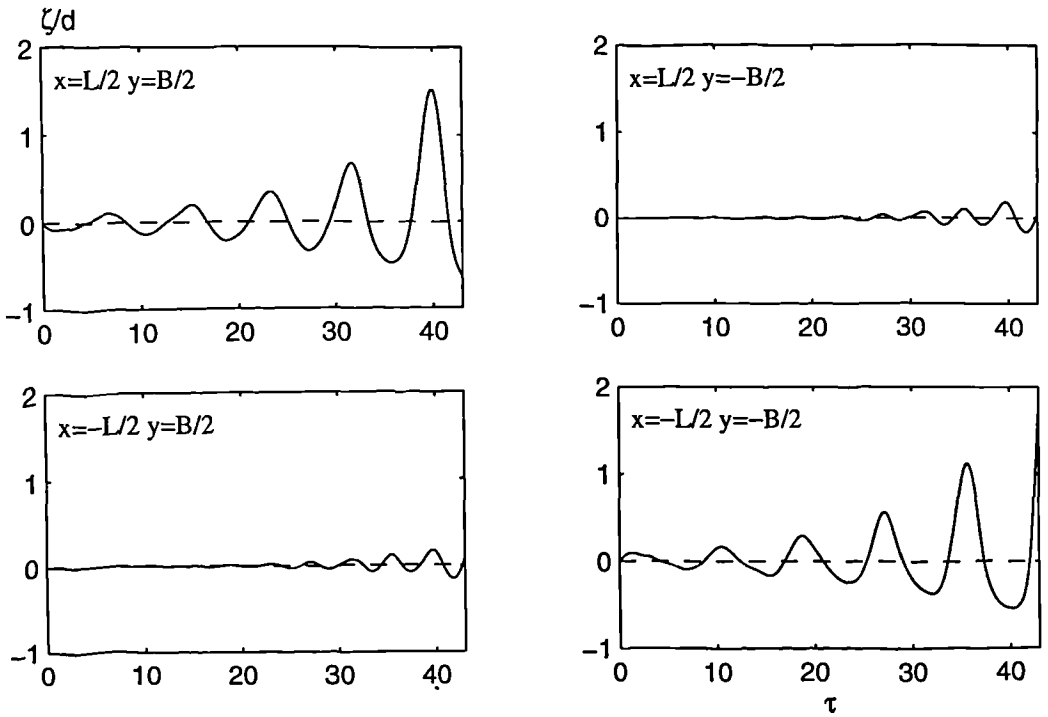

Figure 7.4.20 Wave elevation history at four corners (Case E)
(solid line: u, v given in equation. 25 ; dashed line: $u = v = 0$)

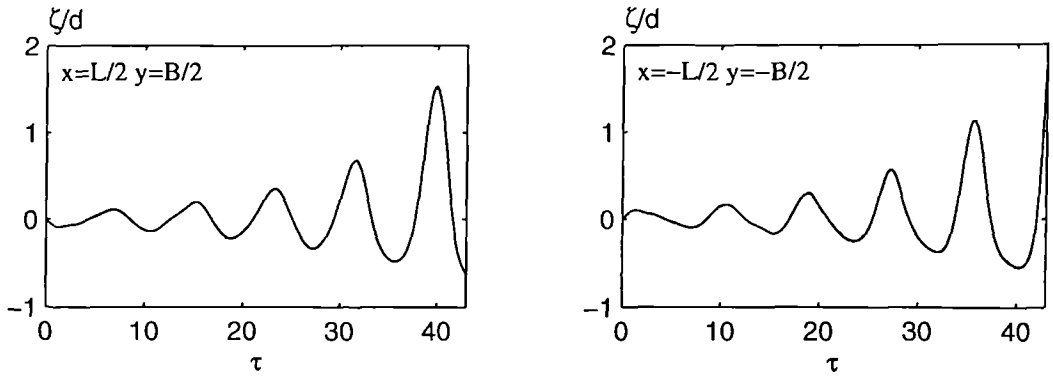

Figure 7.4.21 Wave elevation history at two corners: four lines coincide with each other (Case E, $\omega_z = 0.5\omega_{0x}, 1.0\omega_{0x}, 1.5\omega_{0x}$ and $2.5\omega_{0x}$ and $a_z\omega_z^2 = 0.428$)

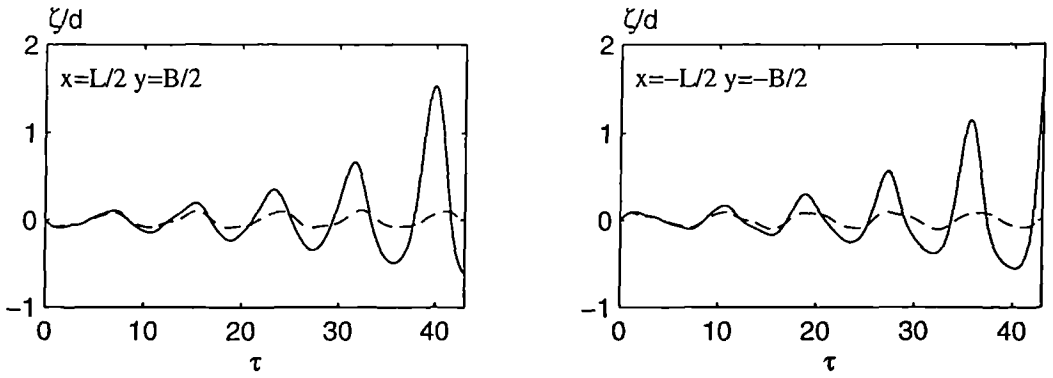

Figure 7.4.22 Wave elevation history at two corners (Case E, $\omega_z = 0.5\omega_{0x}$, solid line: $a_z\omega_z^2 = 0.428$; dashed line: $a_z\omega_z^2 = 0.129$)

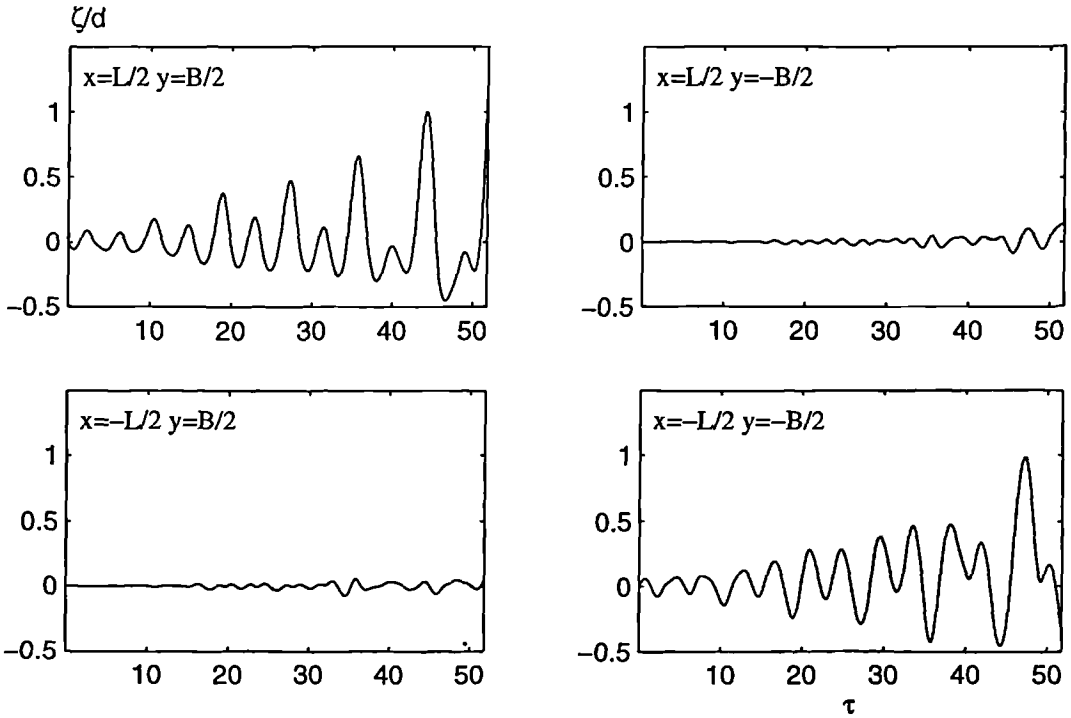

Figure 7.4.23 Wave elevation history at four corners (Case F)

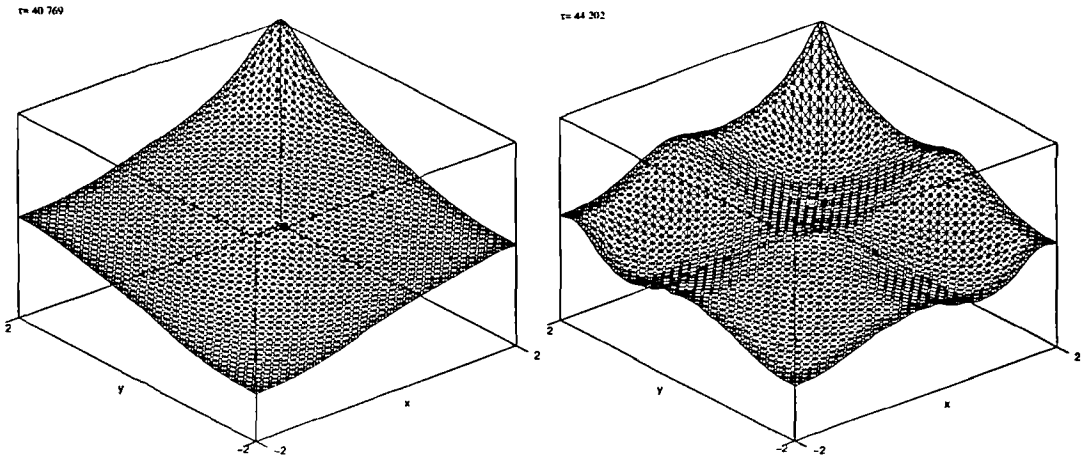

(a) Case E (b) Case F

Figure 7.4.24 Snapshots of wave profile for Case E and Case F
(height of the box=2*d*)

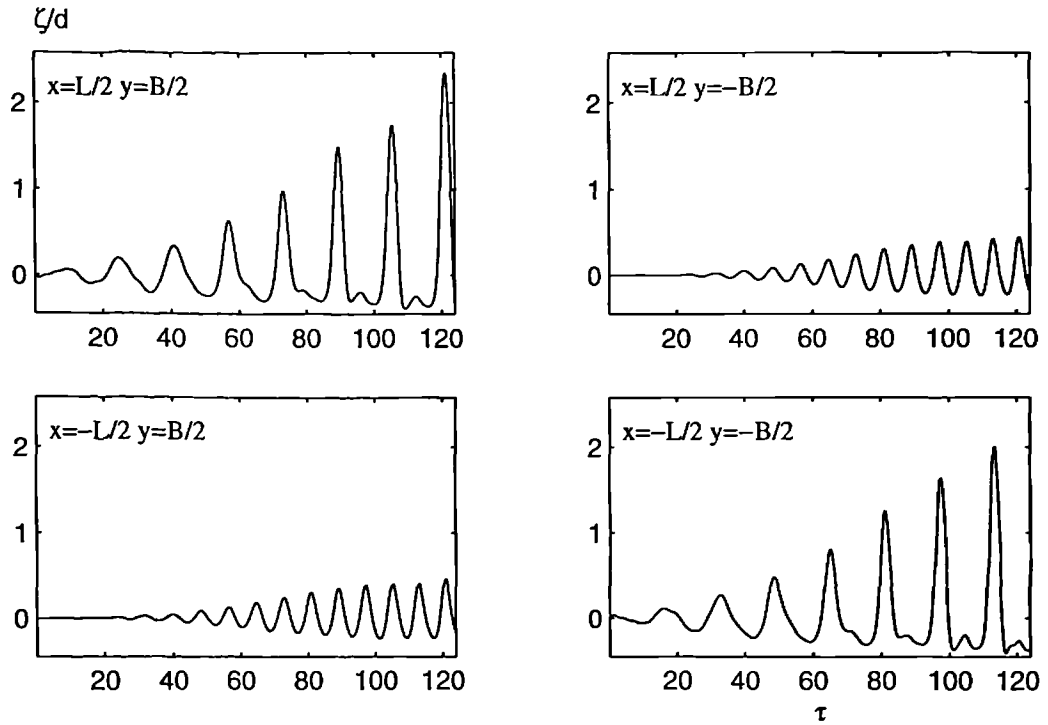

Figure 7.4.25 Wave elevation history at four corners (Case G)

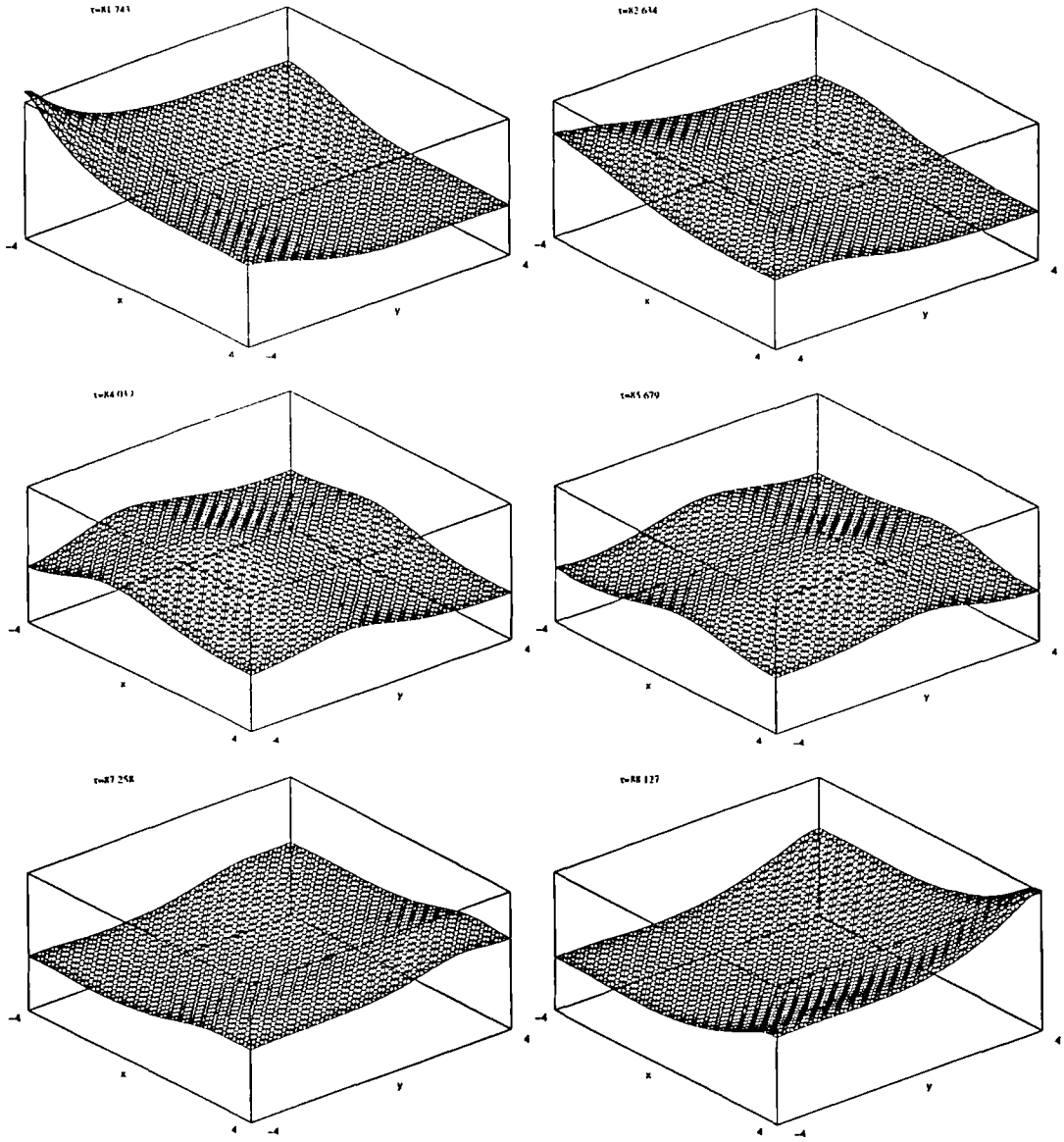

Figure 7.4.26 Snapshots of travelling waves for Case G (height of the box=2*d*)

Case F is similar to case E, except that a horizontal excitation is applied throughout the time history. What is interesting here is that despite the horizontal excitation being applied over the entire period of the calculation, the wave amplitudes in this case (as shown in Figure 7.4.23) are no larger than that in Case E (shown in Figure 7.4.20). The comparison of the free surfaces in these two cases is illustrated in Figure 7.4.24. Compared with Case C, where the horizontal motion is the same as that in Case F but with no vertical motion, the amplitude in Case F is much larger.

Sloshing waves in Cases G and H

In these two cases, the water depth is effectively smaller. In Case G, the ratio of depth/length (= depth/width) is set as 0.125, which is the same as in the 2D case of Figure 7.4.8 where the travelling wave has been observed. The wave elevation histories at the four corners are shown in Figure 7.4.25. Figure 7.4.26 shows a sequence of a wave crest moving from the corner $(-L/2, -B/2)$ to the corner $(L/2, B/2)$. Figure 7.4.27 gives the profiles on two vertical planes, $y = 0$ and $x = 0$, at different time steps. These results clearly show that the travelling wave exists in this case. Figure 7.4.28 illustrates the pressure history at four points: two at the mean free surface and two on the bottom. Compared with Figure 7.4.14, the double peaks do not seem to exist in the pressure at the mean free surface, but there are small peaks superimposed on the primary ones. The pressure on the bottom, on the other hand, has similar behaviour to that in Figure 7.4.15.

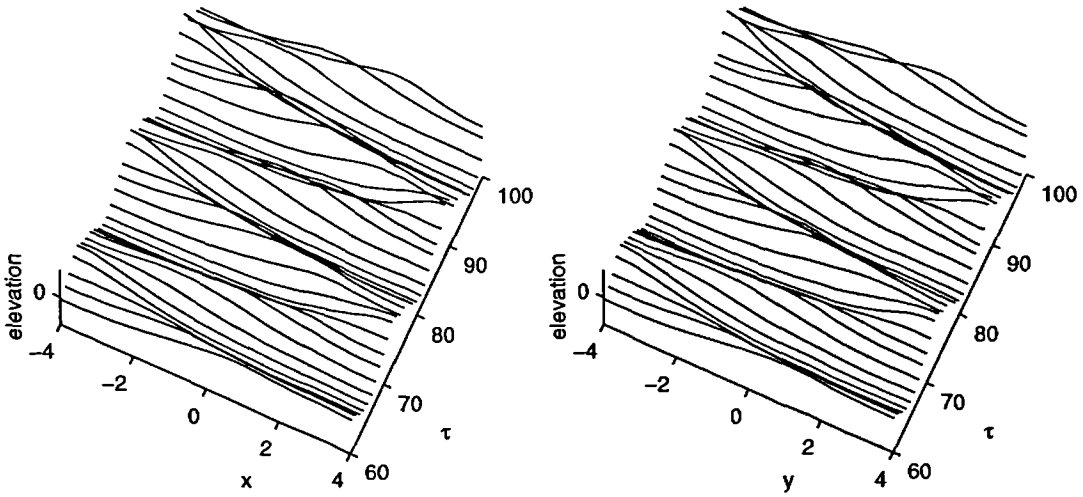

Figure 7.4.27 Wave profiles on two vertical planes (Case G)
((a): on the plane y=0; (b): on the plane x=0)

In Case H, the width is reduced by half and the ratio of length/width is therefore the same as that in Case D. The wave elevation history is shown in Figure 7.4.29. The travelling wave is also evident in this case, as shown in Figure 7.4.30. This is different from what has been observed in Case D, where the water is deeper.

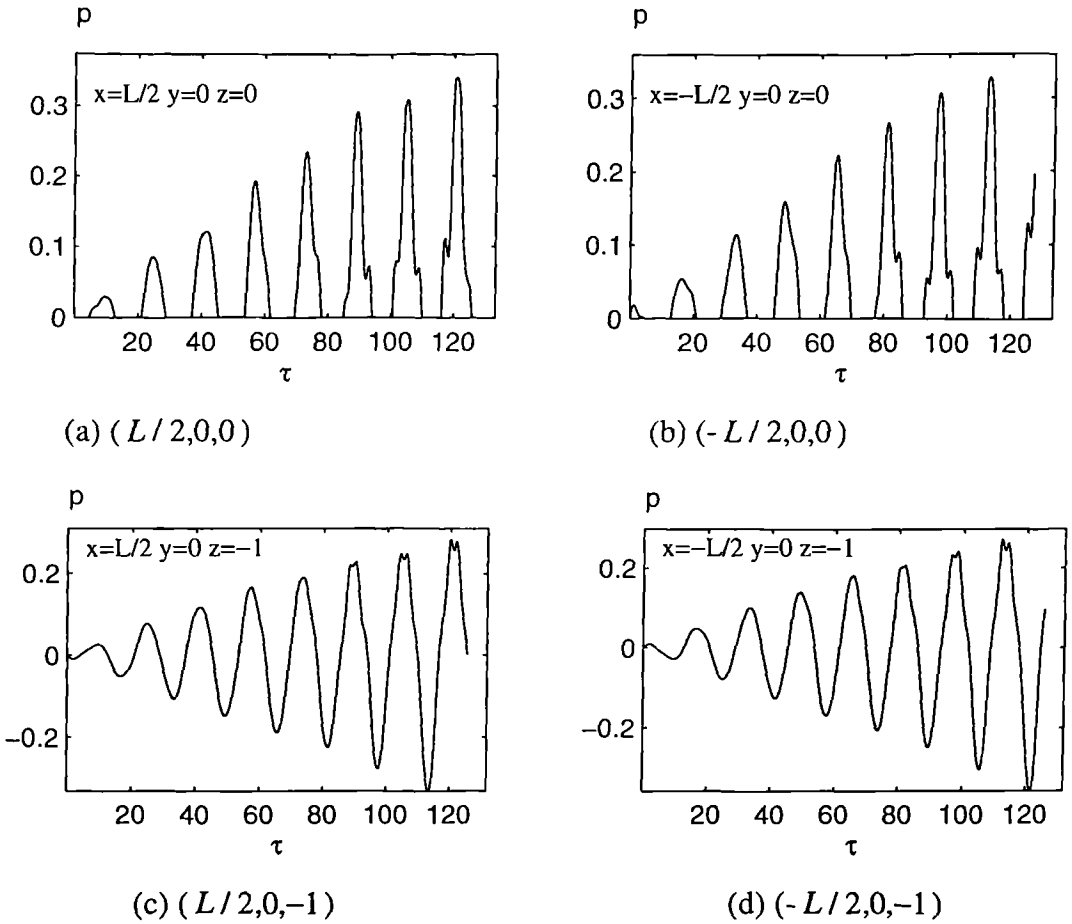

Figure 7.4.28 Pressure history (Case G)

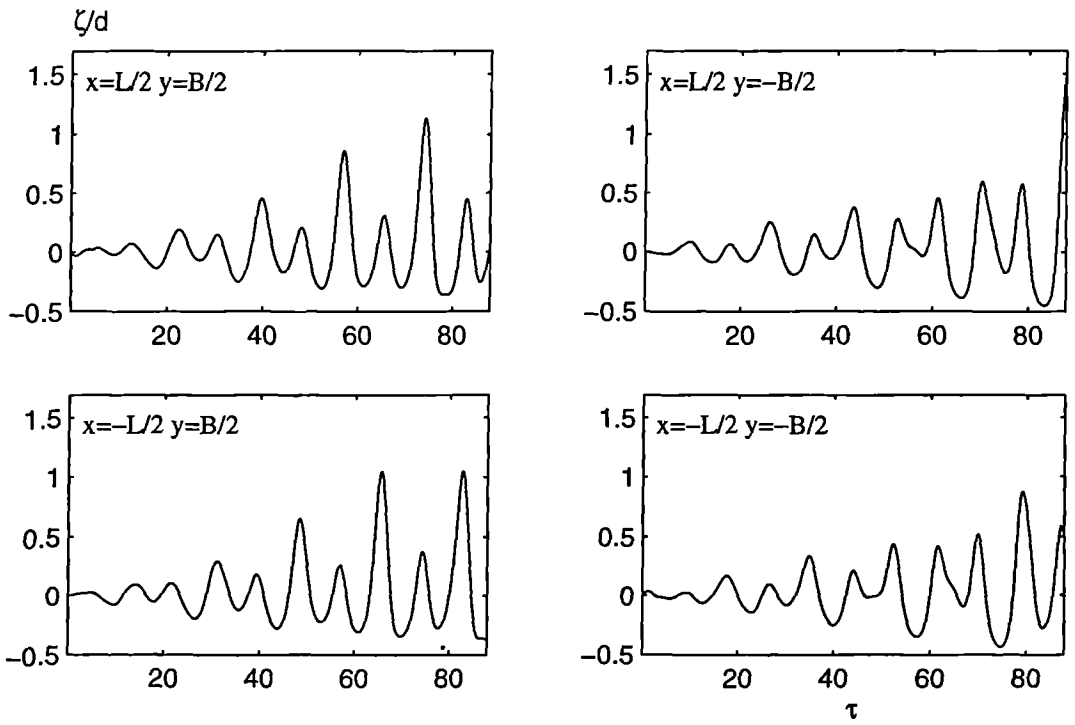

Figure 7.4.29 Elevation history at four corners (Case H)

Sloshing waves for Case S

This is an extremely shallow water case. The tank is undergoing horizontal motion only, at a frequency near to the first natural frequency. As discussed in connection with Figure 7.4.10 for the two dimensional case, a bore may be generated when the water depth is very small. Figure 7.4.31 gives snapshots of the wave profiles for this case. One can see from this figure that the three dimensional bore is travelling from the corner $(-L/2, -B/2)$ to the corner $(L/2, B/2)$.

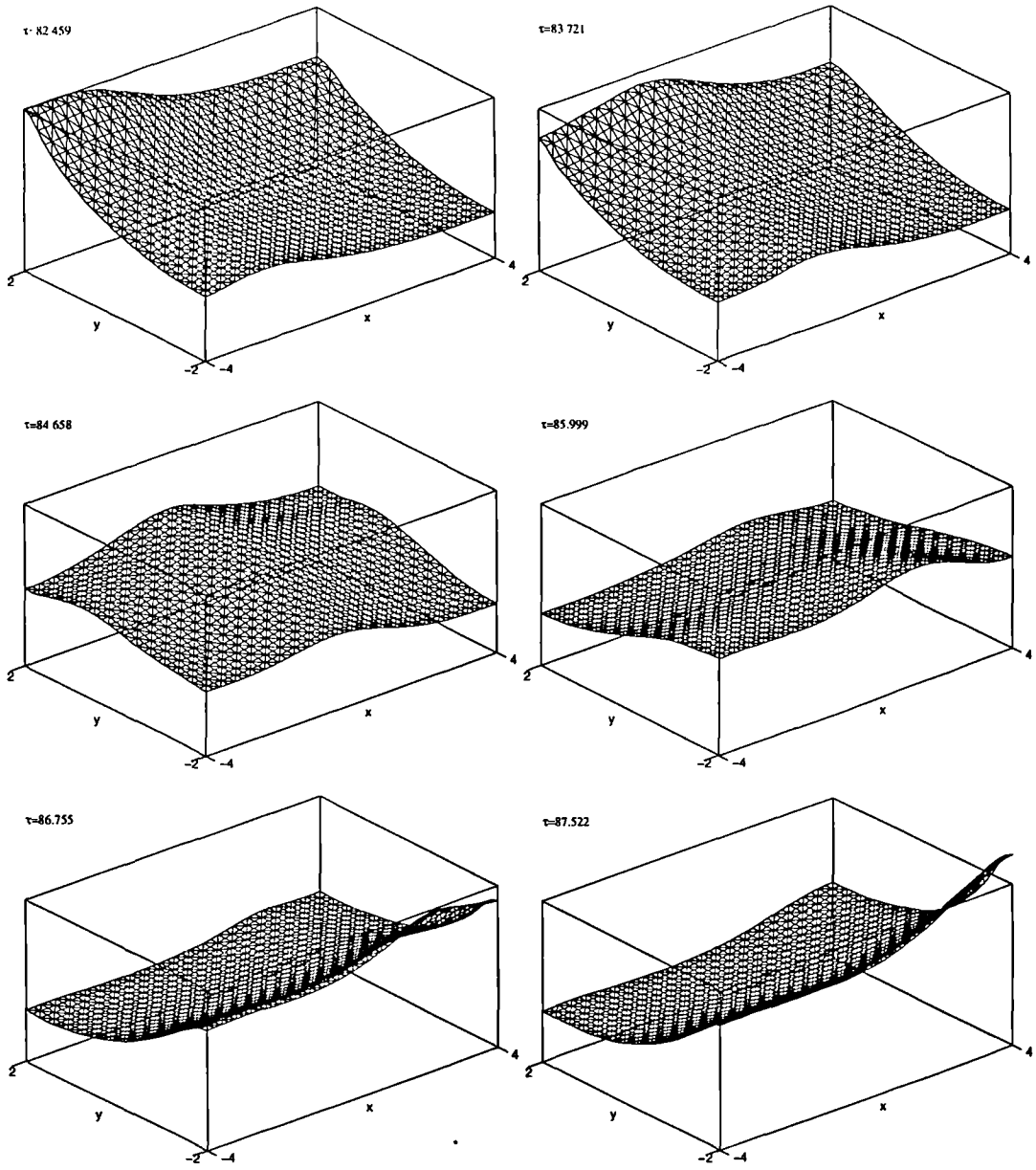

Figure 7.4.30 View of travelling waves for Case H (height of the box=2*d*)

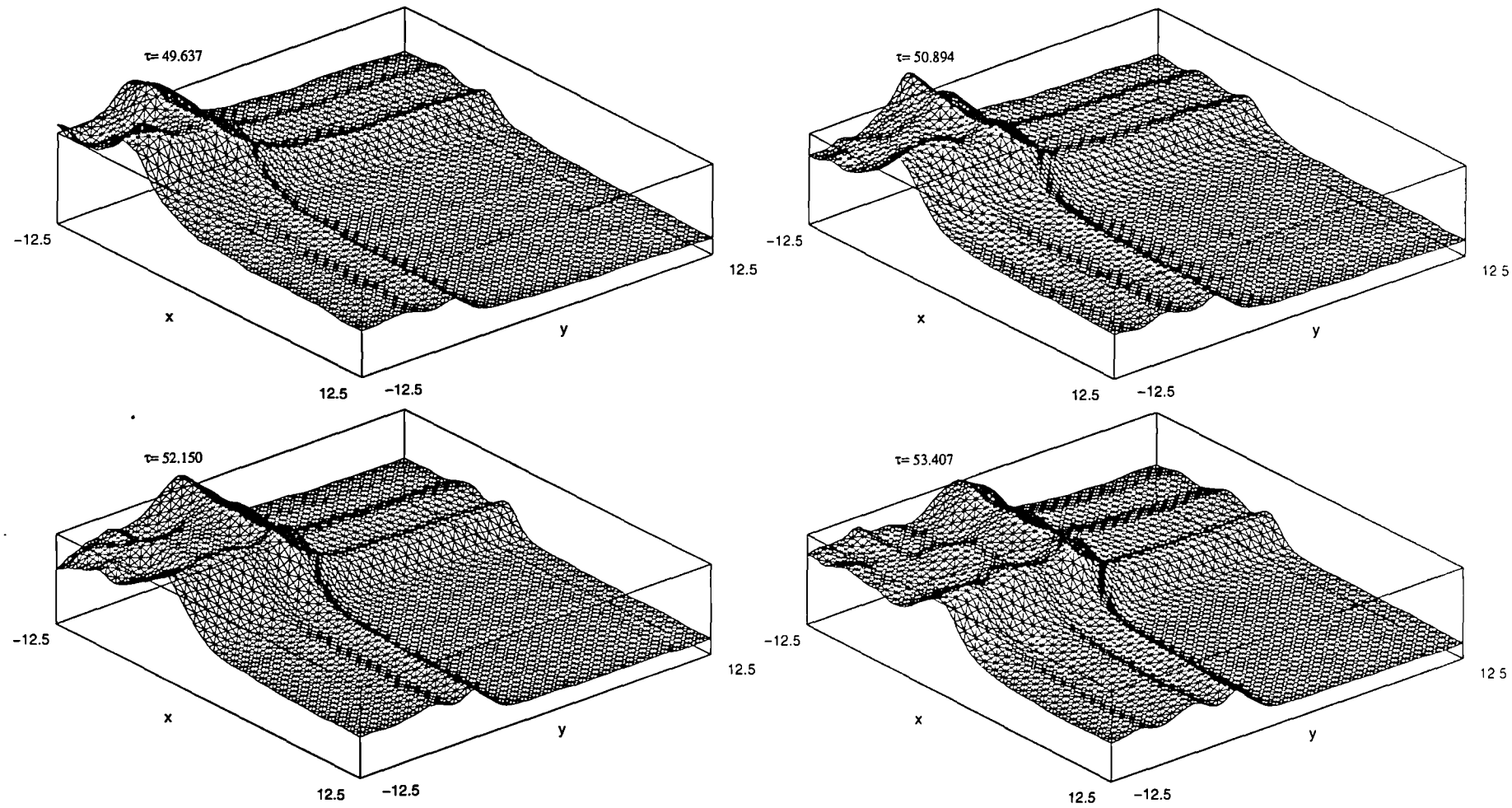

Figure 7.4.31 Surface view of sloshing wave for Case S (height of the box=2*d*)

8. WAVES IN A RECTANGULAR TANK WITH A WAVEMAKER

8.1 Introduction

The simulation of waves generated by a piston-type wavemaker in a rectangular tank is undertaken in this chapter. The wave maker is located at one end of the tank and the generated waves travel to the other end (referred as to 'the far end' herein). Up to two vertical cylinders are inserted in the tank for several cases. The wavemaker problem is important in naval architecture as well as offshore and harbour engineering, as associated model tests are often conducted in such a tank. Some real ocean environment can also be modelled if the tank is wide enough, and side wall effects are negligible.

The generation, propagation and/or scattering of the waves in the tank can be studied by a perturbation expansion in the frequency domain (e.g. Sulisz & Hudspeth, 1993) or in the time domain (e.g. Zhang & Williams, 1996) when the generated waves are small. Although the perturbation method may give good results with a relatively small amount of computation, fully nonlinear theory should be implemented when the waves are large. Over the past decade, many investigations have been devoted to the numerical simulation of the fully nonlinear waves of this kind and their interaction with structures using time step procedures. Most of them are based on a boundary element method. Some of these studies consider waves propagating in a tank, such as Lin, Newman & Yue (1984), Ohyama (1991), She, Greated & Easson (1992) and Wang, Yao & Tulin (1995). Some deal with the interaction between the wave and the bodies, for instance, Sen (1993), Cointe, *et al* (1990) and Contento & Casole (1995). All of these works are concerned with the two dimensional problems. There are also a number of publications, albeit fewer, on three dimensional cases. One of these was presented by Chan & Calisal (1993), where some preliminary results for forces on a cylinder were given. More recently, Celebi & Kim (1997) presented a 3-D simulation based on desingularised boundary element method.

The finite element method developed in this thesis will be applied to investigate the wave problems in various situations. In some cases the analytical solutions will be used for comparison.

It should be noted that when the wave height is very large, and/or the wave travels over a long distance, it may overturn and break (Wang, Yao & Tulin, 1995). In addition, a jet may develop at the wave maker when it moves sufficiently fast, as shown by Greenhow & Lin (1985). In this work, only situations in which neither breaking nor the jet takes place are considered.

The various parameters used in this chapter will be non-dimensionalised as in equation (7.4.17).

8.2 Radiation condition

In modelling the generated progressive waves, the reflection from the far end is usually undesirable. Although a technique for completely removing the reflection of fully nonlinear waves has yet to be developed, researchers have attempted to reduce the reflection as much as possible by imposing an artificial radiation condition on the boundary at the far end. Some principles and techniques used to deal with the radiation condition have been discussed in Chapter 2. In our application, the combination of the damping zone and the Sommerfeld condition will be employed.

The implementation of this condition is illustrated in Figure 8.2.1 with the definitions of some dimensions. Also shown in this figure is a right-hand Cartesian coordinate system: the *oxy* plane being on the mean free surface with the x-axis pointing to the far end; the z-axis pointing upwards; and the origin being at the centre of the mean free surface.

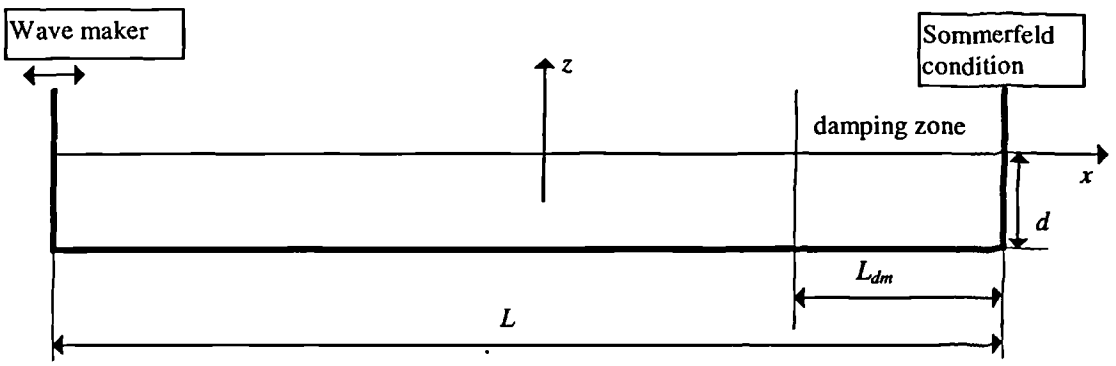

Figure 8.2.1 Tank with the wave maker and the radiation condition (d=1)

The Sommerfeld condition gives

$$\frac{\partial \phi}{\partial t} + c\frac{\partial \phi}{\partial n} = 0 . \qquad (8.2.1)$$

The difficulty in implementing this condition is to evaluate the parameter c. This parameter is the phase velocity of the wave in linear harmonic waves, but its physical meaning cannot exactly be identified when the condition is applied to fully nonlinear waves. In some reported applications, the parameter is simply estimated by the numerical values of $\frac{\partial \phi}{\partial t}$ and $\frac{\partial \phi}{\partial n}$ at each time step from the solutions at previous steps, see, e.g., Orlanski(1976), Zhou & Gu (1990) and Contento & Casole(1995). However, large errors with this approach are not easy to avoid, particularly when the crest or trough of the velocity potential passes the far end boundary. Although this difficulty can be overcome by some approaches, such as using an average value of c found at a number of points near the boundary, as suggested by Contento and Casole (1995), the resulting value can often oscillate rapidly with time. The rapid oscillation may increase the possibility of numerical instability. An alternative to numerical evaluation of c is to take the parameter as a constant, particularly when combining the Sommerfeld condition with other techniques. Ohyama (1991) used $c = 1$ (the phase velocity of a long wave relative to the water depth) when the sponge layer was coupled with the Sommerfeld condition. Arai, Paul, Cheng & Inoue (1993) took c as the phase velocity of the harmonic wave calculated by linear theory when they combined the Sommerfeld condition with a velocity reduction technique. Although these constant values are not consistent with the property of the fully nonlinear wave, they are easier to use, and the above two papers have demonstrated in the combined techniques of the radiation condition that the constant value of the parameter c may lead to good results even when irregular waves comprising components of different phase velocities are simulated.

In our work, this parameter c is chosen in the same way as done by Arai, Paul, Cheng & Inoue (1993), that is:

$$c = \sqrt{\frac{\tanh(k)}{k}}, \qquad (8.2.2)$$

where k is the real root of $\omega^2 = k\tanh(k)$. This choice is partly based on the results of Ohyama (1991) for irregular waves, and also based on the consideration that the irregular wave associated with marine engineering often has a narrow band spectrum. This implies that the wave system is dominated by the components near a particular frequency.

It should be noted that even when the wave is linear and harmonic, equation (8.2.2) is valid only after the generated waves become periodic in the tank. However, before reaching the periodic stage, there is a transient zone between the wave front and the far end boundary. In this zone, the wave is very long, and thus the phase velocity of the wave is different from that in equation (8.2.2) and is close to $c = 1$. Lee and Leonard (1987) have suggested an interpolation between $c = 1$ and $c = \sqrt{\frac{\tanh(k)}{k}}$ for the transient stage. Nevertheless, it is considered to be not necessary to perform the interpolation in our work. The reason is that the wave amplitude in this transient zone is relatively small, which can be further reduced by the damping zone. Therefore the small error in c may not affect the computational results significantly.

The boundary at the far end can be either fixed or non-fixed. If the boundary is fixed, extra effort has to be given to dealing with the situation where the water particles on the boundary move inwards, and thus the boundary becomes detached from the water. In the non-fixed case, the boundary is considered to move with the water particles. However, the boundary in this case may be seriously distorted if each spatial point follows the corresponding water particle. This distortion can lead to numerical difficulties. One way to avoid this is to take the velocity of the boundary motion, U_{rc}, as the average of the x-component of the velocity of water particles on the intersection line between the free surface and the boundary, and the boundary surface is assumed to be a vertical plane at all time.

For the numerical implementation of equation (8.2.1), the time derivative of the velocity potential on the boundary at the far end is expressed as:

$$\frac{d\phi_{rc}}{d\tau} = \frac{\partial\phi_{rc}}{\partial\tau} + U_{rc}\frac{\partial\phi_{rc}}{\partial x} + v\frac{\partial\phi_{rc}}{\partial y} + w\frac{\partial\phi_{rc}}{\partial z} = \frac{\partial\phi_{rc}}{\partial\tau} + U_{rc}u + v^2 + w^2,$$

where u, v and w are the velocities of fluid particles in the x-, y- and z-direction respectively. Inserting equation (8.2.1) into the above equation yields:

$$\frac{d\phi_{rc}}{d\tau} = (U_{rc} - c)u + v^2 + w^2. \qquad (8.2.3)$$

In order to be consistent with the assumption of U_{rc} which is constant in the y-direction, u and w on the boundary can be replaced by their averages at points in the same level of water depth, $\overline{u}$ and $\overline{w}$, and v can be assumed to be zero. The value of the velocity potential on the boundary is, therefore, estimated by:

$$\begin{cases} \phi_{rc} = 0 & \tau < \tau_1 \\ \phi_{rc}\big|_{\tau+\Delta\tau} = \phi_{rc}\big|_{\tau} + \dfrac{d\phi_{rc}}{d\tau}\Delta\tau & \tau > \tau_1 \end{cases} \qquad (8.2.4)$$

where $\tau_1 = L/(1+\beta)$, and β is a coefficient which can be taken as 0.2 according to numerical tests.

It should be noted that there is inconsistency at the intersection line between the free surface and the vertical boundary at the far end. The nonlinear boundary conditions are used on the free surface, but the Sommerfeld condition applied on the vertical surface is linear. The velocity potential is not identical when the points on the intersection line are approached from the two surfaces. This may lead to artificially large velocities and numerical instability. To suppress the problem, a localised interpolation is introduced on the vertical surface in the range $z_s \le z \le z_f$, where z_f is the vertical coordinate of the intersection line and $z = z_s$ is a line below the free surface. In this range, the velocity potential in equation (8.2.4) is replaced by:

$$\begin{aligned} \phi_{rc} = {} & \phi_s\left(1+2\frac{z-z_s}{z_f-z_s}\right)\left(\frac{z-z_f}{z_f-z_s}\right)^2 + \phi_f\left(1-2\frac{z-z_f}{z_f-z_s}\right)\left(\frac{z-z_s}{z_f-z_s}\right)^2 \\ & + w_s(z-z_s)\left(\frac{z-z_f}{z_f-z_s}\right)^2 + w_f(z-z_f)\left(\frac{z-z_s}{z_f-z_s}\right)^2, \end{aligned} \qquad (8.2.5)$$

where (ϕ_f, ϕ_s) and (w_f, w_s) are the potentials and vertical velocities at $z = z_f$ and $z = z_s$, respectively. It is easy to show that the velocity potential in the expression satisfies:

$$\phi_{rc} = \phi_f \qquad \frac{\partial \phi_{rc}}{\partial z} = w_f \qquad \text{for } z = z_f,$$

and

$$\phi_{rc} = \phi_s \qquad \frac{\partial \phi_{rc}}{\partial z} = w_s \qquad \text{for } z = z_s.$$

The length of $(z_f - z_s)$ is found to be suitable if it covers three element lengths in the z-direction regardless of the size of elements.

The damping zone is implemented by adding an artificial viscous term in the free surface conditions near the boundary at the far end. The added term plays a role in removing the energy from water, thereby possibly reducing the reflection. This method has been widely used, as reviewed in Chapter 2.

Both the dynamic and kinematic conditions on the free surface can be modified by adding the viscous term. Numerical tests in our work have shown that the modification to the kinematic condition sometimes causes sawtooth-like waves in the damping zone. Therefore, the modification is adopted only to the dynamic condition below.

After the viscous term is added, the dynamic free surface condition can be written as:

$$\frac{D\phi}{Dt} = N.T - \nu(x)|\phi|\text{sign}(\phi_n), \qquad (8.2.6)$$

where $N.T$ denotes the normal term, $\nu(x) \geq 0$ is a damping coefficient, $\text{sign}(\phi_n)$ is a function of ϕ_n defined by:

$$\text{sign}(\phi_n) = \begin{cases} -1 & \phi_n < 0 \\ 0 & \phi_n = 0 \\ 1 & \phi_n > 0, \end{cases}$$

and ϕ_n denotes the normal velocity on the free surface with $\boldsymbol{n}$ being out of fluid. If the wave is not overturning, ϕ_n has the same sign as the vertical velocity, and hence $\text{sign}(\phi_n)$ can be replaced by $\text{sign}(w)$ in the calculation. The added term in equation (8.2.6) ensures that the damping zone always absorbs energy from the fluid, as suggested by Cao, Beck and Schultz (1993).

The term $\nu(x)$ in equation (8.2.6) is artificially chosen. Its magnitude and form play an important role in the performance of the damping zone. If the value is too small, the absorption is too weak, while if it is too big the zone itself acts like a rigid surface. Large reflection occurs in both cases, although for different reasons. In addition, $\nu(x)$ has to be smooth enough in the zone and at both its ends, otherwise the discontinuity of $\frac{d\nu}{dx}$ and $\frac{d^2\nu}{dx^2}$ may lead to large gradients or even discontinuity of velocities. This not only gives rise to reflection but also may cause the numerical instability. In this work, the following form of $\nu(x)$ is adopted:

$$\nu(x)=\begin{cases}\frac{1}{2}\nu_0\left(1-\cos\left(\frac{\pi(x-x_d)}{L_{dm}}\right)\right) & x\geq x_d \\ 0 & x<x_d,\end{cases}$$

where ν_0 is the magnitude of the damping coefficient, x_d is the x-coordinate of the left end of the zone and L_{dm} is the length of the zone. Apart from the damping coefficient, the efficiency of the damping zone is also dependent on the length L_{dm}. In this thesis, the length is taken as $L_{dm}=\min(3\lambda,3)$, where $\lambda=2\pi/k$. Thus ν_0 is the only parameter to be chosen.

8.3 Monochromatic waves

The monochromatic wave means the wave generated by the wave maker undergoing the following motion:

$$S(\tau) = -a\cos(\omega\tau), \tag{8.3.1}$$

with the velocity:

$$U = a\omega\sin(\omega\tau), \tag{8.3.2}$$

where $S(\tau)$ is the displacement of the wave-maker; a is its amplitude, ω is its frequency and τ denotes time.

8.3.1 Optimisation of parameter ν_0

As mentioned above, there is only one parameter ν_0 to be chosen when the radiation condition is applied. This parameter will be optimised using numerical tests here. Before doing this, an absorption coefficient describing the efficiency of the radiation condition is defined. That is:

$$C_a = 1 - {\Delta A_r}/{A_0}, \tag{8.3.3}$$

where C_a is the absorption coefficient; A_0 is the amplitude of the wave without reflection and ΔA_r is the amplitude of the reflected wave. If there is no reflection, i.e. $\Delta A_r = 0$, then $C_a = 1$; on the other hand if the wave is completely reflected, $C_a = 0$.

Neither A_0 nor ΔA_r is available prior to the simulation; both are determined numerically. ΔA_r is estimated by $\Delta A_r = |A_0 - A_r|$, where A_r is the amplitude of the wave including the reflection. A_r is measured from the envelope of the wave history recorded at point $x = \frac{L}{2} - (L_{dm} + 0.2\lambda)$ which is situated just before the left edge of the damping zone. A_0 is approximated by the amplitude of the waves in a longer tank, recorded at the same point as that for A_r.

In order to find the optimum value of ν_0, a series of cases are tested with ω being in the range from 0.5 to 3.0, which covers the frequency of practical interest, as

suggested by Clement (1996). For each frequency, ν_0 changes from zero to a value which leads to a rapid decrease in C_a. In the shorter tank, the initial distance between the wave maker and the left edge of the damping zone is set at about 4λ; and the distance in the longer tank is about three times as long in the shorter tank. The calculation is made over about 14 periods. The corresponding amplitudes of the wave maker are specified in such a way that the resulting waves have steepness $\varepsilon = H/\lambda \approx 0.005$ according to the numerical tests.

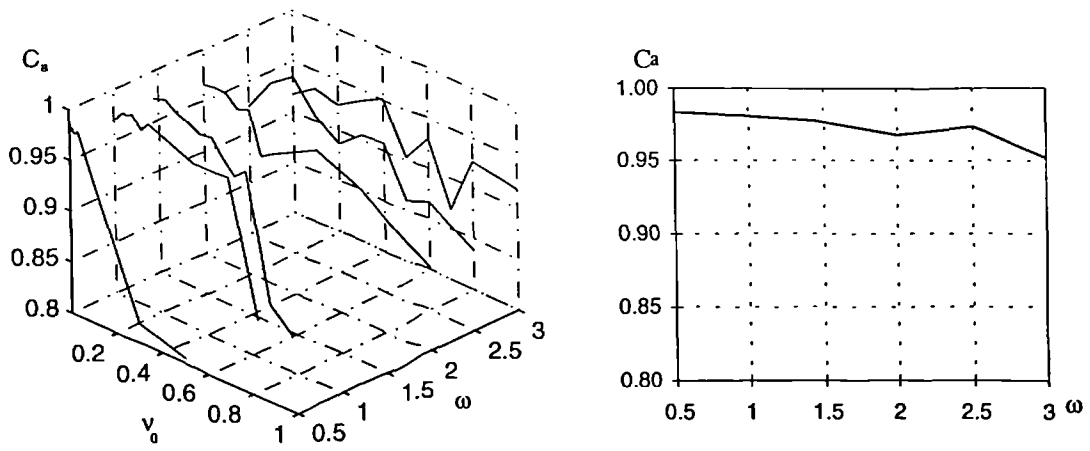

(a) C_a via ω and ν_0 (b)Maximum C_a via ω

Figure 8.3.1 Absorption coefficient for different ω and ν_0

Figure 8.3.1a shows the absorption coefficient against frequency ω and parameter ν_0. For each frequency, one can find a maximum absorption coefficient from this figure, as shown in Figure 8.3.1b. The values of ν_0 corresponding to each of the maximum absorption coefficients are then determined for every frequency. These values against the frequency are plotted as stars in Figure 8.3.2. The discrete numerical values can be fitted into a third order polynomial:

$$\nu_0 = 0.0496\omega^3 - 0.1751\omega^2 + 0.2352\omega - 0.0689, \qquad (8.3.4)$$

which is illustrated as the solid line in Figure 8.3.2. This expression provides a convenient way to implement the damping zone and allows us to set up the radiation

condition in the computer program by choosing parameter v_0 automatically once the frequency is specified.

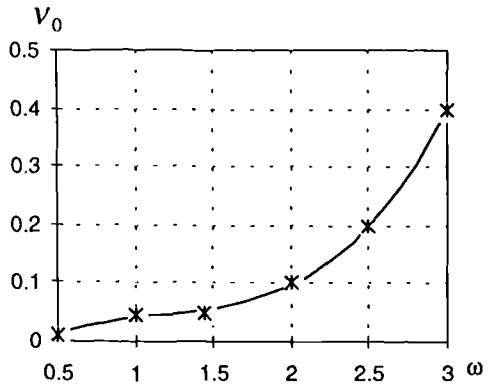

Figure 8.3.2 Optimum v_0 against ω

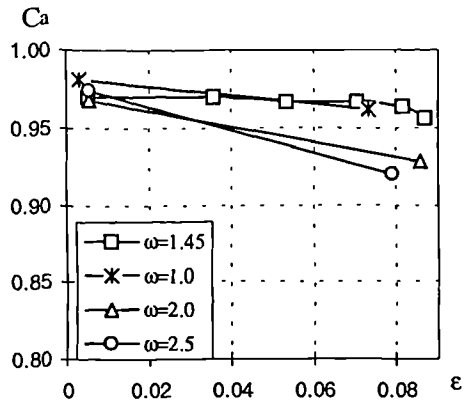

Figure 8.3.3 Absorption coefficient against wave steepness
(v_0 evaluated by equation 8.3.4)

As shown in Figure 8.3.1b, the absorption coefficient can be very close to unity if parameter v_0 is determined by equation (8.3.4). However, that equation is obtained by numerical tests on waves with small steepness. In order to check if it is suitable to waves of larger steepness, the cases with various values of ε are also simulated. For each of these cases, the frequency is kept constant. Figure 8.3.3 plots the obtained absorption coefficients. It can be seen that the absorbing efficiency is still very good even when the wave steepness becomes quite large, although the efficiency decreases slightly with the increase of the steepness.

8.3.2 Monochromatic waves

With the implementation of the above radiation condition and the optimum value of the parameter ν_0, some details about the waves generated by the wave maker moving in a manner defined by equation (8.3.1) are presented in this section. The efficiency of the radiation condition will be alternately demonstrated by the wave history and by profiles.

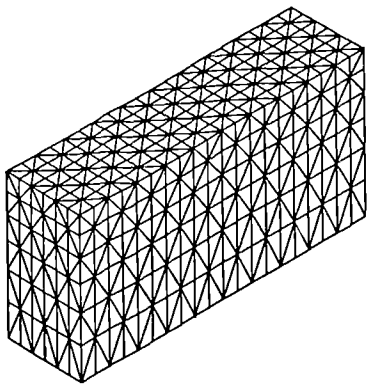

Figure 8.3.4 Typical mesh of the wave-maker tank

Convergence study

Before discussing the details, an investigation on the convergence property in a similar manner to that used in section 7.3.3 is first presented. The cases for this purpose, with different mesh sizes and time steps, are listed in Table 8.3.1. In each case, the frequency and the amplitude of the wavemaker motion are $\omega = 1.45$ and $a = 0.064$, respectively. The steepness of the resulting wave is approximately $\varepsilon \approx 0.07$. The dimensions of the tank are specified as $L = 14.64$ and $B = 0.2$. The tank length is approximately 5λ and the wave period is $T \approx 4.3$. Convergence is examined by comparing the wave history for these cases, which is recorded at point $x \approx 3.74$. The mesh is generated with different divisions along the length and depth, but the divisions along the width are fixed because the resulting wave is now two dimensional. An illustration of a typical mesh is given in Figure 8.3.4.

Table 8.3.1 Parameters for convergence study

case	M_1	M_2	N	$\Delta\tau$
c1	146	4	12	0.021666
c2	292	4	20	0.021666
c3	195	4	12	0.021666
c4	195	4	16	0.021666
c5	195	4	16	0.010833

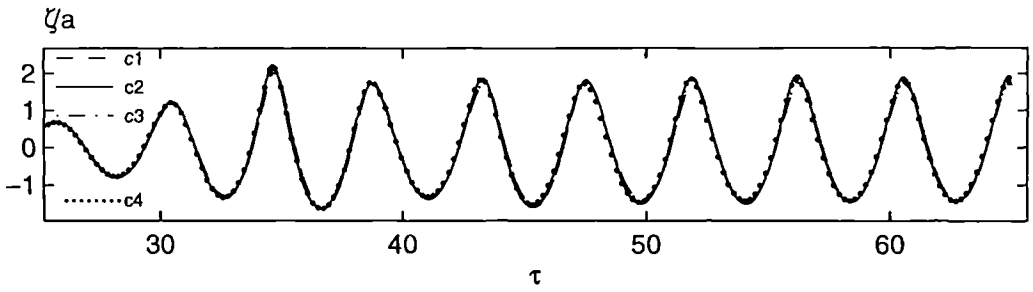

Figure 8.3.5 Time history of the wave elevation for different mesh sizes

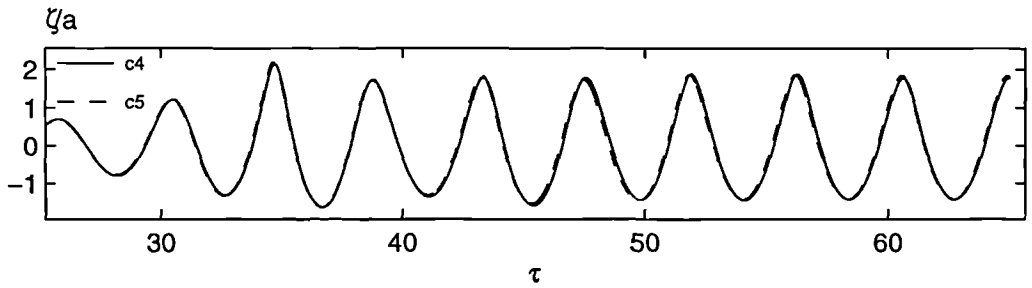

Figure 8.3.6 Time history of the wave elevation for different time steps

Figure 8.3.5 gives the time history of the wave elevation at the point specified above for cases c1-c4, where the mesh varies but the time step is fixed. Figure 8.3.6 presents the time history of the wave elevation for cases c4 and c5, where the mesh is the same but the time steps are different. It can be seen that the results obtained using

different meshes and time steps are hardly visible. This suggests that about 40 divisions in each wave length and 200 time steps in each period may be required to obtain convergent results. As already mentioned in the case of sloshing waves, this requirement may be dependent on the time period over which the calculation is made and on other factors such as the wave amplitude. The results given in this chapter are obtained in a similar way to those for the sloshing waves, that is element sizes and time steps are chosen in such a way that the same degree of accuracy can be achieved.

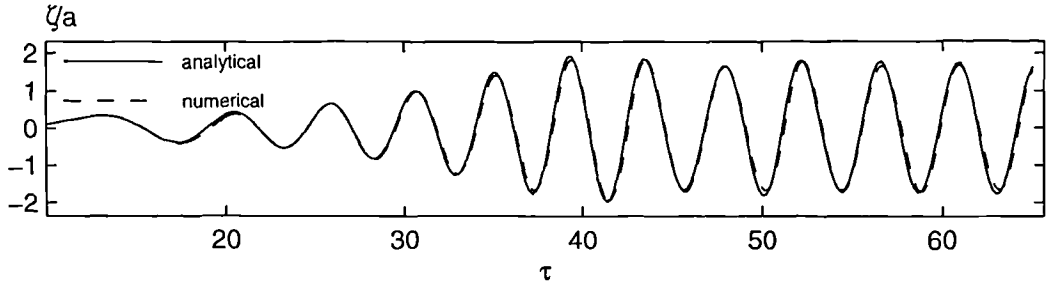

Figure 8.3.7 Comparison of the wave history with the analytical solution at $x \approx 3.74$ for the case with $\omega = 1.45$ and $a = 0.0041$

Comparison with the analytical solution

For the wave with very small steepness, a linearised analytical solution may be found (see Eatock Taylor, Wang and Wu, 1994). This solution can be used as a check on the numerical method. To do so, the numerical and analytical results for the time history of wave elevation at $x \approx 3.74$ are shown in Figure 8.3.7 for the case with the same frequency as in Figure 8.3.5 but a smaller amplitude ($a = 0.0041$). In Figure 8.3.8, the profiles at two instants are plotted for the same case. The numerical analysis is carried out using the same mesh and time step as those in c4 above. The figures show that the numerical results are in very good agreement with the corresponding analytical solutions, although the difference in the profiles is slightly greater within the damping zone, as is expected. The cases with other frequencies and amplitudes used as the damping zone investigation in section 8.3.1 have also been compared with the analytical solution. The results for all of them are in a similar agreement with the analytical solution to that seen in these two figures.

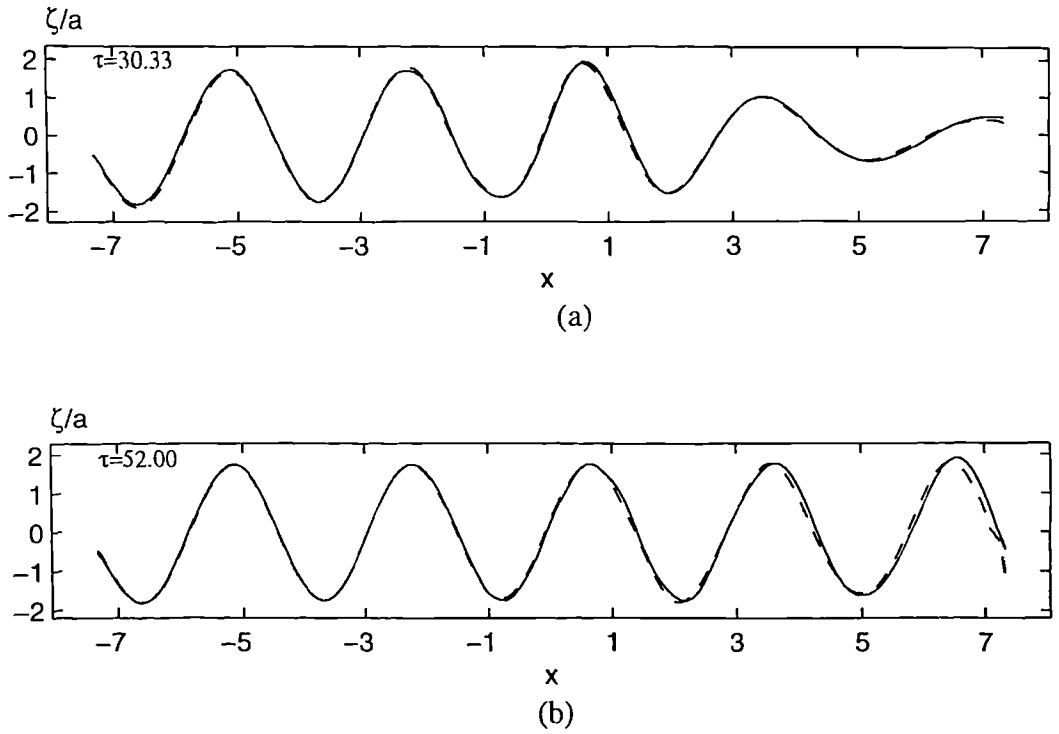

Figure 8.3.8 Comparison of the wave profiles with the analytical solution for the case with $\omega = 1.45$ and $a = 0.0041$. The damping zone begins at $x_d = 4.32$.
(solid line: analytical solution; dashed line: numerical results)

Repeatability

Harmonic waves are often required to estimate the wave loading on structures. For this kind of wave, the wave profile should repeat itself (approximately in practice) from one period to next. The repeatability strongly depends on the property of the radiation condition at the far end. If there are large reflections from this end, the wave profiles will apparently differ in successive periods, even when the wave maker oscillates harmonically with a constant amplitude over a long time. Due to this connection between reflection and repeatability, She, Greated & Easson (1992) and Arai, Paul, Cheng & Inoue (1993) used repeatability to demonstrate the effectiveness of the radiation condition applied in their numerical simulation.

For the purpose of demonstrating the repeatability here, the profiles for three cases are presented in Figures 8.3.9 to Figure 8.3.11. They are recorded from $\tau = 11T$ to $\tau = 15T$, two profiles in each period (corresponding to $\tau = 11T, 11.5T, 12T, 12.5T, \cdots$). Figure 8.3.9 is for the case with $\omega = 1.45$ and $a = 0.0041$. The wave steepness in this case is about $\varepsilon \approx 0.005$, and the shape reflects a typical linear wave. In Figure 8.3.10,

the case with $\omega = 1.45$ and $a = 0.082$ ($\varepsilon \approx 0.087$) is illustrated while Figure 8.3.11 is for $\omega = 2.00$ and $a = 0.043$ ($\varepsilon \approx 0.085$). These two cases show some typical features of steep waves.

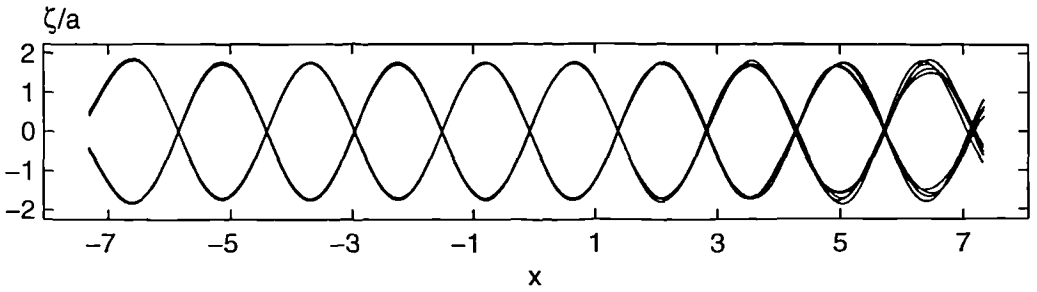

Figure 8.3.9 Profiles from $\tau = 11T$ to $\tau = 15T$, two in each period
($\omega = 1.45$, $a = 0.0041$, $\varepsilon \approx 0.005$, $L = 14.64$, $B = 0.14$;
damping zone beginning at $x_d = 4.32$)

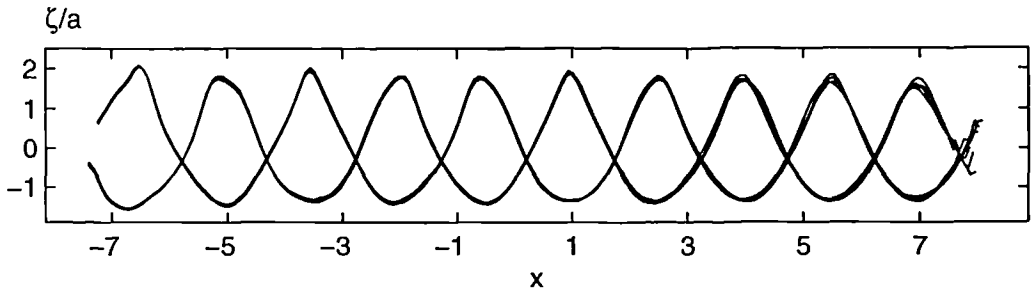

Figure 8.3.10 Profiles from $\tau = 11T$ to $\tau = 15T$, two in each period
($\omega = 1.45$, $a = 0.082$, $\varepsilon \approx 0.087$, $L = 14.64$, $B = 0.14$;
damping zone beginning at $x_d = 4.32$)

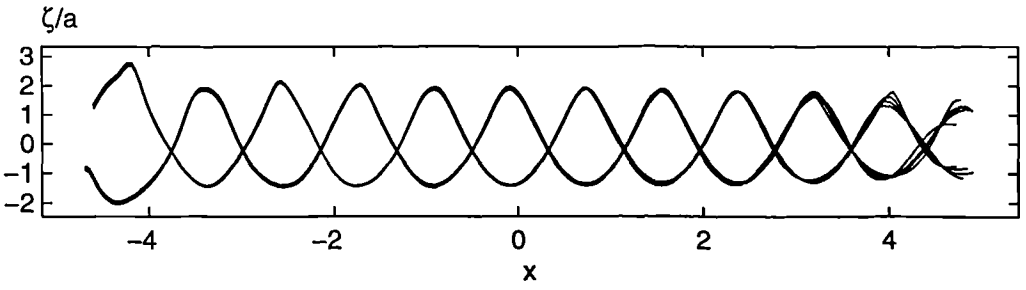

Figure 8.3.11 Profiles from $\tau = 11T$ to $\tau = 15T$, two in each period
($\omega = 2.0$, $a = 0.043$, $\varepsilon \approx 0.085$, $L = 9.28$, $B = 0.08$;
damping zone beginning at $x_d = 1.64$)

It can be seen that the profiles have very good repeatability in both the small steepness cases and the large steepness cases. Similar repeatability can also be observed for waves with other frequencies in our calculations. All of these results confirm that the radiation condition imposed at the far end works well. To further demonstrate this by profiles, the comparison of results in the shorter and longer tanks at $\tau = 15T$ for the above three cases are presented in Figure 8.3.12. Again they are in good agreement in all of cases, except in the damping zone.

As discussed in Section 8.3.1, the absorption coefficient tends to decrease with increasing wave steepness. However, the good repeatability and agreement between the shorter and longer tank results illustrate that the resulting reflection is still not noticeable even when the steepness is quite large.

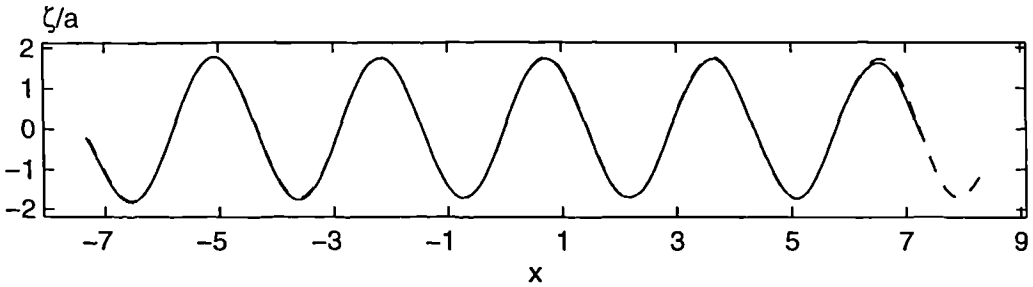

Figure 8.3.12 (a) $\omega = 1.45, a = 0.0041$, $\varepsilon \approx 0.005$, $L = 14.64, 44.64$ damping zone of shorter tank beginning at $x_d = 4.32$

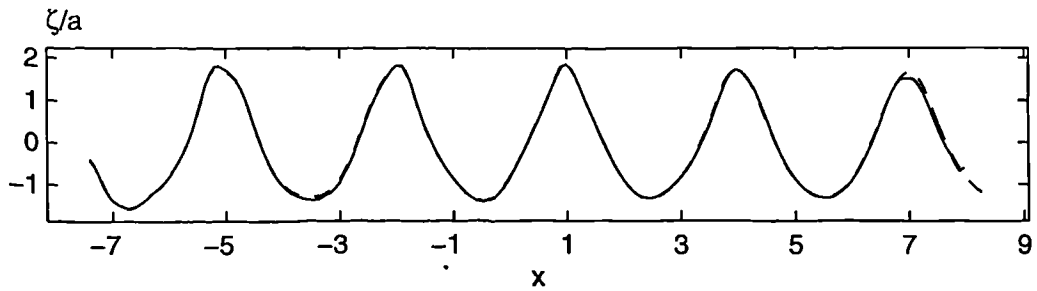

Figure 8.3.12 (b) $\omega = 1.45, a = 0.082$, $\varepsilon \approx 0.087$, $L = 14.64, 44.64$; damping zone of shorter tank beginning at $x_d = 4.32$

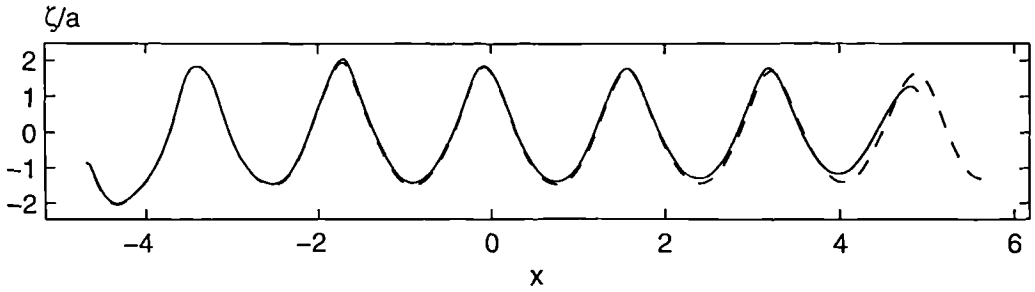

(c) $\omega = 2.0, a = 0.043, \varepsilon \approx 0.085, L = 9.28, 25.28$
damping zone of shorter tank beginning at $x_d = 1.64$

Figure 8.3.12 Wave profiles at $\tau = 15T$ for different length of tank
(solid line: shorter tank; dashed line: longer tank)

Non-linear effects

With increasing the amplitude of the wavemaker, the resulting wave becomes steeper and the nonlinear effects may become more important. From Figure 8.3.9 and Figure 8.3.10, one can find that the wave profiles in two figures are different. The wave in the latter case has flatter troughs and sharper crests. Obviously, this is due to nonlinearity. The nonlinear effects can also be shown by comparing the waves corresponding to the different amplitudes in one figure. For this purpose, Figure 8.3.13 and Figure 8.3.14 are plotted. In Figure 8.3.13, the wave history of different amplitudes recorded at a point before the damping zone is presented for three different frequencies. The corresponding wave profiles at some instants are illustrated in Figure 8.3.14. In addition to the nonlinear behaviour mentioned above, it can also be observed from these figures that the wave with larger steepness travels faster and has longer wavelength than those with a smaller steepness. This phenomenon of the transient wave is similar to the so-called amplitude dispersion of Stock's wave as discussed, for example, by Newman (1977).

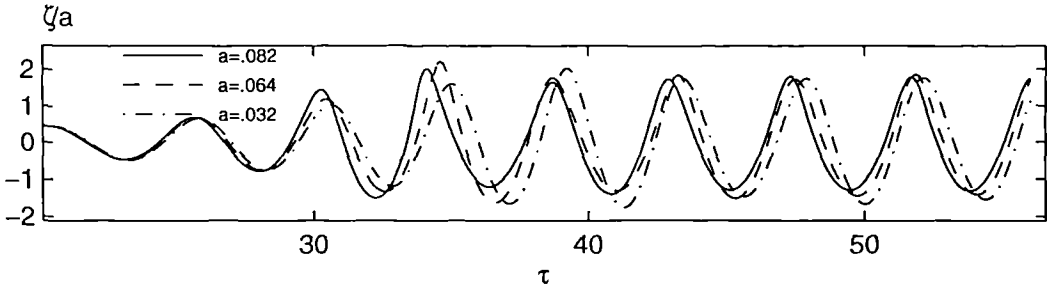

(a) $L = 14.46$; $\omega = 1.45$; recorded at $x \approx 3.74$

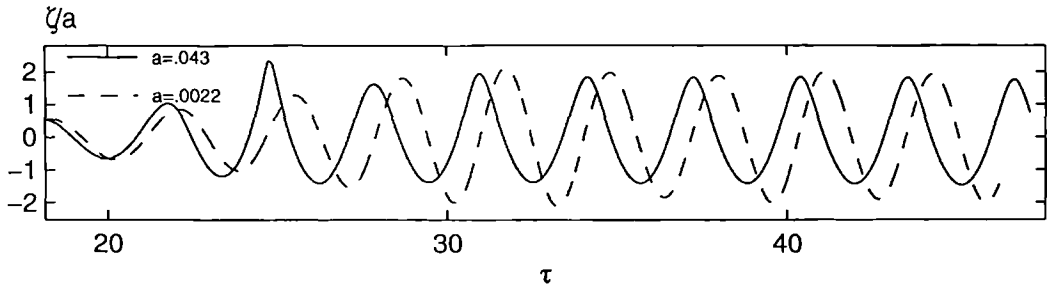

(b) $L = 9.28$; $\omega = 2.0$; recorded at $x = 1.33$

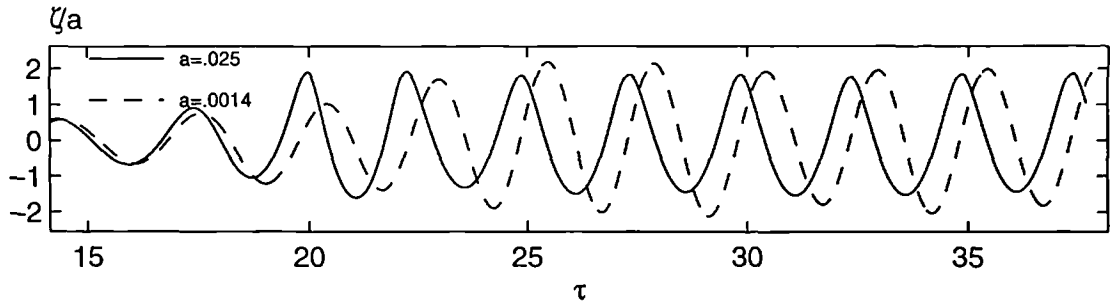

(c) $L = 7.0$; $\omega = 2.5$; recorded at $x = 0.3$

Figure 8.3.13 Wave history for different amplitudes

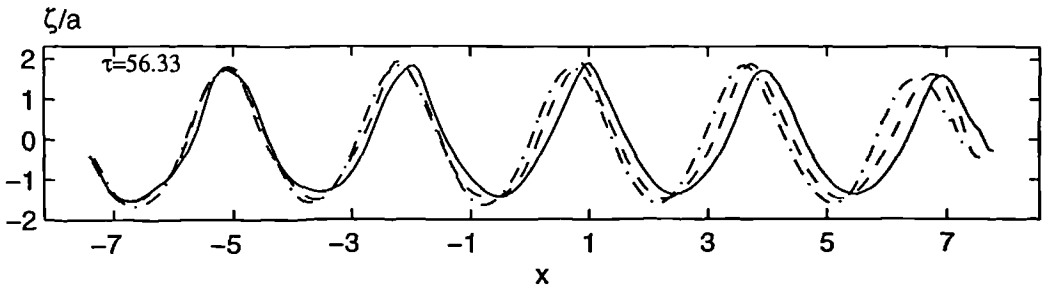

Figure 8.3.14 (a) $\omega = 1.45$; $a = 0.032, 0.064, 0.082$, respectively. Damping zone begins at $x_d = 4.32$ (solid line: $a = 0.082$; dashed line: $a = 0.064$; Dotted line: $a = 0.032$)

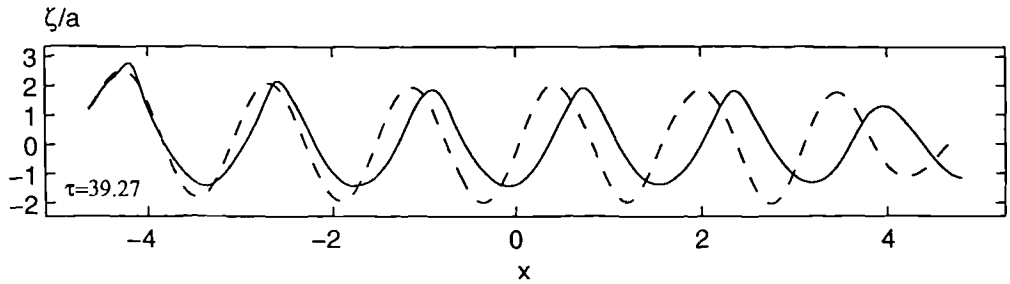

Figure 8.3.14 (b) $\omega = 2.0$; $a = 0.0022, 0.043$, respectively. Damping zone begins at $x_d = 1.64$ (solid line: $a = 0.043$; dashed line: $a = 0.0022$)

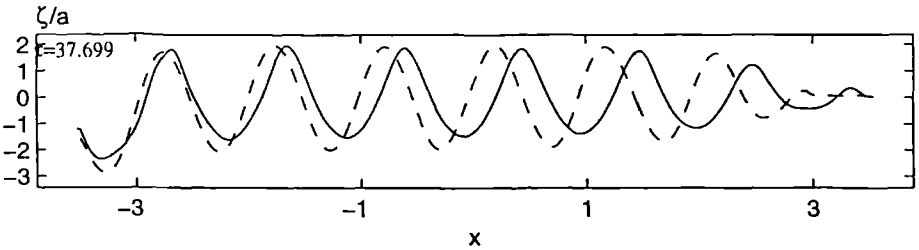

Figure 8.3.14 (c) $\omega = 2.5$; $a = 0.0014, 0.025$, respectively. Damping zone begins at $x_d = 0.5$ (solid line: $a = 0.025$; dashed line: $a = 0.0014$)

Figure 8.3.14 Wave profiles for different amplitudes

8.4 Bichromatic wave and irregular wave

As shown above, the monochromatic wave can be successfully simulated with the application of the radiation condition. It should be mentioned again that this radiation condition is composed of the damping zone and the Sommerfeld condition; the optimum parameter ν_0 associated with the damping zone and the parameter c in the Sommerfeld condition depend on the wave frequency, as discussed in 8.3.1. In order to apply the same technique to simulate the bichromatic wave and irregular wave, the first task is obviously to find the proper frequency which determines the damping coefficient and the value of c. A suggestion about this will be made in the following two sections for the bichromatic and irregular waves, respectively.

8.4.1 Bichromatic wave

The motion of the wave maker in this case consists of two components and can be defined by:

$$S(\tau) = -a_1 \cos(\omega_1 \tau) - a_2 \cos(\omega_2 \tau), \qquad (8.4.1)$$

where $S(\tau)$ is the displacement of the wave maker as before; a_1 and a_2 are the amplitudes corresponding to the components of frequency ω_1 and ω_2, respectively. The corresponding velocity is then written as:

$$U(\tau) = a_1 \omega_1 \sin(\omega_1 \tau) + a_2 \omega_2 \sin(\omega_2 \tau). \qquad (8.4.2)$$

For the bichromatic case, it is suggested that the frequency, ω, used in the radiation condition is taken as the frequency corresponding to the component with a larger amplitude, i.e.:

$$\omega = \begin{cases} \omega_1, & a_1 > a_2 \\ \\ \omega_2, & a_2 > a_1 \end{cases}. \qquad (8.4.3)$$

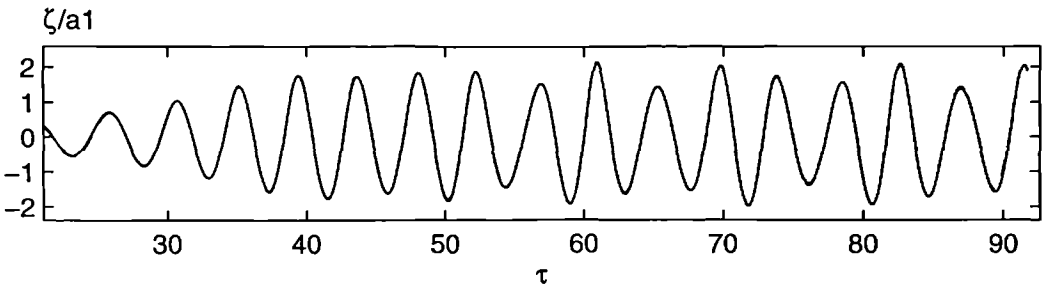

Figure 8.4.1 Wave history recorded at $x \approx 3.74$ ($a_1 = 0.016, \omega_1 = 1.45$; $a_2 = 0.2a_1, \omega_2 = 2.03$; shorter tank $L = 14.64$; longer tank $L = 44.64$; damping zone beginning at $x_d = 4.32$; solid line: shorter tank; dashed line: longer tank)

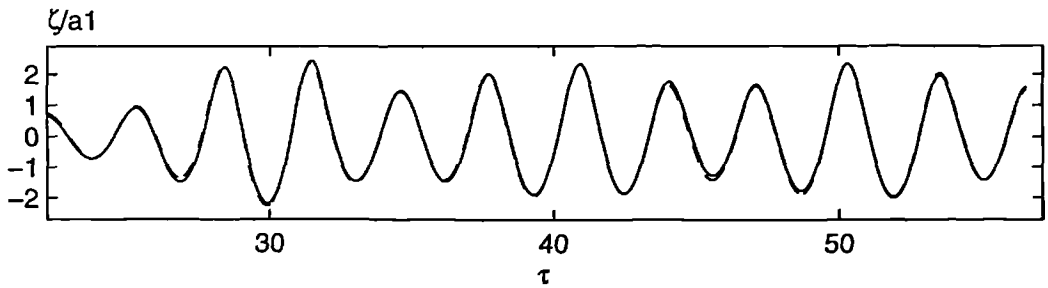

Figure 8.4.2 Wave history recorded at $x \approx 1.33$ ($a_1 = 0.02, \omega_1 = 2.0$; $a_2 = 0.2a_1, \omega_2 = 1.4$; shorter tank $L = 9.28$; longer tank $L = 25.28$; damping zone beginning at $x_d = 1.64$; solid line: shorter tank; dashed line: longer tank)

This suggestion is based on an assumption: the wave component with a larger amount of wave energy will be subjected to a bigger reflection. Whether the suggestion works or not needs to be examined by comparison of the waves generated in the two tanks with different length.

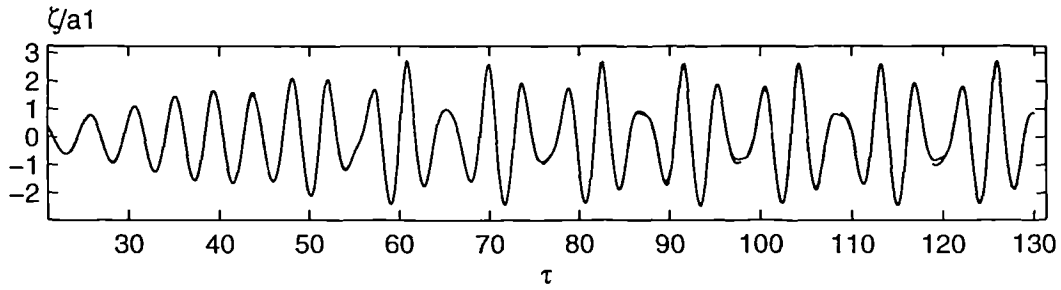

Figure 8.4.3 Wave history recorded at $x \approx 3.74$ ($a_1 = 0.016, \omega_1 = 1.45$; $a_2 = 0.5a_1, \omega_2 = 2.03$; shorter Tank $L = 14.64$; longer Tank $L = 44.64$; damping zone beginning at $x_d = 4.32$; solid line: shorter; dashed line: longer)

It seems reasonable to expect that the frequency chosen in this manner may lead to good results when one of the components is obviously dominant over another. To justify this, the wave history for two cases is illustrated in Figure 8.4.1 and Figure 8.4.2. In both cases, $a_2 / a_1 = 0.2$ but in the first case the frequency is $\omega_1 = 1.45$ while in the second case $\omega_1 = 2.0$. Therefore, the frequency for the radiation condition in both cases is taken as $\omega = \omega_1$. The length of the shorter tank in these simulations is about $5\lambda(\omega)$, where $\lambda(\omega)$ is the wave length of a linear wave corresponding to the frequency ω. The longer tank has approximately three times the length of the shorter one. The waves are recorded at a point, about $0.2\lambda(\omega)$ before the left edge of the damping zone of the shorter tank. These two figures show that the results for the two tanks with different lengths are in good agreement.

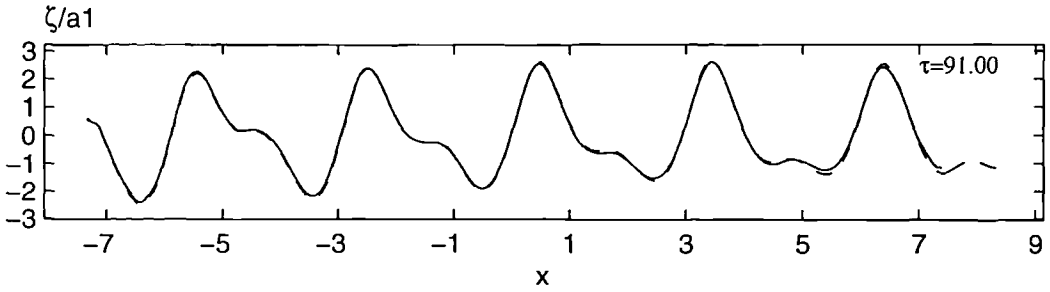

Figure 8.4.4 (a)

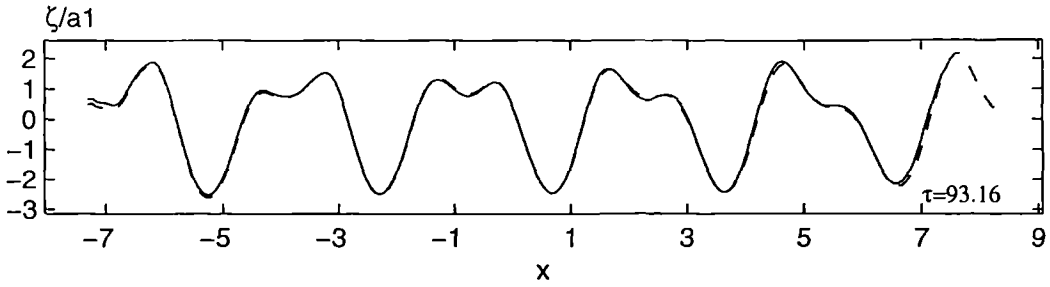

Figure 8.4.4 (b)

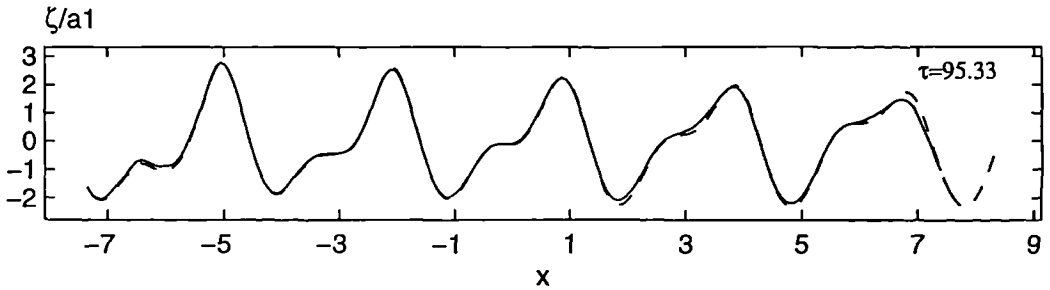

Figure 8.4.4 (c)

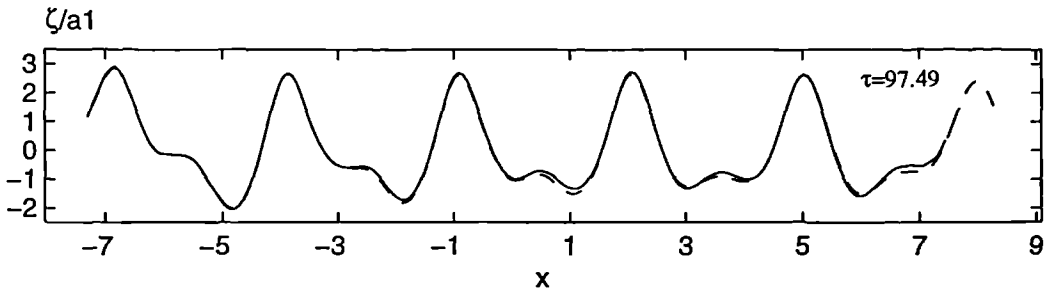

Figure 8.4.4 (d)

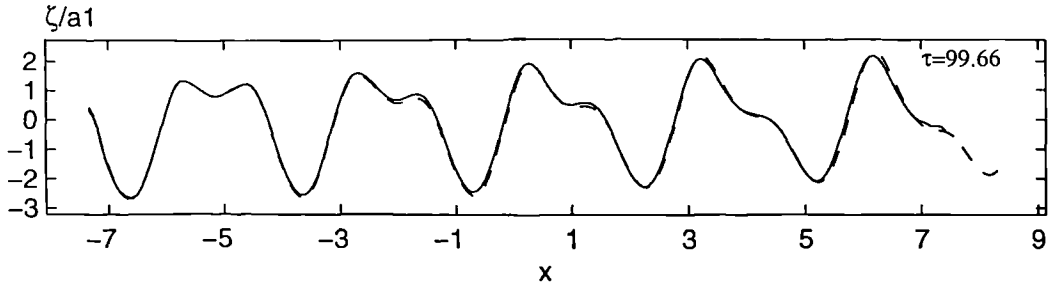

Figure 8.4.4 (e)

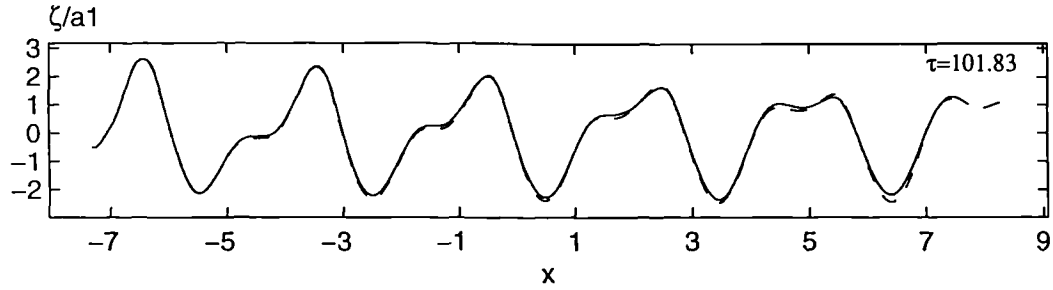

(f)

Figure 8.4.4 Wave profiles at different time instants ($a_1 = 0.016, \omega_1 = 1.45$; $a_2 = 0.5a_1, \omega_2 = 2.03$; shorter tank $L = 14.64$; longer tank $L = 44.64$; *damping zone beginning at* $x_d = 4.32$; *solid line:* shorter; dashed line: longer)

In order to investigate the situation where the two amplitudes are closer in value, we consider a case where $a_2 / a_1 = 0.5$, and the same frequencies and tank length is used as in Figure 8.4.1. The corresponding wave history is presented in Figure 8.4.3 and the wave profiles at several time instants are depicted in Figure 8.4.4. The agreement of the results between the shorter and longer tanks is still very good.

In the critical case of $a_1 = a_2$, the frequency may be chosen as $\omega = \omega_1$ or $\omega = \omega_2$ The two choices have been used to simulate waves generated with parameters $a_1 = a_2$, $\omega_1 = 1.45$ and $\omega_2 = 2.03$, in the same tank as in Figure 8.4.1. The wave history at the corresponding point is shown in Figure 8.4.5. Again the results are in excellent agreement, although the discrepancy in Figure 8.4.5b is slightly more pronounced. The larger difference in the latter figure may suggest that the frequency ω should be taken as the smaller one, when the amplitudes of the two components are about same.

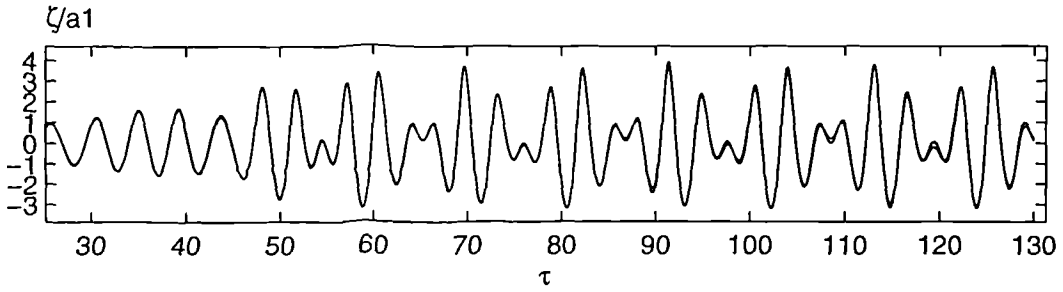

(a) $\omega = \omega_1 = 1.45$, at $x \approx 3.74$

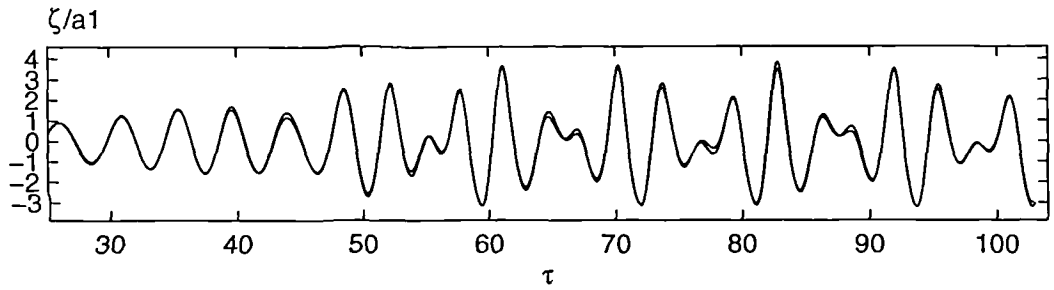

(b) $\omega = \omega_2 = 2.03$, at $x \approx 4.02$

Figure 8.4.5 Wave history for different choice of ω when $a_2 = a_1 = 0.016$ ($\omega_1 = 1.45$; $\omega_2 = 2.03$; shorter tank $L = 14.64$; longer tank $L = 44.64$; solid line: shorter; dashed line: longer)

All of the results show that although the choice of the frequency in equation (8.4.3.) for the radiation condition is somewhat artificial, the reflection generated from the far end is small, and the choice appears to be acceptable for the problems of the kind dealt with here. If we think this frequency should correspond to the dominant component of the bichromatic waves, it is somewhat unexpected that it can give some good results even when the two components have similar amplitudes.

8.4.2 Irregular waves

Irregular waves may be generated by the random motion of the wavemaker. The random motion may be expressed as a Fourier expansion with respect to time. In laboratory, the motion is sometime considered as a sum of the finite number of

monochromatic components with random phases. From this point of view, the bichromatic motion is a particular example of this case. Experience in the simulation of the bichromatic waves suggests that the frequency associated with the radiation condition for irregular wave simulation may be chosen as the one corresponding to the component with the largest energy. It is therefore recommended in this case that the frequency ω for the radiation condition is determined according to the wave spectrum. Specifically, the frequency corresponding to the maximum value of the wave spectrum is taken as ω.

In order to demonstrate whether or not the frequency chosen in this way is suitable, irregular waves in two tanks of different length are examined, which are generated by the wave maker subject to the displacement and velocity shown in Figure 8.4.6. The data given in this figure is up to $\tau \approx 60$. In fact, the wave maker is set to be at rest after $\tau \approx 58$. This motion of the wave maker consists of about 50 components of different frequency. Fourier analysis performed on these data shows that the frequency corresponding to the maximum in the wave spectrum is about 1.20, which is chosen for ω in the radiation condition. The tank length is taken as $L = 20$ and $L = 40$ for the shorter and longer tank, respectively.

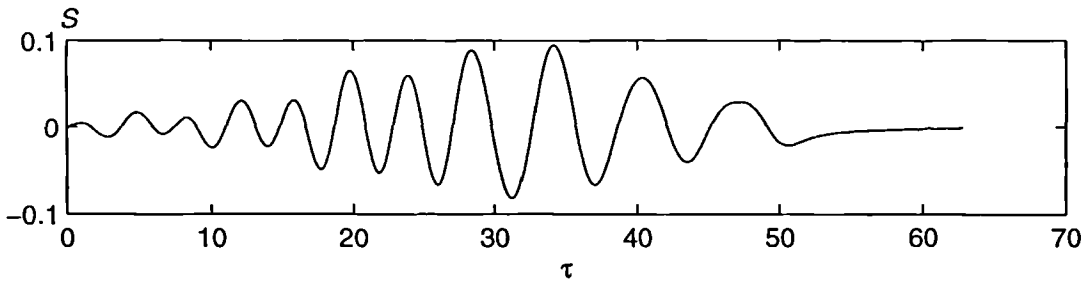

(a)Displacement

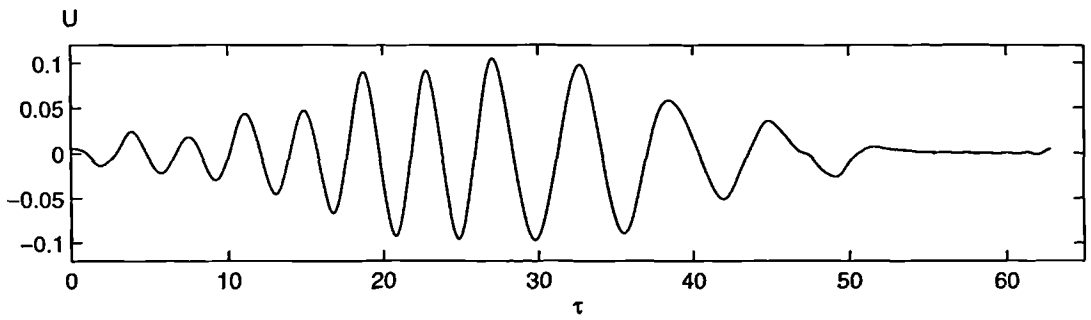

(b) Velocity

Figure 8.4.6 The displacement and velocity of the wave maker generating irregular waves

Figure 8.4.7 shows the wave history recorded at $x = 3.436$ for different lengths of the tank. Figure 8.4.8 presents the profiles at three different time steps and clearly indicates that the wave front has already reached the damping zone ($x_d = 7.0$ in the shorter tank). The good agreement of the results obtained by the shorter and longer tank signifies that the effectiveness of the radiation condition is maintained for this case. This is further demonstrated in Figure 8.4.9 which shows that the wave has obviously died away in the tank, implying the wave is transmitted through the far end with little reflection.

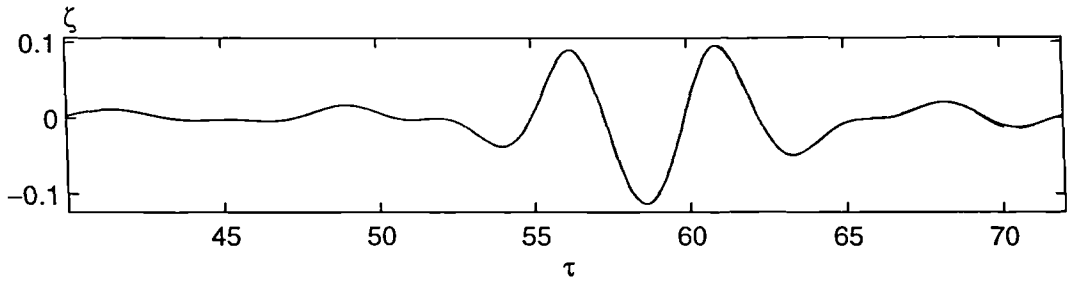

Figure 8.4.7 The history of an irregular wave recorded at $x = 3.436$ for different tank lengths (solid line: shorter tank; dashed line: longer tank; damping zone beginning at $x_d = 7.0$)

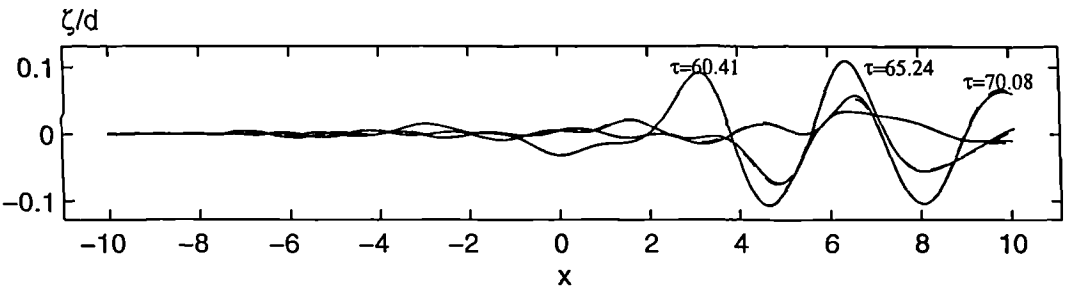

Figure 8.4.8 Profiles of irregular wave at three particular time steps for different tank lengths (solid line: shorter tank; dashed line: longer tank; damping zone beginning at $x_d = 7.0$)

Evaluating ω from the wave spectrum for the radiation conditon is always an approximation. As a result, the sensitivity of the numerical results to this frequency must be investigated. For this purpose, the same case as in Figure 8.4.7 is also simulated by

choosing $\omega = 1.0$ and $\omega = 1.3$, respectively. The results obtained are plotted in Figure 8.4.10, together with those corresponding to $\omega = 1.20$. One can see that the difference between the three cases is not graphically noticeable, which indicates that the wave absorption is not very sensitive to the choice of ω.

Although the effectiveness of the radiation condition in the simulation of the irregular wave with various spectra may need to be investigated more extensively, the evidence gathered here seems to show that this condition can work well for the problems considered in this thesis, particularly for waves of the narrow band spectra. This sort of irregular waves is often dealt with in offshore and naval architecture engineering.

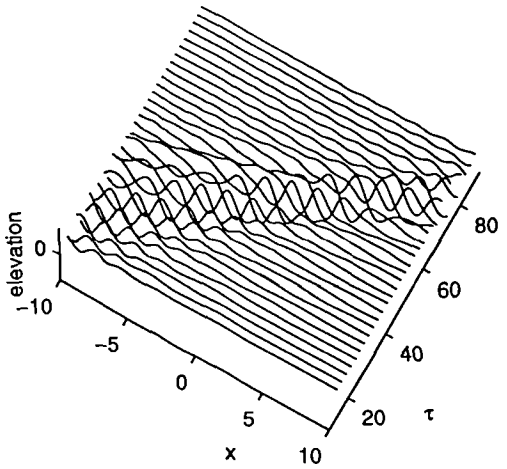

Figure 8.4.9 Irregular wave profiles at different time steps

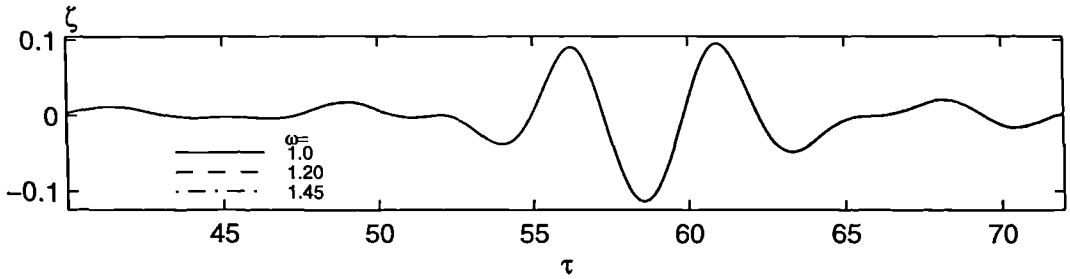

Figure 8.4.10 The history of an irregular wave at $x = 3.436$
for the difference frequencies ω used in the radiation condition

8.5 Interaction between waves and a circular cylinder

The problem of the interaction between waves and a vertical cylinder is now considered. This problem is of interest in offshore engineering since similar structures are widely used in this field. To carry out the investigation, waves are generated in a tank in the manner described in Sections 8.2 and 8.3. A surface-piercing vertical circular cylinder is mounted on the bottom of the tank. The sketch of the problem with the definitions of some dimensions is shown in Figure 8.5.1. A similar coordinate system to that used in Section 8.2 is also defined in the figure, with its origin here being at the centre of the cylinder.

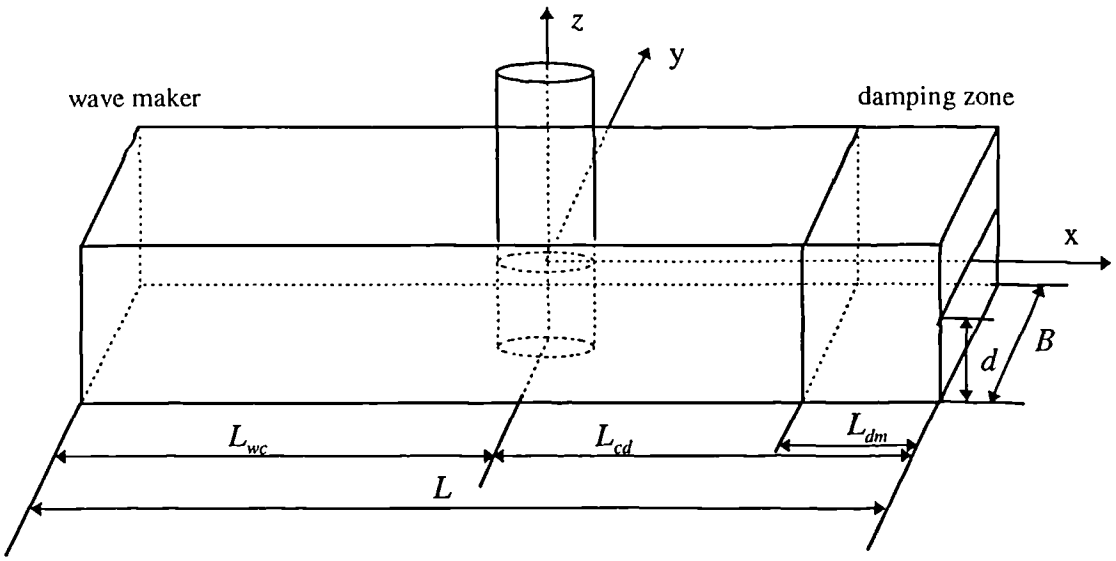

Figure 8.5.1 A cylinder in a wave tank (d=1)

According to linear theory (see, e.g. Eatock Taylor *et al*, 1994), the wave generated by a wave maker may be divided into two parts: the progressive wave and the local wave. The progressive wave travels to infinity whereas the local wave exists only in a region near the wave maker, and decreases with distance from the wave maker at a rate $e^{-\frac{\pi}{2}(x-x_0)}$ (see Crapper, 1984), where x_0 is the position of the wave maker. The interaction between the progressive wave and the cylinder is of concern here. The interaction of the cylinder with the local wave should be avoided. This can be achieved by putting the cylinder sufficiently away from the wave maker. As suggested by Crapper (1984), the effects of local waves can be negligible when $x - x_0 > 2$. In the following, use is made of $L_{wc} > R_0 + 3$ to approximately eliminate the local wave interaction; L_{wc}

is the length between the centre of the cylinder and the wavemaker. When the progressive waves reach the cylinder, they will be reflected and transmitted. The reflected waves from the cylinder travel back towards to the wave maker. The interaction between the reflected waves and the wave maker may distort the original progressive waves. Ideally this type of interaction should be removed. In our work, the cylinder is put at an appropriate position away from the wave maker and the calculation stops before the distorted waves have travelled back to the cylinder. The maximum computational time is estimated by $3L_{wc}/C_g$, where C_g is the group velocity of the wave. Clearly if long-time calculation is required, the value of L_{wc} should be made sufficiently large. This arrangement is very similar to the situation in laboratory experiments, although the influence of the reflected wave may not be avoided completely.

The transmitted waves will propagate towards the far end of the tank. In order to eliminate the reflection from that end, the same radiation condition suggested in Sections 8.2 and 8.3 is imposed. However it should be noted that the transmitted waves are three dimensional. Although the damping zone may be applicable for three dimensional waves, the Sommerfeld condition implemented implies that the waves are two dimensional as the phase velocity of the wave and the moving velocity of the truncated boundary are assumed to be constant across the tank. Therefore it is necessary to investigate the effectiveness of the radiation condition in the three dimensional cases.

Both regular and irregular waves are considered. The interaction between the waves and the cylinder is studied by investigating the force on and the wave around the cylinder. The force is calculated by the direct method, that is the time derivative in the fluid pressure is obtained by solving a boundary value problem. Although the moment of the force can be simultaneously evaluated, the discussion is focused on the force here.

The discretisation of the fluid domain is performed in a manner slightly different from that in Figure 8.3.4. That is, in a subdomain around the cylinder, the two vertical planes are now radial and circumferential. In other areas, the mesh is the same as before. A typical mesh around the cylinder is illustrated in Figure 8.5.2.

Convergence studies have been carried out in a similar way to those in Section 8.3.2, but the details will not be presented here. The parameters corresponding to the spatial

and temporal discretisation have also be chosen to ensure that the same degree of accuracy as that shown in Section 8.3.2 can be maintained.

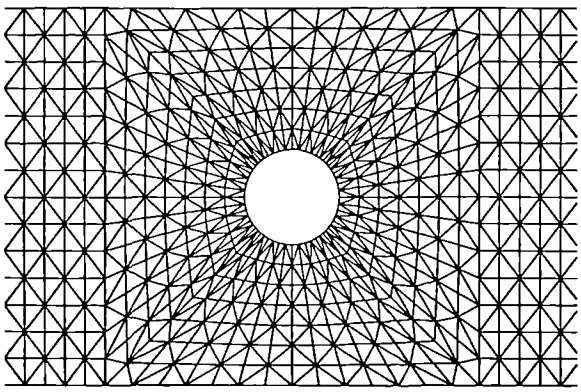

Figure 8.5.2 Mesh around a cylinder

8.5.1 Interaction between regular waves and a circular cylinder

Effectiveness of the Radiation Condition

As in Section 8.3, the effectiveness of the radiation condition is examined by comparing the results obtained using different length tanks, but here the different lengths are established by changing the distance between the cylinder and the far end, L_{cd}. The cases presented are distinguished by different sizes of the tank and the cylinder, and by different amplitudes and frequencies of the wave maker. In the first case, $a = 0.016$ and $\omega = 1.45$. The distance between the wave maker and the centre of the cylinder is taken as $L_{wc} = 10$. $L_{cd} = 6$ and $L_{cd} = 16$ are used for the shorter and longer tanks, respectively, and $B = 0.5$ in both cases. The radius of the cylinder is $R_0 = 0.05$. The force history is shown in Figure 8.5.3, where $f = \dfrac{F_x}{\rho g R_0^2 a}$. Figure 8.5.4 illustrates the time history of the wave runups on the front side of the cylinder surface $(-R_0, 0)$.

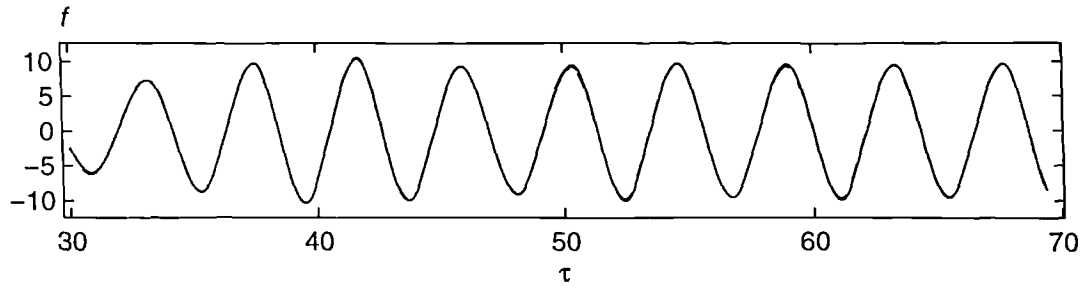

Figure 8.5.3 The time history of the force in the x-direction for $a = 0.016$ and $\omega = 1.45$ (solid line: shorter tank; dashed line: longer tank)

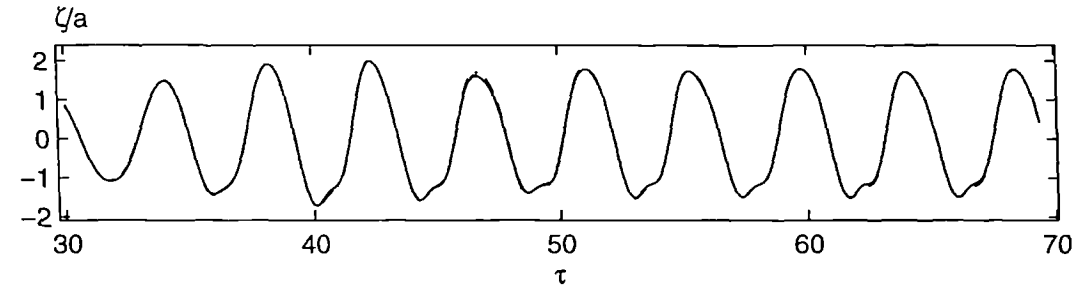

Figure 8.5.4 The time history of runup on the front side of the cylinder surface for $a = 0.016$ and $\omega = 1.45$(solid line: shorter tank; dashed line: longer tank)

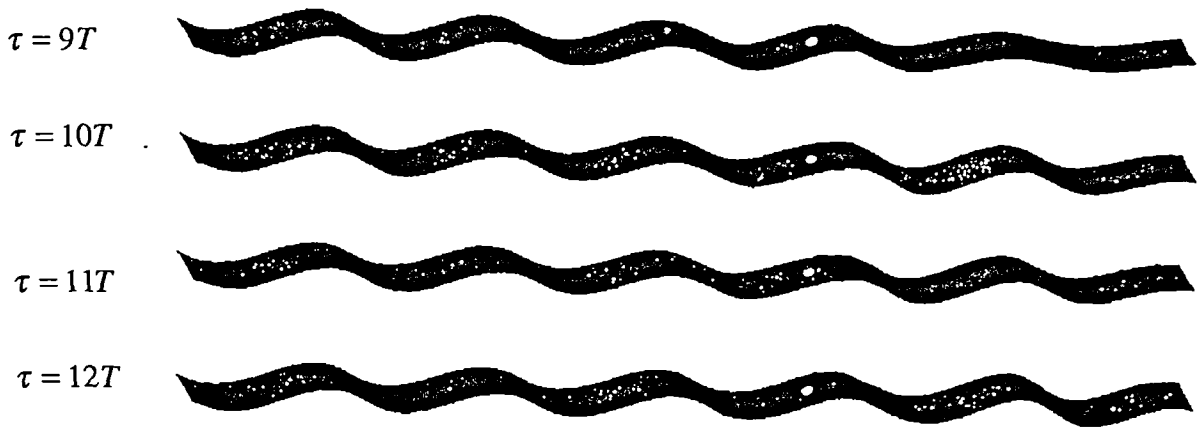

Figure 8.5.5 Snapshots of the free surface at several time steps

It can be seen from these two figures that there is little difference between the results for the two different values of L_{cd}. Figure 8.5.5 gives the snapshots of the free surfaces at several time steps, where $T = \frac{2\pi}{\omega}$ is the wave period. This figure shows that after about

$\tau = 10T$, the wave profile almost repeats itself. All of these indicate that the reflection from the far end is not significant in this case.

In the second case, the various parameters are specified as $a = 0.01$, $\omega = 2.0$, $R_0 = 0.1416$, $B = 0.62$, $L_{wc} = 7.0$, $L_{cd} = 5.0$ for the shorter tank and $L_{cd} = 10.0$ for the longer tank. The obtained forces and wave runups are presented in Figure 8.5.6 and Figure 8.5.7, respectively. Again the results corresponding to tanks of different lengths are in good agreement.

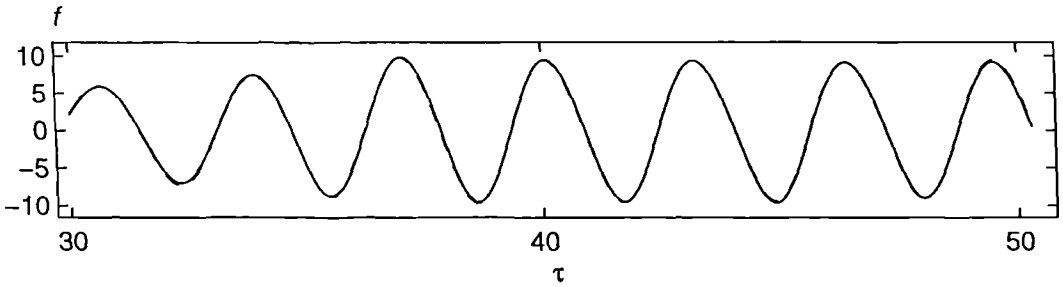

Figure 8.5.6 The time history of the force in the x-direction for $B = 0.62$, $a = 0.01$ and $\omega = 2.0$ (solid line: shorter tank; dashed line: longer tank)

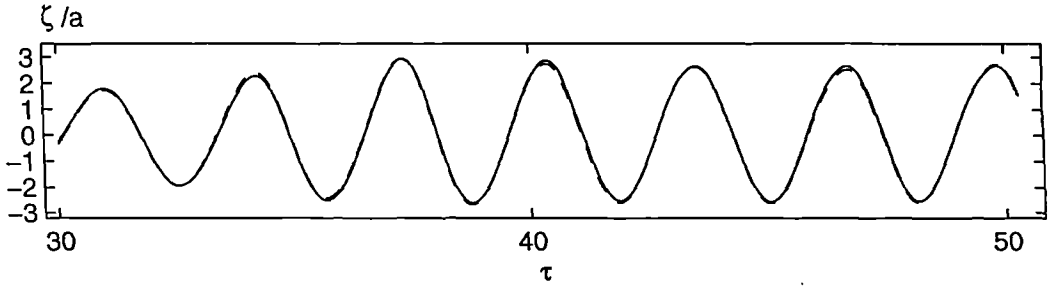

Figure 8.5.7 The time history of the runup on the front side of the vertical surface of the cylinder for $B = 0.62$, $a = 0.01$ and $\omega = 2.0$ (solid line: shorter tank; dashed line: longer tank)

Figure 8.5.8 and Figure 8.5.9 show the results for the same case as the above except that the amplitude of the wave maker is $a = 0.043$. The agreement between these two figures suggests the effectiveness of the radiation condition is retained even when the wave becomes steeper.

In the third case, most of the parameters retain the same as those for Figure 8.5.6 and Figure 8.5.7, except that the width of the tank is now taken as $B = 1.0$, which is bigger. Similar results are plotted in Figures 8.5.10 and 8.5.11. The agreement between the

results corresponding to the shorter and the longer tank is also as good as in Figure 8.5.6 and Figure 8.5.7.

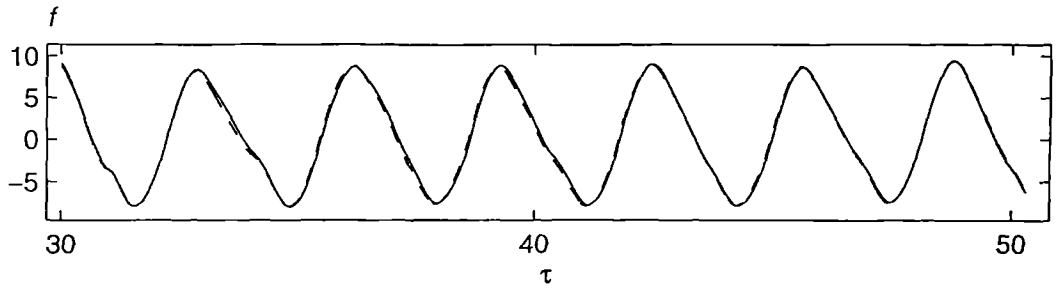

Figure 8.5.8 The time history of the force in the x-direction for $B = 0.62$, $a = 0.043$ and $\omega = 2.0$ (solid line: shorter tank; dashed line: longer tank)

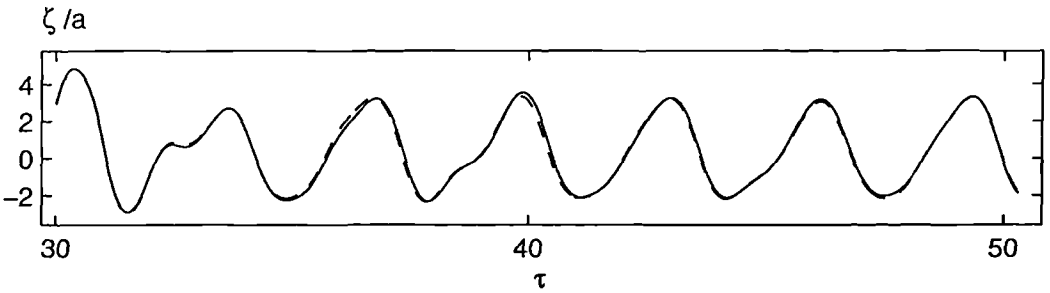

Figure 8.5.9 The time history of the runup on the front side of the vertical surface of the cylinder for $B = 0.62$, $a = 0.043$ and $\omega = 2.0$ (solid line: shorter tank; dashed line: longer tank)

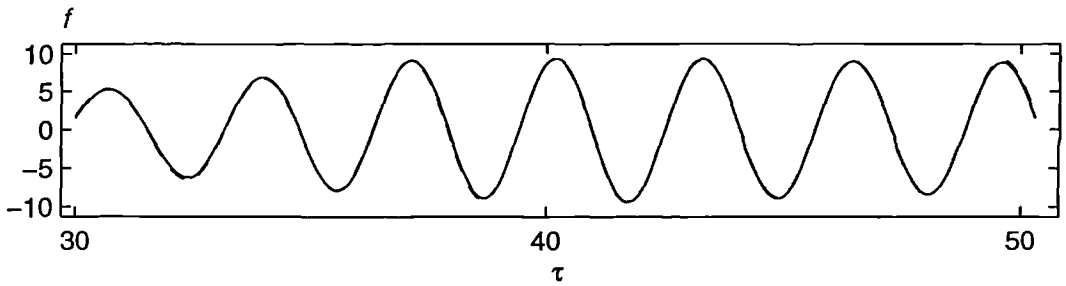

Figure 8.5.10 The time history of the force in the x-direction for $B = 1.0$, $a = 0.01$ and $\omega = 2.0$ (solid line: shorter tank; dashed line: longer tank)

In addition to the above cases, other cases with different frequencies and amplitudes have been simulated. Although the details are not provided here, they also seem to show

that the radiation condition used in the previous sections may be effective in many three dimensional situations.

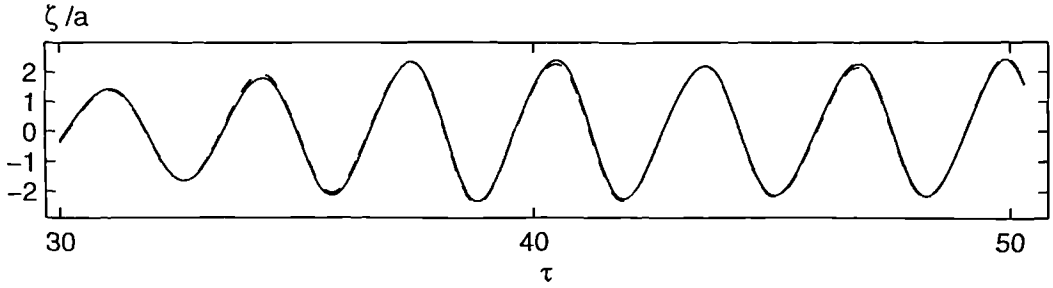

Figure 8.5.11 The time history of the runup on the front side of the vertical surface of the cylinder for $B = 1.0$, $a = 0.01$ and $\omega = 2.0$ (solid line: shorter tank; dashed line: longer tank)

Comparisons with an analytical solution based on linear theory

When a vertical cylinder is mounted in the open sea and is subject to a small incident harmonic wave, an analytical solution was reported by MacCamy & Fuchs (Sarpkaya & Isaacson, 1981) in the frequency domain based on linear theory. Their solution is used here for comparison with our numerical results.

Table 8.5.1 Cases for comparison with the analytical solution

R_0	B	B/R_0	ω	a	kR_0	symbol in Fig 8.5.12
0.05	0.5	10.0	1.45	0.0041	0.108	O
0.1416	1.119	7.9	1.45	0.0041	0.306	O
0.1416	0.62	4.4	2.00	0.0022	0.566	O
0.1416	0.90	6.4	2.00	0.0022	0.566	+
0.175	0.90	5.1	2.00	0.0022	0.701	O
0.19	0.90	4.7	2.00	0.0022	0.761	O
0.20	0.90	4.5	2.00	0.0022	0.801	O

Various cases listed in Table 8.5.1 have been simulated for this purpose. In these cases, different values of kR_0 are obtained by changing the radius of the cylinder and the wave number k, where k is the solution of $\omega^2 = k\tanh(k)$. In order to obtain the linear force amplitude, Fourier analysis is performed on the time history of the force in

the periodic state wherein the amplitude of the force does not change significantly from one period to another. The amplitude of the first component is expressed as F_a. Figure 8.5.12 gives the comparison between the numerical results and the analytical solution of MacCamy & Fuchs. To be consistent with the data given by Sarpkaya & Isaacson(1981), the force in this figure has been nondimensionalised to $\frac{F_a}{\rho g H a d[\tanh(kd)/kd]}$, where H is the wave height from the trough to the crest, which is also determined by Fourier analysis from the wave history but without the cylinder. It can be seen that the agreement between the numerical and analytical results is quite good, although a slightly larger difference is observed in the last five cases of Table 8.5.1. As can be seen from the table, the radii in these cases are relatively larger but the ratios of the tank width to the radii are relatively smaller. Therefore, the larger difference in Figure 8.5.12 may be partly due to the effects of the side walls of the tank. Some comments on these effects will be given in Section 8.6.

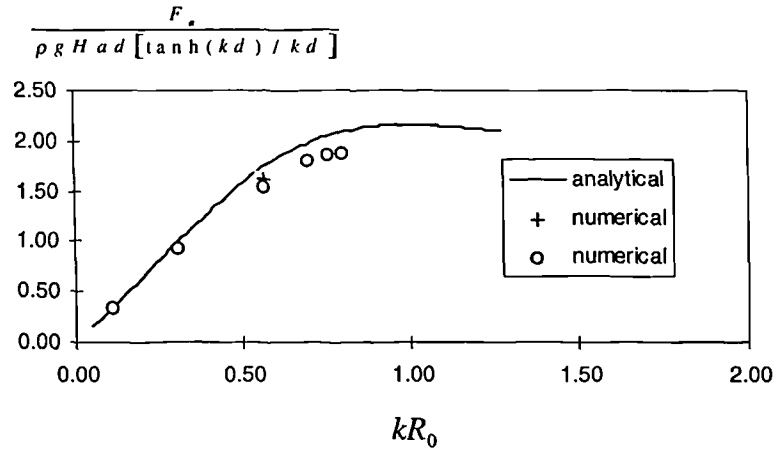

Figure 8.5.12 Comparison of the numerical force in the x-direction with the analytical solution of MacCamy & Fuchs

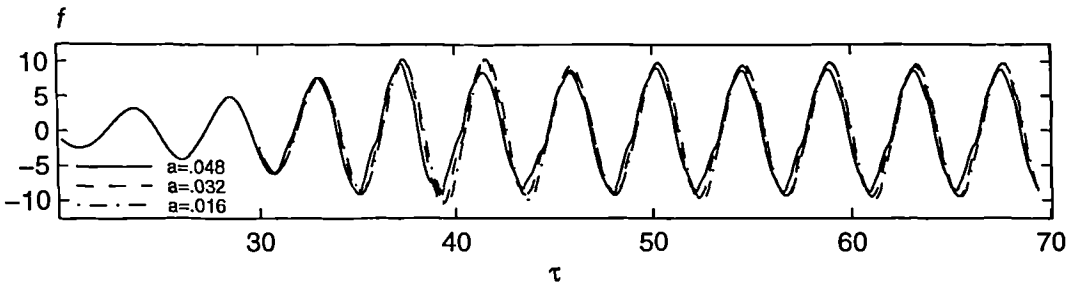

Figure 8.5.13 Forces for different motion amplitudes of the wave maker ($\omega = 1.45$, shorter tank; $f = \frac{F_x}{\rho g R_0^2 a}$)

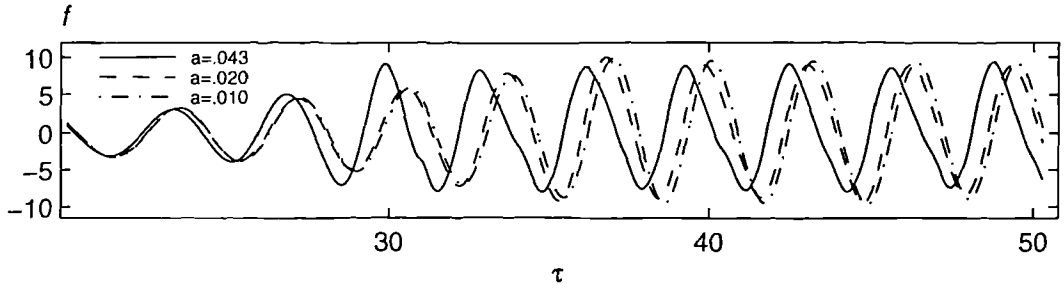

Figure 8.5.14 Forces for different motion amplitudes of the wave maker
($\omega = 2.0$, short tank; $f = \frac{F_x}{\rho g R_0^2 a}$)

Nonlinear effects:

Figures 8.5.13 and 8.5.14 are plotted to show the nonlinear effects in the time history of the wave forces. The motion of the wave maker for the results in Figure 8.5.13 is the same as in Figure 8.5.3, except that the amplitudes are changed from 0.016 to 0.048, and the tank is the shorter one. Figure 8.5.14 is obtained by re-plotting the two solid lines in Figures 8.5.6 and 8.5.8, together with another case of amplitude $a = 0.02$. No significant difference between the results in Figure 8.5.13 has been observed. However, in Figure 8.5.14, the nonlinear effects are clearly visible. That is, the crest is larger than the trough when the wave becomes steeper. In addition, the transient period of the force history corresponding to the steeper wave becomes shorter. This implies that the steeper wave travels faster, reflecting the amplitude dispersion due to nonlinearity as discussed in Section 8.3.2. To further show the nonlinear behaviour of the wave force, Fourier analysis on the time history of the force within the periodic stage of Figures 8.5.13 and 8.5.14 is performed. The nonlinear contributions can be obtained by subtracting the first harmonic component from the total force. Figures 8.5.15 and 8.5.16 depict the nonlinear contribution, f_h, for various cases as well as the corresponding total force in each case. These figures clearly show that the nonlinear contributions become more and more important with increase in amplitude of the wavemaker. In some cases, these contributions may account for 20% of the total force.

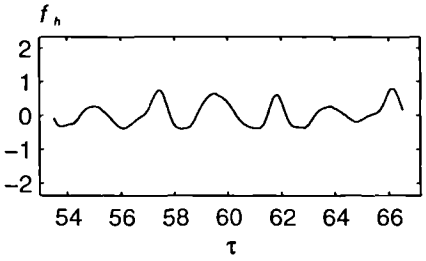

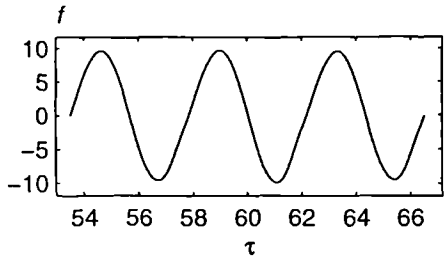

Nonlinear contribution Total force

Figure 8.5.15 (a) $a = 0.016$

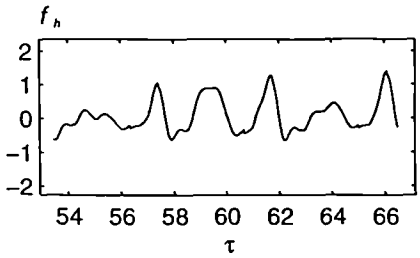

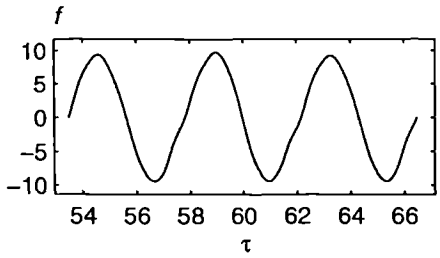

Nonlinear contributions Total force

Figure 8.5.15 (b) $a = 0.032$

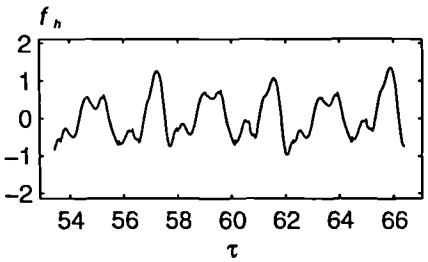

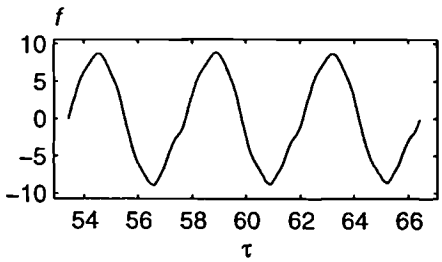

Nonlinear contribution Total force

(c) $a = 0.048$

Figure 8.5.15 Nonlinear contributions to the force obtained by Fourier analysis

$$(\omega = 1.45; f = \frac{F_x}{\rho g R_0^2 a})$$

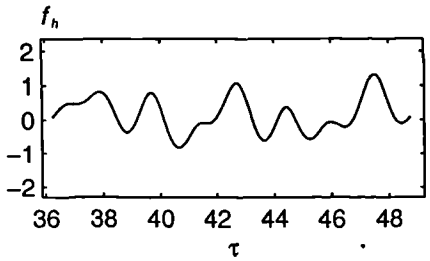

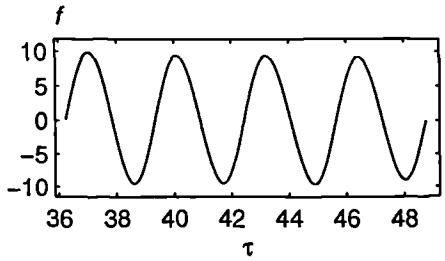

Nonlinear contribution Total force

Figure 8.5.16 (a) $a = 0.01$

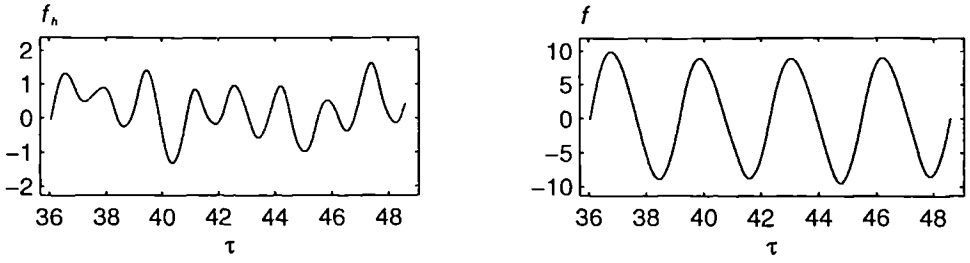

Nonlinear contribution Total force

Figure 8.5.16 (b) $a = 0.02$

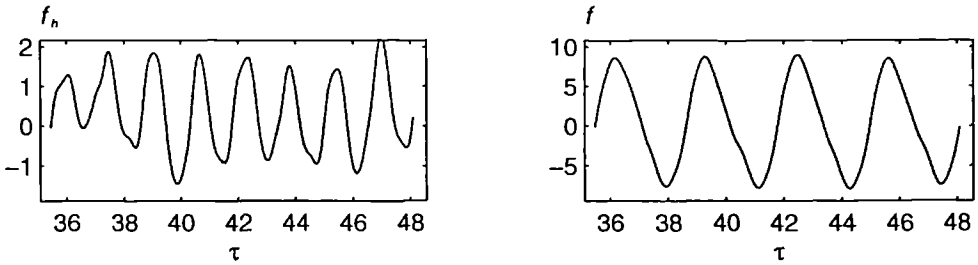

Nonlinear contribution Total force

(c) $a = 0.043$

Figure 8.5.16 Nonlinear contributions to the force obtained by Fourier analysis

$$(\omega = 2.0; f = \frac{F_x}{\rho g R_0^2 a})$$

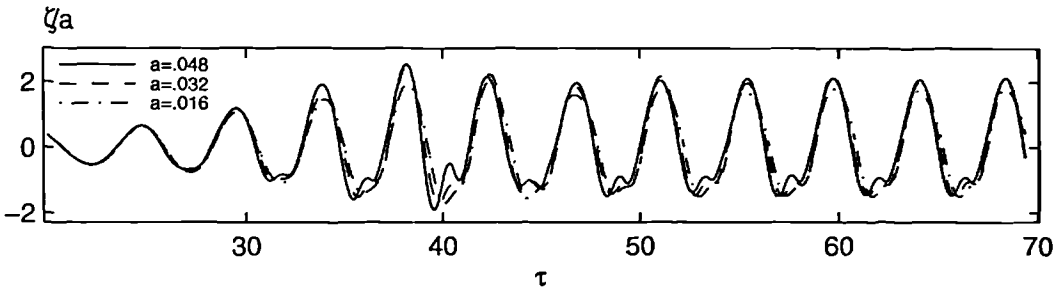

Figure 8.5.17 The time history of the wave runup on the front side of the cylinder surface for different amplitudes of the wave maker ($\omega = 1.45$, shorter tank)

To show the nonlinear effects on waves around the cylinder, the wave runups on the front side of the cylinder surface are plotted in Figures 8.5.17 and 8.5.18, corresponding to Figures 8.5.15 and 8.5.16, respectively. The oscillations with high frequency can be clearly observed in these figures when the waves become steep. In order to demonstrate the behaviour of the wave along the entire waterline of the cylinder, some profiles of the

free surface on the cylinder at several time steps are presented in Figure 8.5.19 and Figure 8.5.20 for $a = 0.01$ and $a = 0.043$, respectively, with the same frequency

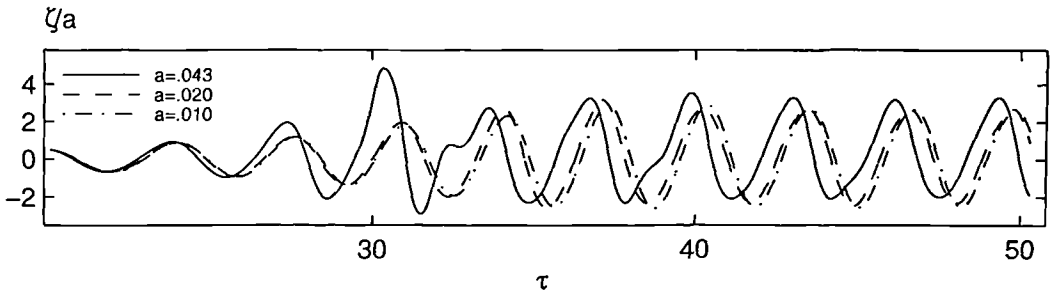

Figure 8.5.18 The time history of wave runup on the front side of the cylinder surface for different amplitudes of the wave maker ($\omega = 2.0$, shorter tank)

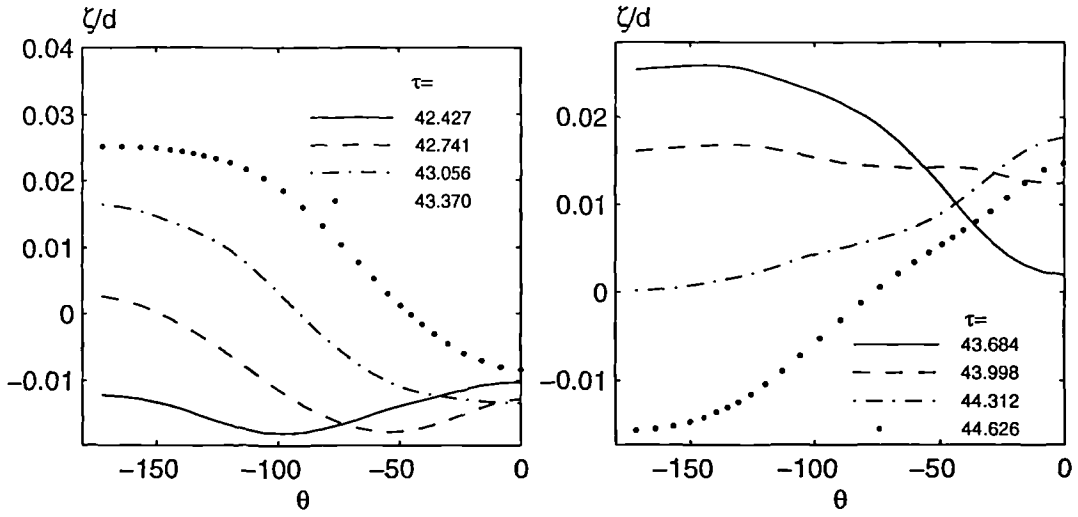

Figure 8.5.19 Wave profiles on the waterline of the cylinder at different time steps ($\omega = 2.0$ and $a = 0.01$)

$\omega = 2.0$. The angle $\theta = -180^\circ$ corresponds to the front side, while $\theta = 0^\circ$ is the lee side in these figures. Very different wave profiles for small and large amplitudes can be seen in these two figures. In particular, in Figure 8.5.20, quite steep wave profiles appear, which are more or less similar to the bores observed in a sloshing tank in Chapter 7. Stansberg (1997) gave us some figures of waves around a cylinder, plotted using his experimental data. The wave patterns in their figures are very similar to those at $\tau = 39.286$ and $\tau = 40.542$ in Figure 8.5.20. Krokstad & Stansberg (1995) also reported some bore-like waves (named as 'hydraulic jumps' in their work) around the

cylinder observed during their experiments. Precise comparison with their work is difficult since the information they gave for wave generation is not sufficient for us to generate identical waves. Nevertheless, the above facts show some similarity between the numerical simulation and their experimental work when the nonlinearity becomes evident. However, further comparison with experiments is clearly required in future work.

To demonstrate the behaviour of the profiles in three dimensions, some 'snapshots' around the cylinder corresponding to Figure 8.5.20 are presented in Figure 8.5.21. The short and steep waves are more clearly observed around the cylinder surface. This is certainly due to the nonlinear effects, and these waves may be part of the nonlinear contribution to the force.

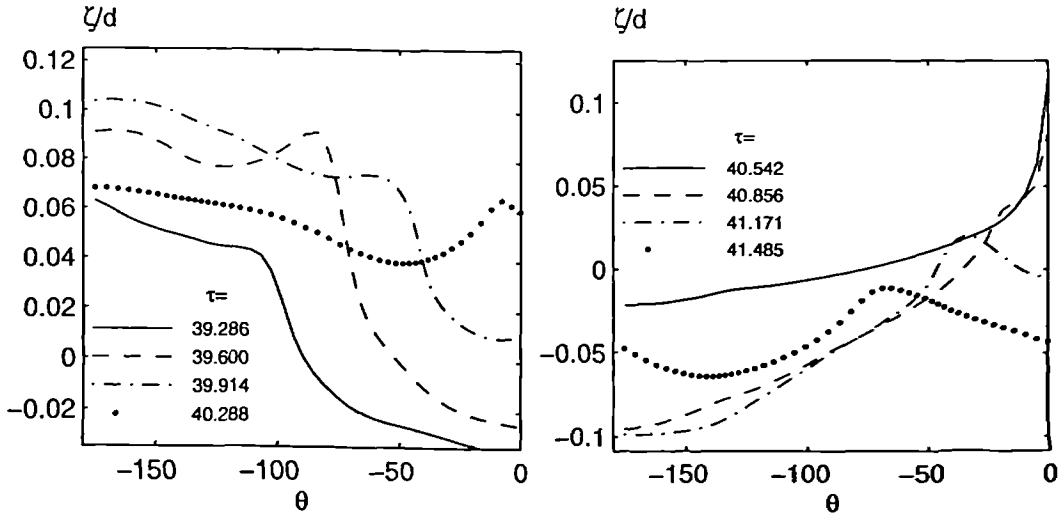

Figure 8.5.20 Wave profiles on the waterline of the cylinder at different time steps($\omega = 2.0$ and $a = 0.043$)

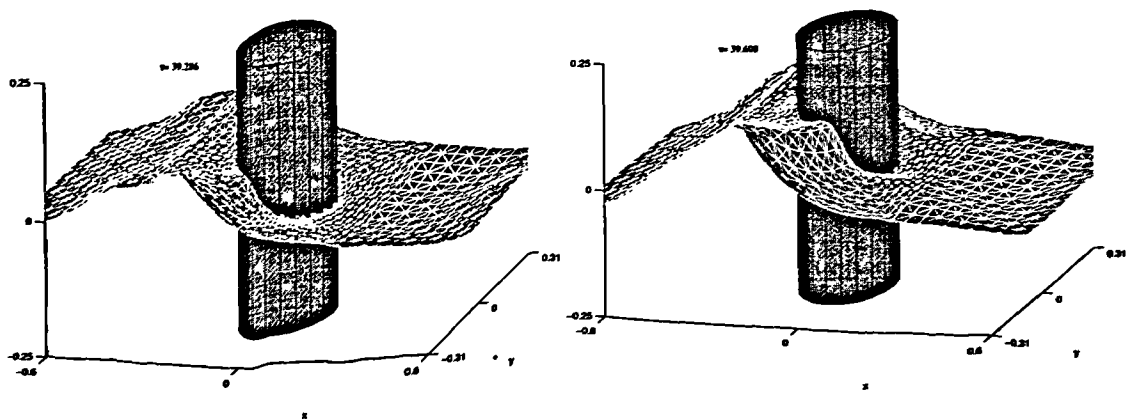

Figure 8.5.21

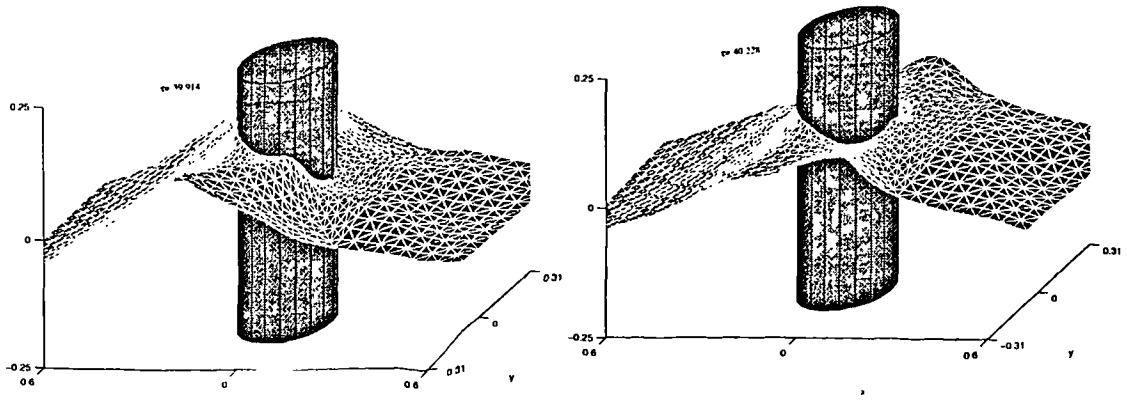

Figure 8.5.21

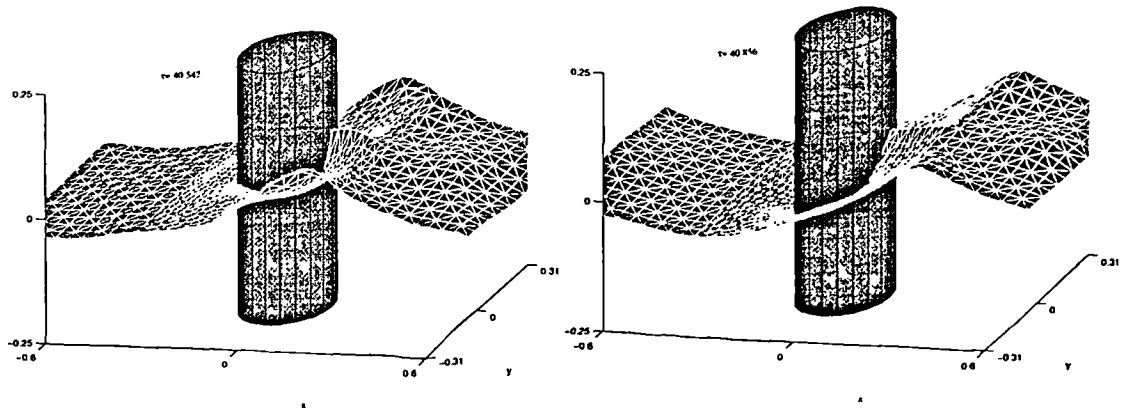

Figure 8.5.21 Snapshots of wave profiles around the cylinder
($\omega = 2.0$ and $a = 0.043$)

8.5.2 Interaction between a circular cylinder and irregular waves

The same motion of the wave maker as that in Figure 8.4.6 is used to generate irregular waves. The damping zone and the Sommerfeld condition are applied at the far end of the tank in the same way as in Section 8.4.2 with the frequency for the radiation condition being taken as $\omega = 1.2$. As in the regular wave cases, the effectiveness is also re-examined by comparing results for the different lengths of the tank. The tank geometry is defined by $B = 1.119$, $L_{cm} = 13.436$ and different distances L_{cd} ($L_{cd} = 8.56$ for the shorter tank while $L_{cd} = 16.56$ for the longer tank). The cylinder in the tank has radius $R_0 = 0.1416$. With these specifications, the centre of the cylinder is located at the same point as that where the wave history in Figure 8.4.7 is recorded. Thus the wave in that figure can be considered as the incident wave on the cylinder.

The time histories of the force and the runup on the front side of the cylinder surface are presented in Figure 8.5.22 and Figure 8.5.23, respectively. Good agreement between the results using the different tank lengths is shown, confirming that the radiation condition works well for these cases.

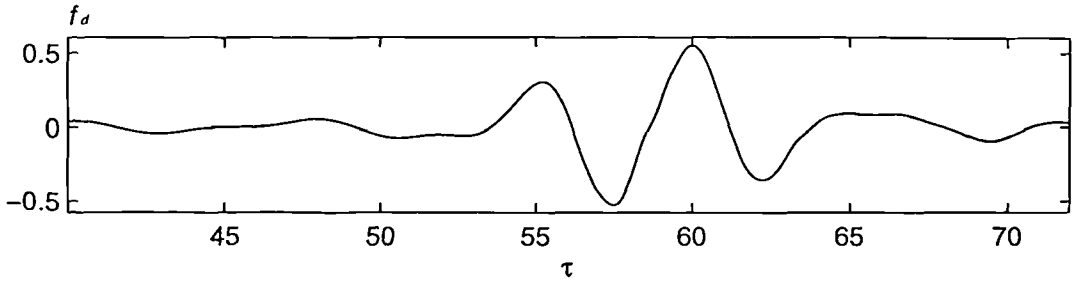

Figure 8.5.22 The time history of the force in x-direction acting on the cylinder in irregular waves(Solid line: shorter tank; Dashed line: longer tank; and $f = \frac{F_x}{\rho g R_0^2 a}$)

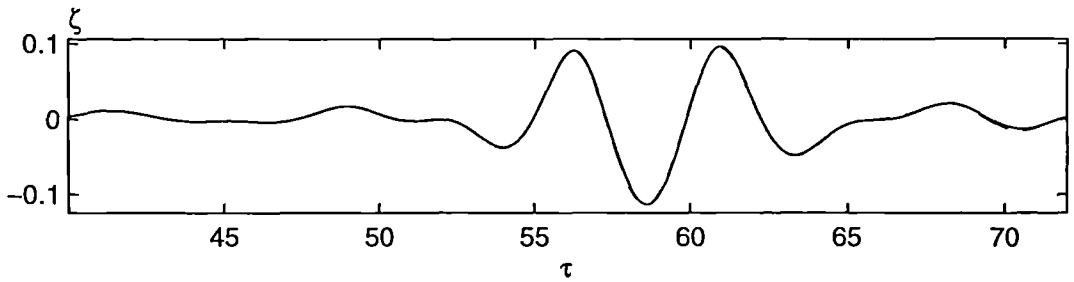

Figure 8.5.23 The time history of the runup on the front side of the cylinder in irregular waves(Solid line: shorter tank; Dashed line: longer tank)

Furthermore, it can be seen from the two figures that there are two peaks in the time histories of the force and the runup. The history of the runup is very similar to the wave history in Figure 8.4.7, that is the amplitudes of the two large peaks are about the same. However, the time history of the force behaves quite differently, where the second peak is obviously larger than the first. Moreover, both peaks of the force occur before the corresponding runup peaks.

Some snapshots of the wave profiles around the cylinder are plotted in Figure 8.5.24. As in Figure 8.5.21, a short and steep wave is also created here when a larger wave passes the cylinder. It may also be noticed, by comparing this figure with Figure 8.5.22,

that when the wave front of the steep wave is travelling half way across the cylinder surface, the largest peak in force history occurs.

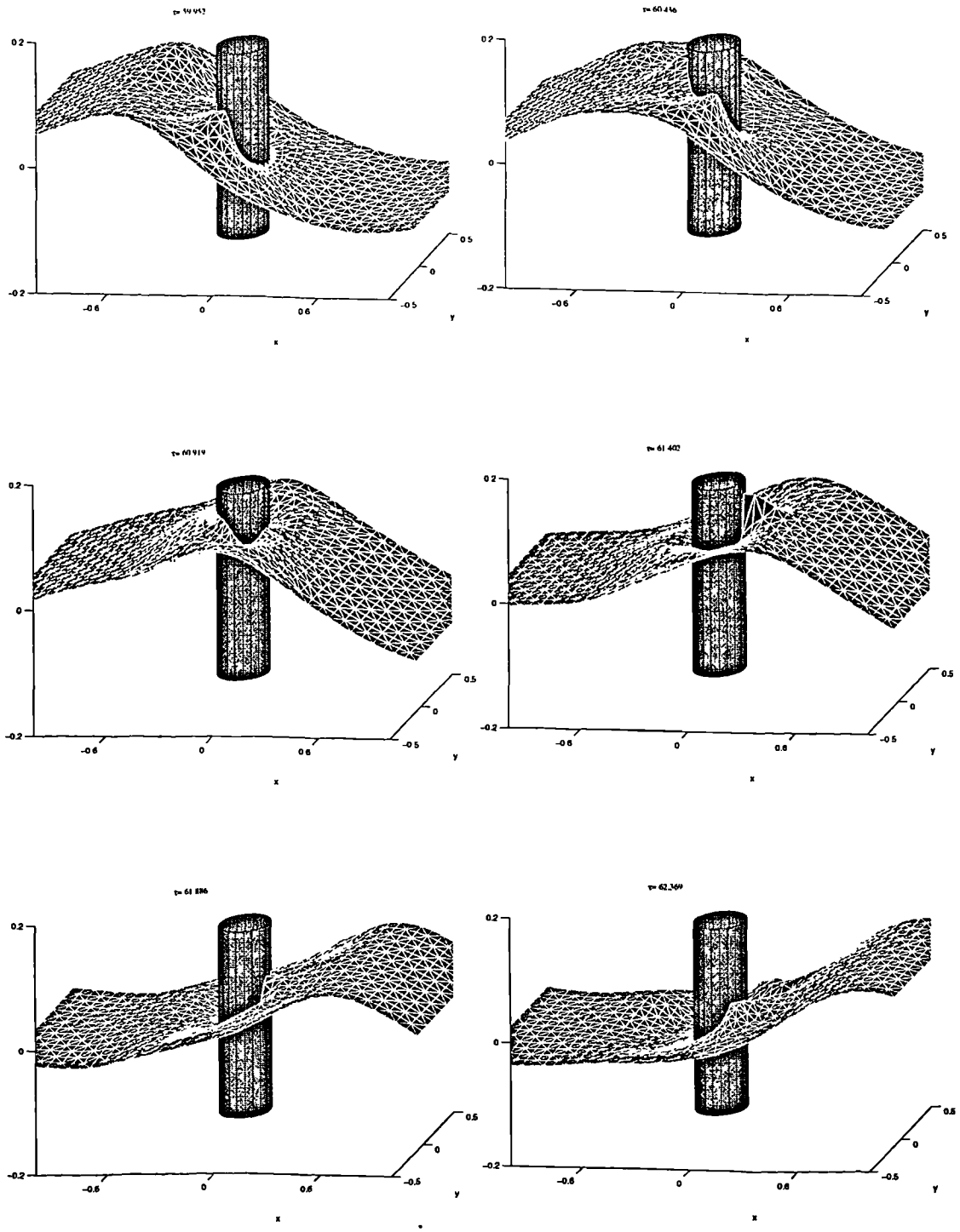

Figure 8.5.24 Snapshots of the wave profiles around the cylinder for irregular waves

8.6 Interaction between waves and two circular cylinders

Two surface-piercing vertical circular cylinders are mounted on the bottom of the tank, and thus the interaction between the waves and the two cylinders can be considered. This problem is also of interest to offshore engineering, like the single-cylinder problem dealt with in previous sections, because the four-cylinder platform subject to the head sea can be investigated using this model. The main difference between the problem involving two cylinders and that involving a single cylinder is that influence of the neighbouring cylinder on the wave loading may exist in the former due to one cylinder being situated in the diffracted wave field of the other. Considerable effort has been made to estimate the influence. Some reviews were given by McIver and Evans (1984) on the linear theory, and by Huang & Eatock Taylor (1997) on the second order theory. However, there are far fewer results for the multiple cylinders based on the fully nonlinear theory.

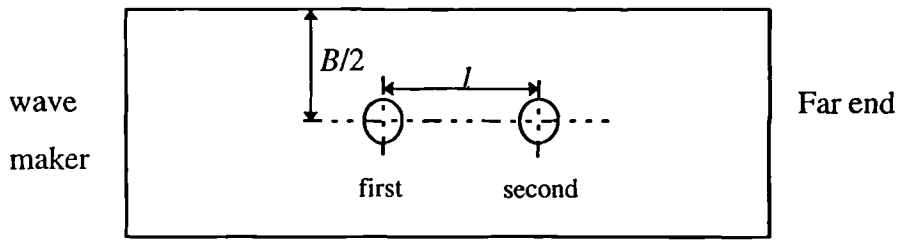

Figure 8.6.1 Sketch of the two-cylinder problem

It is not intended to extensively investigate the interaction between the two cylinders here. Application of the method developed in this thesis to this problem is to further validate it and to demonstrate its flexibility. When the numerical method is used for the two-cylinder problem, no new techniques are required rather than those used for dealing with the single-cylinder problem, although the mesh generation for the two-cylinder case is slightly more complicated. For these reasons, the following presentation will be focused on the numerical results for the case with the various parameters defined as follows: the frequency and the amplitude of the wavemaker are specified as $\omega = 1.6748$

and $a = 0.004$, respectively; two identical vertical circular cylinders of radii $R_0 = 0.1416$ (corresponding to $kR_0 = 0.4$) are situated at the centreline of the tank with the distance (l) between their centres being varied; the distance from the wavemaker to the centre of the first cylinder is about 6.35 while the distance from the centre of the second cylinder to the far end is about 5; the width of the tank is set as $B = 2.832$. All of the given parameters have been nondimensionalised as in equation 7.4.17. The sketch of the problem is illustrated in Figure 8.6.1.

A linearised analytical solution for multiple cylinders in the open sea has been presented by Spring & Monkmeyer (1974) based on the exact formulation, and by McIver & Evans (1984) based on an approximation. In particular, the latter paper gave various results for two cylinders. According to the examples presented therein, the force on the first cylinder is clearly affected due to the presence of the second cylinder, while the influence of the first cylinder on the second is almost negligible when $kl \geq 2$. Their solution is used here for comparison with our numerical results. To do so, the Fourier analysis is performed on the time history of the force in the periodic state to obtain the first harmonic component.

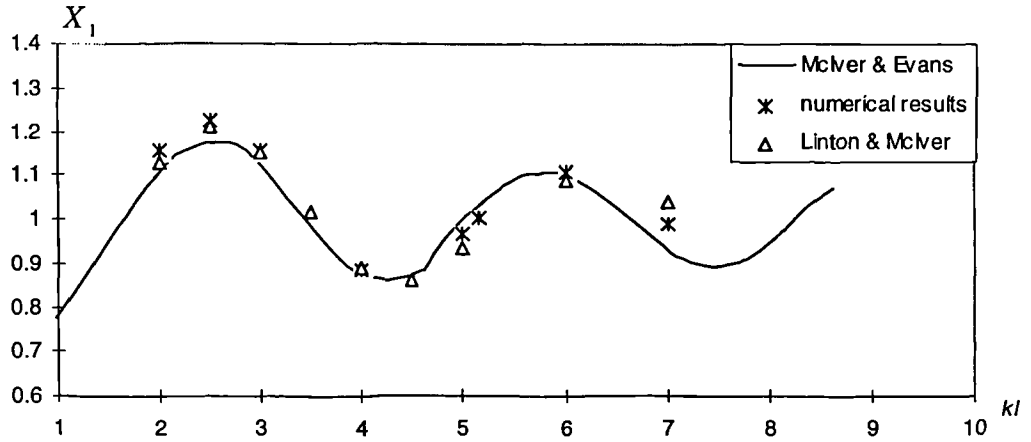

Figure 8.6.2 Comparison of the numerical force on the first cylinder with the analytical solutions

The comparison between the numerical results and the analytical solutions is presented in Figure 8.6.2, where the solid line is for the analytical solution taken from McIver & Evans (1984). In this figure, $X_1 = F_{x1}/F_x$ is the ratio of the force (F_{x1}) in

the x-direction on the first cylinder to the same force (F_x) on a single cylinder. The numerical results of X_1 are calculated from the force F_{x1}, and F_x obtained in the same tank without the second cylinder. This figure shows that the results agree well with the analytical solution, although some difference is visible. It should be noticed that the solid line corresponds to the force in the open sea, and thus the difference may result from the effects of the walls of the tank. A body of work has been devoted to the effects of the walls by considering an array of cylinders in a channel, based on the linear theory. One of the papers is that by Linton and McIver (1996), who used the multipole method and presented the analytical results for the force on two cylinders against different values of $kB/2\pi$ for $2R_0/B = 1/12$ and $2l/B = 0.5$. They carried out some additional calculations for the case concerned here, and kindly provided and agreed for us to publish their results which are also plotted as triangles in Figure 8.6.2. Evidently the numerical force is closer to the solution of Linton and McIver (1996).

It is also useful to present other results from the numerical simulation, such as the time history of the force and the wave profiles, but it is not attempted to give all the results corresponding to different values of kl. In the following, results of this type are presented only for the case with $kl = 2$. Figure 8.6.3 illustrates the time history of the forces on the two cylinders, while Figure 8.6.4 illustrates the time history of the moments on the cylinders about the bottom of each. The moments are nondimensionalised as $f_m = \dfrac{N_y}{\rho g a d R_0^2}$, where N_y is the component of the moment in the y-direction. It can be seen that the shapes of the curve of the moment history are very similar to those of the force history. For this reason, we present only the force for most cases in this thesis. In order to illustrate the three dimensional views of the wave in the tank, Figures 8.6.5 and 8.6.6 are plotted. The former shows the wave profiles in the whole tank, while the latter is the corresponding local view around the cylinders.

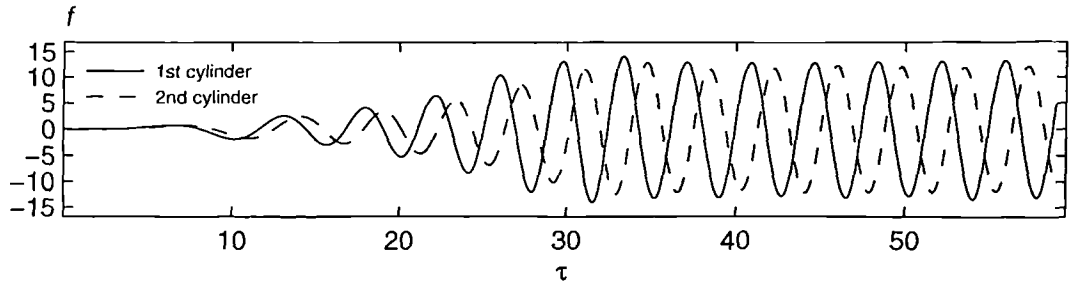

Figure 8.6.3 The time history of forces on two cylinders ($kl = 2$)

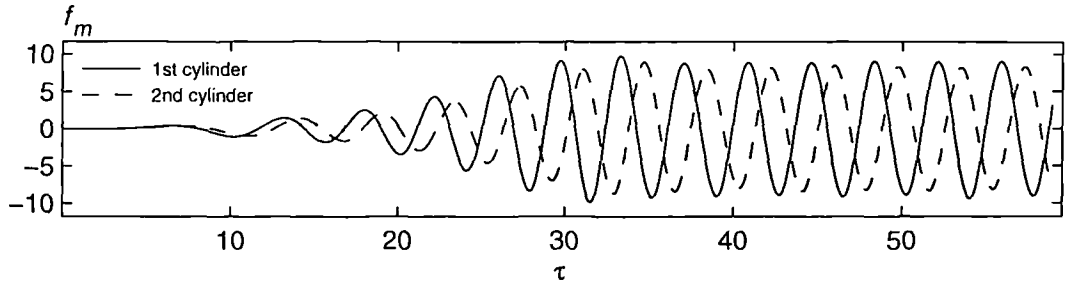

Figure 8.6.4 The time history of moments $f_m = \dfrac{M_y}{\rho g a d R_0^2}$ about the bottom of each cylinder ($kl = 2$)

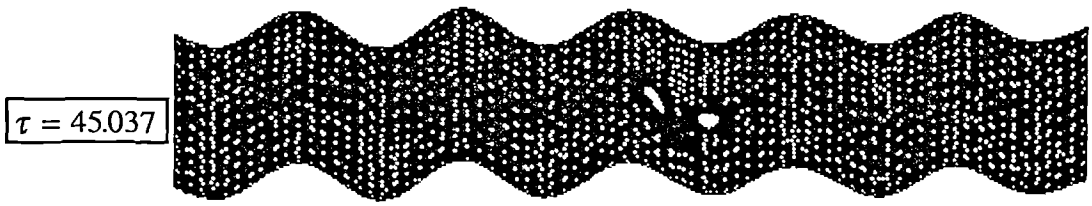

Figure 8.6.5 (a)

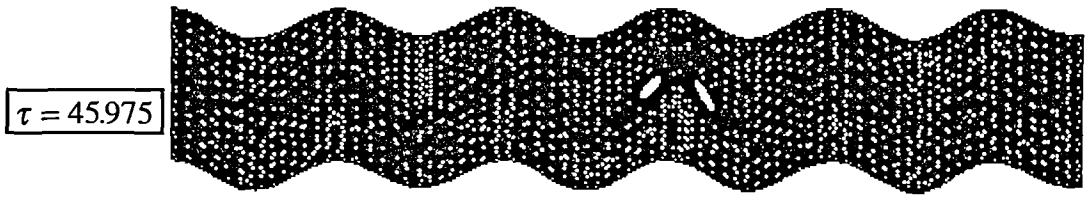

Figure 8.6.5 (b)

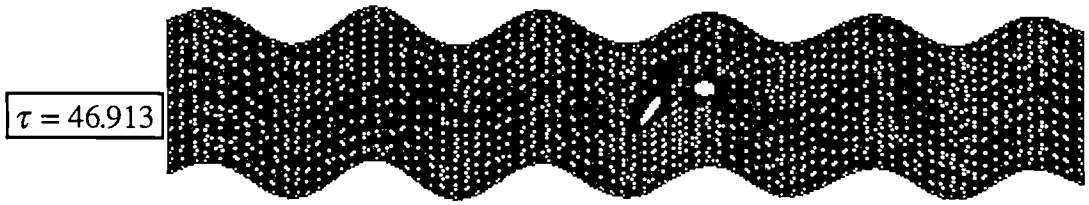

Figure 8.6.5 (c)

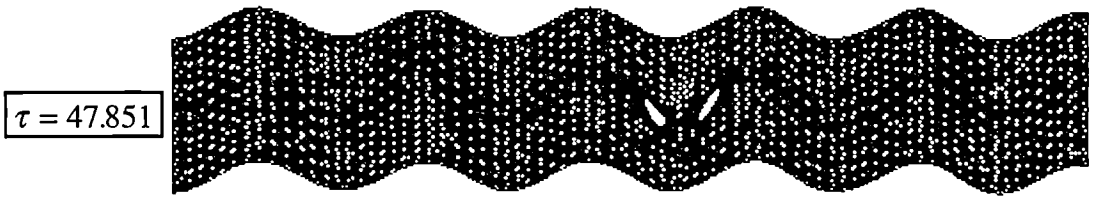

Figure 8.6.5 (d)

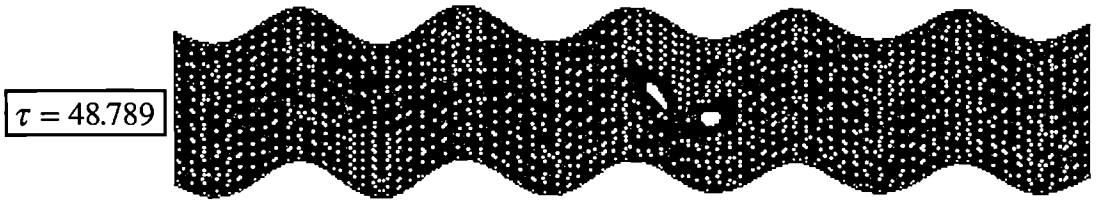

Figure 8.6.5 (e)

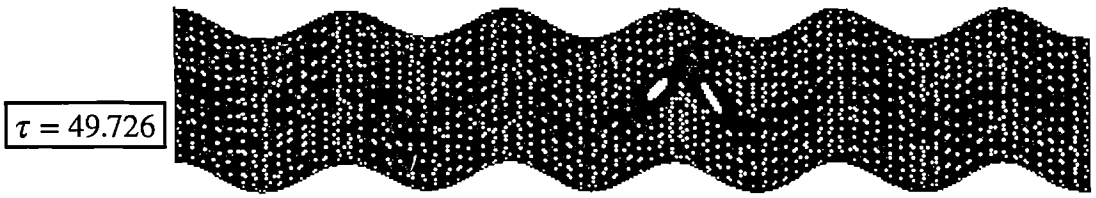

Figure 8.6.5 (f)

Figure 8.6.5 Snapshots of the wave profiles in whole tank ($kl = 2$)

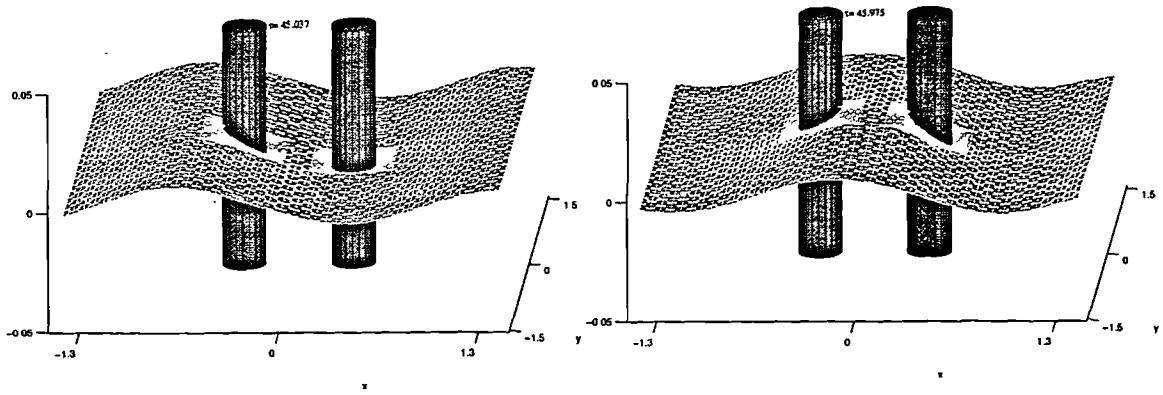

Figure 8.6.6 (a)

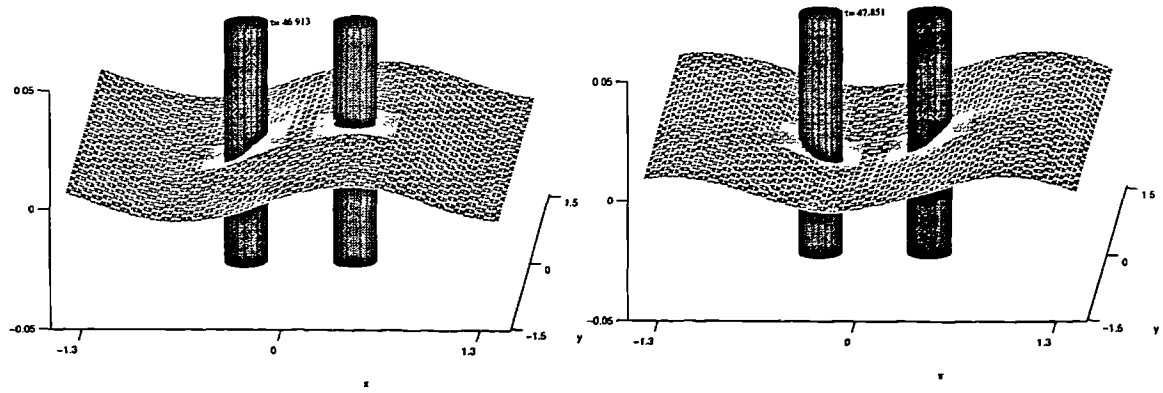

Figure 8.6.6 (b)

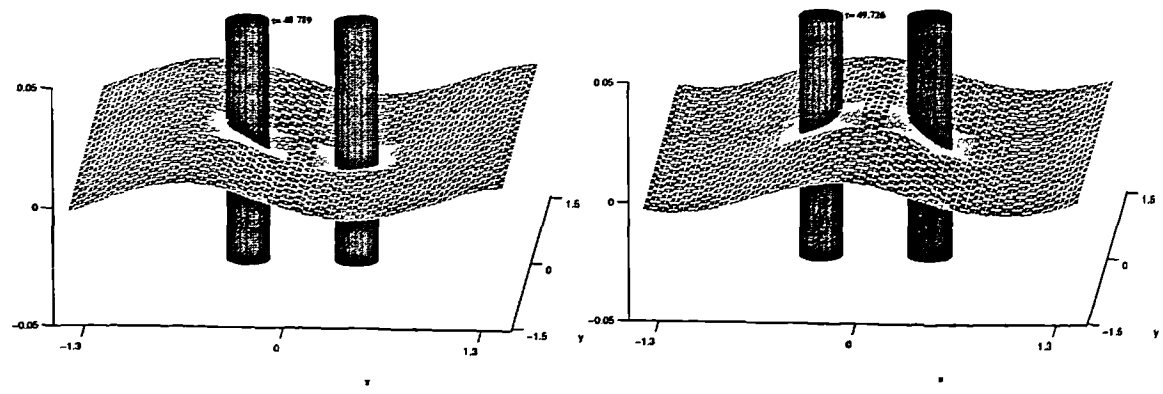

Figure 8.6.6 (c)

Figure 8.6.6 Snapshots of the wave profiles around the two cylinders ($kl = 2$)

9. CONCLUSION AND RECOMMENDATIONS

In this study, a methodology and the corresponding numerical algorithm have been developed to simulate the three dimensional interaction between structures and steep waves by the time marching procedure based on fully nonlinear potential theory. The main feature is that the boundary value problem at each time step is solved by a finite element method. The problem is numerically formulated by transforming the Laplace equation and the boundary conditions of the fluid flow into an integral equation, and by imposing the equation on tetrahedral elements discretising the fluid domain. On each element, the unknown velocity potential is simply assumed to be linear, and is determined by the potential values at the nodes. These nodal values are solved from an algebraic equation, in which the influence coefficients are easily evaluated, as shown in Chapter 5. The computer code has been developed during the course of this study and has been applied to two kinds of wave problems which are of interest to the offshore engineers and naval architects.

Numerical results have been compared with analytical solutions in several cases and good agreement has been achieved. The flexibility of the numerical method has been demonstrated by different computational domains, such as circular domains, rectangular domains and their combinations. It has also been illustrated by varying different methods to generate waves, including the initial free surface elevation, the motion of the tank and the motion of a wave maker, and by dealing with different types of waves: standing waves, sloshing waves, progressive waves (monochromatic, bichromatic or irregular), or their combination. All of the results presented in this thesis have been obtained on Alpha workstations.

In conclusion, the developed methodology based on the finite element method is shown to be a good alternative to the existing techniques for the simulation of steep waves. Its accuracy, flexibility and efficiency demonstrated by various numerical examples appears to be quite favourable.

9.1 Numerical algorithm

In addition to the numerical formulation of the boundary value problem using the finite element method, other associated numerical techniques are also discussed. The technique for the time integration, necessary to update the information on the free surface, is based on an open trapezoidal rule, in which the information at two time steps are used. The tests carried out in this work suggests that the scheme works well, although it is relatively simple.

The fluid velocity is evaluated by a differential method, using the nodal values of the velocity potential. Various cases tested showed that this method is easy to use and can give very accurate results. However, the method is suitable only for the type of mesh used in this thesis.

A patch recovery technique is adopted to postprocess the finite element solutions. The main idea of the technique is that the velocity is assumed to be fitted by a polynomial over a patch of elements on the free surface. The coefficients included in the polynomial are obtained by a least-square method. This technique can improve the accuracy of numerical results without increasing the number of elements, as shown in Chapter 5.

The efficiency of the numerical simulation of concern in this thesis largely depends upon the efficiency of solving the algebraic equations. There are a large number of techniques available for solving the equations, but the efficiency of each method is indeed problem-dependent. Application of FEM to steep-wave problems is currently being investigated. In order to chose an efficient solver, a direct method and an iterative method with two different preconditioners have been studied and compared with each other. The results obtained so far suggest that the conjugate-gradient iterative method with SSOR preconditioner is the most suitable to the problems of concern here. An artificial coefficient is included in this preconditioner, a proper value of which has been recommended following numerical tests. Compared to the Choleski factorisation direct method, the iterative method requires ten times as little CPU time and storage memory in some cases considered in this thesis.

In order to calculate the hydrodynamic forces (and the moments), an integrated method is suggested , in which the integration over the body surface is replaced by the integration over the free surface, the truncated surface (fixed) and the body surface. As

discussed in Chapter 4, this method can overcome the difficulties associated with treating the time derivative of the velocity potential, but it can only be used in cases where the integration over the truncated surface can be conveniently obtained. A direct-force method is also examined, in which the time derivative of the velocity potential is found by solving a boundary value problem similar to that for the potential itself. This method requires a higher computational cost than the former one, but the limitations with the former do not exist here. The test case used in Chapter 7 shows that these two methods can give graphically indistinguishable results. The comparisons made in Chapter 8 confirm that the calculated forces agree well with corresponding analytical solutions.

9.2 Application to sloshing waves

The developed method is first applied to simulate sloshing waves, generated either by the initial free-surface elevation in a circular tank with or without an inner cylinder, or by the translational motion of a rectangular tank. For the circular tank case, an analytical solution in time domain is derived based on second order perturbation theory, which provides a tool for the validation. The numerical results have been compared with this analytical solution and very good agreement has been found.

For the case of sloshing waves generated by a moving rectangular tank, the obtained numerical results have been compared with some published data and good agreement has also been achieved. When simulating the cases in which the tank moves in two and three directions, some interesting results have been observed. As presented in Section 7.4.3, the transient waves caused by the vertical oscillation, with an initially prescribed perturbation in horizontal direction, seem to depend only on the amplitude of the acceleration of the tank. When the water depth is relatively shallow, the travelling waves are shown by the numerical simulation. Moreover, in the extremely shallow water, three dimensional bores with undulations have been seen to occur. All of these demonstrate significant effects of nonlinearity.

Although these simulations were not directly associated with particular engineering problems, it seems to be quite straightforward to use the method for the wave motion in a storage tank and in a reservoir undergoing an earthquake, for the trapped waves in harbours, and for the liquid motion in a vehicle. It may also be used to simulate the

motion of the water on deck of ships if the angular motions are included by necessary extension.

9.3 Application to the interaction between progressive waves and cylinders.

In the second application, the interaction between vertical circular cylinders and progressive waves is simulated. The wave is generated by a wave maker in a tank. At the far end (i.e. opposite end to the wave maker), the radiation condition is modelled by the combination of the damping zone and the Sommerfeld condition. The artificial viscous coefficient included in the damping zone is optimised and is related to the frequency by a fitted formula, and thus the coefficient can be automatically evaluated when the frequency is specified. The numerical results have shown that the reflection from the far end is negligible in various cases tested, including not only monochromatic waves but also bichromatic and narrow-band irregular waves.

The nonlinearity has been examined by comparing waves generated by different amplitudes of the wavemaker. It is shown that when the amplitude is sufficient large, the so-called amplitude-dispersion phenomenon can be observed in addition to the troughs and crests becoming flat and sharp, respectively.

The forces have been evaluated for cases where one or two cylinders subject to the generated waves are involved. When the wave is small, the obtained forces agree very well with published analytical solutions. The nonlinear effects on the forces are investigated by using Fourier analysis and the nonlinear contribution is clearly demonstrated in several cases.

The numerical results have shown that when the incoming wave is large enough, very steep local waves (somewhat like bores) may appear around the cylinder due to the nonlinear effects. These local waves seems to contribute to the nonlinear behaviour of the force.

In this work, some preliminary results for the interaction between cylinders and waves have been obtained. However, these results indicates that it may be possible to apply the developed method to many practical problems like the evaluation of ringing-loading on monotower platforms and four-leg fixed structures. It could also be used to study the interaction between the columns of the two- or four-leg structures under head seas.

9.4 Recommendations

With respect to future work on the development and extension of the numerical method, the following is recommended:

1). Structured meshes have been used throughout this thesis. They can lead to good results and can be generated very efficiently. In order to simulate more complicated situations, such as breaking waves, more sophisticated mesh-generation techniques should be employed. Adaptive meshes based on an octree technique, as discussed by Greaves (1995), may be an appropriate option.

2). The method for computing the velocities suggested in Chapter 5 appears to be quite accurate and efficient, as demonstrated in various cases. Nevertheless, this method may not be applicable when unstructured meshes are used and when extremely steep waves or breaking waves are simulated. Galerkin formulation for the velocities or a least-square-based method may be suitable for these cases, as suggested and used by Wu and Eatock Taylor (1994) for two dimensional cases. However, their efficiency and accuracy should be investigated for three dimensional cases.

3). Although the numerical results have been compared with some analytical solutions and with some experimental data quantitatively and qualitatively, further validation using experiments are desired, particularly for cases with strong nonlinear effects such as the bores with undulations and local waves around cylinders.

4). All of the test cases were confined to a tank. The extension to problems in the open sea may be possible by applying a similar radiation condition discussed in Chapter 8 to all truncated boundaries.

5). The methodology may also be extended to investigate other problems in many fields of research. One of these is the interaction of the steep waves with moving bodies, such as TLPs, ships and mooring storage tanks. Similar wave problems with viscous effects could be considered by applying the finite element method to the Navier-Stokes equations. Other moving boundary problems, such as two phase fluid flow, could also be possible extensions of this method.

REFERENCES

Abramson, H.N. 1966, "The dynamic behaviour of liquid in moving containers". Report SP 106 of NASA.

Arai, M., Paul, U.K., Cheng L.Y. & Inoue Y., 1993, "A technique for open boundary Treatment in numerical wave tanks", *J. Society of Naval Architects of Japan*, Vol.173, pp.45-50.

Armenio, V. & La Rocca, M., 1996, "On the analysis of sloshing of water in rectangular containers: numerical study and experimental validation", *Ocean Eng.*, Vol. 23, No. 8, pp705-739.

Axelsson, O. , 1976, "Solution of linear systems of equations: iterative methods". In *Sparse Matrix Techniques*, ed. V.A. Barker. Berlin: Springer-Verlag.

Axelsson, O. , 1994, "Iterative solution methods". Cambridge University Press.

Bai, K.L. & Yeung, R.W., 1974, "Numerical solutions of free surface problems", *Proc. 10th Symp. Naval Hydro.*, pp. 573-596.

Baker, G.R., Meiron, D.I. & Orszag, S.A., 1981, "Generalised vortex methods for free surface flow problem", *J. Fluid Mech.* Vol.123, pp477-501.

Bayliss, A. & Turkel, E., 1982, "Far field boundary conditions for compressible flows", *J. Comp. Physics*, Vol.48, pp.182-199.

Beck, R.F, 1994, "Time domain computations for floating bodies", *Applied Ocean Res.*, Vol. 16, pp. 267-282.

Beck, R.F., Cao, Y., Scorpio, S., & Schultz, W.W.,1994, "Nonlinear ship motion computations using the desingularised method", *Proc. 20th Symp. Naval Hydro., U.C., Santa Barbara, CA.*

Beck, R.F. & Liapis, S., (1987), "Transient motions of floating bodies with forward speed", *J. Ship Res.*, Vol. 31, pp. 164-176.

Beck, R.F. & Magee, A.R., 1990 , "Time domain analysis for predicting ship motions", *Proc. IUTAM Symp. Dynamics of Marine Vehicle and Structures in Waves*, London.

Benjamin, T.B. & Ursell, F., 1954, "The stability of the plane free surface of a liquid in vertical periodic motion", *Proc. Roy. Soc. Lond.* A. 225, pp. 505-515.

Bettess. P.L. & Mohamad, T.T., 1982, "Water waves: a time varying unlinearized boundary element approach", *Proc. 4th Int. Symp. on Finite Element Methods in Flow Problems*, Tokyo, pp923-929.

Bingham, H.B., Korsmeyer, F.T. & Newman, J.N., 1994, "Predicting the seakeeping characteristics of ships", *Proc. 20th Symp. Naval Hydro.*, Santa Barbara.

Bratland, A.K., Korsmeyer, F.T. & Newman, J.N., 1997, "Time domain calculation in finite water depth", *12th international Workshop on Water Waves and Floating Bodies*, Carry-le-Rouet, France.

Broeze, J, & Romate, J.E., 1992, "Absorbing boundary condition for free surface wave simulations with a panel method", *J. Comp. Physics*, Vol. 99, pp. 146-158.

Bruaset, A.M., 1995, "A survey of preconditioned iterative methods", *Pitman Research Notes in Mathematics Series, Longman Scientific & Technical*

Cai, X., Langtangen, H.P., Nielsen, B.F. & Tveito, A. 1998, "A finite element method for fully nonlinear water waves", *J. Comp. Physics*, 1998, Vol.143, No.2, pp.544-568.

Cao, Y., Beck, R.F. & Schultz, W.W.,1994, " Nonlinear computation of waves loads and motions of floating bodies in incident waves," *9th Workshop on Water Waves and Floating Bodies*, Kuju, Oita, Japan.

Cao, Y., Beck, R.F. & Schultz, W., 1993, "An absorbing beach for numerical simulation of non-linear waves in a wave tank", *8th Workshop on Water Waves and Floating Bodies*, St. John's, Newfoundland

Cao, Y., Schultz, W.W. & Beck, R.F., 1991, "Three-dimensional desingularised boundary integral method for potential problems", *International Journal for Numerical Methods in Fluid*, Vol. 12, pp. 785-803

Chan, R.K.-C, 1975, "Two dimensional time dependent calculations of large amplitude surface gravity waves due to a surface disturbance", *Proc. 1st Int. Conf. on Numerical Ship Hydrodynamics*, Bethesda, Maryland, pp315-331.

Chan, R.K.-C., 1977, "Finite difference simulation of the planar motion of a ship", *Proc. 2nd Int. Conf on Numerical Ship Hydrodynamics*, Berkeley, Calif. USA, pp39-56.

Chan, J.L.K & Calisal, S.M., 1993, "A numerical procedure for time domain nonlinear surface wave calculations", *Ocean Eng.*, Vol.20, No.1, pp19-32.

Chaplin, J.R., Rainey, R.C.T. & Yemm. R.W., 1997, "Ringing of a vertical cylinder in waves", *J. Fluid Mech.*, 1997, Vol.350, pp.119-147

Chen, W. Haroun, M.A. & Liu, F., 1996. "Large amplitude liquid sloshing in seismically excited tanks", *Earthquake Engineering and Structural Dynamics*, Vol. 25, pp. 653-669.

Celebi, M.S. & Kim, M.H., 1997, "Nonlinear wave-body interactions in a numerical wave tank", *12th International Workshop on Water Waves and Floating Bodies*, Carry-le-Rouet, France.

Chester, W., 1968, "Resonant oscillation of water waves, Part I: Theory", *Proc. Roy. Soc.* A. 306, pp. 5-22.

Chester, W. & J.A. Bones, 1968, "Resonant oscillation of water waves, Part II: Experiment", *Proc. Roy. Soc.* A. 306, pp. 23-39.

Clark, P.J., Bettess, P., Hearn, G.E. & Downie, M.J., 1991, "The application of finite element analysis to the solution of Stokes wave diffraction problems", *Int. J. for Numerical Method in Fluids*, Vol. 12, pp. 343-367.

Clement, A. & Domgin, J.F, 1995, "Wave absorption in a 2-D numerical wave basin by coupling two methods", *10th International Workshop on Water Waves and Floating Bodies*, Oxford, UK.

Clement, A., 1996, "Coupling of two absorbing boundary conditions for 2D time-domain simulations of free surface gravity waves", *J. Comp. Physics*, Vol. 126, pp. 139-151.

Clement, A., 1997, "A shortcut for computing time-domain free-surface potentials avoiding Green function evaluation", *12th International Workshop on Water Waves and Floating Bodies*, Carry-le-Rouet, France.

Cointe, R., Geyer, P., King, B., Molin, B. & Tramoni, M., 1990, "Nonlinear and linear motions of a rectangle barge in a perfect fluid," *Proc. 18th Symp. Naval Hydro.*, Univ. of Michigan, Ann Arbor, pp. 85-98.

Contento, G. & Casole, S., 1995, "On the generation and propagation of waves in 2D numerical wave tanks", *ISOPE'95*, The Netherlands, Vol.3 pp10-18.

Cooker, M.J., Weidman, P.D. & Bale, D.S., 1997, "Reflection of a high-amplitude solitary wave as a vertical wall", *J. Fluid Mech.* Vol. 342, pp. 141-158.

Crapper, G.D., 1984, "Introduction to water waves", Ellis Horwood, LtD.

Dommermuth, D.G., & Yue, D.K., 1987b, "Numerical simulations of nonlinear axisymmetric flows with a free surface", *J. Fluid Mech.* Vol.178, pp. 195-219.

Eatock Taylor, R. & Hung, S.M., (1987), "Second order diffraction forces on a vertical cylinder in regular waves", *Applied Ocean Res.* Vol. 9, pp.19-30.

Eatock Taylor, R. & Zeitsman, J., 1982, "Hydrodynamic loading on multi-component bodies", *BOSS*, pp.424-443.

Eatock Taylor, R, Wang, B.T. & Wu, G.X., 1994, "On the transient analysis of the wavemaker", *9th International Workshop on Water Waves and Floating Bodies*, Japan.

Faltinsen, O.M., 1978, "A numerical non-linear method of sloshing in tanks with two dimensional flow", *J. Ship Res.*, Vol. 18, No. 4, pp224-241.

Faltinsen O.M., 1977 "Numerical solution of transient nonlinear free surface motion outside or inside moving bodies", *Proc. 2nd International conference on Numerical ship hydrodynamics*, U.C. Berkeley, Calif., USA, pp.347-357.

Faltinsen, O.M., 1990, "Sea loads on Ships and Offshore structures", Cambridge University Press.

Faltinsen, O.M., Newman, J.N.& Vinje, T., 1995, "Nonlinear wave loads on a slender vertical cylinder", *J. Fluid Mech.*, Vol.289, pp.179-198

Ferrant, P. 1988, "A fast computational method for transient 3D wave-body interactions", in *Computer modelling in Ocean Engineering*, pp.463-470. Balkema: Rotterdam.

Ferrant, P., 1994, "Radiation and diffraction of nonlinear waves in three dimensions", *BOSS*, MIT, pp.507-524.

Ferrant, P., 1995, "Nonlinear wave loads and runup upon a surface piercing cylinder", *10th International Workshop on Water Waves and Floating Bodies*, Oxford, UK.

Greaves, D.M., 1995, "Numerical modelling of laminar separated flows and inviscid steep waves using adaptive hierarchical meshes", *DPhil thesis, University of Oxford.*

Greenhow, M. & Lin, R.M., 1985, "Numerical simulation of nonlinear free surface flows generated by wedge entry and wavemaker motion", *Proc. 4th International Conference on Numerical Ship Hydrodynamics*, Washington, D.C.

Greenhow, M. 1987, "Wedge entry into initially calm water", *Applied Ocean Res.* Vol.9, pp214-223

Grue, J. & Palm, E., 1993, "The mean drift force and yaw moment on marine structures in waves and current", *J. Fluid Mech.*, Vol.250, pp. 121-142

Haussling, H.J. & Coleman, R.M. 1977, "Finite-difference computations using boundary-fitted coordinates for free-surface potential flows generated by submerged bodies", *Proc. 2nd International conference on Numerical Ship Hydrodynamics*, Berkeley, Calif.

Haussling, H.J. & Coleman, R.M. 1979, "Nonlinear water waves generated by an accelerated circular cylinder", *J. Fluid Mech.*, Vol.92, pp757-781.

Huang, J.B. & Eatock Taylor, R., 1996 "Semi-analytical solution for second-order wave diffraction by a truncated circular cylinder in monochromatic waves", *J. Fluid Mech.*, Vol.319, pp. 171-199.

Huang, J.B. & Eatock Taylor, R., 1997, "Evaluation of second-order forces on an array of truncated cylinders by a semi-analytical method", *OMAE*, 1997, Vol.1, pp.401-408.

Huang. Z.J. & Hsiung, C.C. 1996, "Nonlinear shallow-water flow on deck". *J. Ship Res.*, Vol. 40, No. 4, pp303-315.

Hung, S.M. & Eatock Taylor, R., 1987, "Second order time harmonic forces on bodies in waves", 2nd *International Workshop on Water Waves and Floating Bodies*, Bristol, UK.

Hunt, J.N. & Baddour, R.E., 1981, "Diffraction of nonlinear progressive waves by a vertical cylinder", *Q. J. Mech. Math.*, Vol. 34, pp. 69-87.

Hunt, J.N. & Baddour, R.E., 1980, "Nonlinear standing waves bounded by cylinders", *Q. J. Mech. Math.*, Vol. 33, pp. 357-371.

Isaason. M. St. Q. 1982, "Nonlinear wave effects on fixed and floating bodies", *J. Fluid Mech.* Vol.120, pp267-281.

Isaacson, M., & Cheung, K.F., 1990, "Time-domain solution for second-order wave diffraction", *J. Waterway, Port, Coastal and Ocean Engineering*, Vol.116, No.2, pp.191-210.

Isaacson, M., & Cheung, K.F., 1991, "Second order wave diffraction around two-dimensional bodies by time domain method", *Applied Ocean Res.*, Vol. 13, pp.175-186.

Isaacson, M., & Ng., J.Y.T. , 1993, "Time-domain second-order wave radiation in two dimensions", *J. Ship Res.*, Vol.37, No.1, pp.25-33.

Israeli, M. & Orszag, S.A., 1981, "Approximation of radiation boundary condition", *J. Comp. Phys.*, Vol.41, pp.115-135.

Jefferys, E.R. & Rainey, R.C.T, 1994, "Slender body Models of TLP and GBs Ringing", *BOSS*, Vol.2, pp587-605.

Jones, A.F. & Hulme, A., 1987, "The hydrodynamics of water on deck", *J. Ship Res.*, Vol. 31, No. 2, pp. 125-135.

Jiang, L., Ting, C.L., Perlin, M. & Schultz, W., 1996, "Moderate and steep Faraday waves: instabilities, modulation and temporal asymmetries", *J. Fluid Mech.*, Vol. 329, pp. 275-307.

Kang, C.-G. & Gong, I.-Y., 1990, "A numerical solution method for three-dimensional nonlinear free surface problems", *Proc. 18th Symp. Naval Hydro.*, Ann, Arbor, Michigan, pp427-430.

Kang, C.-G. & Troesch, A.W., 1988, "Nonlinear interaction between axisymmetric bodies and free surface in water of finite depth", *Seminar on Ship Hydrodynamics in Honour of Professor J.H. Hwang, Seoul, Korea.*

Korn, G.A & Korn, T.M, 1968: "Mathematical Handbook for Scientists and Engineers", McGraw-hill Book Company, New Yok.

Krokstad, J.R. & Stansberg, C.T., 1995, "Ring load models verified against experiments", OMAE'95, Vol.1, pp.223-233.

Lee, J.F. & Leonard, J.W., 1987, "A time-dependent radiation condition for transient wave-structure interactions", *Ocean Eng.*, Vol. 14, No. 6, pp. 469-488.

Lennon, G.P., Liu, Ph.L.-F., & Ligget, J.A., 1982, "Boundary integration solutions of water wave problem", *J. Hydraulic Div., Proc. of ASCE*, Vol.108, pp921-931.

Lin, W.M., Newman, J.N. & Yue, D.K., 1984, "Nonlinear forced motion of floating bodies," *Proc. 15th Symp. Naval Hydro.*, Hamburg, Germany, pp33-49.

Linton, C.M. & McIver, P., 1996, "The scattering of the water waves by an array of circular cylinders in a channel", *Journal of Engineering Mathematics*, Vol. 30, pp.661-682.

Linton, C.M. & Evans, D.V., 1992, "The radiation and scattering of surface waves by a vertical circular cylinder in a channel", *Philosophical Transactions Of The Royal Society Of London. A*, Vol. 338, pp. 325-357.

Longuet-Higgins, M.S. & Cokelet, E.D., 1976, "The deformation of steep surface waves on water: I. a numerical method of computation", *Proc. R. Soc. London*, A Vol.350, pp.1-26.

Ma, Q.W, Wu, G.X. & Eatock Taylor, R.,1997. "Finite element analysis of the non-linear transient waves in three dimensional long tank". *12th International Workshop on Water Waves and Floating Bodies*, Carry-le-Rouet, France.

MacCluer, C.R., 1994, "Boundary Value Problems and Orthogonal Expansions", IEEE Press.

Maisondieu, C. & Clement, A., 1993, "A realisable force feedback-feedforward control loop for a piston wave absorber", *8th International Workshop on Water Waves and Floating Bodies*, St. John's, Newfoundland.

Malenica, S. & Molin, B., 1995, "Third-harmonic wave diffraction by a vertical cylinder", *J. Fluid Mech.*, Vol.302, pp.203-229.

Manteuffel, T.A., 1980, "An incomplete factorisation techniques for positive definite linear systems", *Mathematics of Computation*, Vol. 34, No. 150, pp473-497.

Marion, J.B., 1965, "Classical Dynamics", Academic Press, London.

Maskell, S.J. & Ursell, F., 1970, "The transient motion of a floating body ", *J. Fluid Mech.*, Vol.44, No.2, pp.303-313.

Mayer, S., Garapon, A. & Sorensen, L., 1997, "Wave tank simulations using a fractional-step method in a cell-centred finite volume implementation", *12th International Workshop on Water Waves and Floating Bodies, Carry-le-Rouet.*

McIver, P. & Evans, D.V., 1984, "Approximation of wave forces on cylinder arrays", *Applied Ocean Res.*, Vol. 6, No.2, pp. 101-107.

McIver, P, 1994, "Transient fluid motion due to the forced horizontal oscillations of a vertical cylinders", *Applied Ocean Res.* Vol. 16, pp. 347-351.

Mei, C.C. 1989, "The Applied Dynamics of Ocean Surface waves", World Scientific.

Meijerink, J.A. & H.A., van der Vorst, 1977, "An iterative solution method for linear system of which the coefficient matrix is a symmetric M-matrix", *Math. Comput.* Vol. 31, pp. 148-162

Miles, J.W. & Henderson, D.M., 1990, "Parametrically forced surface waves", *Ann. Rev. Fluid Mech.*, Vol. 22, pp.143-165.

Nagai, S., 1969, "Pressure of standing waves on vertical walls", *J. Waterways and Harbours Div. ASCE 95*, WW1, pp. 53-76.

Nakayama, T. & Washizu, K., 1980, "Nonlinear analysis of liquid motion in a container subjected to forced pitching oscillations", *Int. J. for Numerical Method in Fluids*, Vol. 15, pp. 1207-1220.

Newman, J.N. 1967, "The drift Force and Moment on ships in waves", *J. Ship Res.*, Vol.11, pp.51-60

Newman, J.N., 1977, "Marine Hydrodynamics," MIT press.

Newman, J.N. 1993, "Wave drift damping of floating bodies", *J. Fluid Mech.* Vol. 249, pp51-60.

Ng, J.Y.T. & Isaacson, M., 1993, "Time-domain second-order diffraction-radiation by two-dimensional floating bodies", *Proc. 3rd International Offshore and Polar Engineering Conference*, pp.368-375.

Ohyama, T., 1991, "Development of a numerical wave tank for analysis of non-linear and irregular wave field", *Fluid Dynamics Research*, Vol. 8, pp231-251.

Okamoto, T. & Kawahara, M. 1990, "Two-dimensional sloshing analysis by Lagrangian finite element method", *International Journal for Numerical Methods in Fluids*, Vol. 11, pp453-477.

Orlanski, I., 1976, "A simple Boundary condition for unbounded hyperbolic flows". *J. Comp. Physics*, Vol.21, pp251-269.

Peregrine, D.H., 1972, "Flow due to vertical plate moving in a channel", Unpublished note.

Peregrine, D.H., 1966, "Calculations of the development of an undular bore", *J. Fluid Mech.*, Vol. 25, pp. 321-330.

Pissanetzky, S., 1984, "Sparse matrix technology", Academic Press.

Rainey, R.C.T. 1997, "Violent surface motion around vertical cylinders in large, steep waves- is it the result of the step change in relative acceleration? ", *12th International Workshop on Water Waves and Floating Bodies, Carry-le-Rouet.*

Reddy, J.N., 1984, "An introduction to the finite element method", Mcgrow-Hill Book Company.

Romate, J.E. 1989,"The Numerical simulation of nonlinear gravity waves in three dimensions using a higher order panel method", PhD Thesis, University of Twente, Enschede, The Netherlands.

Romate, J.E., 1992, "Absorbing boundary conditions for free surface waves", *J. Comp. Physics*, Vol.99, pp.135-145.

Sarpkaya, T. & Issacson, M.St.Q., 1981, "Mechanics of Wave Forces on Offshore Structures", Van Nostrand Reinold, New York.

Sclavounos, P.D. & Kim, Y.W. 1995, " Third order diffraction of surface waves by a time-domain ranking panel method", *10th International Workshop on Water Waves and Floating Bodies*, Oxford, UK.

She, K., Greated. C.A. & Easson, W.J., 1992, "Development of a two-dimensional numerical wave tank", *Proc. 2nd International offshore and Polar Engineering Conference*, San Francisco, USA, Vol.3, pp102-109.

Sen, D., 1993, "Numerical simulation of motions of two-dimensional floating bodies", *J. Ship Res.*, Vol.37, No.4, pp307-330.

Skourup, J., Buchmann, B. & Bingham, H., 1997, "A second order 3D BEM for wave-structure interaction", *12th International Workshop on Water Waves and Floating Bodies, Carry-le-Rouet*, France.

Skourup, J. & Schaffer, H.A., 1997, "Wave generation and active absorption in a numerical wave flume", *Proceedings of the International Offshore and Polar Engineering Conference*, 1997, Vol.3, pp.85-91.

Solaas, F., 1995, "Analytical and numerical studies of sloshing in tanks", PhD thesis, Department of Marine Hydrodynamics, The Norwegian Institute of Technology.

Solaas, F. & Faltinsen, O.M, 1997, "Combined numerical solution for sloshing in two-dimensional tanks of general shape". *J. Ship Res.*, Vol. 41, No.2, pp 118-129.

Spring, B.H. & Monkmeyer, P.L., 1974, "Interaction of plane waves with vertical cylinders", *Proc. 14th International Conference on Coastal Engineering*, Copenhagen, Denmark, ASCE, pp. 1828-1847.

Stansberg, C.T., 1997, "Experimental local wave pattern around cylinder", Private Communication.

Stansberg, C.T., Huse, E., Krokstad, J.R. & Lehn, E., 1995, "Experimental study of nonlinear loads on vertical cylinders in steep random waves", *Proc. 5th Int. Offshore and Polar Engineering Conf.*, Vol. 1, pp 75-82.

Su, T.C. & Wang, Y., 1986, "Numerical simulation of three-dimensional large amplitude liquid sloshing in rectangular containers subjected to vertical excitation", *Seismic*

Engineering for Piping Systems, Tanks and Power Plant Equipment, Vol. 108, ASME, pp. 149-154.

Sulisz, W. & Hudspeth, R.T., 1993, "Complete second-order solution for water waves generated in wave flumes", *J. Fluids and Structures*, Vol. 7, pp. 253-268.

Telste, J.G., 1985, "Calculation of fluid motion resulting from large amplitude forced heave motion of two-dimensional cylinder in a free surface", *Proc. 4th Int. Conf. On Numerical Ship Hydro.*, pp 81-93, Washington, USA.

Tsai, C.P. & Jeng, D.S., 1994, "Numerical Fourier solution of standing waves in finite water depth", *Applied Ocean Res.*, Vol. 16, pp. 185-193.

Ursell, F., 1964, "The decay of the free motion of a floating body", *J. Fluid Mech.*, Vol. 19, pp. 305-319.

Vinje, T. & Brevig, P. 1981, "Nonlinear ship motions", *Proc. 3rd international Conference on Numerical Ship Hydrodynamics*, Paris pp.257-268.

van Daalen, E.F.G, 1993, "Numerical and theoretical studies of water waves and floating bodies", PhD Thesis, University of Twente, Enschede, The Netherlands.

Wang, M.L., Troesch, A.W. & Maskew, B. 1996, "Comparison of two different mixed Eulerian-Lagrangian scheme based on a study of flare-slamming hydrodynamics", *J. Offshore Mechanics and Arctic Engineering*, Vol. 118, pp.175-183

Wang, P., Yao, Y. & Tulin, M., 1995, "An efficient numerical tank for nonlinear water waves, based on the multi-subdomain approach with BEM", *Int. J. for Numerical Method in Fluids*, Vol.20, pp1315-1336.

Wang, X.M., & Spaulding, M.L., 1988, "A two-dimensional potential flow model of the wave field generated by a semi-submerged body in heaving motion", *J. Ship Res.* Vol.32, pp.83-91.

Wang, K.H. & Chwang, A.T., 1989, "Nonlinear free surface flow around an impulsively moving cylinder", *J. Ship Res.* Vol. 33, No.3, pp. 194-202.

Wehausen, J.V. & Laitone, E.V., 1960, "Surface waves", *Handbuck der Physik IX*

Wiberg, N.E., Abdulwahab, F. & Ziukas, S., 1994, "Enhanced superconvergent patch recovery incorporating equilibrium and boundary conditions", *International Journal of Numerical method in Engineering*, Vol. 37, pp. 3417-3440.

Westhuis, J.H. & Andonowati , 1998, "Applying the finite element method in numerically solving the two dimensional free-surface water wave equations", *13th International*

Workshop on Water Waves and Floating Bodies, Alphen aan den Rijn, The Netherlands.

Wu, G.X. & Eatock Taylor, R., 1994, "Finite element analysis of two dimensional non-linear transient water waves," *Applied Ocean Res.*, Vol.16, pp.363-372.

Wu, G.X. & Eatock Taylor, R., 1995, "Time stepping solutions of the two dimensional non-linear wave radiation problem,", *Ocean Eng.* Vol. 22, pp. 785-798.

Wu, G.X., Ma, Q.W., & Eatock Taylor, R., 1995, "Nonlinear Wave Loading on a Floating Body", *10th International Workshop on Water Waves and Floating Bodies*, Oxford, UK.

Wu, G.X. & Ma, Q.W., 1995, " Finite element analysis of nonlinear interactions transient waves with a cylinder", *OMAE'95*, Vol.1, part A, pp329-339.

Wu, G.X. & Eatock Taylor, 1996, "Transient motion of a floating body in steep water waves", *11th International Workshop on Water Waves and Floating Bodies*, Hamburg, Germany.

Wu, G.X. & Eatock Taylor, 1987, "Hydrodynamic forces on submerged oscillating cylinders at forward speed", *Proc. Of the Royal Society of London*, A414, pp. 149-170.

Xue, M. & Yue, D.K., 1995, " Fully nonlinear three dimensional interaction between water waves and a surface-piercing body", *10th International Workshop on Water Waves and Floating Bodies*, Oxford, UK.

Yen, S.M., & Hall, D.R., 1981, "Implementation of open boundary conditions for nonlinear free surface wave problems", *Proc. 3rd Int. Conf. on Numerical Ship Hydrodynamics*, Paris, pp163-176.

Yeung, R.W. & Wu, C.F., 1989, "Nonlinear wave-body motion in a closed domain", *Computers and Fluids* Vol. 17, pp351-370.

Yeung, R.W. & Vaidhanathan, M., 1990, "Nonlinear wave diffraction over submerged obstacles", *5th Workshop on Water waves and Floating Bodies*, Manchester, U.K.

Yim, B., 1985, "Numerical solution for two-dimensional wedge slamming with a nonlinear free surface condition", *Proc. 4th International Conference on Numerical Ship Hydrodynamics*, Washington, D.C.

Zhang, S. & Williams, A.N., 1996, "Time-domain simulation of the generation and propagation of second-order Stokes waves in a two-dimensional wave flume. Part I: Monochromatic wavemaker motions", *J. Fluid and Structure*, Vol. 10, pp. 319-335.

Zhao, R. & Faltinsen, O.M., 1989, "Interaction between current, waves and marine structures", *5th Int. Conf. On Num. Hydrodynamics*. Hiroshima, National Academy Press, Washington.

Zhou, Z. & Gu, M., 1990, "A numerical research of nonlinear body-wave interaction, *Proc. 18th Symp. Naval Hydro.*, Ann Arbor, Michigan. pp.103-117.

Zienkiewicz, O.C. & Taylor, R.L. 1994, "The Finite Element Method", Vol.1 and Vol. 2, McGraw-Hill Book Company.

Zienkiewicz, O.C. & Zhu, J.Z., 1992, "The superconvergent patch recovery and a posterior error estimators. Part 1: The recovery technique", *International Journal of Numerical method in Engineering*, Vol. 33, pp. 1331-1364.

APPENDIX A

Transformation Matrix

Here, the transformation matrix from one Cartisian coordinate system to another will be derived based on Euler angles. Furthermore, the relationship between angular velocity and Euler angles as well as their derivatives will also be given. A similar procedure to that mentioned by Marion(1965) will be employed.

For convenience, we define another coordinate system $o_1x_1y_1z_1$ which is moving with translation. Its origin is the same as that of $o_bx_by_bz_b$, and x_1-, y_1- and z_1- axis is parallel to x-, y- and z-axis respectively, at all times. It is apparent that this system coincides with $o_bx_by_bz_b$ when the body is at rest. However, they will not coincide generally if the body has rotation, as shown in Figure A.1.

Suppose that $o_1x_1y_1z_1$ can be transformed to $o_bx_by_bz_b$ by the following three successive rotations:

(1) The first rotation is about the x_1-axis ($o_1x_1y_1z_1$ to $o_1x_1'y_1'z_1'$) by an angle α. After the rotation, z_1'-axis lies in a plane determined by x_1-axis and z_b-axis, as shown in Figure A.2. The transformation relationship is

$$\begin{Bmatrix} x_1 \\ y_1 \\ z_1 \end{Bmatrix} = \begin{bmatrix} 1 & 0 & 0 \\ 0 & \cos\alpha & -\sin\alpha \\ 0 & \sin\alpha & \cos\alpha \end{bmatrix} \begin{Bmatrix} x_1' \\ y_1' \\ z_1' \end{Bmatrix} = [T_1] \begin{Bmatrix} x_1' \\ y_1' \\ z_1' \end{Bmatrix} \tag{A.1.1}$$

(2) The second rotation is about the y_1'-axis ($o_1x_1'y_1'z_1'$ to $o_1x_1''y_1''z_1''$) by an angle β which transforms the z_1'-axis to the z_b-axis, as shown in Figure A.3. Then the transformation relationship is:

$$\begin{Bmatrix} x_1' \\ y_1' \\ z_1' \end{Bmatrix} = \begin{bmatrix} \cos\beta & 0 & \sin\beta \\ 0 & 1 & 0 \\ -\sin\beta & 0 & \cos\beta \end{bmatrix} \begin{Bmatrix} x_1'' \\ y_1'' \\ z_1'' \end{Bmatrix} = [T_2] \begin{Bmatrix} x_1'' \\ y_1'' \\ z_1'' \end{Bmatrix} \tag{A.1.2}$$

(3) The final rotation is about the z_1''-axis (that is z_b-axis) by an angle γ to transform x_1''-axis (or y_1''-axis) to x_b-axis(or y_b-axis), as shown in Figure A.4. The transformation relationship is

$$\begin{Bmatrix} x_1'' \\ y_1'' \\ z_1'' \end{Bmatrix} = \begin{bmatrix} \cos\gamma & -\sin\gamma & 0 \\ \sin\gamma & \cos\gamma & 0 \\ 0 & 0 & 1 \end{bmatrix} \begin{Bmatrix} x_b \\ y_b \\ z_b \end{Bmatrix} = [T_3] \begin{Bmatrix} x_b \\ y_b \\ z_b \end{Bmatrix} \tag{A.1.3}$$

where α, β and γ are called Euler angles. The combined transformation matrix from $o_1x_1y_1z_1$ to $o_bx_by_bz_b$ is then:

$$[T] = [T_1][T_2][T_3]. \tag{A.1.4}$$

Substituting equations (A.1.1)-(A.1.3) into equation (A.1.4), it follows that

$$[T] = \begin{bmatrix} \cos\beta\cos\gamma & -\cos\beta\sin\gamma & \sin\beta \\ \sin\alpha\sin\beta\cos\gamma + \cos\alpha\sin\gamma & -\sin\alpha\sin\beta\sin\gamma + \cos\alpha\cos\gamma & -\sin\alpha\cos\beta \\ -\cos\alpha\sin\beta\cos\gamma + \sin\alpha\sin\gamma & \cos\alpha\sin\beta\sin\gamma + \sin\alpha\cos\gamma & \cos\alpha\cos\beta \end{bmatrix}. \tag{A.1.5}$$

The matrices in equations (A.1.1) to (A.1.3) have the following properties:

$$\underset{\text{Inverse}}{[T_i]^{-1}} = \underset{\text{transpose}}{[T_i]'} \qquad (i = 1,2,3)$$

and therefore

$$[T]^{-1} = [T]'. \tag{A.1.5}$$

Noting that the systems $o_1x_1y_1z_1$ and *oxyz* are linked through the following relationship:

$$\begin{Bmatrix} x \\ y \\ z \end{Bmatrix} = \begin{Bmatrix} x_c \\ y_c \\ z_c \end{Bmatrix} + \begin{Bmatrix} x_1 \\ y_1 \\ z_1 \end{Bmatrix}, \tag{A.1.6}$$

one can obtain

$$\begin{Bmatrix} x \\ y \\ z \end{Bmatrix} = \begin{Bmatrix} x_c \\ y_c \\ z_c \end{Bmatrix} + [T] \begin{Bmatrix} x_b \\ y_b \\ z_b \end{Bmatrix}. \tag{A.1.7}$$

Next we will find the relationship between the angular velocity Ω and the Euler angles as well as their derivatives. It is noted that, similarly to the finite rotation above, a general infinitesimal rotation associated with the angular velocity Ω can also be considered as consisting of three successive infinitesimal rotations with angular velocities $\dot{\alpha}, \dot{\beta}$ and $\dot{\gamma}$. Therefore the angular velocity Ω can be determined by the sum of the three separate angular velocity vectors

$$\Omega = \dot{\alpha} + \dot{\beta} + \dot{\gamma}, \tag{A.1.8}$$

where $\dot{\alpha}$, $\dot{\beta}$ and $\dot{\gamma}$ are in the direction of x_1-axis, y_1'-axis and z_b-axis, respectively, as shown in Figure A.2 to A.4. From the rotational process discussed above, $\dot{\alpha}, \dot{\beta}$ and $\dot{\gamma}$ can be written in the moving system $o_b x_b y_b z_b$ as:

$$\begin{Bmatrix} \dot{\alpha}_1 \\ \dot{\alpha}_2 \\ \dot{\alpha}_3 \end{Bmatrix} = [T]^{-1} \begin{Bmatrix} \dot{\alpha} \\ 0 \\ 0 \end{Bmatrix},$$

$$\begin{Bmatrix} \dot{\beta}_1 \\ \dot{\beta}_2 \\ \dot{\beta}_3 \end{Bmatrix} = [T_3]^{-1}[T_2]^{-1} \begin{Bmatrix} 0 \\ \dot{\beta} \\ 0 \end{Bmatrix},$$

$$\begin{Bmatrix}\dot{\gamma}_1\\ \dot{\gamma}_2\\ \dot{\gamma}_3\end{Bmatrix}=[T_3]^{-1}\begin{Bmatrix}0\\0\\\dot{\gamma}\end{Bmatrix},$$

So that

$$\begin{Bmatrix}\Omega_1\\ \Omega_2\\ \Omega_3\end{Bmatrix}=\begin{Bmatrix}\dot{\alpha}\cos\beta\cos\gamma+\dot{\beta}\sin\gamma\\ \dot{\beta}\cos\gamma-\dot{\alpha}\cos\beta\sin\gamma\\ \dot{\gamma}+\dot{\alpha}\sin\beta\end{Bmatrix}. \tag{A.1.9}$$

Finally, the expression for $\frac{d[\hat{T}]}{dt}$ used in Section 3.4 is deduced. Since $[\hat{T}]\equiv[T]^{-1}=[T]'$, the term $\frac{d[\hat{T}]}{dt}$ can be written as

$$\frac{d[\hat{T}]}{dt}=\begin{bmatrix}\frac{d\hat{T}_{11}}{dt} & \frac{d\hat{T}_{12}}{dt} & \frac{d\hat{T}_{13}}{dt}\\ \frac{d\hat{T}_{21}}{dt} & \frac{d\hat{T}_{22}}{dt} & \frac{d\hat{T}_{23}}{dt}\\ \frac{d\hat{T}_{31}}{dt} & \frac{d\hat{T}_{32}}{dt} & \frac{d\hat{T}_{33}}{dt}\end{bmatrix},$$

where

$$\frac{d\hat{T}_{11}}{dt}=-\dot{\beta}\sin\beta\cos\gamma-\dot{\gamma}\cos\beta\sin\gamma,$$

$$\frac{d\hat{T}_{12}}{dt}=\dot{\alpha}(\cos\alpha\sin\beta\cos\gamma-\sin\alpha\sin\gamma)+\dot{\beta}\sin\alpha\cos\beta\cos\gamma+\dot{\gamma}(\cos\alpha\cos\gamma-\sin\alpha\sin\beta\sin\gamma),$$

$$\frac{d\hat{T}_{13}}{dt}=\dot{\alpha}(\sin\alpha\sin\beta\cos\gamma+\cos\alpha\sin\gamma)-\dot{\beta}\cos\alpha\cos\beta\cos\gamma+\dot{\gamma}(\cos\alpha\sin\beta\sin\gamma+\sin\alpha\cos\gamma),$$

$$\frac{d\hat{T}_{21}}{dt}=\dot{\beta}\sin\beta\sin\gamma-\dot{\gamma}\cos\beta\cos\gamma,$$

$$\frac{d\hat{T}_{22}}{dt} = -\dot{\alpha}(\cos\alpha\sin\beta\sin\gamma + \sin\alpha\cos\gamma) - \dot{\beta}\sin\alpha\cos\beta\sin\gamma$$
$$- \dot{\gamma}(\sin\alpha\sin\beta\cos\gamma + \cos\alpha\sin\gamma),$$

$$\frac{d\hat{T}_{23}}{dt} = \dot{\alpha}(\cos\alpha\cos\gamma - \sin\alpha\sin\beta\sin\gamma) + \dot{\beta}\cos\alpha\cos\beta\sin\gamma$$
$$+ \dot{\gamma}(\cos\alpha\sin\beta\cos\gamma - \sin\alpha\sin\gamma),$$

$$\frac{d\hat{T}_{31}}{dt} = \dot{\beta}\cos\beta,$$

$$\frac{d\hat{T}_{32}}{dt} = -\dot{\alpha}\cos\alpha\cos\beta + \dot{\beta}\sin\alpha\sin\beta,$$

and

$$\frac{d\hat{T}_{33}}{dt} = -\dot{\alpha}\sin\alpha\cos\beta - \dot{\beta}\cos\alpha\sin\beta.$$

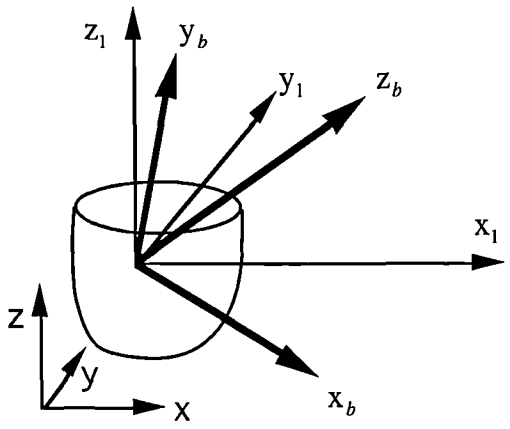

Figure A.1 Two coordinate systems

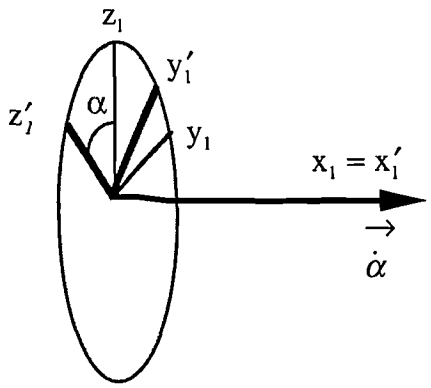

Figure A.2 Rotation about x_1

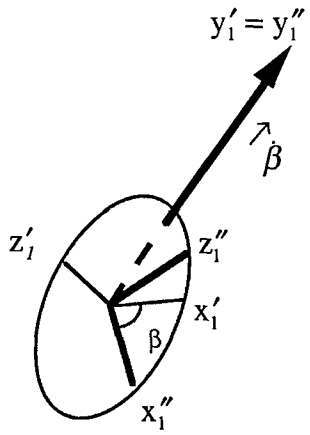

Figure A.3 Rotaion about y_1'

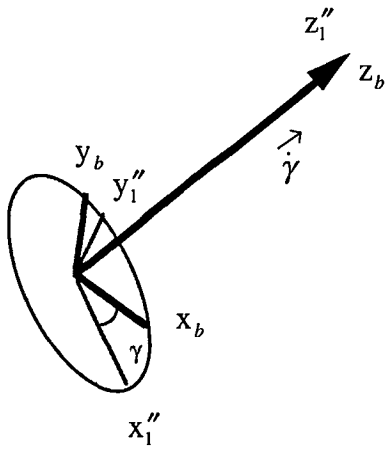

Figure A.4 Rotaion about z_1''

APPENDIX B

Integral Involving the Normal Velocity on a Rigid Boundary

In this appendix, the expression (5.5.10) will be derived. It is assumed that element e_k includes node I and has a common surface (triangle *i-j-m*) with S_n, as shown in the following figure.

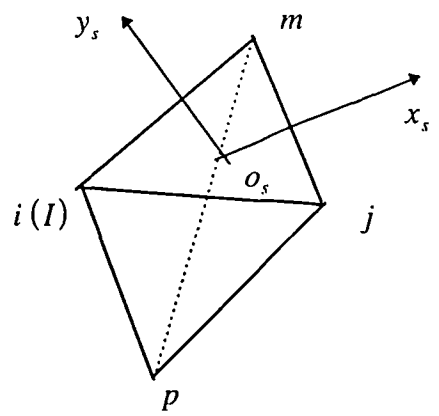

Figure B.1 Element e_k and local coordinate system

For convenience, a local coordinate system $o_s x_s y_s$, in the same plane as the triangle *i-j-m*, is established in Figure B.1 with the origin o_s being defined in such a way that:

$$x_{si} + x_{sj} + x_{sm} = 0 \qquad y_{si} + y_{sj} + y_{sm} = 0\ , \tag{B.1}$$

where (x_{si}, y_{si}), (x_{sj}, y_{sj}) and (x_{sm}, y_{sm}) are the coordinates of node *i*, *j* and *m* in the local system, respectively. On the triangles' surface, a two dimensional shape function is defined in the manner:

$$P_i^{e_k} = \frac{1}{2\Delta}\left(a_{si} + b_{si} x_s + c_{si} y_s\right) \qquad (i = i, j, m)\,, \tag{B.2}$$

where Δ (corresponding to ΔS^e in equation 5.510) is area of the triangle *i-j-m*. The coefficients in (B.2) are determined as:

$$\begin{aligned} a_{si} &= \frac{2\Delta}{3} \\ b_{si} &= y_{sj} - y_{sm} \\ c_{si} &= x_{sm} - x_{sj}. \end{aligned} \tag{B.3}$$

From equations (B.2) and (B.3), it can be verified that:

$$P_i^{e_k} = \begin{cases} 1 & (x_s, y_s) = (x_{si}, y_{si}) \\ 0 & (x_s, y_s) = (x_{sj}, y_{sj}), (x_{sm}, y_{sm}) \end{cases} \qquad i \neq j,m \tag{B.4}$$

and

$$\begin{aligned} b_{si}x_{si} + c_{si}y_{si} &= \frac{4\Delta}{3} \\ b_{si}x_{sj} + c_{si}y_{sj} &= -\frac{2\Delta}{3} \\ b_{si}x_{sm} + c_{si}y_{sm} &= -\frac{2\Delta}{3}. \end{aligned} \tag{B.5}$$

As both $N_i^{e_k}$ in Section 5.5 and $P_i^{e_k}$ here are linear functions, and because both equations (5.4.7) and (B.4) hold, the two shape functions must be equal on the triangular surface *i-j-m*. Therefore the integration on $N_i^{e_k}$ can be replaced by the integration on $P_i^{e_k}$ over the surface *i-j-m*.

Next we consider the following integral over the surface *i-j-m*:

$$\begin{aligned} \iint_{i-j-m} P_i^{e_k} P_j^{e_k} dx_s dy_s = \frac{1}{4\Delta^2} \iint_{i-j-m} \Big[& a_{si}a_{sj} + (a_{si}b_{sj} + a_{sj}b_{si})x + (a_{si}c_{sj} + a_{sj}c_{si})y \\ & (b_{si}b_{sj}x_s^2 + c_{si}c_{sj}y_s^2) + (b_{si}c_{sj} + b_{sj}c_{si})xy \Big] dx_s dy_s. \end{aligned} \tag{B.6}$$

With the use of the following identities (see Zienkiewicz & Taylor 1994):

$$\iint_{i-j-m} x_s dx_s dy_s = \iint_{i-j-m} x_s dx_s dy_s = 0$$

$$\iint_{i-j-m} x_s^2 dx_s dy_s = \frac{\Delta}{12}\left(x_{si}^2 + x_{sj}^2 + x_{sm}^2\right)$$

$$\iint_{i-j-m} y_s^2 dx_s dy_s = \frac{\Delta}{12}\left(y_{si}^2 + y_{sj}^2 + y_{sm}^2\right) \tag{B.7}$$

$$\iint_{i-j-m} x_s y_s dx_s dy_s = \frac{\Delta}{12}\left(x_{si} y_{si} + x_{sj} y_{sj} + x_{sm} y_{sm}\right),$$

and equation (B.5), one can obtain

$$\iint_{i-j-m} P_i^{e_k} P_j^{e_k} dx_s dy_s = \begin{cases} \dfrac{\Delta}{6} & i = j \\ \dfrac{\Delta}{12} & i \neq j \end{cases} \qquad i, j = i, j, m \tag{B.8}$$

In order to calculate $B_{12}^{e_k}$, it is assumed that f_n on the triangle *i-j-m* is linear, and can be expressed as:

$$\begin{aligned} f_n &= \left(f_n\right)_i N_i^{e_k} + \left(f_n\right)_j N_j^{e_k} + \left(f_n\right)_m N_m^{e_k} \\ &= \left(f_n\right)_i P_i^{e_k} + \left(f_n\right)_j P_j^{e_k} + \left(f_n\right)_m P_m^{e_k} \end{aligned} \tag{B.9}$$

on the surface *i-j-m* .

Using equation (B.8), it follows that:

$$\iint_{i-j-m} N_i^{e_k} f_n dx_s dy_s = \iint_{i-j-m} P_i^{e_k} f_n dx_s dy_s = \frac{\Delta}{3}\left[\frac{\left(f_n\right)_i}{2} + \frac{\left(f_n\right)_j}{4} + \frac{\left(f_n\right)_m}{4}\right]. \tag{B.10}$$

If f_n is assumed to be constant, i.e. $\left(f_n\right)_i = \left(f_n\right)_j = \left(f_n\right)_m = f_n$, equation (B.10) then becomes

$$\iint_{i-j-m} N_i^{e_k} f_n dx_s dy_s = \iint_{i-j-m} P_i^{e_k} f_n dx_s dy_s = \frac{\Delta}{3} f_n \tag{B.11}$$

APPENDIX C

Interpolation in a Triangle on the Free Surface

Here, the interpolation in a triangle on the free surface will be discussed. Suppose the nodal values (q_1, q_2, q_3) of a function $q(x,y,z)$ are known on the triangle $a_1a_2a_3$ which is part of the free surface, as shown in Figure C.1 below, where $a_1'a_2'a_3'$ represents the projection of $a_1a_2a_3$ on the *oxy* plane.

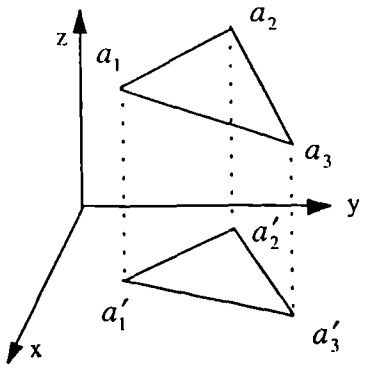

Figure C.1

Similar to the interpolation in an element, the function $q(x,y,z)$ is assumed to be a linear function over the triangle. Noting that a flat triangle itself can be expressed as $z = z(x,y)$ which is also a linear function, $q(x,y,z)$ can therefore be rewritten as $q(x,y)$. Since $q(x,y)$ is a linear function, the interpolation in the triangle $a_1a_2a_3$ can be performed in the triangle $a_1'a_2'a_3'$.

Let $p_j(x,y) = \alpha_j + \beta_j x + \gamma_j y$ be the interpolation function; then $q(x,y)$ is written as

$$q(x,y) = \sum_{j=1}^{3} f_j p_j(x,y) \qquad (j = 1, 2, 3) \tag{C.1}$$

where $p_j(x,y)$ should satisfy:

$$p_j\left(x_{a_i'}, y_{a_i'}\right) = \begin{cases} 1 & i = j \\ 0 & i \neq j \end{cases}, \tag{C.2}$$

in order to ensure $q\left(x_{a_i'}, y_{a_i'}\right) = q_i$. From equation (C.2), one can obtain

$$\begin{cases} \alpha_i = \dfrac{1}{2\Delta}(x_j y_m - y_j x_m \\ \beta_i = \dfrac{1}{2\Delta}\left(y_j - y_m\right) & \left(i, j, m = 1, 2, 3\right) \\ \gamma_i = -\dfrac{1}{2\Delta}\left(x_j - x_m\right) \end{cases} \tag{C.3}$$

where Δ is the area of the triangle $a_1'a_2'a_3'$. The interchange order is:

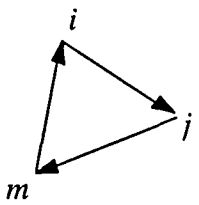

Equation (C.1) can be rewritten in another form, namely:

$$q(x, y) = a + bx + cy, \tag{C.4}$$

where

$$\begin{bmatrix} a \\ b \\ c \end{bmatrix} = \begin{bmatrix} \alpha_1 & \beta_1 & \gamma_1 \\ \alpha_2 & \beta_2 & \gamma_2 \\ \alpha_3 & \beta_3 & \gamma_3 \end{bmatrix} \begin{Bmatrix} q_1 \\ q_2 \\ q_3 \end{Bmatrix} \tag{C.5}$$

Equation (C.4) is frequently used in Chapter 5.

It is should be noted that the above interpolation is not valid when the triangles are perpendicular to the *oxy* plane. This situation corresponds to the angle of the wave slope equal to 90^0. This case is not considered in this work.